
Lattice QCD studies of observables extracted from the hadronic vacuum polarization

Dissertation zur Erlangung des Grades
“Doktor der Naturwissenschaften”
am Fachbereich Physik, Mathematik und Informatik
der Johannes Gutenberg-Universität
in Mainz

Hanno Horch
geb. in Kirchheimbolanden

Mainz, den 8. November 2016

Abstract

Simulations of Quantum Chromodynamics (QCD) on the lattice allow for the computation of observables from first principles at low energies where perturbation theory breaks down. In this study we use lattice QCD to compute the hadronic vacuum polarization (HVP) in order to extract the leading hadronic contribution to the anomalous magnetic moment of the muon (a_μ^{HLO}), the Adler function, and the shift of the running of the fine structure constant ($\Delta\alpha_{\text{QED}}^{\text{had}}$). Our work is based on ensembles generated by the Coordinated Lattice Simulations (CLS) collaboration. We use two dynamical, degenerate, non-perturbatively $O(a)$ -improved Wilson fermions. The strange- and charm-quark contributions are partially quenched. We use partially twisted boundary conditions to increase the momentum resolution of the HVP.

α_{QED} is known to high precision at vanishing momentum, but at the mass of the Z this precision deteriorates by five orders of magnitude, due to hadronic effects. The low-energy hadronic contributions to α_{QED} are currently estimated with dispersive methods. Using lattice QCD we can provide an estimate from first principles. The Adler function is related to the shift of α_{QED} and can be determined from the derivative of the HVP. We extract the Adler function from fits using linear interpolations to obtain the slope of the HVP. Two procedures are presented for the selection of the fit ranges for these interpolations. The Adler function at the physical point is obtained by a simultaneous fit to the Q^2 -behaviour, the lattice spacing, and the pion mass dependence. We explore a number of different ansätze for the simultaneous fits that we use to estimate systematic uncertainties. We find agreement with phenomenology for intermediate $Q^2 \sim 2 - 3 \text{ GeV}^2$ for our four-flavour result. We use the fit results of the Adler function to estimate $\Delta\alpha_{\text{QED}}^{\text{had}}$ at the physical point. Our four-flavour result agrees with the five-flavour result from phenomenology for $0 < Q^2 < 5.0 \text{ GeV}^2$, due to the small effect of the bottom quark at this energy.

a_μ^{HLO} is one of the most precisely measured quantities today, but there is a discrepancy of $\sim 3.6\sigma$ between results from theory and experiment. Since theoretical results are based on dispersive methods using experimental input at low energies, a precise determination of a_μ^{HLO} from first principles is desirable. To determine a_μ^{HLO} one performs a convolution integral. The kernel of the convolution integral has a peak near $Q^2 \sim m_\mu^2$ thus a precise determination of the HVP in this regime is crucial. It is advantageous to use a continuous description in the vicinity of the peak of the convolution integral and switch to a numerical procedure for larger Q^2 . We discuss two strategies for the continuous description, the first uses fits to the HVP, while the second is based on time moments. We estimate systematic uncertainties by testing several ansätze for the continuum and chiral extrapolation. We observe a difference of $\sim 1.2\sigma$ between our four-flavour result and the result based on the dispersive approach.

Zusammenfassung

Gittersimulationen der Quantenchromodynamik (QCD) ermöglichen die Berechnung von Observablen bei niedrigen Energien, bei denen Störungstheorie nicht anwendbar ist, von ersten Prinzipien ausgehend. Wir nutzen Gitter-QCD, um die hadronische Vakuumpolarisation (HVP) zu bestimmen. In dieser Arbeit bestimmen wir aus der HVP den führenden Beitrag zum anomalen magnetischen Moments des Muons (a_μ^{HLO}), den hadronischen Beitrag zur Adler-Funktion sowie den hadronischen Anteil der Änderung der laufenden elektromagnetischen Kopplung ($\Delta\alpha_{\text{QED}}^{\text{had}}$). Unsere Berechnungen basieren auf Ensembles der Coordinated Lattice Simulations (CLS) Kollaboration. Diese verwenden nicht-perturbative $O(a)$ -verbesserte Wilson-Fermionen mit zwei dynamischen, entarteten leichten Quarks. Wir benutzen “partially twisted” Randbedingungen, um eine höhere Impulsauflösung der HVP zu erreichen. In dieser Arbeit werden Strange- und Charm-Quarks nur als Valenzquarks behandelt.

α_{QED} ist bei verschwindendem Impuls mit hoher Präzision bekannt, aber bei der Masse des Z reduziert sich diese Präzision um fünf Größenordnungen durch hadronische Effekte, die zur Zeit mit dispersiven Methoden bestimmt werden. Mittels Gitter-QCD ist es möglich, bei niedrigen Energien den hadronischen Beitrag zu α_{QED} von ersten Prinzipien ausgehend zu bestimmen. Die Adler-Funktion wird definiert über die Änderung von α_{QED} und kann aus der Ableitung der HVP berechnet werden. Wir erhalten die Adler-Funktion aus Fits basierend auf linearen Interpolationen, mit denen wir die Steigung der HVP abschätzen. Wir präsentieren zwei Prozeduren, um die Fitintervalle für diese Interpolationen auszuwählen. Durch simultane Fits an die Q^2 -Abhängigkeit, den Gitterabstand und die Pionmassenabhängigkeit bestimmen wir die Adler-Funktion am physikalischen Punkt. Um systematische Unsicherheiten abzuschätzen verwenden wir verschiedene Ansätze für den simultanen Fit. Unser vier Quark-Flavour Resultat stimmt mit dem der Phänomenologie für $Q^2 \sim 2 - 3 \text{ GeV}^2$ überein. Aus den Resultaten für die Adler-Funktion bestimmen wir $\Delta\alpha_{\text{QED}}^{\text{had}}$ am physikalischen Punkt. Da das bottom-Quark nur einen geringen Einfluss bei diesen Energien hat, stellen wir Übereinstimmung von unserem Vier-Flavour Resultat mit dem Fünf-Flavour Resultat aus der Phänomenologie fest.

a_μ^{HLO} gehört zu den am besten bestimmten Größen, aber derzeit besteht eine Diskrepanz von $\sim 3.6\sigma$ zwischen Theorie und Experiment. Da die theoretischen Resultate auf Dispersionsrelationen basieren, sind präzise Berechnungen von ersten Prinzipien ausgehend gefragt. Um a_μ^{HLO} zu bestimmen, wird ein Konvolutionsintegral ausgewertet. Der Integrand hat ein Maximum in der Nähe von $Q^2 \sim m_\mu^2$, daher ist eine präzise Bestimmung der HVP in diesem Regime wichtig. Es ist vorteilhaft in der Nähe des Maximums des Integranden eine kontinuierliche Beschreibung anzuwenden und für große Q^2 zu einer numerischen Beschreibung überzugehen. Wir diskutieren zwei Strategien für die kontinuierliche Beschreibung. Bei der ersten handelt es sich um Fits an die HVP und die

zweite basiert auf zeitlichen Momenten. Um systematische Unsicherheiten abzuschätzen verwenden wir mehrere Ansätze für die Kontinuums- und chirale Extrapolation. Zwischen unserem Vier-Flavour Resultat und dem Ergebnis aus Dispersionsrelationen besteht eine Differenz von $\sim 1.2\sigma$.

Contents

Contents	iv
1 Introduction	2
1.1 Motivation	2
1.2 Particle content and symmetries of the Standard Model	3
1.3 QCD in the continuum	4
1.4 QCD on the lattice	6
1.4.1 Discretisation of the QCD action	6
1.4.2 Symanzik improvement	11
1.4.3 Monte Carlo	13
1.4.4 Generation of gauge configurations	14
1.4.5 The Hybrid Monte Carlo	15
1.4.6 Example of a thermalization process	16
1.4.7 Auto-correlations of configurations	20
1.4.8 Measurement of observables	20
1.4.9 The statistical bootstrap method	24
1.4.10 The extended frequentist method	24
1.4.11 Scale setting and physical results	27
2 The hadronic vacuum polarization	30
2.1 Determination of the hadronic vacuum polarization on the lattice	30
2.1.1 Definitions, lattice regularization, and renormalization	30
2.1.2 Partially twisted boundary conditions	33
2.1.3 Lattice setup	35
2.2 Ward identities of the vacuum polarization	37
3 The running of $\alpha_{\text{QED}}^{\text{had}}$ from the Adler function	41
3.1 The running of α_{QED} and the definition of the Adler function	41
3.2 The Adler function extracted from lattice data of the hadronic vacuum polarization	44
3.2.1 Methods to determine the Adler function	44
3.2.1.1 Method 1: Plateau of Slopes method	44
3.2.1.2 Method 2: Curvature Limit method	47
3.2.2 Extrapolation of the Adler function to the physical point	53
3.2.2.1 The light-quark contribution	55
3.2.2.2 The strange-quark contribution	60
3.2.2.3 The charm-quark contribution	65

3.2.2.4	Summed contributions and comparison to perturbative QCD	71
3.3	Determination of the running of α_{QED} from the Adler function on the lattice	72
3.3.1	The light-quark contribution	72
3.3.2	The strange-quark contribution	74
3.3.3	The charm-quark contribution	75
3.3.4	Summed contributions and comparison to phenomenology	76
3.3.5	Conclusions	78
3.3.5.1	Remarks on the Adler function	78
3.3.5.2	Remarks on the calculation of $\Delta\alpha_{\text{QED}}^{\text{had}}$	79
4	The anomalous magnetic moment of the muon	81
4.1	a_μ from experiment	81
4.2	a_μ from theory	82
4.3	Extraction of the hadronic anomalous magnetic moment of the muon from lattice data	84
4.3.1	The extraction of a_μ^{HLO} with the hybrid method	87
4.3.1.1	The light-quark contribution	89
4.3.1.2	The strange-quark contribution	90
4.3.1.3	The charm-quark contribution	92
4.3.2	The extraction of a_μ^{HLO} via time moments	96
4.3.2.1	The light-quark contribution	102
4.3.2.2	The strange-quark contribution	103
4.3.2.3	The charm-quark contribution	106
4.3.3	The extrapolation to the physical point for a_μ^{HLO}	110
4.3.3.1	The light-quark contribution	110
4.3.3.2	The strange-quark contribution	116
4.3.3.3	The charm-quark contribution	117
4.3.4	Results at the physical point for a_μ^{HLO}	120
4.3.5	Determination of a_μ^{HLO} via the Adler function	122
4.3.6	Comparison of a_μ^{HLO} from different methods	124
4.3.7	Conclusions	125
5	Conclusions and Outlook	129
A	Definitions	133
A.1	Generators of $SU(3)$	133
A.2	Link differential operator	134
A.3	Euclidean gamma matrices	134
A.4	Derivation of the hadronic vacuum polarization	135
B	Fit results for the extrapolation of the Adler function to the continuum	138
B.1	The light quark contribution: the Curvature Limit method.	138
B.2	The strange quark contribution: the Curvature Limit method.	141
B.3	The charm quark contribution: the Curvature Limit method.	143

B.4	a_μ^{HLO} determined via the Adler function	146
C	Fit results for the extraction of a_μ^{HLO}	149
C.1	Fits to the VPF for the hybrid method	149
C.1.1	The light-quark contribution	149
C.1.1.1	Fit ansatz: Padé [1,1]	149
C.1.1.2	Fit ansatz: Padé [2,1]	159
C.1.2	The strange-quark contribution	169
C.1.2.1	Fit ansatz: Padé [1,1]	169
C.1.2.2	Fit ansatz: Padé [2,1]	180
C.1.3	The light-quark contribution	191
C.1.3.1	Fit ansatz: Padé [1,1]	191
C.1.3.2	Fit ansatz: Polynomial of $O(Q^2)$	202
C.2	Results for the time moments	213
C.2.1	The light-quark contribution	213
C.2.2	The strange-quark contribution	214
C.2.3	The charm-quark contribution	219
C.3	The extrapolation to the physical point	223
C.3.1	Results for the hybrid method	223
C.3.1.1	The light-quark contribution	223
C.3.2	Results for a_μ^{HLO} via time moments	223
C.3.2.1	The light-quark contribution	223
	List of Figures	227
	List of Tables	231
	Bibliography	234

Publications

Parts of this work have already been presented in:

- A. Francis, V. Gülpers, G. Herdoíza, H. Horch, B. Jäger, H. B. Meyer and H. Wittig, *Study of the hadronic contributions to the running of the QED coupling and the weak mixing angle*, PoS LATTICE **2015** (2015) 110 arXiv:1511.04751.
- M. Della Morte, G. Herdoiza, H. Horch, B. Jäger, H. Meyer and H. Wittig, *The hadronic vacuum polarization function with $O(a)$ -improved Wilson fermions - an update*, PoS LATTICE **2015** (2015) 111 arXiv:1602.03976.
- A. Francis, G. Herdoíza, H. Horch, B. Jäger, H. B. Meyer and H. Wittig, *Study of the Couplings of QED and QCD from the Adler Function*, PoS LATTICE **2014** (2014) 163 arXiv:1412.6934.
- M. Bruno, H. Horch *et al.*, *Simulation of QCD with $N_f = 2 + 1$ flavors of non-perturbatively improved Wilson fermions*, JHEP **1502** (2015) 043 doi:10.1007/JHEP02(2015)043 arXiv:1411.3982.
- A. Francis, H. Horch *et al.*, *Lattice QCD Studies of the Leading Order Hadronic Contribution to the Muon $g - 2$* , arXiv:1411.3031.
- M. Della Morte, A. Francis, G. Herdoiza, H. Horch, B. Jäger, A. Jüttner, H. Meyer and H. Wittig, *Study of the anomalous magnetic moment of the muon computed from the Adler function*, PoS LATTICE **2014** (2014) 162 arXiv:1411.1206.
- A. Francis, V. Gülpers, G. Herdoiza, H. Horch, B. Jäger, H. B. Meyer and H. Wittig, *The leading hadronic contribution to $(g-2)$ of the muon: The chiral behavior using the mixed representation method*, PoS LATTICE **2014** (2015) 127 arXiv:1410.7491.
- B. B. Brandt, H. Horch *et al.*, *Low-Energy Precision Physics and Lattice QCD*,
- G. Herdoiza, H. Horch, B. Jäger and H. Wittig, *Fitting the Lattice Vacuum Polarisation Function to Perturbation Theory*, PoS LATTICE **2013** (2014) 444.
- H. Horch, G. Herdoíza, B. Jäger, H. Wittig, M. Della Morte and A. Jüttner, *Computing the Adler function from the vacuum polarization function*, PoS LATTICE **2013** (2014) 304 arXiv:1311.6975.

Chapter 1

Introduction

1.1 Motivation

The Standard Model (SM) predicts many processes reliably to a very high precision. But we can also think of the SM as an effective theory which is only valid in a certain energy range. There are two approaches to find the limitations of the SM. One way is to increase the energy in experiments in search for new physics for which the Large Hadron Collider (LHC) is the prime example. Such machines search for signals of new particles that are predicted in various theoretical extensions of the SM. Of course the scale of experiments of this type lead to very long planning and construction times.

Another approach is to perform more precise measurements of observables, for which there is either some tension or even a discrepancy between experiment and theory, at lower energies. One such case is the anomalous magnetic moment of the muon (a_μ) given by

$$a_\mu = \frac{g_\mu - 2}{2}, \quad (1.1)$$

which is one of the most precisely known observables today. There is currently a discrepancy of $\sim 3.6\sigma$ between the estimates from theory and experiment [1],

$$a_\mu^{\text{exp}} = 116\,592\,091(54)(33) \cdot 10^{-11}, \quad (1.2)$$

$$a_\mu^{\text{th}} = 116\,591\,803(1)(42)(26) \cdot 10^{-11}. \quad (1.3)$$

The hadronic contribution dominates the uncertainty of the theoretical determination, which relies on a dispersive approach. As experiments reach higher precision in their measurements, as for instance in the planned $(g - 2)$ experiment at Fermilab [2], and test new extensions of the SM like the *dark photon* [3–5], e.g. at MAMI (Mainz) [6],

more precise calculations from theory are needed. The weak and electromagnetic sector can be described very well by perturbation theory. The same holds for the strong force, described by Quantum Chromodynamics [QCD], at large energies, where the coupling decreases. This effect is known as asymptotic freedom [7], and Gross, Politzer and Wilczek received the Nobel prize in 2004 for its discovery. At low energies perturbation theory is no longer applicable because the coupling increases and thus higher order contributions can no longer be considered small corrections. There are various ways to approach this problem. Chiral perturbation theory can provide an expansion on the light-quarks mass of a class of hadronic observables. However, the low-energy constants, corresponding to the various coefficients of the expansion, are not fixed by the effective theory itself and need to be determined by a combination of experimental and theoretical input. Another approach is to simulate QCD on a lattice of discretised space-time, which allows to calculate observables from first principles. The only input needed from the physics point of view in these simulations are the coupling and the quark masses. With lattice QCD we can estimate the leading order hadronic contribution to a_μ using the renormalized hadronic vacuum polarization $\hat{\Pi}(Q^2)$,

$$a_\mu^{\text{HLO}} = \left(\frac{\alpha}{\pi}\right)^2 \int_0^\infty dQ^2 f(Q^2) \hat{\Pi}(Q^2), \quad (1.4)$$

$$f(Q^2) = \frac{m_\mu^2 Q^2 Z^3 (1 - Q^2 Z)}{1 + Q m_\mu^2 Q^2 Z^2}, \quad Z = -\frac{Q^2 - \sqrt{Q^4 + 4m_\mu^2 Q^2}}{2m_\mu^2 Q^2}. \quad (1.5)$$

The convolution integral is peaked close to the squared muon mass, thus the HVP is required at this range with high precision.

We continue with a brief presentation of the SM and QCD in the continuum before introducing QCD on the lattice.

1.2 Particle content and symmetries of the Standard Model

The Standard Model of particle physics is one of the most successful theories known today. The particle content is shown in figure 1.1. It is based on the fundamental gauge principle with the full symmetry group

$$SU(3) \times SU(2)_L \times U(1)_Y. \quad (1.6)$$

$SU(2)_L \times U(1)_Y$ refers to the electroweak interactions. These interactions are mediated by the massless photon (γ), and the massive Z and W . The index L refers to the chirality of the fermions. Y refers to the hypercharge. This symmetry is spontaneously broken to $SU(2)_L \times U(1)_Y \rightarrow U(1)_{em}$ by the Higgs mechanism, which gives rise to masses of

u	c	t	g	H
d	s	b	γ	
e	μ	τ	Z	
ν_e	ν_μ	ν_τ	W	

FIGURE 1.1: Particle content of the Standard Model of particle physics.

the Z and W gauge bosons. The charged leptons (e, μ, τ) and quarks (u, d, c, s, t, b) receive masses through Yukawa-coupling to the Higgs-boson. Neutrinos (ν_e, ν_μ, ν_τ) are massless in the SM, but many extensions of the SM expect them to be massive. Since the discovery of neutrino-oscillation, we know that neutrinos have to be massive, because neutrino-oscillation would not be possible for vanishing neutrino masses. Arthur McDonald and Takaaki Kajita received the Nobel prize in 2015 for the experimental discovery of neutrino-oscillation. The strong force has the symmetry group $SU(3)$ with the gluon (g) as gauge boson. Only the quarks interact via the strong force, which is for example responsible for the binding energy of nuclei. The particle content of the SM has recently been completed by the discovery of the Higgs boson at the Large Hadron Collider (LHC) at CERN [8, 9]. Peter Higgs and François Englert were awarded the Nobel prize for their theoretical prediction of the Higgs-boson in 2013.

1.3 QCD in the continuum

QCD is given by the gauge theory fulfilling local $SU(3)$ symmetry transformations. The Euclidean action of QCD in the continuum is given by

$$S_{QCD} = \int d^4x \sum_f^{N_f} \bar{\psi}^{(f)}(x) [\gamma_\mu D_\mu(x) + m^{(f)}] \psi^{(f)}(x) + \frac{1}{4g^2} \text{Tr} [F_{\mu\nu} F^{\mu\nu}], \quad (1.7)$$

with the quark mass m_f for each flavor, g represents the gauge coupling, $\bar{\psi}$ and ψ are the quark fields. The gauge fields A_μ enter via the covariant derivative $D_\mu = \partial_\mu + iA_\mu(x)$ and γ_μ are 4×4 matrices acting in Dirac space. To preserve local $SU(3)$ symmetry the quark fields transform as

$$\psi(x) \rightarrow \psi'(x) = \Omega(x)\psi(x), \quad \bar{\psi}(x) \rightarrow \bar{\psi}'(x) = \bar{\psi}(x)\Omega^\dagger(x), \quad (1.8)$$

and the gauge fields as

$$A_\mu(x) \rightarrow A'_\mu(x) = \Omega(x)A_\mu(x)\Omega^\dagger(x) + i(\partial_\mu\Omega(x))\Omega^\dagger(x), \quad (1.9)$$

where $\Omega(x) \in SU(3)$ is a 3×3 matrix acting in colour space, which depends on space time. $F_{\mu\nu}$ is the field strength tensor given by

$$F_{\mu\nu}(x) = \sum_{i=1}^8 F_{\mu\nu}^{(i)}(x)T_i, \quad (1.10)$$

$$F_{\mu\nu}^{(i)}(x) = \partial_\mu A_\nu^{(i)}(x) - \partial_\nu A_\mu^{(i)}(x) - f_{ijk}A_\mu^{(j)}(x)A_\nu^{(k)}(x), \quad (1.11)$$

where T_i are the 8 generators of $SU(3)$ defined by $[T_i, T_j] = if_{ijk}T_k$ with the structure constants f_{ijk} of $SU(3)$. Since $SU(3)$ is a non-abelian symmetry the trace in color space of the field strength tensor in eq. (1.7) leads to three- and four-point self-interactions of gauge fields, illustrated in figure 1.2.

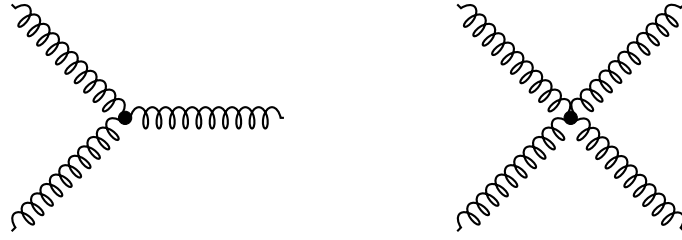


FIGURE 1.2: Diagrams for the self-interactions of gluons.

In the limit of vanishing quark masses eq. (1.7) is invariant under chiral rotations of the quark fields,

$$\psi \rightarrow \psi' = e^{i\alpha\gamma_5}\psi, \quad \bar{\psi} \rightarrow \bar{\psi}' = \bar{\psi}e^{i\alpha\gamma_5}. \quad (1.12)$$

This chiral symmetry leads to the definition of the projectors

$$P_R = \frac{\mathbb{1} + \gamma_5}{2}, \quad P_L = \frac{\mathbb{1} - \gamma_5}{2}, \quad (1.13)$$

which have the properties

$$P_{R/L}^2 = P_{R/L}, \quad P_R P_L = P_L P_R = 0, \quad P_R + P_L = \mathbb{1} \quad (1.14)$$

$$\gamma_\mu P_L = P_R \gamma_\mu, \quad \gamma_\mu P_R = P_L \gamma_\mu. \quad (1.15)$$

These projectors act on the fermion fields as

$$\psi_R = P_R \psi, \quad \psi_L = P_L \psi, \quad \bar{\psi}_R = \bar{\psi} P_L, \quad \bar{\psi}_L = \bar{\psi} P_R. \quad (1.16)$$

With these projectors eq. (1.7) can be written in terms of the left and right handed quark fields,

$$S_{QCD} = \int dx^4 \sum_f^{N_f} \bar{\psi}_L^{(f)}(x) \not{D}(x) \psi_L^{(f)}(x) + \bar{\psi}_R^{(f)}(x) \not{D}(x) \psi_R^{(f)}(x) + m^{(f)} \left(\bar{\psi}_R^{(f)}(x) \psi_L^{(f)}(x) + \bar{\psi}_L^{(f)}(x) \psi_R^{(f)}(x) \right) + \frac{1}{4g^2} \text{Tr} [F_{\mu\nu} F^{\mu\nu}], \quad (1.17)$$

where we used the abbreviation $\not{D} = \gamma_\mu D_\mu$ and found that left and right handed quark fields only mix in the mass term $m^{(f)}(\dots)$. In the chiral limit, i.e. for vanishing quark masses, left and right handed quark fields decouple.

Furthermore, S_{QCD} is invariant under charge conjugation C , time reversal T , and parity transformations P .

1.4 QCD on the lattice

There are several steps from the continuum theory to QCD on the lattice. First one has to discretise space-time and in order to perform simulations the volume has to be finite. The next step is the discretisation of the action. The lattice field theory is then quantized by the Euclidean path integral. Observables are obtained through Monte Carlo techniques. In the following we will give a brief introduction to lattice QCD based on [10]¹.

1.4.1 Discretisation of the QCD action

To perform simulations of QCD a discretisation of space-time is required,

$$\Lambda = \{n = (n_0, n_1, n_2, n_3) \mid n_\mu = 0, 1, \dots, N_\mu - 1, \text{ for } \mu = 0, 1, 2, 3\}, \quad (1.18)$$

where we introduced a finite volume, which is necessary since any simulation run on a computer will have only a finite amount of memory. For many applications it is advantageous to choose an asymmetric lattice where the time extent is $N_0 = 2N_i$ for $i = 1, 2, 3$. For example this allows for a more reliable determination of ground states of correlation functions, avoiding contamination by excited states.

To introduce the gauge field on the lattice we consider the gauge transporter, which is given by the path-ordered exponential integral of the gauge field A_μ along some curve

¹There are a number of books and reviews available that include detailed introductions to the topic [10–14].

C_{xy} that connects the points x and y given by

$$G(x, y) = P \exp \left(i \int_{C_{xy}} A \cdot ds \right). \quad (1.19)$$

The transporter transforms as

$$G(x, y) \rightarrow \Omega(x)G(x, y)\Omega^\dagger(y). \quad (1.20)$$

The gauge field on the lattice is basically a special case of the gauge transporter in the continuum, i. e. $U_\mu(n) = G(n, n + \hat{\mu}) + O(a)$. $U_\mu(n)$ connects two neighbouring points on the lattice n and $n + \hat{\mu}$, thus $U_\mu(n)$ can be interpreted as the lattice version of the gauge transporter. The $U_\mu(n)$ are also called link variables and transform as

$$U_\mu(n) \rightarrow U'_\mu(n) = \Omega(n)U_\mu(n)\Omega^\dagger(n + \hat{\mu}). \quad (1.21)$$

Since the gauge fields on the lattice are elements of the gauge symmetry group one has to transport gauge fixing conditions also to the lattice formulation. The link variables can be written in terms of the algebra-valued lattice gauge fields $A_\mu(n)$,

$$U_\mu(n) = \exp [iaA_\mu(n)]. \quad (1.22)$$

For example for temporal gauge, which is given by $A_0(x) = 0$ in the continuum, the lattice equivalent is $U_0(n) = \mathbb{1}$, i.e. setting all time-like links to $\mathbb{1}$. In the continuum gauge fixing is required to avoid zero-modes by pure gauges, which lead to singularities of the gluon propagator. On the lattice this is not required, but one may choose to use a particular gauge to simplify a calculation. In this work no gauge fixing is used. The link variables are illustrated in figure 1.3.

The plaquette is the shortest, nontrivial closed loop of link variables:

$$U_{\mu\nu}(n) = U_\mu(n)U_\nu(n + \hat{\mu})U_\mu^\dagger(n + \hat{\nu})U_\nu^\dagger(n), \quad (1.23)$$

which is illustrated in figure 1.3, and transforms under gauge transformations as

$$U_{\mu\nu}(n) \rightarrow U'_{\mu\nu}(n) = \Omega(n)U_{\mu\nu}(n)\Omega^\dagger(n). \quad (1.24)$$

Thus the trace of a plaquette is gauge invariant. The Wilson gauge action written in terms of the plaquette reads

$$S_G[U] = \frac{2}{g^2} \sum_{n \in \Lambda} \sum_{\mu < \nu} \text{Re}(\text{Tr} [\mathbb{1} - U_{\mu\nu}(n)]), \quad (1.25)$$

where each plaquette is counted only in one direction hence $\mu < \nu$ and the factor $2/g^2$ ensures that the gauge action on the lattice approaches the gauge action in the continuum limit $a \rightarrow 0$.

The quark fields are located on lattice sites, i.e. $\psi(x) \rightarrow \psi(n)$, $\bar{\psi}(x) \rightarrow \bar{\psi}(n)$ with

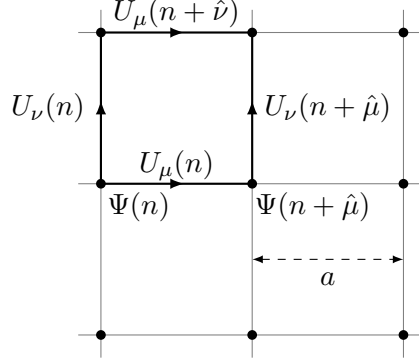


FIGURE 1.3: Illustration of the discretisation of the quark and gauge fields. The quark fields are located on lattice sites while the gauge fields are represented by the links between lattice sites. The plaquette is minimal non trivial closed loop of gauge fields and is the basic quantity required for the gluon action. The lattice spacing is given by a .

$n \in \Lambda$. Since quark fields are fermions they have to be implemented as Grassmann numbers, which means they have to obey the anti-commutation rules

$$\left\{ \psi_{\alpha,a}^{(f)}(n), \psi_{\alpha',a'}^{(f')}(n') \right\} = \left\{ \bar{\psi}_{\alpha,a}^{(f)}(n), \bar{\psi}_{\alpha',a'}^{(f')}(n') \right\} = \left\{ \bar{\psi}_{\alpha,a}^{(f)}(n), \psi_{\alpha',a'}^{(f')}(n') \right\} = 0, \quad (1.26)$$

for all combinations of indices f, f' (flavour), n, n' (lattice coordinates), α, α' (Dirac indices), and a, a' (colour). Furthermore, we need a discretised derivative to compute the fermion action on the lattice

$$\partial_{\mu} \psi(x) = \frac{1}{2a} (\psi(n + \hat{\mu}) - \psi(n - \hat{\mu})). \quad (1.27)$$

In the free case, ($U_{\mu}(n) = \mathbb{1}$), the fermion action is given by

$$S_F[\psi, \bar{\psi}, U = \mathbb{1}] = a^4 \sum_{n \in \Lambda} \bar{\psi}(n) \left(\sum_{\mu=1}^4 \frac{\gamma_{\mu}}{2a} [\psi(n + \hat{\mu}) - \psi(n - \hat{\mu})] + M\psi(n) \right), \quad (1.28)$$

where M is the fermion mass. We can rewrite this action to

$$S_F[\psi, \bar{\psi}, U] = a^4 \sum_{n \in \Lambda} \sum_{a,b,\alpha,\beta} \bar{\psi}_{\alpha}^a(n) D_{\alpha\beta}^{ab}(n|m) \psi_{\beta}^b(m), \quad (1.29)$$

where we used the Dirac operator in the free case

$$D_{\alpha\beta}^{ab}(n|m) = \sum_{\mu=1}^4 \frac{(\gamma_{\mu})_{\alpha\beta}}{2a} \left[\delta^{ab} \delta_{n+\hat{\mu},m} - \delta^{ab} \delta_{n-\hat{\mu},m} \right] + M \delta_{\alpha\beta} \delta^{ab} \delta_{nm}. \quad (1.30)$$

The Fourier transform of the free Dirac operator on the lattice is given by

$$\tilde{D}(p) = M\mathbb{1} + \frac{i}{a} \sum_{\mu=1}^4 \gamma_{\mu} \sin(p_{\mu}a), \quad (1.31)$$

and its inverse, which is required to compute the quark propagator $D^{-1}(n|m)$, reads

$$\tilde{D}^{-1}(p) = \frac{M\mathbb{1} - ia^{-1} \sum_{\mu} \gamma_{\mu} \sin(p_{\mu}a)}{M^2 + a^{-2} \sum_{\mu} \sin(p_{\mu}a)^2}. \quad (1.32)$$

From this relation we see that in the massless case ($M = 0$) the momentum space propagator $\tilde{D}^{-1}(p)$ has a physical pole at $p = (0, 0, 0, 0)$ but also 15 unphysical poles for $p = (\pi/a, 0, 0, 0), (0, \pi/a, 0, 0), \dots, (\pi/a, \pi/a, \pi/a, \pi/a)$. These poles are called doublers. The Nielsen-Ninomiya theorem [15–17] states that there is no Dirac operator on the lattice that is

1. hermitian and local,
2. preserves chiral symmetry,
3. approaches the correct continuum limit,
4. and has only one fermion species.

The conditions (1) and (3) can not be violated if the simulations should connect to the physical world. There are different formulations of the fermion action that either have multiple fermion species or break chiral symmetry. An example for the first are staggered fermions, which preserve chiral symmetry and reduce the number of fermion species to four [18]. Here we will discuss the action proposed by Wilson [19]. The doublers can be removed by adding a term to the momentum space Dirac operator,

$$\tilde{D}(p) = M\mathbb{1} + \frac{i}{a} \sum_{\mu=1}^4 \gamma_{\mu} \sin(p_{\mu}a) + \frac{\mathbb{1}}{a} \sum_{\mu=1}^4 (1 - \cos(p_{\mu}a)), \quad (1.33)$$

while explicitly breaking chiral symmetry. The additional term acts like a mass term such that the doublers have the mass $M + 2l/a$ where l is the number of momentum components with $p_{\mu} = \pi/a$. In the continuum limit the mass of the doublers is increased and they decouple from the theory, thus leaving only the physical pole.

When we want to include interactions of fermions with gauge fields, i.e. $U_\mu(n) \neq \mathbb{1}$, the simple derivative of eq. (1.27) is insufficient, since the action we obtain with it is not gauge invariant. We introduce the covariant derivative on the lattice,

$$\nabla_\mu \psi(n) = \frac{1}{a} [U_\mu(n) \psi(n + \hat{\mu}) - \psi(n)], \quad (1.34)$$

$$\nabla_\mu^* \psi(n) = \frac{1}{a} [\psi(n) - U_\mu^\dagger(n - \hat{\mu}) \psi(n - \hat{\mu})]. \quad (1.35)$$

With this notation the Wilson-Dirac operator in position space reads

$$D^{(f)} = \frac{1}{2} [\gamma_\mu (\nabla_\mu^* + \nabla_\mu) - a \nabla_\mu^* \nabla_\mu] + M^{(f)}, \quad (1.36)$$

where we used the bare quark mass $M^{(f)}$ for each flavour. Then the fermion action is given by

$$S_F^{(f)}[\psi, \bar{\psi}, U] = a^4 \sum_n \bar{\psi}^{(f)}(n) D^{(f)} \psi^{(f)}(n). \quad (1.37)$$

Thus the complete Wilson action then reads

$$\begin{aligned} S_{\text{Wilson}}[\psi, \bar{\psi}, U] &= S_G[U] + S_F[\psi, \bar{\psi}, U] \\ &= \frac{2}{g^2} \sum_{n \in \Lambda} \sum_{\mu < \nu} \text{Re}(\text{Tr}[\mathbb{1} - U_{\mu\nu}(n)]) + \\ &\quad a^4 \sum_{f=1}^{N_f} \sum_{n \in \Lambda} \bar{\psi}^{(f)}(n) D^{(f)} \psi^{(f)}(n). \end{aligned} \quad (1.38)$$

Another representation of the Dirac operator is

$$D = C(\mathbb{1} - \kappa H) \quad \text{with} \quad \kappa = \frac{1}{2(am + 4)}, \quad C = m + \frac{4}{a}, \quad (1.39)$$

$$H_{\alpha\beta}^{ab} = \sum_{\mu=\pm 1}^{\pm 4} (\mathbb{1} - \gamma_\mu)_{\alpha\beta} U_\mu^{ab}(n) \delta_{n+\hat{\mu}, m}, \quad (1.40)$$

where the nearest neighbour terms of the Dirac operator are collected in H , which is also called hopping matrix. κ is a real number and is referred to as hopping parameter. The constant C is usually absorbed in a redefinition of the quark fields $\psi \rightarrow \psi\sqrt{C}$, $\bar{\psi} \rightarrow \bar{\psi}\sqrt{C}$. In this work we follow this notation and list the hopping parameter κ of the different quark flavours instead of listing quark masses directly.

1.4.2 Symanzik improvement

Due to the derivatives involved in eq. (1.38) lattice artefacts in the Wilson action are of $O(a)$ for the fermionic part and of $O(a^2)$ for the gluonic part. Symanzik proposed a method to systematically remove lattice artefacts order by order [20, 21]. For any lattice action with a finite lattice spacing a , we can add additional terms which vanish in the continuum limit. To this end we interpret the lattice action as an effective action given by

$$S_{\text{eff}} = \int d^4x \left(L^{(0)}(x) + aL^{(1)}(x) + a^2L^{(2)}(x) + \dots \right), \quad (1.41)$$

where the higher order terms $L^{(k)}$ are to be constructed of gauge and fermion fields in such a way that they have mass dimensions of $k + 4$. This may be achieved by using additional derivatives or factors of the quark mass M . We use

$$\vec{D}_\mu(x)\psi(x) = [\partial_\mu + A_\mu(x)]\psi(x), \quad (1.42)$$

$$\bar{\psi}(x)\overleftarrow{D}_\mu(x) = \bar{\psi}(x) \left[\overleftarrow{\partial}_\mu - A_\mu(x) \right], \quad (1.43)$$

as the covariant derivative in this case. The possible dimension-5 operators for the leading correction $L^{(1)}$ have to be invariant under gauge and parity transformations, charge-conjugation, and discrete rotations [22], thus there are five possible terms,

$$L_1^{(1)}(x) = \bar{\psi}(x)\sigma_{\mu\nu}F_{\mu\nu}(x)\psi(x), \quad (1.44)$$

$$L_2^{(1)}(x) = \bar{\psi}(x)\vec{D}_\mu(x)\vec{D}_\mu(x)\psi(x) + \bar{\psi}(x)\overleftarrow{D}_\mu(x)\overleftarrow{D}_\mu(x)\psi(x), \quad (1.45)$$

$$L_3^{(1)}(x) = M \text{Tr} [F_{\mu\nu}(x)F_{\mu\nu}(x)], \quad (1.46)$$

$$L_4^{(1)}(x) = M \left(\bar{\psi}(x)\gamma_\mu\vec{D}_\mu(x)\psi(x) - \bar{\psi}(x)\gamma_\mu\overleftarrow{D}_\mu(x)\psi(x) \right), \quad (1.47)$$

$$L_5^{(1)}(x) = M^2\bar{\psi}(x)\psi(x), \quad (1.48)$$

where we used the abbreviation $\sigma_{\mu\nu} = \frac{1}{2i}[\gamma_\mu, \gamma_\nu]$. By using the field equation $(\gamma_\mu D_\mu + M)\psi = 0$ one finds the relations

$$L_1^{(1)} - L_2^{(1)} + 2L_3^{(1)} = 0, \quad L_4^{(1)} + 2L_5^{(1)} = 0, \quad (1.49)$$

which remove the terms $L_2^{(1)}$ and $L_4^{(1)}$, this holds beyond tree level [23, 24]. Furthermore $L_3^{(1)}$ and $L_5^{(1)}$ are already included in the action in eq. (1.38) and thus can be absorbed in a redefinition of the quark mass M and the coupling g . Thus it is sufficient to add

$L_1^{(1)}$ to obtain the $O(a)$ improved action

$$S_I = S_{\text{Wilson}} + c_{sw} a^5 \sum_{n \in \Lambda} \sum_{\mu < \nu} \bar{\psi}(n) \frac{1}{2} \sigma_{\mu\nu} \hat{F}_{\mu\nu}(n) \psi(n), \quad (1.50)$$

where c_{sw} is referred to as the Sheikholeslami-Wohlert coefficient since they first presented the improved Wilson action in [22]. A convenient but not unique choice for the discretised version of the field strength tensor, used in the improved action, is

$$\hat{F}_{\mu\nu}(n) = -\frac{i}{8a^2} (Q_{\mu\nu}(n) - Q_{\nu\mu}(n)), \quad (1.51)$$

where we wrote the sum of 4 plaquettes in the $\mu - \nu$ plane as

$$Q_{\mu\nu}(n) = U_{\mu,\nu}(n) + U_{\nu,-\mu}(n) + U_{-\mu,-\nu}(n) + U_{-\nu,\mu}(n). \quad (1.52)$$

Figure 1.4 shows an illustration of this term, which due to its shape is also referred to as the clover term. For the regime we are interested in, it is necessary to determine the

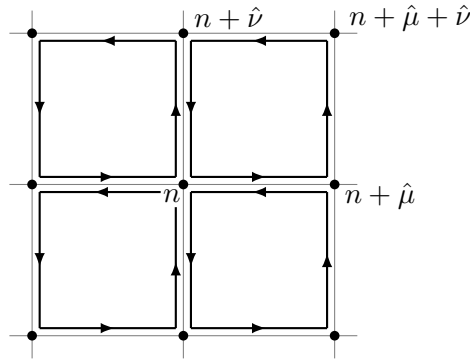


FIGURE 1.4: Illustration of the terms contributing to $Q_{\mu\nu}(n)$ in the $\mu - \nu$ plane.

improvement coefficient c_{sw} non-perturbatively. c_{sw} can be obtained from improvement conditions which rely on the violation of chiral symmetry due to $O(a)$ effects. For the Wilson action with two dynamical flavours one finds the parametrization [25],

$$c_{sw} = \frac{1 - 0.454g^2 - 0.175g^4 + 0.012g^6 + 0.045g^8}{1 - 0.720g^2}, \quad (1.53)$$

which holds for $\beta \equiv \frac{6}{g^2} \geq 5.2$. The improved action yields improved on-shell observables such as hadron masses. However, for matrix elements containing currents this is insufficient. In principle it is possible to improve the interpolating operators, such as vector currents, using a similar approach by adding correctional terms. In this work we determine the vacuum polarization via a four-dimensional Fourier transform of the vacuum polarization tensor and thus it is an off-shell quantity. So that even if the currents are improved, the vacuum polarization would not be improved by only applying

the Symanzik on-shell improvement program. We perform our calculations using an improved action, while the vector currents are not improved.

1.4.3 Monte Carlo

To estimate an observable O we need to compute the path integral

$$\langle O \rangle = \frac{1}{Z} \int \mathcal{D}[U] e^{-S_G[U]} \mathcal{D}[\psi, \bar{\psi}] e^{-S_F[U, \psi, \bar{\psi}]} O[\psi, \bar{\psi}, U], \quad (1.54)$$

where $\mathcal{D}[\psi, \bar{\psi}] = \prod_{n \in \Lambda} d\psi(n) \prod_{m \in \Lambda} d\bar{\psi}(m)$ refers to the Grassmann-valued measures for the fermions and $\mathcal{D}[U] = \prod_{n \in \Lambda} \prod_{\mu=1}^4 dU_\mu(n)$ to the $SU(3)$ group-valued measures for the gauge fields known as Haar measure. Due to the nature of the fermionic fields, we can replace the integration over the fermions by the determinant of the Dirac operator for two degenerate quarks,

$$\langle O \rangle = \frac{1}{Z} \int \mathcal{D}[U] e^{-S_G[U]} \det(D[U])^2 O[\psi, \bar{\psi}, U]. \quad (1.55)$$

Z is called the partition function, which is given by

$$Z = \int \mathcal{D}[U] e^{-S_G[U]} \det(D[U])^2. \quad (1.56)$$

For many applications it is convenient to separate the generation of the gauge fields from the actual calculation of the observables. In the past one had to resort to so-called quenched simulations where interactions between the sea quarks and the gauge fields were neglected by setting $\det(D[U]) = 1$. Nowadays, it is possible to include these interactions and for our calculations we included the light-quarks in the sea. The strange- and charm-quarks are not yet included in the sea, and in the following we will refer to the studies with valence strange- and charm-quarks as partially quenched.

To evaluate eq. (1.55) we use the Monte Carlo method with importance sampling. This allows us to approximate the path integral over the gauge fields in eq. (1.55) by the gauge average,

$$\langle O \rangle = \lim_{N \rightarrow \infty} \frac{1}{N} \sum_{n=1}^N O[U_n], \quad (1.57)$$

where the fermion determinants and the Boltzman factor $e^{-S_G[U]}$ are already included in the stored gauge configurations. The U_n are samples distributed according to the

Gibbs measure

$$dP(U) = \frac{W[U, \psi, \bar{\psi}] \mathcal{D}[U]}{\int \mathcal{D}[U] W[U, \psi, \bar{\psi}]}, \quad (1.58)$$

where we use the weight

$$W[U, \psi, \bar{\psi}] = Z^{-1} e^{-S_G[U]} \det(D_u[U]) \det(D_d[U]). \quad (1.59)$$

The number of gauge configurations U_n required to measure a given observable $\langle O \rangle$ depends on the observable and the associated auto-correlation time, which we discuss in 1.4.7. In practice one is limited to several hundred gauge configurations. For sufficiently decorrelated configurations this approximation introduces a statistical error proportional to $1/\sqrt{N}$. As N grows to infinity the exact result is recovered.

1.4.4 Generation of gauge configurations

We use Markov chains to generate the gauge configurations via the Monte Carlo method. From a given starting point U_0 the Markov chain constructs a sequence of gauge configurations,

$$U_0 \rightarrow U_1 \rightarrow U_2 \dots, \quad (1.60)$$

such that after a certain number of Monte Carlo steps (i.e. $U_n \rightarrow U_{n+1}$), the gauge configurations are distributed according to the equilibrium distribution $P(U)$. Here we give a brief description of the Metropolis algorithm [26]. To perform the Monte Carlo step for a given gauge configuration U_n to some new configuration U_{n+1} there are three steps in this algorithm:

1. Generate a candidate U' for U_{n+1} according to an a priori selection probability $T_0(U'|U_n)$.
2. The new configuration U' is accepted with the probability

$$T_A = \min \left(1, \frac{T_0(U|U') e^{-S[U']}}{T_0(U'|U) e^{-S[U]}} \right), \quad (1.61)$$

if U' is not accepted, U_n is used as U_{n+1} and used for the starting point of the next Monte Carlo step.

3. This procedure is repeated until sufficient gauge configurations are generated.

When the Markov process has reached its equilibrium the probability to change from one configuration U_n to another U_{n+1} has to be equal to the probability of the change from U_{n+1} to U_n . The Metropolis algorithm fulfills this, as it satisfies the detailed balance condition for the total transition probability $T = T_0 T_A$,

$$T(U'|U)e^{-S[U]} = T(U|U')e^{-S[U']}. \quad (1.62)$$

There are a number of update algorithms in use today, such as Heat bath [27], Overrelaxation [28, 29], Microcanonical [30, 31], Hybrid Monte Carlo [32], and Langevin [33–35]. For the generation of the ensembles used in this study (see table 2.1) the Hybrid Monte Carlo method was used with deflation acceleration, domain decomposition [36–38], and mass preconditioning [39].

1.4.5 The Hybrid Monte Carlo

For the description of the Hybrid Monte Carlo algorithm (HMC) we follow the explanation of [38]. Since the HMC updates all link variables in a single step it scales better with the lattice volume than algorithms that only update one link per step. In the following we limit the discussion to the gauge action $S[U]$. We begin with the introduction of an auxiliary $SU(3)$ algebra-valued field

$$\pi_\mu(n) = \pi_\mu^a(n)T^a, \quad \pi_\mu^a(n) \in \mathbb{R}, \quad (1.63)$$

where we used the generators T^a of $SU(3)$, as defined in appendix A.1. One interprets the field $\pi_\mu(n)$ as the canonical momentum of the gauge field and associates the Hamilton function

$$H[\pi, U] = \frac{1}{2}(\pi, \pi) + S[U], \quad \text{where } (\pi, \pi) = \sum_{n,\mu} \pi_\mu^a(n)\pi_\mu^a(n), \quad (1.64)$$

with it. The auxiliary momentum field does not change the physics, since the change in the path integral can be absorbed in a constant factor c ,

$$\int \mathcal{D}[U]O[U]e^{S[U]} = c \int \mathcal{D}[\pi]\mathcal{D}[U]O[U]e^{H[\pi,U]}. \quad (1.65)$$

The Hamilton equations are also called “molecular-dynamics equations”, they are given by

$$\dot{\pi}_\mu(n) = -F_\mu(n), \quad F_\mu^a(n) = \left. \frac{\partial S [\exp \{ \omega_\mu^a(n) T^a \} U_\mu(n)]}{\partial \omega_\mu^a(n)} \right|_{\omega=0}, \quad (1.66)$$

$$\dot{U}_\mu(n) = \pi_\mu(n)F_\mu(n), \quad (1.67)$$

where $\omega_\mu^a(n) \in \mathbb{R}$. The derivatives of $\pi_\mu(n)$ and $U_\mu(n)$ are to be taken with respect to a fictitious time t . $F_\mu^a(n)$ is called the force field of the gauge field. The solutions of these equations are unique and depend only on the initial value of the fields at $t = 0$ and can be interpreted as trajectories in field space along the time t .

To propagate from a gauge field U to U' the HMC takes the following steps:

1. Generate the momentum field π according to a probability density, which is proportional $e^{-\frac{1}{2}(\pi, \pi)}$.
2. Integrate the molecular-dynamics equations (1.66, 1.67) from $t = 0$ to $t = \tau$ with $\tau > t$ using U and π as the initial fields.
3. U' is set to U_τ with the probability

$$P(\pi, U) = \min \left\{ 1, e^{-\Delta H(\pi, U)} \right\}, \quad (1.68)$$

where we used

$$\Delta H(\pi, U) = \{H(\pi_\tau, U_\tau) - H(\pi, U)\}. \quad (1.69)$$

For the integration of the molecular-dynamics equations one uses a numerical procedure, e.g. the leap-frog integrator. The choice of τ has an impact on the integration of the molecular-dynamics equations and on the auto-correlation of the gauge configurations and thus has to be chosen carefully. In the following description of an example of a thermalization process using the HMC we used $\tau = 2$.

1.4.6 Example of a thermalization process

To monitor the progress of the simulation in configuration space and to see when the simulation enters the equilibrium one measures one or more observables and observes how they evolve in MDUs (molecular dynamics units)². The process of running the simulation until the equilibrium is reached is called thermalization. The configurations generated during the thermalization are discarded.

As an example we discuss the strategy used for the thermalization of the ensembles generated in the CLS $N_f = 2+1$ effort [40], where we used in the sea non-perturbatively improved Wilson fermions and the Lüscher–Weisz action for the gluons [41]. We observe the thermalization by measuring the scale parameter t_0 using the Wilson flow [42]. To

²MDUs are given by the product $\tau \times$ number of configurations.

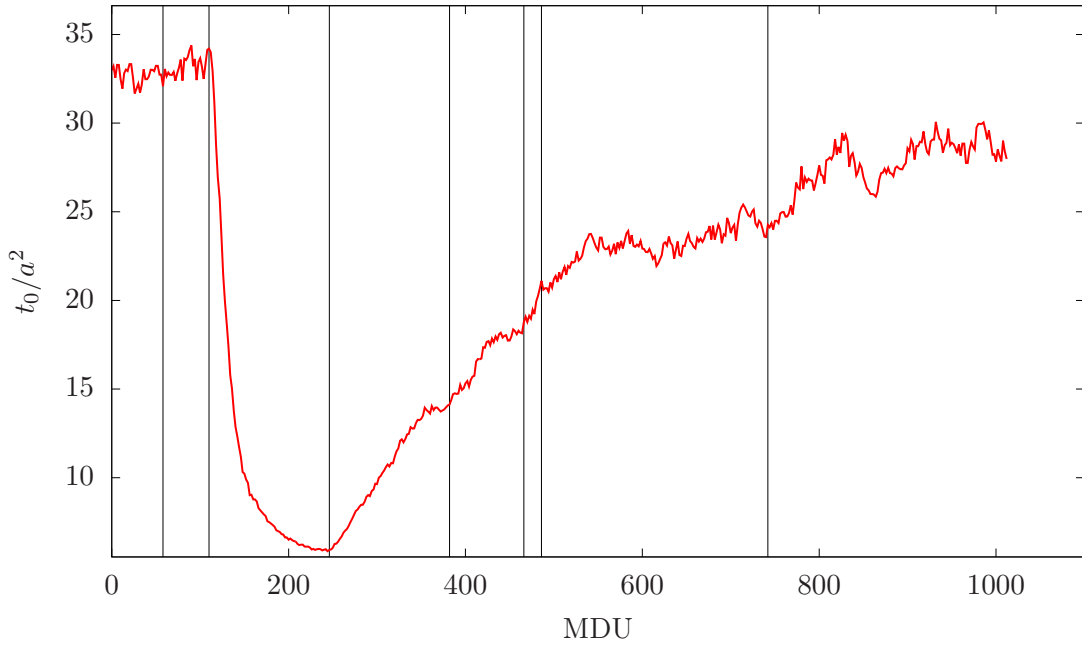


FIGURE 1.5: We show the start of thermalization process of the D100t ensemble with the scale parameter t_0 as an example for the $N_f = 2 + 1$ CLS effort. The starting point was a configuration of the A5 ($32^3 \times 64$) chain of the $N_f = 2$ CLS effort. The vertical lines indicate changes in the simulation algorithm, such as a decrease in the quark mass, adding the strange-quark, or variations in the parameters for the twisted-mass reweighting or the rational approximation of the strange-quark. The target parameters of $m_{\text{PS}} \approx m_\pi$ and $a = 0.086$ fm were reached after $O(2000)$ MDUs.

obtain t_0 the smoothing flow equation is applied to the gauge fields $U(x, \mu)$,

$$\partial_t V_t(x, \mu) = -g_0^2 [\partial_{x,\mu} S_W(V_t)] V_t(x, \mu), \quad V_t(x, \mu)|_{t=0} = U(x, \mu), \quad (1.70)$$

where S_W is the Wilson action and t refers to the flow time. The link differential operator $\partial_{x,\mu}^a$ is defined in A.2. To compute the time slice energy $E(x_0, t)$, we use the field strength tensor $\hat{G}_{\mu\nu}$, which is constructed from the smooth fields V_t ,

$$E(x_0, t) = -\frac{a^3}{2L^3} \sum_{\vec{x}} \text{Tr} \left[\hat{G}_{\mu\nu}(x, t) \hat{G}_{\mu\nu}(x, t) \right]. \quad (1.71)$$

The definition of t_0 then reads

$$t^2 \langle E(t) \rangle|_{t=t_0} = 0.3, \quad (1.72)$$

where we used the vacuum expectation value of the time slice energy $\langle E(t) \rangle$. As an example for the evolution of t_0 we show its behaviour with respect to MDUs in figure 1.5.

During the thermalization process the quark masses and algorithmic parameters are

tuned. We list the parameters that were changed frequently in the thermalization process here.

- Solvers: Iteration counts, residue values, and the number of Krylov-subspace vectors.
- Deflation: Size of the deflation subspace, the number of deflation modes, and the number of inverse iteration steps.
- Actions: The number of pseudo-fermion fields and the values of the corresponding twisted-mass reweighting parameters.
- The number of steps used in the integration of the molecular-dynamics equations.

The inverse gauge coupling β was fixed from the start since a rough estimate of the associated lattice spacing was known. For a complete list of all parameters and a more detailed explanations we refer to the documentation of the openQCD-package [43].

Once the target mass is reached it is fixed. Algorithmic parameters may still be tuned in this final thermalization process to optimize the required computer time. When the simulation is sufficiently thermalized all parameters are fixed.

As an example we give a brief description of the thermalization of the D100t [40] ensemble for the CLS $N_f = 2+1$ effort with the target parameters $V = 128 \times 64^3$, $m_\pi \approx m_\pi^{\text{phys}}$, and $a \approx 0.086$ fm. The starting point was a configuration of the A5 ensemble generated in the CLS $N_f = 2$ effort with $V = 64 \times 32^3$, $m_\pi = 331$ MeV, and $a = 0.0755(9)(7)$ fm, cf. [44] and table 2.1. We began the simulation with $V = 128 \times 32^3$ by copying an A5 configuration in the two halves of the new volume and using open boundary conditions [45–47] instead of periodic boundary conditions. Now points that were previously located at the boundary of the A5 configuration would be in the middle of the lattice. To smooth the effect of the change in the boundary conditions and the points in the middle of the lattice we ran the simulation for $O(100)$ MDUs with $N_f = 2$. At this stage we kept all other parameters of the simulation as they were used for A5, including the Wilson plaquette action for the gluons. At a later stage we added the strange-quark, for which we used a very heavy degenerate mass for all quarks, $m_{u/d} = m_s$. Using a heavy quark mass reduces the required computer time for simulations significantly and helps to avoid numerical instabilities, e.g. exceptional configurations, since simulations with heavy quark masses have a more beneficial condition number of the Dirac operator. Furthermore, for three degenerate quark masses the spectral range required for the strange-quark Dirac operator is also reduced, which also improves the stability of the simulation. We also switched to the Lüscher-Weisz action for the gluons at this point. The drastic change in the mass leads to the dramatic change of t_0 in the thermalization

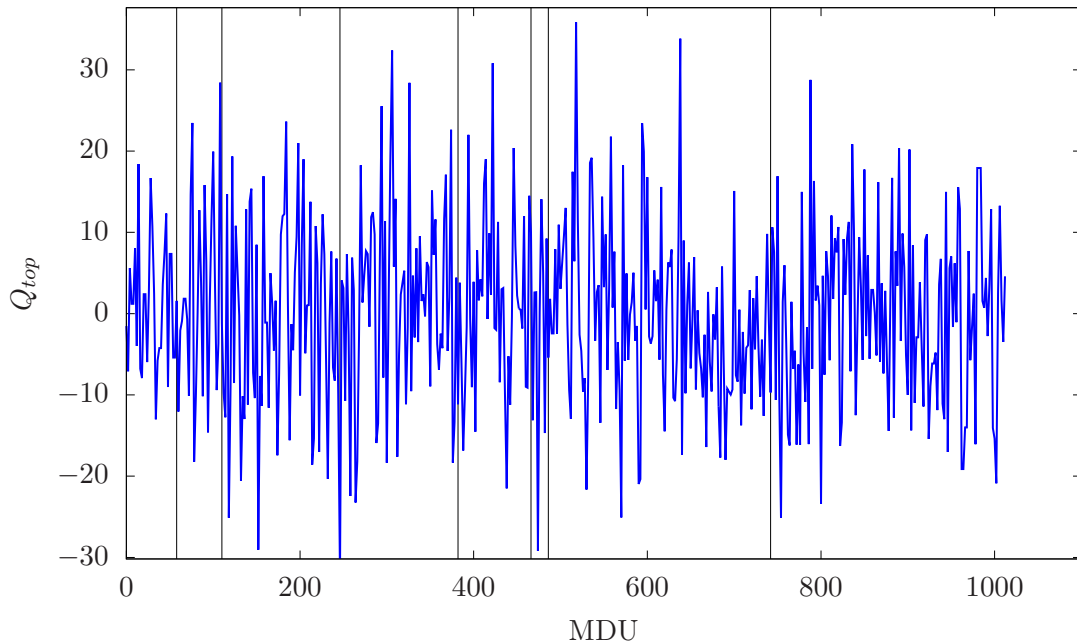


FIGURE 1.6: The evolution of the topological charge Q_{top} of D100t in MDUs. Vertical lines indicate changes in the simulation algorithm. Further details of this simulation are included in the text.

history shown in figure 1.5 in the third panel from the left. In the following steps we reduced the light-quark mass while the strange-quark mass was increased. After reaching the physical point we tuned the algorithm to reduce the run time per MDU, thus concluding the thermalization phase.

If the configuration space has topologically different sectors, it can be problematic for the Monte Carlo update algorithm to connect these sectors. This is known as topological freezing [45, 48, 49]. To counter this problem we use open boundary conditions in the time direction for the $N_f = 2 + 1$ CLS ensembles, while space is treated with periodic boundary conditions. In order to monitor whether the algorithm tunnels between different topological sectors at a sufficient rate, we measure the topological charge,

$$Q_{\text{top}}(t) = -\frac{a^4}{32\pi} \sum_x \epsilon_{\mu\nu\rho\sigma} \text{Tr} \left[\hat{G}_{\mu\nu}(x, t) \hat{G}_{\rho\sigma}(x, t) \right]. \quad (1.73)$$

As an example we show the evolution of Q_{top} as a function of MDUs at vanishing flow time in figure 1.6. A clear evidence of topological freezing would imply that Q_{top} remains stuck around a given value over many MDUs of the HMC algorithm. At the value of the lattice spacing, $a \approx 0.086$ fm, of the ensemble D100t shown in figure 1.6, there are no signs of a large effect from such slow modes of the algorithm.

1.4.7 Auto-correlations of configurations

Due to the use of Markov chains in the Monte Carlo algorithm, consecutively generated configurations are not independent. The auto-correlations between configurations can be measured for a given observable O by the auto-correlation function,

$$\Gamma_O(t) = \langle O_t O_0 \rangle - \langle O \rangle^2, \quad (1.74)$$

where t is the index of a given configuration in the Markov chain. To determine the time separation between sufficiently decorrelated configurations one uses the normalized auto-correlation function $\rho_O(t) = \Gamma_O(t)/\Gamma_O(0)$ to compute the integrated auto-correlation time,

$$\tau_{\text{int}}(O) = \frac{1}{2} + \sum_{t=1}^{\infty} \rho_O(t). \quad (1.75)$$

The auto-correlations depend on the observable. One usually monitors observables with particularly long auto-correlation times, such as the action density, eq. (1.71), or the topological charge, eq. (1.73). In figure 1.7 we show an example of the auto-correlation function and the integrated auto-correlation time taken from [50].

1.4.8 Measurement of observables

Hadron masses are among the most basic fermionic observables one can measure on the lattice. Hadron spectroscopy calculations are on the one hand a test for QCD when the resulting masses are compared to experimental measurements, and on the other hand allow also predictions, when states are found which have not yet been observed in experiments. The first step of a spectroscopy calculation is the choice of the interpolating operators, which represent the corresponding particles of interest.

Interpolating operators of a mesons are given by connecting a quark and an anti-quark field with a suitable combination of gamma-matrices, which have the transformation properties (scalar, pseudo-scalar, vector, or axial vector), and the necessary behaviour under charge conjugation as well as the correct quantum numbers. The interpolating operator for pions with degenerate up- and down-quark masses is

$$O_\pi(n) = \bar{\psi}(n)\gamma_5\psi(n). \quad (1.76)$$

The choice of the inserted γ -matrices is not unique, instead of γ_5 we could also have used $\gamma_4\gamma_5$.

The construction of baryon interpolators is similar. The corresponding Hilbert space

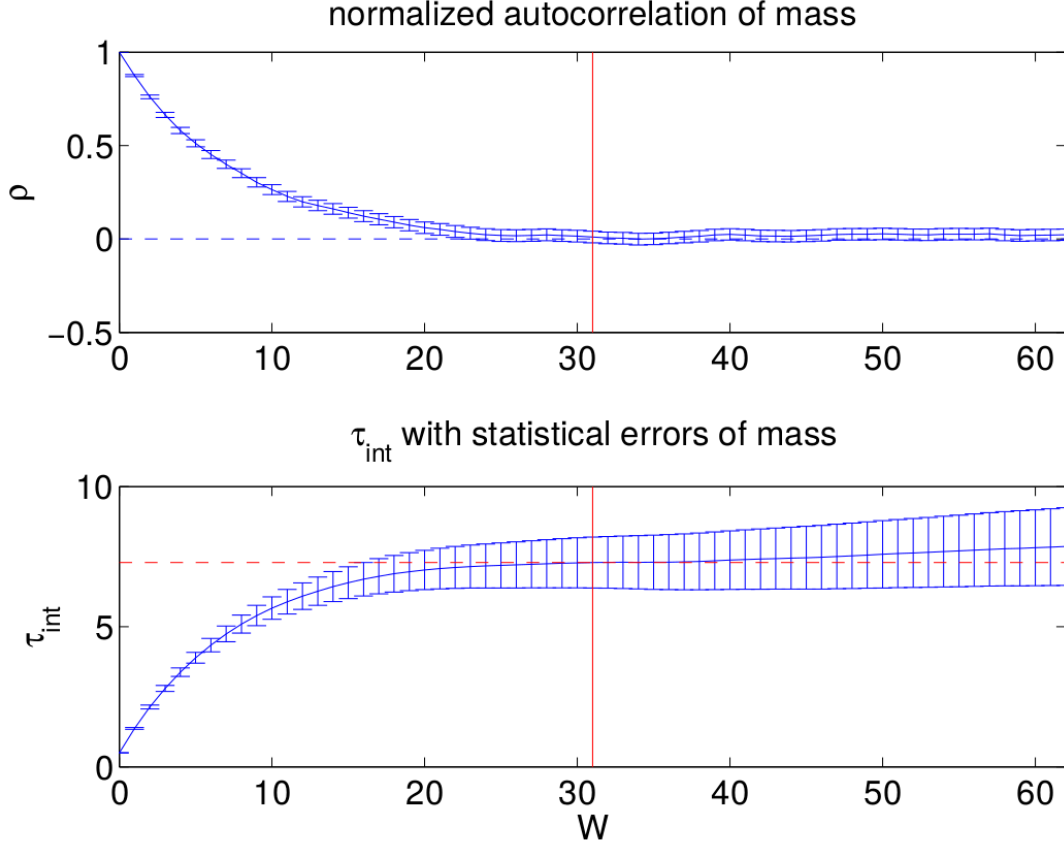


FIGURE 1.7: As an example we show a plot from [50], where the window method was used. The normalized auto-correlation function ρ is shown at the top and the corresponding integrated auto-correlation time with respect to the window size W , which replaces the upper bound of the sum in eq. (1.75), is shown at the bottom.

operator \hat{O} has to project onto the state of interest. Three quark fields are required to build baryon operators, e.g. the interpolator of a nucleon can be written as

$$O_N(n) = \epsilon_{abc} \psi_a(n) (\psi_b^T(n) C \gamma_5 \psi_c(n)), \quad (1.77)$$

where the indices a, b, c refer to colour-space and the charge conjugation matrix C^3 was used. ϵ_{abc} is the usual anti-symmetric tensor. Also for baryons the choice of the interpolating operator is not unique. Which of the interpolating operators couples best to the observable of interest is not known a priori and needs to be determined in simulations. The spectrum of a particle can then be obtained from the correlation function. The correlation function of a meson (M) evaluated for a single configuration reads

$$\langle O_M(n) \bar{O}_M(m) \rangle_F = \langle \bar{\psi}(n) \Gamma \psi(n) \bar{\psi}(m) \Gamma \psi(m) \rangle_F \quad (1.78)$$

$$= -\text{Tr} [\Gamma D^{-1}(n|m) \Gamma D^{-1}(m|n)] \\ + \text{Tr} [\Gamma D^{-1}(n|n)] \text{Tr} [\Gamma D^{-1}(m|m)], \quad (1.79)$$

³The charge conjugation matrix can be written as $C = i\gamma_2\gamma_4$ using the definitions in appendix A.3



FIGURE 1.8: Quark flow diagram of the quark-connected part of a meson 2-point correlation function on the left and for the quark-disconnected contribution on the right.

where we used Wick's theorem for the fermion contractions, and the fact that the propagator of a quark from n to m is given by the inverse of the Dirac operator $D^{-1}(m|n)$. The trace acts in Dirac and colour space. $\langle \dots \rangle_F$ implies that the expectation value is only taken with respect to the fermionic measure. The first line of eq. (1.79) refers to the quark-connected part and the second line is the quark-disconnected contribution, i. e. two quark loops that only interact with each other via the gauge field. Figure 1.8 shows the two contributions to eq. (1.79) in a quark flow diagram. Quark-disconnected contributions are in general much more difficult to calculate and a lot more statistics are needed, since the all-to-all propagator ($D^{-1}(n|n)$) is needed. An introduction to techniques that allow for estimates of the all-to-all propagator are beyond the scope of this thesis. Instead we focus on the quark-connected contributions from now on.

The quark propagator is obtained by solving the equation

$$D_f \psi = \eta, \quad (1.80)$$

iteratively to get the inverse of the Dirac operator for the source η and the solution of the Dirac equation ψ . The solver used in this work is taken from the DD-HMC package [51].

Depending on the observable of interest one may either use point sources or extended sources to optimize the overlap of the interpolating operator. For the two-point functions used in this work so called point-to-all propagators are used, i. e. one inverts the Dirac operator for a fixed point n to all points m . For a point source we have

$$\eta_{n,n_0,\alpha,\alpha_0,c,c_0} = \delta_{n,n_0} \delta_{\alpha,\alpha_0} \delta_{c,c_0}, \quad (1.81)$$

which has only one non-vanishing entry at the lattice position n_0 , for Dirac index α_0 , and for colour index c_0 . To compute the two-point correlation function all 12 components of the point-to-all propagator are needed. They are obtained by inverting eq. (1.80) with the 12 possible combinations of Dirac and colour indices of eq. (1.81) at a given point

n_0 .

For other applications it is advantageous to use extended sources. Extended sources can improve the overlap of a given interpolator with the ground state. This is particularly helpful for correlation functions with bad signal-to-noise ratios, such as nucleons, where the signal decays exponentially. The idea is to “smear” a quark field with an operator $M(m, n)_{\alpha\beta}^{cd}$ (c, d are colour indices, α, β are Dirac indices) in the vicinity of the source location [52]. We obtain the smeared source by

$$\tilde{\eta}(m)_\alpha^a = M(m, n)_{\alpha\beta}^{ab} \eta(n)_\beta^b. \quad (1.82)$$

For example using Gaussian smearing [53–55] one can smear the quark field in such a way that it takes an approximately Gaussian shape with

$$M = (\mathbb{1} + \kappa_G H)^k, \quad (1.83)$$

where H is the hopping matrix defined in eq. (1.40) and $\kappa_G \in \mathbb{R}$ and $k \in \mathbb{N}$. κ_G and k have to be tuned to achieve the best overlap with the ground state of a given interpolator. In practice the source-smeared propagator is obtained by replacing the source of eq. (1.80) with a smeared source,

$$D_f \tilde{\psi} = \tilde{\eta}. \quad (1.84)$$

The smeared-smeared propagator is obtained by smearing the solution of eq. (1.84),

$$\tilde{\psi}'(m)_\alpha^a = M(m, n)_{\alpha\beta}^{ab} \psi(n)_\beta^b. \quad (1.85)$$

Since we use a local vector-current for the calculation of the HVP we are restricted to using point sources. We take the results of the vector masses from data generated in the course of [56], where smeared sources were used.

Once the correlation function is computed we can relate it to the states of a particle by considering

$$\begin{aligned} C_O(\vec{p}, t) &= \langle O(\vec{x}, t) \bar{O}(\vec{0}, 0) \rangle \\ &= \sum_n \langle 0 | O | n \rangle \langle n | O^\dagger | 0 \rangle e^{-E_n(\vec{p})t} \\ &= A_0 e^{-E_0(\vec{p})t} + A_1 e^{-E_1(\vec{p})t} + \dots, \end{aligned} \quad (1.86)$$

where we used the translation operator $O(x) = e^{ipx} O(0) e^{-ipx}$ and inserted a complete set of states, i. e. $\mathbb{1} = \sum_n |n\rangle \langle n|$. In the limit of $t \rightarrow \infty$ only the ground state survives, thus the amplitude $A = A_0$ and mass $m = E_0(\vec{p} = 0)$ of the ground state can be obtained

from a fit to the correlation function at vanishing momentum at Euclidean times, where the excited states are sufficiently suppressed.

1.4.9 The statistical bootstrap method

To compute the errors of simulations introduced by the use of the Monte Carlo method reliably, resampling methods are used frequently. One such method is the statistical bootstrap method [57], which is also used in this work. For a given sample of N data one randomly chooses N data points, where values may appear more than once, computes the average and repeats this K times. The central value is given by the average over all N data written as \bar{O} . The statistical error is given by the central 68% of the distribution of bootstrap samples. In principle one has an upper and lower error, but, for convenience, we use a symmetrized error in this work. The result we cite for a given observable is

$$\langle O \rangle = \bar{O} \pm \delta. \quad (1.87)$$

As a rule of thumb one should use $K \geq 3N$. Since resampling is cheap in terms of computer time, the size of K can be determined by increasing it until stability of the error is observed. As an example we show the relative error of the vacuum polarization, which is introduced in chapter 2, for the first Fourier momentum on an ensemble with $m_\pi = 185$ MeV, $a = 0.0658$ fm with $V = 128 \times 64^3$ (shown in table 2.1 with the label G8), with respect to the number of bootstrap samples K in figure 1.9. Since we need the same number of bootstraps for all ensembles we choose to use 10000 bootstrap samples, even though figure 1.9 suggests that $K \approx 600$ should be sufficient. An alternative to the bootstrap method is the jackknife method. As it is not used in this study we refer to [10] for a description of this method.

1.4.10 The extended frequentist method

In our analysis we use the extended frequentist method [58, 59]. This method allows us to build distributions of variations that we use in our calculations. From these distributions we estimate statistical and systematic errors of the observables. For this method we need the unweighted and weighted medians.

The **unweighted median** of the observable O_i with K bootstrap samples is given by sorting the O_i by size and using the central value and the central 68%,

$$\bar{O} = O_{\lfloor K/2 \rfloor} \pm \frac{1}{2} [(O_{\lfloor K/2 \rfloor} - O_{\lfloor 0.16K \rfloor}) + (O_{\lfloor 0.84K \rfloor} - O_{\lfloor K/2 \rfloor})], \quad (1.88)$$

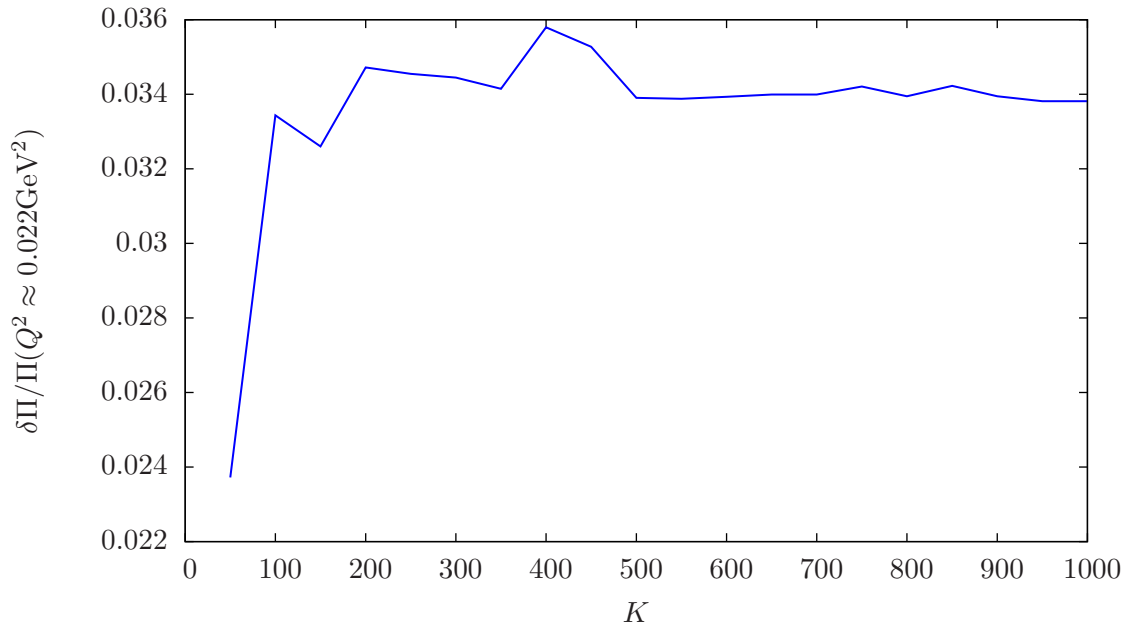


FIGURE 1.9: Plot of the change in the relative error of the result for the vacuum polarization at $Q^2 \approx 0.022 \text{ GeV}^2$ on G8 with respect to the number of bootstrap samples K for 2816 measurements. We find that there is no significant change for $K > 600$.

where the lower and upper errors are averaged. $[i]$ implies rounding to the lower integer number of i .

To determine the **weighted median** the results O_i and their corresponding weights p_i are sorted by the size of the O_i . For the weights we use p-values of fits. We define

$$p_i(M_i, n_i) = 1 - \frac{1}{\Gamma(n_i)} \int_0^{M_i} m^{n_i-1} e^{-m} dm, \quad (1.89)$$

where we used the complete Γ -function. The p-values are then given by inserting the result of the minimization of a least squared fit, $M_i = \chi_i^2/2$, and the degrees of freedom $n_i = (N_i^{\text{points}} - N_i^{\text{parameters}})/2$. A part of the analysis uses an unweighted procedure, in these cases we set all $p_i = 1$. The sum of all weights is $P = \sum_i p_i$. The central value is given by the maximal index c that satisfies

$$\sum_{i=1}^c p_i \leq P/2, \quad (1.90)$$

the indices for the lower (l) and upper (u) bounds are given by the central 68% of the weights,

$$\sum_{i=1}^l p_i \leq 0.16P, \quad \text{and} \quad \sum_{i=1}^u p_i \leq 0.84P. \quad (1.91)$$

The method may underestimate errors for distributions based on a number of weights which are of different orders of magnitude or too few variations. Thus one has to either ensure that $l \neq c \neq u$ and $l \neq u$ by supplying weights of similar sizes or set all weights to 1, while including a sufficient number of variations. With these definitions the estimate is given by

$$\bar{O} = O_c \pm \frac{1}{2} [(O_c - O_l) + (O_c - O_u)], \quad (1.92)$$

where we symmetrised the lower and upper errors. Now we have the necessary definitions to use the extended frequentist method.

For M different procedures with K bootstrap samples we have the individual results $x_{m,k}$ and their weights $w_{m,k}$. To estimate the statistical error we compute the weighted median for each bootstrap sample k using the sum of the weights $W_k = \sum_{m=1}^M w_{m,k}$,

$$\sum_{m=1}^c w_{m,k} \leq W_k/2 \quad \Rightarrow \quad \tilde{x}_k = x_{c,k}. \quad (1.93)$$

The statistical error is then given by the central 68% of the unweighted median of the bootstrap samples \tilde{x}_k ,

$$\sigma_{\text{stat}} = \frac{1}{2} [(\tilde{x}_{\lfloor K/2 \rfloor} - \tilde{x}_{\lfloor 0.16K \rfloor}) + (\tilde{x}_{\lfloor 0.84K \rfloor} - \tilde{x}_{\lfloor K/2 \rfloor})], \quad (1.94)$$

where the lower and upper error are symmetrised. To estimate the central value and the systematic error, we compute the unweighted medians (over the bootstrap samples) for all M procedures,

$$\bar{x}_m = x_{m, \lfloor K/2 \rfloor}, \quad \text{with the respective weights} \quad \bar{w}_m = w_{m, \lfloor K/2 \rfloor}. \quad (1.95)$$

The central value and the systematic error are then given by the weighted median of the M procedures using the sum $W = \sum_m \bar{w}_m$,

$$\sum_{m=1}^{c'} \bar{w}_m \leq W/2, \quad \sum_{m=1}^l \bar{w}_m \leq 0.16W, \quad \sum_{m=1}^u \bar{w}_m \leq 0.84W, \quad (1.96)$$

$$\Rightarrow \sigma_{\text{sys}} = \frac{1}{2} [(\bar{x}_{c'} - \bar{x}_l) + (\bar{x}_u - \bar{x}_{c'})], \quad (1.97)$$

where we symmetrised the systematic error. We quote

$$\bar{X} = \bar{x}_{c'} \pm \sigma_{\text{stat}} \pm \sigma_{\text{sys}} \quad (1.98)$$

as the final result. We estimate the different systematic error contributions by building subsets of the data, which we relate for example to different types of lattice artefacts

or chiral extrapolations. On these subsets we perform the extended frequentist method and the standard deviation of the results for the different subsets gives a rough estimate for the size of the contribution to the total systematic error. Although this procedure is aiming at a separation of the various systematic effects, it is not exact since the investigated effects may be intertwined. Nevertheless, it provides some information about the hierarchy among the different contributions. Note that we normalize over the different contributions to the systematic error which we consider for a given analysis. Thus we only quote the relative size of the various systematic effects when we discuss our results.

1.4.11 Scale setting and physical results

Lattice simulations are performed at unphysical parameters. The simulations use a finite volume and lattice spacing, and often heavier quark masses than observed in nature. Increasing the volume, reducing the lattice spacing, and reducing the quark mass, increases the cost of the simulations. The finite volume and lattice spacing cannot be overcome as they are inherent to simulations on a computer. To increase the volume more CPUs may be required to decrease the computing time or supply the necessary memory. Reducing the lattice spacing may lead to topological freezing of the simulation [45, 48, 49]. Open boundary conditions, as demonstrated in the previous chapter, can help to reduce the lattice spacing further, but simulations should always be tested for this effect. The third parameter is the quark mass, which when reduced too far leads to critical slowing down of the simulation [60]. Algorithmic improvements allowed many groups to push the pion mass of their simulation to the physical point. The most chiral ensembles used in this work is G8 with $m_\pi \approx 190$ MeV (see table 2.1). The next generation of CLS ensembles with $N_f = 2 + 1$ will include ensembles at physical pion mass.

We have to extrapolate our lattice results to the continuum limit and the physical pion mass. The exact form of these extrapolations depends on the observable. Chiral perturbation theory may be used as a guidance for the description of the quark mass behaviour. The continuum extrapolation depends on the level of the improvement, e.g. the leading term for an $O(a)$ -improved action is proportional to $O(a^2)$. In principle finite size effects also need to be checked. In our measurements of the vacuum polarization a direct numerical study of finite size effects has not been carried out due to the absence of ensembles differing only by their volume. For many observables one expects finite size effects to begin to play a role for $m_\pi L < 4$. The ensembles in table 2.1 fulfill $m_\pi L > 4$, except for G8 which has $m_\pi L \approx 3.9$.

The lattice spacing a is not known a priori and has to be determined in the course of the simulations. To make contact with the physical world one observable has to be used

to determine the scale, such as a hadron mass or a decay constant. For the determination of the scale one uses one observable O^{phys} from experiment and measures the same observable on the lattice O^{lat} . The scale is then obtained by the relation

$$a[\text{fm}] = \frac{aO^{\text{lat}}}{O^{\text{phys}}[\text{MeV}]} \hbar c, \quad \text{with } [\hbar c] = \text{MeV fm}. \quad (1.99)$$

In this work we use CLS ensembles with $N_f = 2$ with the scale setting via the kaon decay constant F_K [44]. Different scale setting procedures may result in different results for the scale, but the results for the continuum extrapolation of a given observable do not change when different scale setting schemes are used.

Chapter 2

The hadronic vacuum polarization

2.1 Determination of the hadronic vacuum polarization on the lattice

2.1.1 Definitions, lattice regularization, and renormalization

To determine the hadronic vacuum polarization function (VPF) we start from the hadronic vacuum polarization tensor, which is given by

$$\Pi_{\mu\nu}^{(f)}(Q) = \int d^4x e^{iQx} \langle J_\mu^{(f)}(x) J_\nu^{(f)}(0) \rangle, \quad (2.1)$$

where Q is the euclidean momentum. The vector current is defined as

$$J_\mu^{(f)}(x) = q_f \bar{\psi}_f(x) \gamma_\mu \psi_f(x), \quad (2.2)$$

with the electric charges are $q_f = (2/3, -1/3, -1/3, 2/3)$ for the flavours $f = (u, d, s, c)$. On the lattice, the integral in eq. (2.1) is replaced by a sum over all lattice points n . We use a conserved current ($V_\mu^{(f,c)}(n)$) and a local vector current $V_\mu^{(f,l)}(n)$ given by

$$V_\mu^{(f,c)}(n) = \frac{q_f}{2} \left(\bar{\psi}_f(n + a\hat{\mu})(1 + \gamma_\mu) U_\mu^\dagger(n) \psi_f(n) - \bar{\psi}_f(n)(1 - \gamma_\mu) U_\mu(n) \psi_f(n + a\hat{\mu}) \right), \quad (2.3)$$

$$V_\mu^{(f,l)}(n) = Z_V q_f \bar{\psi}_f(n) \gamma_\mu \psi_f(n), \quad (2.4)$$

to compute the current-current correlator. This is a compromise between the cost of the calculation and the loss in precision due to the use of the local vector-current, since it needs to be renormalized by Z_V . Had we used two conserved vector-currents five inversions would have been required to compute the current-current correlator instead

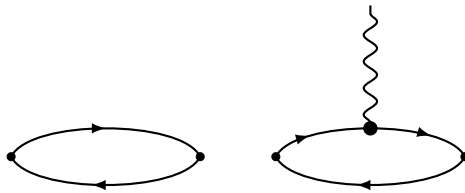


FIGURE 2.1: The two diagrams for the non-perturbative determination of Z_V . On the left we show the two-point function, on the right the three-point function, where the vector current is inserted.

of just one inversion. The renormalization Z_V^I of the improved vector-current involves a term proportional to the quark mass,

$$Z_V^I = Z_V(1 + b_V am_f), \quad (2.5)$$

where b_V can be determined non-perturbatively [61]. For small quark masses the term proportional to b_V is numerically small and cut-off effects are expected to be small. However, we study the light-, strange-, and charm-quark contributions in this work. At the charm-quark mass cut-off effects are not negligible and, even though the currents we use are not $O(a)$ improved, subtracting mass-dependent cut-off effects from the renormalization allows for a more reliable extrapolation to the continuum limit. We use a non-perturbative determination of Z_V which includes the mass dependence.

To this end we define the meson two- and three-point functions at $t = T/2$ as

$$C_2(T/2) = \sum_{\vec{x}} \left\langle O(\vec{x}, T/2) O^\dagger(\vec{0}, 0) \right\rangle, \quad (2.6)$$

$$C_3(\tau, T/2) = \sum_{\vec{x}, \vec{y}} \left\langle O(\vec{x}, T/2) J_0(\vec{y}, \tau) O^\dagger(\vec{0}, 0) \right\rangle, \quad (2.7)$$

where we suppressed flavour indices and used $O = \bar{\psi}_2 \gamma_5 \psi_1$, and $J_0 = \bar{\psi}_1 \gamma_0 \psi_1$. We show the diagrams of the two- and three-point functions in figure 2.1. We take the ratio

$$R(\tau, T/2) = \frac{C_3(\tau, T/2)}{C_2(T/2)}, \quad (2.8)$$

and the difference

$$d(t) = R(t, T/2) - R(t + T/2, T/2) = Q_V \quad (2.9)$$

then gives the vector charge Q_V . Z_V is determined by imposing the condition $Z_V Q_V = 1$. We show the estimates of Z_V used in this work¹ in subsection 2.1.3, where we collect the parameters of our simulations.

We can write the quark-connected contribution to the HVP tensor on the lattice in terms

¹We thank Jeremy Green for the estimates of Z_V .

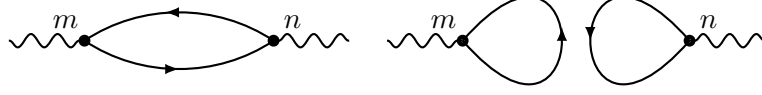


FIGURE 2.2: Quark flow diagram of the connected (left) and disconnected (right) contribution of the hadronic vacuum polarization.

of propagators as

$$\Pi_{\mu\nu}^{(f),\text{conn.}}(Q) = Z_V q_f^2 \frac{a^4}{4} \sum_n e^{iQ(n+a\hat{\mu}/2)} \quad (2.10)$$

$$\begin{aligned} & \left\langle -\text{Tr} \left[\gamma_\nu \gamma_5 S^\dagger(n+a\hat{\mu}, 0) \gamma_5 (1+\gamma_\mu) U_\mu^\dagger(n) S(n, 0) \right] \right. \\ & \left. + \text{Tr} \left[\gamma_\nu \gamma_5 S^\dagger(n, 0) \gamma_5 (1-\gamma_\mu) U_\mu(n) S(n+a\hat{\mu}, 0) \right] \right\rangle, \quad (2.11) \end{aligned}$$

the derivation of the trace of this relation can be found in A.4. The additional shift in the exponent of the Fourier transform $a\hat{\mu}/2$ is due to the conserved current. The current-current correlator also gives rise to so called quark-disconnected contributions,

$$\begin{aligned} \left\langle V_\mu^{(f,c)}(n) V_\nu^{(f,l)}(m) \right\rangle^{\text{disc.}} &= \frac{q_f^2 Z_V}{2} \left\langle \text{Tr} [\gamma_\nu S(m, m)] \text{Tr} \left[(1+\gamma_\mu) U_\mu^\dagger(n) S(n, n+a\hat{\mu}) \right] \right. \\ & \left. - \text{Tr} [\gamma_\nu S(m, m)] \text{Tr} \left[(1-\gamma_\mu) U_\mu(n) S(n, n+a\hat{\mu}) \right] \right\rangle. \quad (2.12) \end{aligned}$$

To estimate $S(m, m)$ one needs the all-to-all propagator, which is very costly to compute. Disconnected contributions to the hadronic vacuum polarization could be as large as -10% of the connected contribution [62]. A first numerical test based on the time-momentum representation [63] showed that the upper bound is of the order of $4-5\%$ [64]. The quark flow diagrams of both connected and disconnected contributions are shown in figure 2.2. In this work we neglect disconnected contributions.

The renormalized vacuum polarization may also be obtained through the time-momentum representation, which relies on the mixed-representation Euclidean correlator [63],

$$G(x_0) \delta_{kl} = \int d^3x \langle J_k(x) J_l(0) \rangle. \quad (2.13)$$

The renormalized VPF can then be obtained by integrating over the correlator,

$$\hat{\Pi}^{(f)}(Q^2) = \frac{1}{4\pi^2} \int_0^\infty dx_0 G(x_0) \left[x_0^2 - \frac{4}{Q_0^2} \sin^2 \left(\frac{1}{2} Q_0 x_0 \right) \right]. \quad (2.14)$$

The strategy here is to interpolate the correlation function at small x_0 to perform the integration. At large x_0 , where excited states are sufficiently suppressed, the correlation function is replaced by an approximation of its exponential decay using the estimate of the ground state. In the following we focus the determination of the HVP tensor defined in eq. (2.11).

The relation to determine the VPF follows from Euclidean invariance and current conservation

$$\Pi_{\mu\nu}^{(f)}(Q) = (Q_\mu Q_\nu - \delta_{\mu\nu} Q^2) \Pi^{(f)}(Q^2). \quad (2.15)$$

The renormalized VPF is defined as

$$\hat{\Pi}^{(f)}(Q^2) = 4\pi^2 \left[\Pi^{(f)}(Q^2) - \Pi^{(f)}(Q^2 = 0) \right]. \quad (2.16)$$

The leading order hadronic contribution to the anomalous magnetic moment of the muon is then given by inserting the renormalized VPF into eq. (1.4),

$$a_\mu^{\text{HLO}} = \left(\frac{\alpha}{\pi} \right)^2 \int_0^\infty dQ^2 f(Q^2) 4\pi^2 \left[\Pi^{(f)}(Q^2) - \Pi^{(f)}(Q^2 = 0) \right]. \quad (2.17)$$

2.1.2 Partially twisted boundary conditions

Using periodic boundary conditions on the lattice limits the accessible momenta to

$$p_i = \frac{2\pi n_i}{L}, \text{ and } p_0 = \frac{2\pi n_0}{T}. \quad (2.18)$$

Imposing partially twisted boundary conditions [65–67],

$$\psi(n + L\hat{k}) = e^{i\theta_k} \psi(n), \quad (2.19)$$

is equivalent to boosting the momentum of the quark field in a given direction by the twist angle θ_k . The boosted momenta are given by

$$p_i = \frac{2\pi n_i}{L} + \frac{\theta_k}{L}. \quad (2.20)$$

The momentum in time direction remains unchanged, as we impose twisted boundary conditions only in the spatial directions. The convolution integral in eq. (2.17) is dominated by contributions close to $Q^2 \approx m_\mu^2$. This technique allows to probe the low Q^2 -regime in more detail, which improves the estimate of the convolution integral. Furthermore, the additional intermediate Q^2 values allow for local interpolations, which we use to extract the Adler function from the VPF.

In practice one imposes twisted boundary conditions by interpreting the exponential as a constant $U(1)$ background field, which is multiplied with the gauge fields. From this one concludes that contracting two propagators with the same twist angle cancels the effect of the twisting. To circumvent this one redefines the currents in the presence of twists to

$$V_\mu^{(f,c)}(n, \Theta, \Theta') = \frac{q_f}{2} \left(\bar{\psi}_{f,\Theta}(n + a\hat{\mu})(1 + \gamma_\mu)U_\mu^\dagger(n)\psi_{f,\Theta'}(n) \right. \quad (2.21)$$

$$\left. - \bar{\psi}_{f,\Theta}(n)(1 - \gamma_\mu)U_\mu(n)\psi_{f,\Theta'}(n + a\hat{\mu}) \right),$$

$$V_\mu^{(f,l)}(n, \Theta', \Theta) = Z_V q_f \bar{\psi}_{f,\Theta'}(n)\gamma_\mu\psi_{f,\Theta}(n). \quad (2.22)$$

The introduction of two separate twist angles on the quark fields breaks iso-spin symmetry and thus leads to modifications of the Ward-Takahashi identities of the VPF. We discuss this issue later in 2.2. The current-current correlator used in the calculation of the VP tensor then reads with twisted boundary conditions

$$\begin{aligned} \left\langle V_\mu^{(f,c)}(n, \Theta, \Theta') V_\nu^{(f,l)}(0, \Theta', \Theta) \right\rangle = \\ \left\langle \text{Tr} \left[-\gamma_\nu \gamma_5 S_{f,\Theta}^\dagger(n + a\hat{\mu}, 0) \gamma_5 (1 + \gamma_\mu) U_\mu^\dagger(n) S_{f,\Theta'}(n, 0) \right. \right. \\ \left. \left. + \gamma_\nu \gamma_5 S_{f,\Theta}^\dagger(n, 0) \gamma_5 (1 - \gamma_\mu) U_\mu(n) S_{f,\Theta'}(n + a\hat{\mu}, 0) \right] \right\rangle \end{aligned} \quad (2.23)$$

The twisted propagator $S_{f,\Theta}(n + a\hat{\mu}, a\hat{\nu})$ is related to the untwisted propagator $S_f(n + a\hat{\mu}, a\hat{\nu})$ by a phase factor

$$S_{f,\Theta}(n + a\hat{\mu}, a\hat{\nu}) = \exp \left[i \frac{\Theta_\mu - \Theta_\nu}{L} \right] S_f(n + a\hat{\mu}, a\hat{\nu}), \quad (2.24)$$

and thus the result for the VP tensor with twisted boundary conditions reads

$$\begin{aligned} \Pi_{\mu\nu}^{(f)}(Q) = Z_V q_f^2 \frac{a^4}{4} \sum_n e^{iQ(n+a\hat{\mu}/2)} \\ \text{Tr} \left[-\exp \left(-\frac{i\Theta_\mu}{L} \right) \gamma_\nu \gamma_5 S_{f,\Theta}^\dagger(n + a\hat{\mu}, 0) \gamma_5 (1 + \gamma_\mu) U_\mu^\dagger(n) S_f(n, 0) \right. \\ \left. + \exp \left(\frac{i\Theta'_\mu}{L} \right) \gamma_\nu \gamma_5 S_{f,\Theta}^\dagger(n, 0) \gamma_5 (1 - \gamma_\mu) U_\mu(n) S_f(n + a\hat{\mu}, 0) \right], \end{aligned} \quad (2.25)$$

where now the momentum is modified to

$$Q = \left(\frac{2\pi n_t}{T}, \frac{2\pi \vec{n}}{L} + \frac{\vec{\Theta} - \vec{\Theta}'}{L} \right). \quad (2.26)$$

Label	V	β	a [fm]	m_π [MeV]
A3	64×32^3	5.20	0.0755(9)(7)	495
A4	64×32^3	5.20	0.0755(9)(7)	381
A5	64×32^3	5.20	0.0755(9)(7)	331
B6	96×48^3	5.20	0.0755(9)(7)	280
E5	64×32^3	5.30	0.0658(7)(7)	437
F6	96×48^3	5.30	0.0658(7)(7)	311
F7	96×48^3	5.30	0.0658(7)(7)	265
G8	128×64^3	5.30	0.0658(7)(7)	185
N5	96×48^3	5.50	0.0486(4)(5)	441
N6	96×48^3	5.50	0.0486(4)(5)	340
O7	128×64^3	5.50	0.0486(4)(5)	268

TABLE 2.1: The CLS ensembles used in this study. We use the scale determination via f_K [44, 68, 69]. The values of m_π listed here were determined in [56]. Note that in the following errors on the lattice spacing will be neglected.

Label	κ_{ud}	κ_s	κ_c
A3	0.1358	0.135364355	0.12552
A4	0.1359	0.135303471	0.12525
A5	0.13594	0.135275643	0.12515
B6	0.13597	0.135257096	0.12506
E5	0.13625	0.135802302	0.12724
F6	0.13635	0.135766419	0.12713
F7	0.13638	0.135755498	0.12713
G8	0.13642	0.135740236	0.12710
N5	0.1366	0.136275891	0.13026
N6	0.13667	0.136263492	0.13026
O7	0.13671	0.136256771	0.13022

TABLE 2.2: Hopping parameters κ_f used in this study [44]. The light-quark masses are degenerate.

2.1.3 Lattice setup

Our calculations are performed using ensembles generated within the CLS effort using $N_f = 2$ degenerate, $O(a)$ -improved Wilson fermions for the light-quarks. The strange- and charm-quarks are quenched in our calculations, meaning that only their valence contributions are included. In table 2.1 we give the details of the ensembles. In table 2.2 we show the hopping parameters κ_f for the flavours included in this study. The number of measurements performed for the VPF on each ensemble is listed in table 2.3. To illustrate the effect of partially twisted boundary conditions we show the results for the VPF on our most chiral ensemble G8 in figure 2.3 without including the renormalization coefficient Z_V for the light-quark contribution. In this study we use the data from periodic boundary conditions and twisted boundary conditions. We use only one twist angle $\vec{\Theta} = (1.44720, 0.0, 0.0)$. In table 2.4 we collect the non perturbative estimates of

Label	N_{cfg}	$N_{\text{src}}^{(ud)}$	$N_{\text{src}}^{(s)}$	$N_{\text{src}}^{(c)}$
A3	251	4	4	4
A4	400	4	4	4
A5	251	4	4	4
B6	306	4	4	4
E5	1000	4	4	4
F6	300	4	4	4
F7	250	4	4	4
G8(<i>ud</i>)	176/153	16/12	-	-
G8(<i>s, c</i>)	205	-	4	4
N5	347	4	4	4
N6	559	4	4	4
O7	149	16	4	4

TABLE 2.3: The number of configurations N_{cfg} and source positions N_{src} used on each of the CLS ensembles.

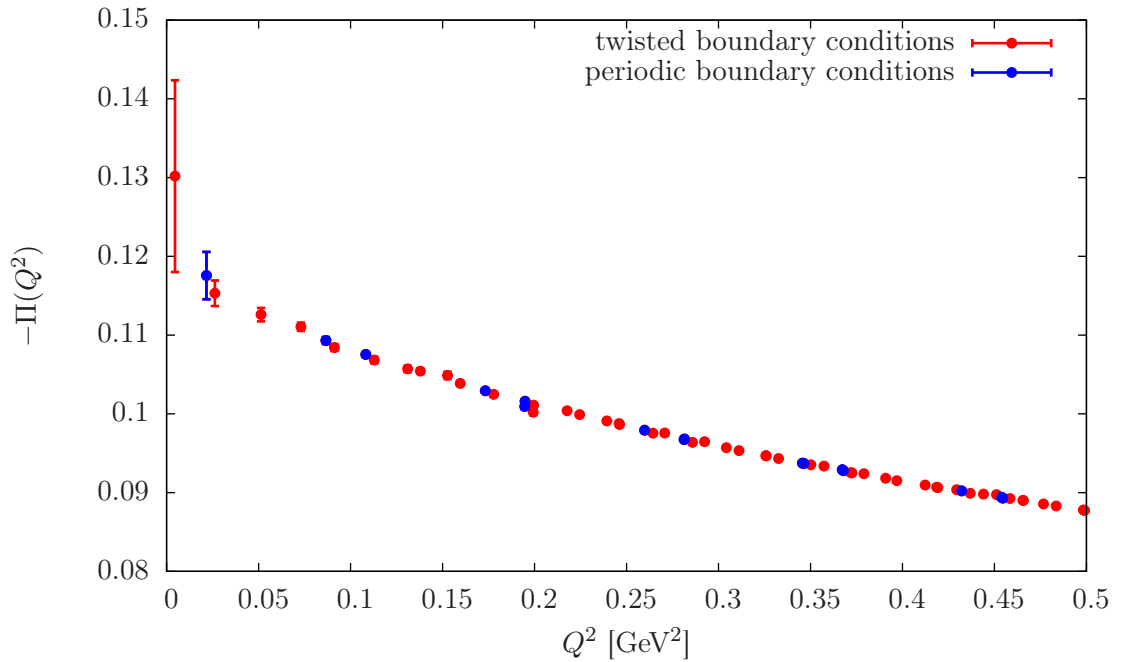


FIGURE 2.3: Comparison of the results for the VPF on G8 with twisted boundary conditions (red) and periodic boundary conditions (blue) for the light-quark contribution. In the low momentum region errors increase for both types of boundary conditions. Thus there is still a limit to the momenta one can probe, even with twisted boundary conditions.

Z_V used for the renormalization of our results, and a plot of the same is shown in figure 2.4. There is only a $\approx 1\%$ change in the renormalization between the light-quark and the strange-quark contribution. For the charm-quark contribution the mass dependence gives a much larger renormalization factor and also inverts the trend with respect to the lattice spacing.

Ensemble	$Z_V(u)$	$Z_V(s)$	$Z_V(c)$
A3	0.7323(3)	0.7463(3)	1.0894(6)
A4	0.7292(4)	0.7477(2)	1.0991(3)
A5	0.7272(4)	0.7480(2)	1.1017(6)
B6	0.7265(4)	0.7487(2)	1.1053(3)
E5	0.7442(3)	0.7583(2)	1.0463(4)
F6	0.7414(1)	0.7592(1)	1.0495(3)
F7	0.7401(2)	0.7595(1)	1.0497(3)
G8	0.7389(1)	0.7598(1)	1.0504(2)
N5	0.7652(1)	0.7751(1)	0.9670(1)
N6	0.7632(2)	0.7755(1)	0.9666(2)
O7	0.7619(1)	0.7756(1)	0.9675(2)

TABLE 2.4: Non perturbative estimates of Z_V for the flavours considered in this work taking the mass dependence into account [70].

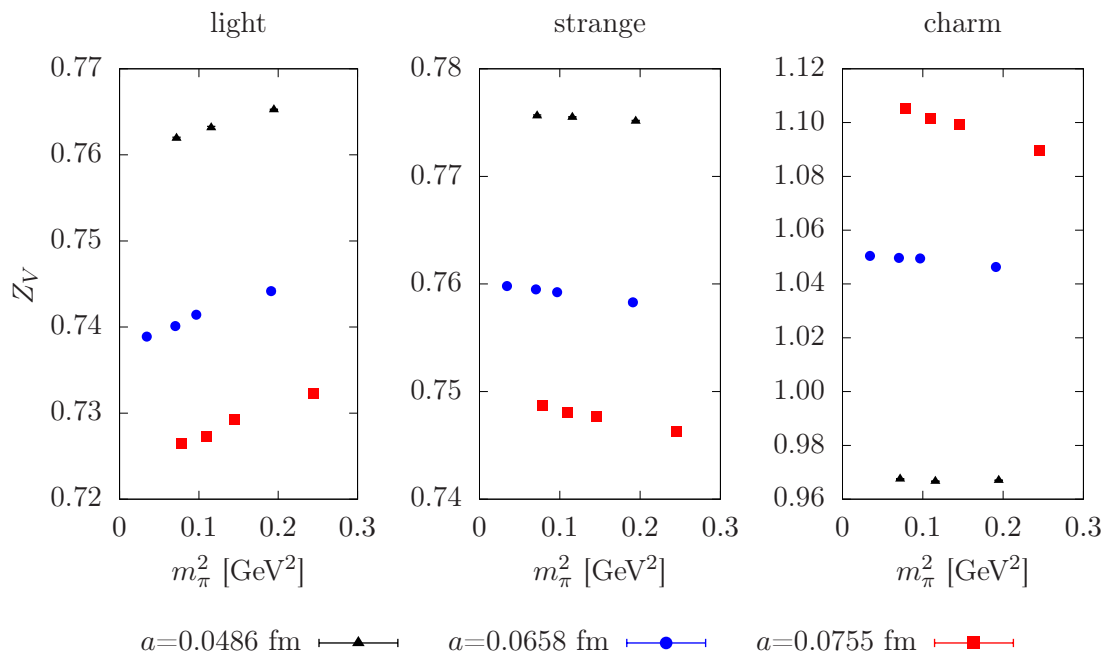


FIGURE 2.4: From left to right the non-perturbative estimates of Z_V for the light-, strange-, and charm-quark contributions are shown.

2.2 Ward identities of the vacuum polarization

In the continuum the VP tensor fulfills the Ward identities exactly

$$\sum_{\mu} q_{\mu} \Pi_{\mu\nu}(q) = \sum_{\nu} q_{\nu} \Pi_{\mu\nu}(q) = 0. \quad (2.27)$$

On the lattice these relations are violated by the use of a local non-conserved current or by the boundary conditions [71]. The partially twisted boundary conditions are introduced in the calculation as a constant $U(1)$ background field $B_{\mu} = \Theta_{\mu}/L$. Since we

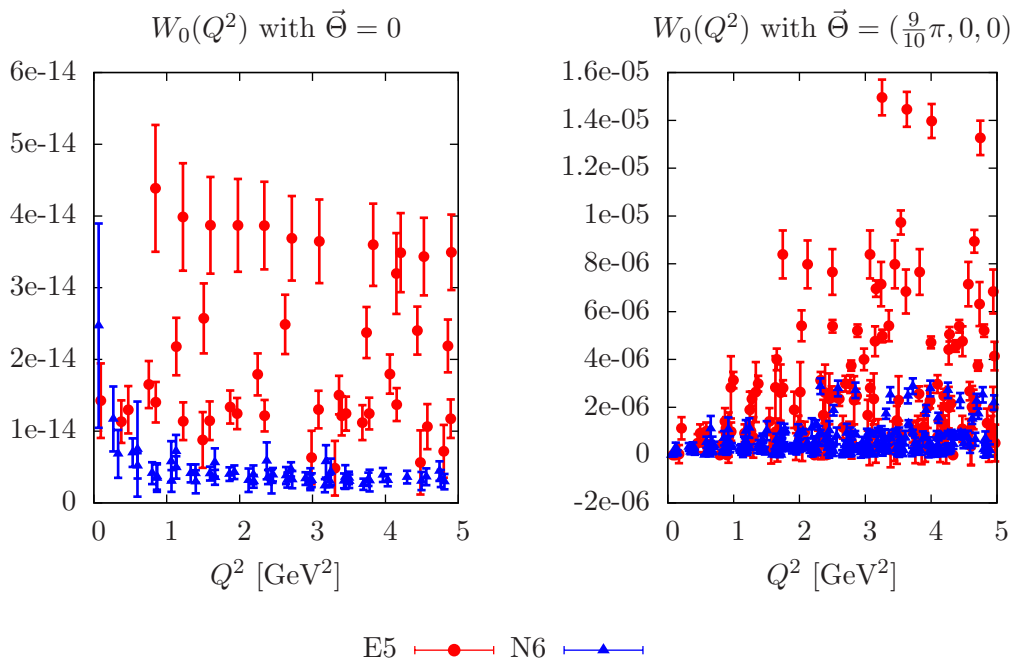


FIGURE 2.5: Comparison of the results for $W_0(Q^2)$ on E5 ($L \approx 2.0$ fm) and N6 ($L \approx 2.4$ fm). Left: For vanishing twist angles the Ward identity of the conserved current is fulfilled almost to machine precision. Right: For non-vanishing twist the violation of the Ward identity is related to the box size L .

use two different twist angles for the two quark propagators for the calculation of $\Pi_{\mu\nu}(Q)$ iso-spin symmetry is broken and thus the Ward identities of eq. (2.27) are violated. In the infinite volume limit, the effect of B_μ vanishes and thus the Ward identities of eq. (2.27) are restored. To study this effect, we define the quantity [72]

$$W_\nu(Q^2) = \left\langle \left| \sum_\mu Q_\mu \Pi_{\mu\nu}(Q) \right| \right\rangle_{Q^2}, \quad (2.28)$$

where, in order to avoid compensating effects, we average results from degenerate values of Q^2 only after taking the absolute value of each contribution. In the following, we discuss results for the light-quark contribution, because it is the dominant contribution to the HVP. Figure 2.5 shows the comparison of $W_0(Q^2)$ for vanishing and non-vanishing twist on the left and on the right, respectively. We find that for vanishing twist the Ward identity is fulfilled almost to machine precision, while for $\vec{\Theta} \neq 0$ the violation is of $O(10^{-5})$ at most and diminishes with increasing L . Figure 2.6 demonstrates that the violation defined in eq. (2.28) increases with increasing twist angle. To quantify the impact on our calculation we define the dimensionless ratio

$$R_\nu(Q^2) = \frac{W_\nu(Q^2)}{Q_\nu Q^2 \langle \Pi(Q^2) \rangle_{Q^2}}. \quad (2.29)$$

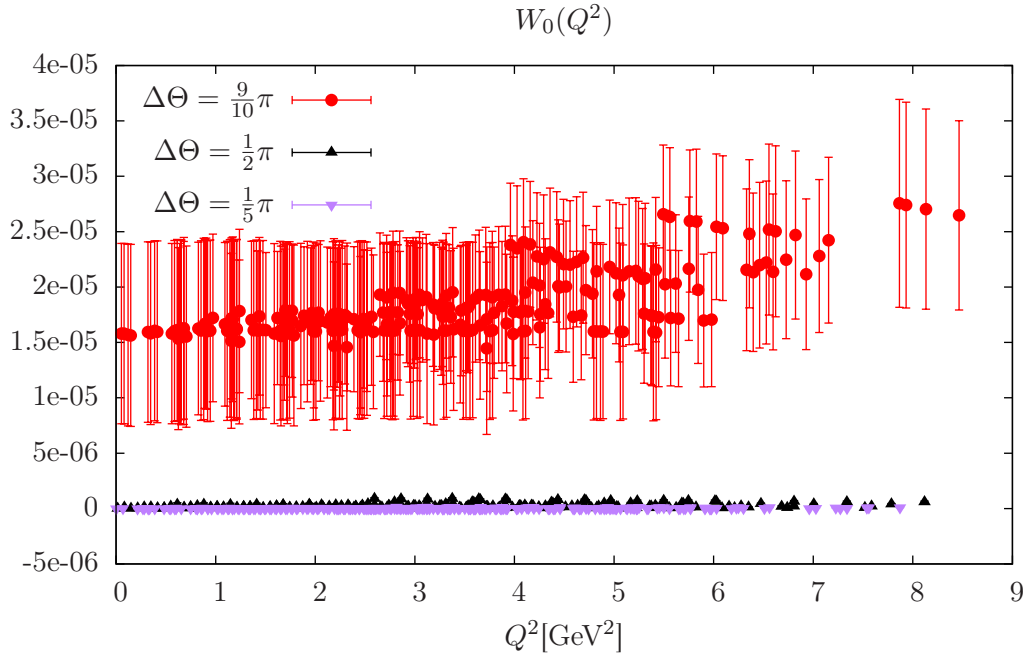


FIGURE 2.6: Results for $W_0(Q^2)$ on N6 for various twist angles. The violation of the Ward identity is proportional to the size of the twist angle.

This ratio in the time direction is shown in figure 2.7. We find that the effect of the violation of the Ward identity due to the presence of non vanishing twist angles can be neglected, since the effect is several orders of magnitude smaller than the precision of our calculation of the VPF.

Note that the relation between twist angles and the violation of the Ward identities is based on lower statistics than listed in table 2.3, but using three twist angles [72]. Since the effect of the violation of the Ward identity is much smaller than the precision we reach in our calculation, the same argument holds for the data with increased statistics used in the rest of this study as well. The violation of the Ward identity in the presence of twisted boundary conditions was discussed in [71], where also the modification of eq. (2.15) was shown that is required to preserve the Ward identities of eq. (2.27). Our numerical investigations show that the effect associated with the breaking of flavour symmetry by the use of twisted boundary conditions is negligible compared to the current precision of our calculation of the vacuum polarization function.

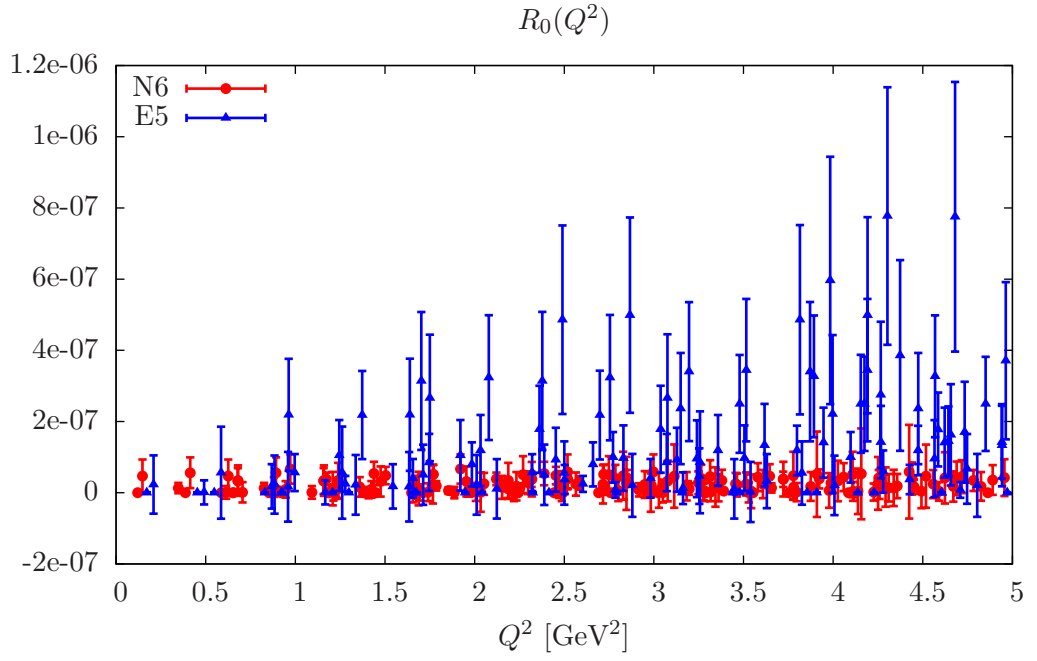


FIGURE 2.7: The ratio defined in eq. (2.29) is for the ensembles E5 and N6 in the time direction at most of $O(10^{-6})$, which leads to the conclusion that the violation of the Ward identity is several orders of magnitude below the current precision of our calculation for the VPF.

Chapter 3

The running of $\alpha_{\text{QED}}^{\text{had}}$ from the Adler function

3.1 The running of α_{QED} and the definition of the Adler function

The running coupling of a gauge theory is encoded in its beta function. For QED this reads [73–75]

$$\beta(\alpha_{\text{QED}}) = \mu \frac{d}{d\mu} \alpha_{\text{QED}}(\mu) = \frac{\alpha_{\text{QED}}^3(\mu)}{12\pi^2} + \frac{\alpha_{\text{QED}}^5(\mu)}{64\pi^2} + O(\alpha_{\text{QED}}^7(\mu)), \quad (3.1)$$

where μ is the energy scale at which the coupling is probed. With increasing energy the coupling increases monotonously. This is due to charge screening by vacuum polarization effects. The running of the coupling can be parameterized as

$$\alpha_{\text{QED}}(Q^2) = \frac{\alpha_{\text{QED}}^0}{1 - \Delta\alpha_{\text{QED}}(Q^2)}, \quad (3.2)$$

where we introduced the shift in the coupling as $\Delta\alpha_{\text{QED}}(Q^2)$. While the coupling at vanishing Q^2 is known with high accuracy [1],

$$\alpha_{\text{QED}}^0 = \alpha_{\text{QED}}(Q^2 = 0) = 1/137.035999074(44), \quad (3.3)$$

this accuracy deteriorates by five orders of magnitude as the mass of the Z is approached. The theoretical value at m_Z [76] is

$$\alpha_{\text{QED}}^{\text{th.}}(Q^2 = M_Z^2) = 1/128.952(14). \quad (3.4)$$

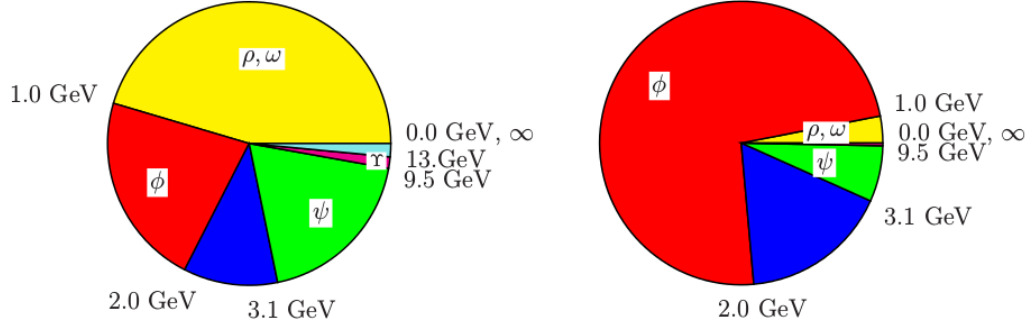


FIGURE 3.1: Hadronic contributions to the running of $\Delta\alpha_{\text{QED}}^{\text{had}}$ (left) and the corresponding error budget (right) with the associated particle resonances evaluated at $Q = 2.5$ GeV, taken from [80].

The experimental determination [77] is in agreement with the theoretical prediction but less precisely known

$$\alpha_{\text{QED}}^{\text{exp.}}(Q^2 = M_Z^2) = 1/127.9_{-2.8}^{+2.1}. \quad (3.5)$$

For high precision experiments this is a limiting factor, e.g. the future ILC. A large part of the loss of precision is due to hadronic effects. At present these are estimated by dispersive methods [76, 78, 79] with the help of e^+e^- cross-section data,

$$R_\gamma(s) = \frac{\sigma(e^+e^- \rightarrow \gamma^* \rightarrow \text{hadrons})}{\sigma(e^+e^- \rightarrow \gamma^* \rightarrow \mu^+\mu^-)}, \quad (3.6)$$

where s is the center of mass energy squared. The shift $\Delta\alpha_{\text{QED}}^{\text{had}}$ in the coupling is then computed via a split in the integration, where for the low energy range the cross-section data is used and for the high energy regime perturbative QCD (pQCD) is applied,

$$\Delta\alpha_{\text{QED}}^{(5)}(s) = -\frac{s\alpha_{\text{QED}}^0}{3\pi} \left(\int_{4m_\pi^2}^{E_{\text{cut}}^2} ds' \frac{R_\gamma^{\text{data}}(s')}{s'(s'-s)} + \int_{E_{\text{cut}}^2}^{\infty} ds' \frac{R_\gamma^{\text{pQCD}}(s')}{s'(s'-s)} \right). \quad (3.7)$$

The shift $\Delta\alpha_{\text{QED}}^{\text{had}}$ receives a sizeable contribution from the whole energy region. In order to obtain a smooth behaviour for the running of $\Delta\alpha_{\text{QED}}^{\text{had}}$ one typically matches perturbative QCD to the cross-section measurements at $Q_{\text{match}}^2 \approx 6.0$ GeV², but for $1.0 \lesssim Q^2 \lesssim 4.0$ GeV² the dispersive approach is poorly constrained by the data [80]. This observation is illustrated in figure 3.1, where the absolute contribution and the corresponding contribution to the error of $\Delta\alpha_{\text{QED}}^{\text{had}}$ are shown. In the low Q^2 regime lattice QCD can improve the calculation.

The Adler function is defined as the hadronic contribution to the derivative of the shift

of the fine structure constant [81],

$$D(Q^2) = \frac{3\pi Q^2}{\alpha} \frac{d}{dQ^2} \Delta\alpha_{\text{QED}}^{\text{had}}(Q^2) = -12\pi^2 Q^2 \frac{d\Pi(Q^2)}{dQ^2}. \quad (3.8)$$

$\Delta\alpha_{\text{QED}}^{\text{had}}$ can be obtained from the renormalized VPF (defined in eq. (2.16)),

$$\Delta\alpha_{\text{QED}}^{\text{had}}(Q^2) = \frac{\alpha_{\text{QED}}^0}{3\pi} \hat{\Pi}(Q^2), \quad (3.9)$$

such that to obtain $\Delta\alpha_{\text{QED}}^{\text{had}}$ at the physical point the renormalized VPF is also needed at the physical point. Although it is possible to define a global fit function for the VPF data, each ensemble would require an additional fit coefficient to determine the additive renormalization $\Pi(Q^2 = 0)$, which leads to much more difficult fits. We find that it is advantageous to determine the Adler function first using a global fit and then use the result to compute the renormalized VPF.

From the definition in eq. (3.8) we see that we can compute the Adler function using the derivative of the VPF and we will make use of this fact in 3.2.1. Experimentally the Adler function can be extracted from e^+e^- -annihilation experiments via the cross section ratio defined in eq. (3.6) [82]. The Adler function is then given by the dispersion integral,

$$D(Q^2) = Q^2 \int_{4m_\pi^2}^{\infty} \frac{R^{\text{exp}}(s)}{(s + Q^2)^2} ds, \quad (3.10)$$

where s is the center of mass energy squared. The Adler function can also be computed using perturbative QCD, the operator product expansion (OPE), and an estimate of the non-perturbative part using the dispersion integral of eq. (3.10) [83],

$$D(Q^2) = D^{(0)}(Q^2) + D^{(1)}(Q^2) + D^{(2)}(Q^2) + \dots + D^{NP}(Q^2), \quad (3.11)$$

where the perturbative expressions $D^{(n)}(Q^2)$ are proportional to $(\alpha_s/\pi)^n$ and $D^{NP}(Q^2)$ is the non-perturbative part. For a detailed discussion of this approach and the explicit expressions used in eq. (3.11), see [83].

3.2 The Adler function extracted from lattice data of the hadronic vacuum polarization

3.2.1 Methods to determine the Adler function

Eq. (3.8) relates the derivative of the VPF directly to the Adler function. The simplest way to determine this derivative would be to fit the VPF data and then insert the fit parameters into the derivative of the fit-ansatz. We will use a Padé [2,2] approximant [84, 85], i.e.

$$\begin{aligned}\Pi_{[2,2]}(Q^2) &= a_0 + Q^2 \left(\frac{a_1}{Q^2 + b_1} + \frac{a_2}{Q^2 + b_2} \right), \\ \frac{d}{dQ^2} \Pi_{[2,2]}(Q^2) &= \frac{a_1 b_1}{(Q^2 + b_1)^2} + \frac{a_2 b_2}{(Q^2 + b_2)^2}\end{aligned}\tag{3.12}$$

as a reference. Another option is to approximate the slope of the VPF by local linear fits at a given value of Q^2 . The determination of the slope at a single point in Q^2 from points of the HVP in a finite Q^2 interval inevitably leads to a systematic error. To counter this problem we study how these linear fits behave for several fit ranges, since we have a large number of points available due to the use of partially twisted boundary conditions. We developed two independent procedures to check for systematic effects. Both of these use local linear fits to determine the derivative of the VPF for a given Q^2 , but how the fit ranges are selected depends on the procedure. Figure 3.2 shows the results for the VPF on G8 for each flavour. We observe a significant curvature for the light- and the strange-quark contributions at small Q^2 , which diminishes as Q^2 is increased until an almost linear behaviour is found for large Q^2 . The curvature of the charm-quark contribution is smaller than the one of the light- or strange-quark contributions. The choice of the fit ranges should reflect changes in the behaviour of the VPF at small and large Q^2 and for the different flavours. Due to the different scales and general behaviours of the contributions we use a different set of parameters for the numerical methods to compute the Adler function for each flavour.

3.2.1.1 Method 1: Plateau of Slopes method

The first method to compute the Adler function is divided into the following steps.

1. For a given interval $[(Q_{\text{HVP}}^2)(n), (Q_{\text{HVP}}^2)(m)]$ we perform linear fits to the VPF,

$$\Pi^{\text{fit}}(Q^2) = a + bQ^2,\tag{3.13}$$

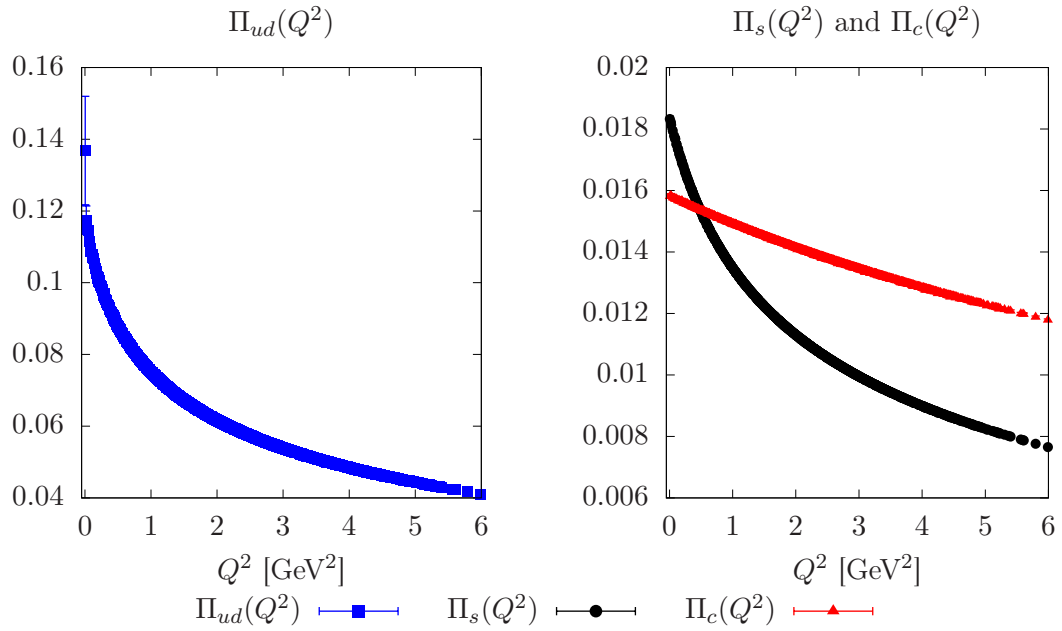


FIGURE 3.2: The VPF for all considered flavours on G8 ($a = 0.0658$ fm, $m_\pi = 185$ MeV). Left: The light-quark contribution to the VPF. Right: The strange and charm-quark contributions, which, though they are roughly of the same size, behave quite differently. The difference in the results for the leading order hadronic contribution to the anomalous magnetic moment of the muon is due to the kernel of the convolution integral, which is dominated by the low Q^2 -regime, where the strange-quark contribution is larger than the charm-quark contribution.

with a fit range starting from the n -th to the m -th data point. We repeat this fit for several fit ranges,

$$\begin{aligned}
 & [(Q_{\text{HVP}}^2)(n), (Q_{\text{HVP}}^2)(m + \epsilon)], \\
 & [(Q_{\text{HVP}}^2)(n), (Q_{\text{HVP}}^2)(m + 2\epsilon)], \\
 & \vdots \\
 & [(Q_{\text{HVP}}^2)(n), (Q_{\text{HVP}}^2)(m + l\epsilon)],
 \end{aligned} \tag{3.14}$$

by adding ϵ points to the upper bound of the fit interval m and repeating this l times. For the i th fit range we have the corresponding $(\chi_{\text{HVP}}^2)_i$. This step is illustrated at the top of figure 3.3. The Q^2 -value of the slope of the i th fit b_i is given by the average of the Q^2 values of the fit range $[(Q_{\text{HVP}}^2)(n), (Q_{\text{HVP}}^2)(m + i\epsilon)]$, which we refer to as Q_D^2 . At the bottom of figure 3.3 we show the slopes determined via the linear fits shown at the top of that figure.

2. To find the region where the linear coefficients b_i from these l fits are stable with respect to the fit range we apply weighted averages, i.e. we apply a constant fit,

to all possible consecutive combinations of b_i ,

$$\begin{aligned}\bar{b}_0 &= \langle b_0, b_1 \rangle_{\text{WA}}, \\ \bar{b}_1 &= \langle b_0, b_1, b_2 \rangle_{\text{WA}}, \\ \bar{b}_{\dots} &= \langle b_0, b_1, \dots, b_l \rangle_{\text{WA}}, \\ &\vdots \\ \bar{b}_k &= \langle b_{l-1}, b_l \rangle_{\text{WA}},\end{aligned}\tag{3.15}$$

where $\langle \dots \rangle_{\text{WA}}$ refers to the weighted average and k is the number of possible combinations. For each of these weighted averages we have the result of the minimization of the fit, $(\chi_{\text{WA}}^2)_0, \dots, (\chi_{\text{WA}}^2)_k$. From these we select the minimum,

$$(\chi_{\text{WA}}^2)_{\min} = \min \{ (\chi_{\text{WA}}^2)_0, \dots, (\chi_{\text{WA}}^2)_k \}.\tag{3.16}$$

The indices of the slopes b_i that enter the weighted average of this minimum are in the interval $r < i < s$ with $0 \leq r < s \leq l$.

3. The slope b_{\min} used in the calculation of the Adler function is the one corresponding to the minimal χ_{HVP}^2 ,

$$(\chi_{\text{HVP}}^2)_{\min} = \min \left\{ (\chi_{\text{HVP}}^2)_r, (\chi_{\text{HVP}}^2)_{r+1}, \dots, (\chi_{\text{HVP}}^2)_{s-1}, (\chi_{\text{HVP}}^2)_s \right\}.\tag{3.17}$$

Thus we choose the best fit to the HVP with a fit range suitable to describe the HVP in this regime with a linear ansatz. The Adler function is then given by $D(Q_D^2) = -12\pi^2 b_{\min} Q_D^2$.

4. To obtain the Adler function at larger Q^2 we shift the lower and upper bounds by δ points,

$$\begin{aligned}n &= n + \delta, \\ m &= m + \delta,\end{aligned}\tag{3.18}$$

and then restart the procedure from the first step. We repeat this until the lower bound n is larger than the largest available point Q_{HVP}^2 , computed in the course of the simulations.

5. The previous step, the shift by δ points to restart the procedure, may lead to an artificially large amount of points for the Adler function, such that we may end up with more points for the Adler function than there are points for the VPF in an interval of two consecutive points $[Q_{\text{HVP}}^2(n), Q_{\text{HVP}}^2(n+1)]$. The final step of this procedure is the removal of these redundant points. In a given Q^2 -interval there

may be a number of points for the Adler function with,

$$D((Q_D^2)_1), D((Q_D^2)_2), \dots, D((Q_D^2)_u), \quad (3.19)$$

which fulfill,

$$(Q_{\text{HVP}}^2)(n) < (Q_D^2)_1 < (Q_D^2)_2 < \dots < (Q_D^2)_u < (Q_{\text{HVP}}^2)(n+1), \quad (3.20)$$

we have for each of the Adler function points the corresponding

$$[(\chi_{\text{HVP}}^2)_{\text{min}}]_1, [(\chi_{\text{HVP}}^2)_{\text{min}}]_2, \dots, [(\chi_{\text{HVP}}^2)_{\text{min}}]_u. \quad (3.21)$$

We select as the final point for the description of the Adler function in the interval $(Q_{\text{HVP}}^2)(n) < Q^2 < (Q_{\text{HVP}}^2)(n+1)$ the point corresponding to the minimum

$$[(\chi_{\text{HVP}}^2)_{\text{min}}]_{\text{best fit}} = \min \left\{ [(\chi_{\text{HVP}}^2)_{\text{min}}]_1, [(\chi_{\text{HVP}}^2)_{\text{min}}]_2, \dots, [(\chi_{\text{HVP}}^2)_{\text{min}}]_u \right\}. \quad (3.22)$$

As an example for this method we show the results for the different flavours in figure 3.4, where the result of eq. (3.12) is shown as a reference.

3.2.1.2 Method 2: Curvature Limit method

The general idea of the second method we developed is very similar to the first method, thus the steps 4. and 5. are the same as for the Plateau of Slopes method. The difference is that we apply selection criteria instead of searching for stability of the slopes of the linear fits with respect to the different fit ranges.

1. For a given interval $[(Q_{\text{HVP}}^2)(n), (Q_{\text{HVP}}^2)(m)]$ we perform linear and quadratic fits,

$$\Pi_{\text{lin.}}^{\text{fit}}(Q^2) = a_{\text{lin.}} + b_{\text{lin.}}Q^2, \quad (3.23)$$

$$\Pi_{\text{quad.}}^{\text{fit}}(Q^2) = a_{\text{quad.}} + b_{\text{quad.}}Q^2 + c_{\text{quad.}}Q^4, \quad (3.24)$$

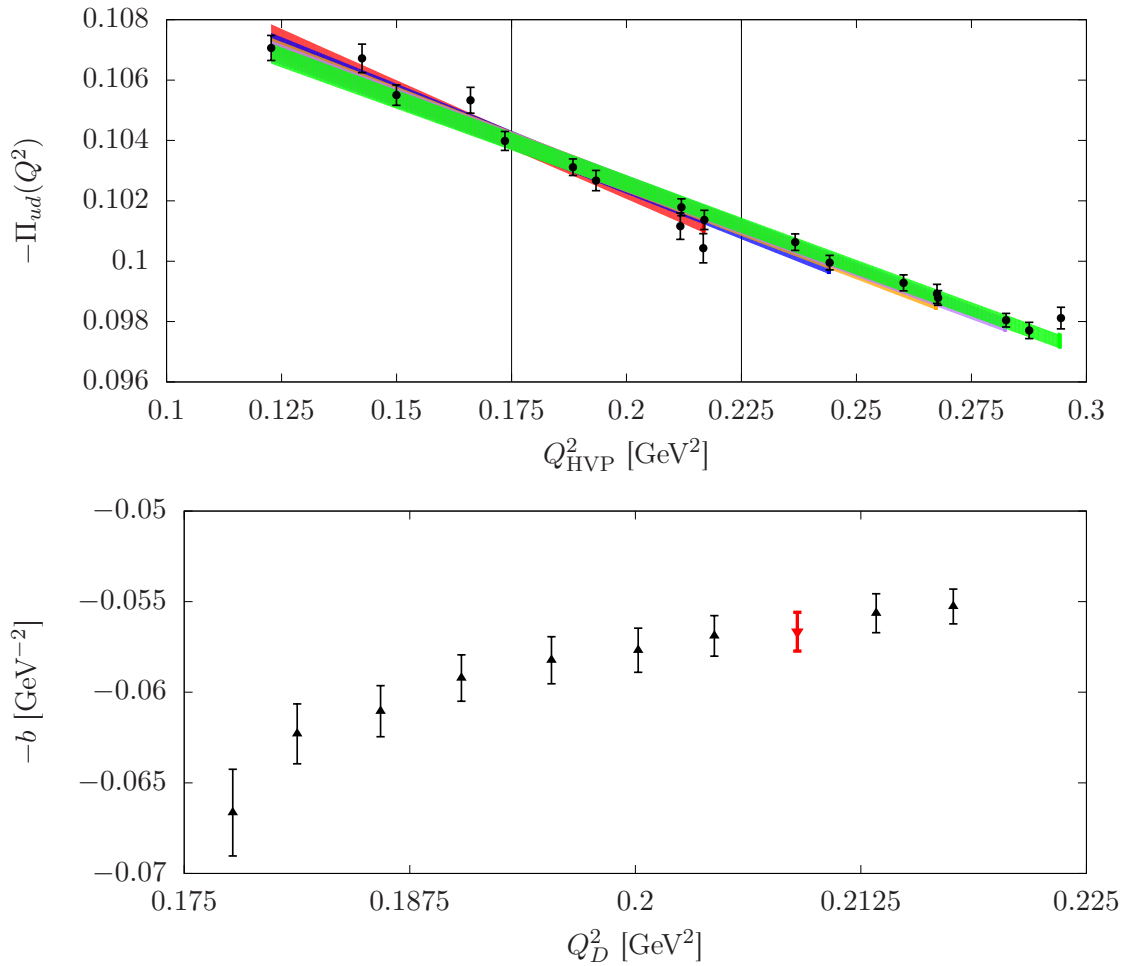


FIGURE 3.3: An example of results for the intermediate steps on G8 for the light-quark contribution for the Plateau of Slopes method. Top: Demonstration of the first step, where linear fits are applied to the VPF with increasing upper bounds for $0.125 < Q^2 < 0.3 \text{ GeV}^2$, which refers to the actual momenta of the VPF. Bottom: Illustration of the second step where we scan the results for the linear coefficient b obtained from the linear fits in the top figure for a region in Q_D^2 where they are stable using weighted averages to all possible combinations, which in this case means 36 combinations. The label Q_D^2 refers to the average of the momenta of the points entering the respective fits to the VPF. The value of b which is chosen to compute the Adler function in this particular example is shown in red with a triangle pointing down. Note that the position values of Q_D^2 for the slope are within the bounds of the interval shown in vertical lines in the top figure and that in the figure at the top only 5 fits are shown for visibility, though 10 fits to the VPF were performed, cf. the figure at the bottom where all 10 results for the slopes are shown.

with a fit range starting from the n -th to the m -th data point. We repeat this fit for several fit ranges,

$$\begin{aligned}
 & [(Q_{\text{HVP}}^2)(n), (Q_{\text{HVP}}^2)(m + \epsilon)], \\
 & [(Q_{\text{HVP}}^2)(n), (Q_{\text{HVP}}^2)(m + 2\epsilon)], \\
 & \vdots \\
 & [(Q_{\text{HVP}}^2)(n), (Q_{\text{HVP}}^2)(m + l\epsilon)],
 \end{aligned} \tag{3.25}$$

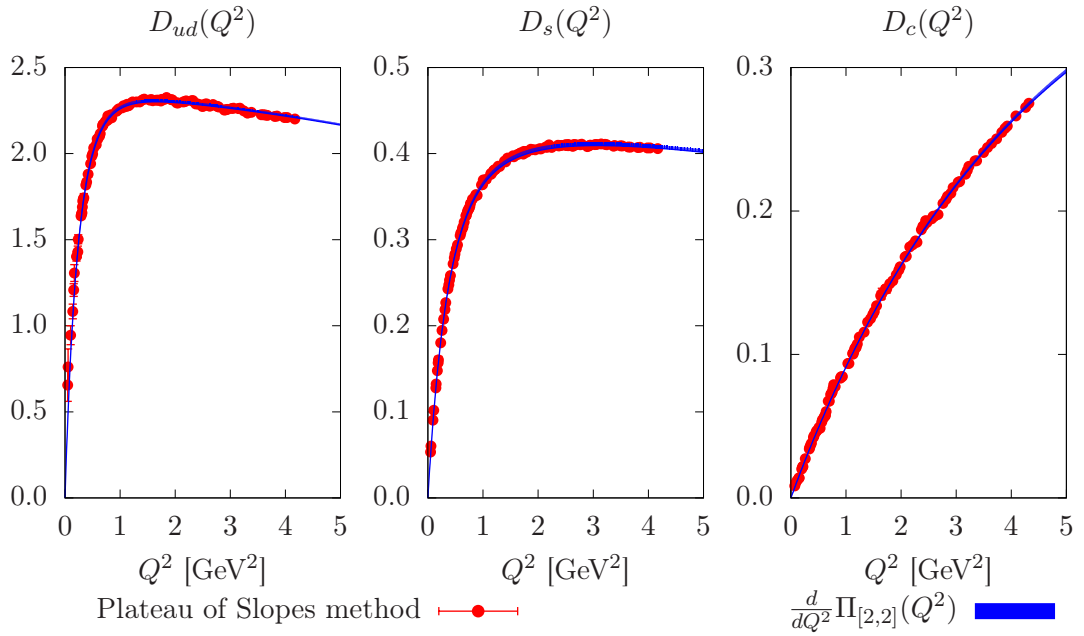


FIGURE 3.4: Example of the results for the Plateau of Slopes method on G8. The light-, strange-, and charm-quark contributions are shown from left to right, respectively. We find that the results are in agreement with the result where we directly fit the VPF with a Padé ansatz. Note that Z_V is not yet applied.

by adding ϵ points to the upper bound of the fit interval m and repeating this l times. For the i th fit range we have the corresponding $(\chi_{\text{HVP,lin.}}^2)_i$ and $(\chi_{\text{HVP,quad.}}^2)_i$. The Q^2 -value of the slope of the i th fit b_i is given by the average of the Q^2 values of the fit range $[(Q_{\text{HVP}}^2)(n), (Q_{\text{HVP}}^2)(m + i\epsilon)]$, which we refer to as Q_D^2 . The quadratic fit is only used for the selection criteria we apply in the next step.

2. Then we impose the following conditions on the fit results,

$$|c_{\text{quad.}}| < \gamma_{\text{crit}} \Delta c_{\text{quad.}} \quad (3.26)$$

$$|b_{\text{lin.}} - b_{\text{quad.}}| < \beta_{\text{crit}} \sqrt{(\Delta b_{\text{lin.}})^2 + (\Delta b_{\text{quad.}})^2} \quad (3.27)$$

$$(\chi_{\text{HVP,lin.}}^2) \geq \chi_{\text{crit}}^2, \quad (3.28)$$

where $\Delta b_{\text{lin.}}, \Delta b_{\text{quad.}}, \Delta c_{\text{quad.}}$ refer to the statistical errors of the corresponding fit parameters, $b_{\text{lin.}}, b_{\text{quad.}}, c_{\text{quad.}}$. The values of $\gamma_{\text{crit}}, \beta_{\text{crit}}$, and χ_{crit}^2 are set by hand and the actual values are the result of tuning to improve the performance of the procedure. With eq. (3.26) we remove fits with a too large curvature, we found that $\gamma_{\text{crit}} = 10$ gives the best results. This imposes a constraint on fits with large fit intervals where the data begin to show a curvature which can not be described by a linear fit. Eq. (3.27) checks that the slope of the linear fit is not too different from the quadratic fit. In our calculations we use $\beta_{\text{crit}} = 10$. The last

condition, eq. (3.28), removes fits where the $\left(\chi_{\text{HVP,lin.}}^2\right)_i$ is artificially small, which can happen when we go to very small fit intervals of 3 to 4 points, which are in a very small range of Q^2 but show fluctuations. These fluctuations consequently lead to fluctuations in the Adler function of several sigma, which would be unexpected given the precision of the VPF that we start from. We use $\chi_{\text{crit}}^2 = 2 \cdot 10^{-6}$. Figure 3.5 shows an example of the results for this intermediate step.

3. For each of these fits we have

$$B_i = \left(\frac{|b_{\text{lin.}} - b_{\text{quad.}}|}{\sqrt{(\Delta b_{\text{lin.}})^2 + (\Delta b_{\text{quad.}})^2}} \right)_i. \quad (3.29)$$

We use the coefficient $b_{\text{lin.}}$ of the minimum,

$$B_{\text{min}} = \min \{B_1, B_2, \dots, B_l\}, \quad (3.30)$$

to compute the Adler function, $D(Q_D^2) = -12\pi^2 b_{\text{lin.}}^{\text{min}} Q_D^2$.

4. To obtain the Adler function at larger Q^2 we shift the lower and upper bounds by δ points,

$$\begin{aligned} n &= n + \delta, \\ m &= m + \delta, \end{aligned} \quad (3.31)$$

and then restart the procedure from the first step. We repeat this until the lower bound n is larger than the largest available point Q_{HVP}^2 , computed in the course of the simulations.

5. The previous step, the shift by δ points to restart the procedure, may lead to an artificially large amount of points for the Adler function, such that we may end up with more points for the Adler function than there are points for the VPF in an interval of two consecutive points $[Q_{\text{HVP}}^2(n), Q_{\text{HVP}}^2(n+1)]$. The final step of this procedure is the removal of these redundant points. In a given Q^2 -interval there may be a number of points for the Adler function with,

$$D((Q_D^2)_1), D((Q_D^2)_2), \dots, D((Q_D^2)_u), \quad (3.32)$$

which fulfill,

$$(Q_{\text{HVP}}^2)(n) < (Q_D^2)_1 < (Q_D^2)_2 < \dots < (Q_D^2)_u < (Q_{\text{HVP}}^2)(n+1), \quad (3.33)$$

we have for each of the Adler function points the corresponding

$$[(\chi_{\text{HVP}}^2)_{\text{min}}]_1, [(\chi_{\text{HVP}}^2)_{\text{min}}]_2, \dots, [(\chi_{\text{HVP}}^2)_{\text{min}}]_u. \quad (3.34)$$

We select as the final point for the description of the Adler function in the interval $(Q_{\text{HVP}}^2)(n) < Q^2 < (Q_{\text{HVP}}^2)(n+1)$ the point corresponding to the minimum

$$[(\chi_{\text{HVP}}^2)_{\text{min}}]_{\text{best fit}} = \min \left\{ [(\chi_{\text{HVP}}^2)_{\text{min}}]_1, [(\chi_{\text{HVP}}^2)_{\text{min}}]_2, \dots, [(\chi_{\text{HVP}}^2)_{\text{min}}]_u \right\}. \quad (3.35)$$

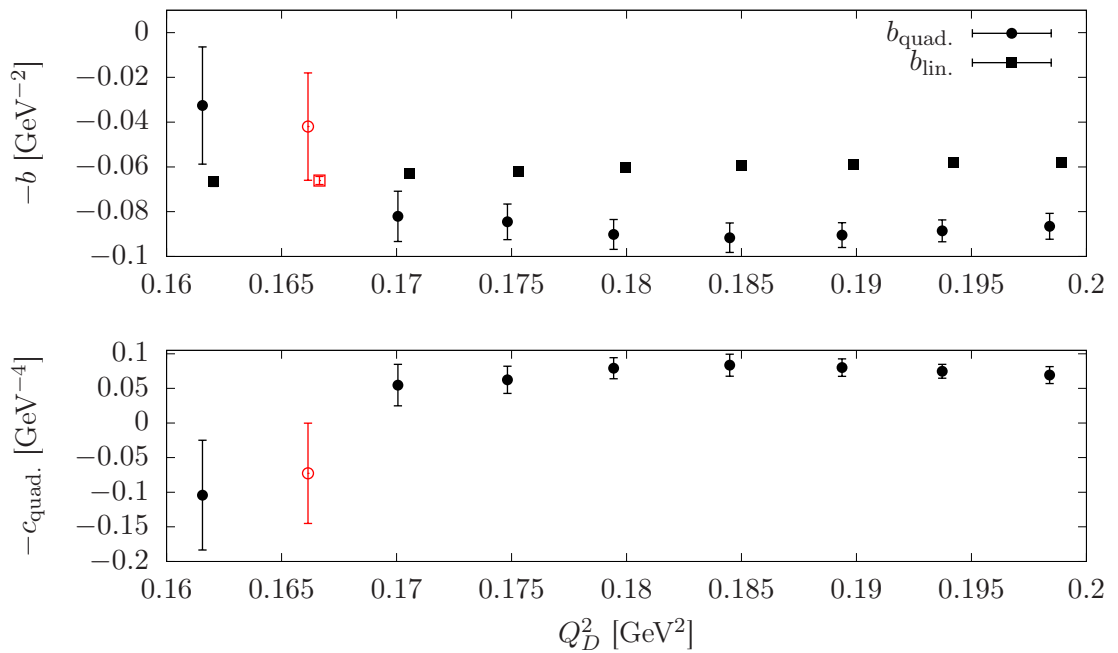


FIGURE 3.5: Illustration of the intermediate steps for the Curvature Limit method on G8 for the light-quark contribution. Top: The linear coefficients of the linear fit and the quadratic fit are shown as squares and circles, respectively. We observe that the result of the linear fit is quite stable for the chosen fit ranges, while the quadratic fit is unstable for smaller fit ranges. Bottom: The curvature of the quadratic fit vanishes at small Q^2 , and it grows for larger fit ranges as one would expect. The open symbols in red refer to the value which was selected to compute the Adler function in this example.

Figure 3.6 shows an example for the second method we use to compute the Adler function on G8. We show again the result of the derivative of the fit to the VPF, where we use the Padé [2,2] for the ansatz as a reference. For both methods we vary the minimal $N_{\text{min}}^{\text{fit}}$ and maximal $N_{\text{max}}^{\text{fit}}$ number of points for each fit, the number of points ϵ added to the upper bound in step one, and the number of points δ added to the lower bound in the last step gradually from small Q^2 to large Q^2 , since the curvature of the VPF changes in different regimes of Q^2 . These variations depend on the chosen method and may be different for both methods for a given range in Q^2 . In general we find that smaller fit ranges are advantageous in the low- Q^2 regime and larger fit ranges stabilize

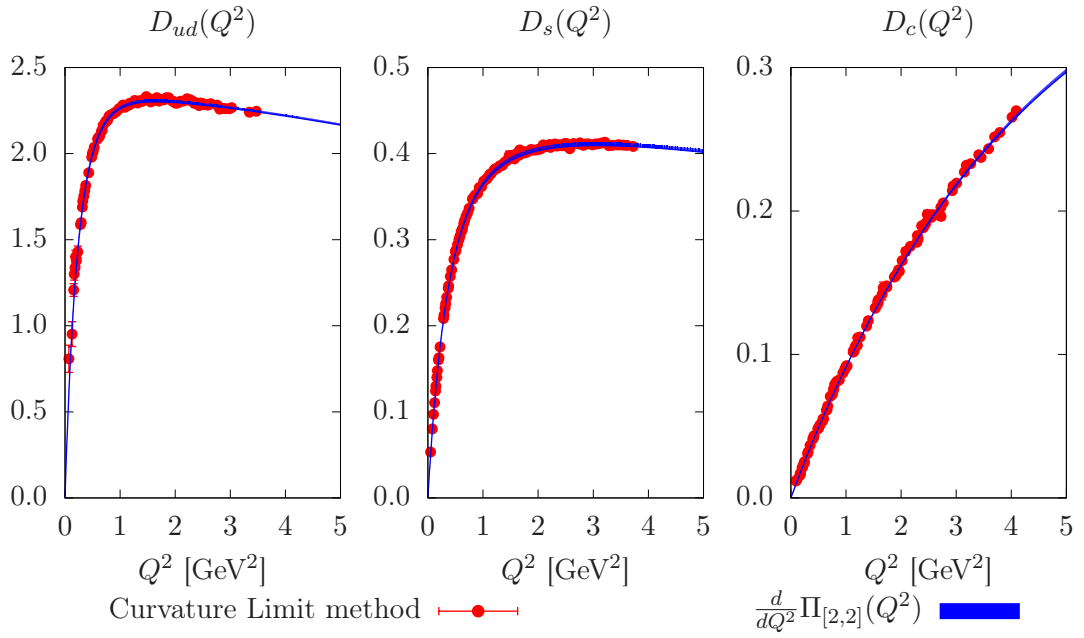


FIGURE 3.6: Results of the Adler function for the different flavours for the Curvature Limit method on G8. We also find that the results agree with the derivative in eq. (3.12) of the Padé ansatz we use to fit the VPF. The different flavours are shown separately, from left to right we show the light, strange and charm quark contributions, respectively. Note that Z_V is applied at a later stage in the calculation.

the behaviour of the Adler function for larger Q^2 . It should also be noted that a given interval $[Q_1^2, Q_2^2]$ with parameters $p = (N_{\min}^{\text{fit}}, N_{\max}^{\text{fit}}, \epsilon, \delta)$ may overlap with neighbouring intervals which use a different combination of parameters.

We show a comparison of the Plateau of Slopes and the Curvature Limit methods in figure 3.7 for G8 for the light-, strange-, and charm-quark contribution. We observe that both methods show the same trends for the Adler function. A one to one comparison of the points is difficult since the two methods return the Adler function at different points in Q^2 , thus the points need not necessarily match within errors, especially for the low Q^2 -range where the Adler function increases rapidly. Furthermore, we find that on G8 the Curvature Limit method has some difficulties to select points for the Adler function at large Q^2 , thus the range of the Adler function is slightly reduced for this method. For the fit ranges discussed for the extraction of the Adler function at the physical point this is not a problem, since for most of the ensembles we cover a much larger range in Q^2 with both methods to compute the Adler function than the range shown here as an example for G8.

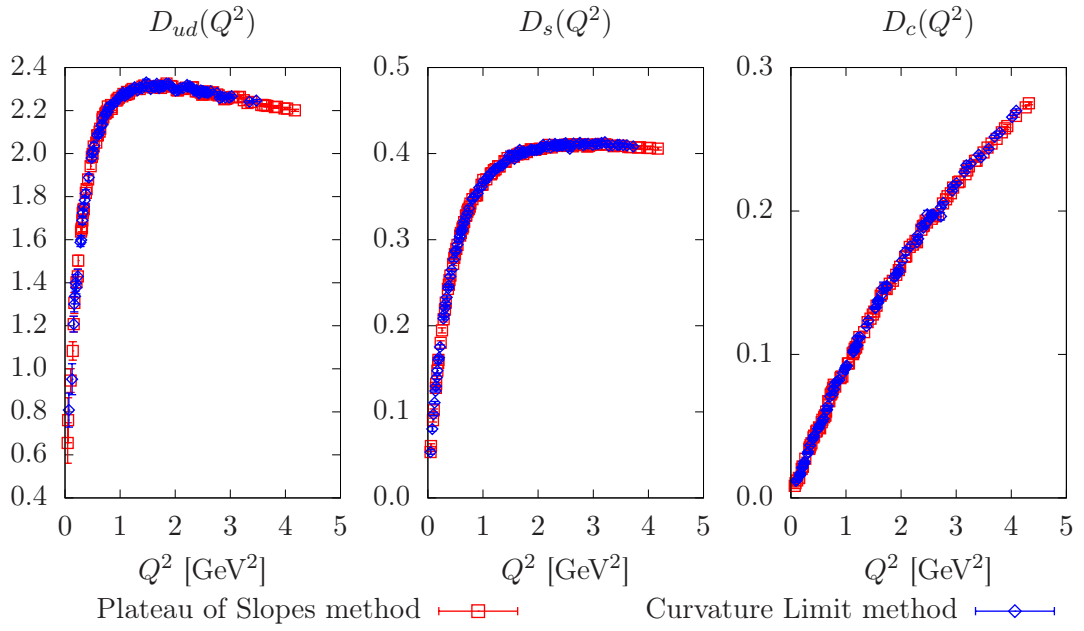


FIGURE 3.7: The results for the Plateau of Slopes (red) and the Curvature Limit (blue) methods show similar trends for all three flavours. Since both methods return the Adler function at different values in Q^2 a one to one comparison of the points is impossible. Thus the points need not necessarily agree within errors, especially in the low Q^2 -regime where the Adler function grows rapidly. The shorter range in Q^2 of the Curvature Limit method is not a problem for our fits, since we cover a much larger range in Q^2 on most ensembles than shown here on G8.

3.2.2 Extrapolation of the Adler function to the physical point

We extrapolate the Adler function to the physical point with simultaneous fits in Q^2 , m_π^2 , and the lattice spacing a with the general fit ansatz:

$$D_{i,j,k}(Q^2, m_\pi^2, a) = Q^2 P'_{[i,j]}(Q^2) (1 + g(a, Q) + h_k(m_\pi^2, Q^2)). \quad (3.36)$$

The product $Q^2 P'_{[i,j]}(Q^2)$ contains the Q^2 -dependence at the physical point. As mentioned in subsection 3.2.1, it is natural to assume that the Q^2 -dependence of the Adler function follows the derivative of a Padé ansatz multiplied with Q^2 . We use the Padé approximants written as [84, 85]:

$$P_{[i+1,i]}(Q^2) = Q^2 \left(a_0 + \sum_{j=1}^i \frac{a_j}{b_j + Q^2} \right), \quad (3.37)$$

$$P_{[i,i]}(Q^2) = Q^2 \left(\sum_{j=1}^i \frac{a_j}{b_j + Q^2} \right). \quad (3.38)$$

The derivatives of equations (3.37, 3.38) with respect to Q^2 read

$$\frac{d}{dQ^2}P_{[i+1,i]}(Q^2) = P'_{[i+1,i]}(Q^2) = a_0 + \sum_{j=1}^i \frac{a_j b_j}{(b_j + Q^2)^2}, \quad (3.39)$$

$$\frac{d}{dQ^2}P_{[i,i]}(Q^2) = P'_{[i,i]}(Q^2) = \sum_{j=1}^i \frac{a_j b_j}{(b_j + Q^2)^2}. \quad (3.40)$$

Since the goal of the combined fit is to describe a long range in Q^2 with $0 < Q^2 < 5 \text{ GeV}^2$ we investigate, depending on the contribution, the Padé approximants from [1,1] to [4,3]. The pion mass dependence and a part of the Q^2 dependence at unphysical pion mass is described by $h_k(m_\pi^2, Q^2)$,

$$h_1(m_\pi^2) = \frac{c_1}{c_2 + Q^2} \left(m_\pi^2 - (m_\pi^{\text{exp}})^2 \right) \quad (3.41)$$

$$h_2(m_\pi^2) = \frac{c_1}{c_2 + Q^2} \left(m_\pi^2 - (m_\pi^{\text{exp}})^2 \right) + \frac{c_3}{c_4 + Q^4} \left(m_\pi^2 - (m_\pi^{\text{exp}})^2 \right)^2. \quad (3.42)$$

We found that leaving the fit parameters c_2 and c_4 for the position of the poles free can lead to artefacts for $0 < Q^2 < 0.5 \text{ GeV}^2$ for the ensembles with heavy pion mass, since the pole positions may approach $-Q^2 \rightarrow 0$. To prevent these artefacts, we use the same fit parameters b_1, b_2 that we used in the equations (3.39, 3.40):

$$h_3(m_\pi^2) = \frac{c_1}{b_1 + Q^2} \left(m_\pi^2 - (m_\pi^{\text{exp}})^2 \right) + \frac{c_2}{b_2 + Q^4} \left(m_\pi^2 - (m_\pi^{\text{exp}})^2 \right)^2, \quad (3.43)$$

$$h_4(m_\pi^2) = \frac{c_1}{b_1 + Q^2} \left(m_\pi^2 - (m_\pi^{\text{exp}})^2 \right). \quad (3.44)$$

For the description of the lattice spacing dependence we use

$$g(a, Q) = d_1(aQ) + d_2(4\pi f_K^{\text{exp}} a), \quad (3.45)$$

where the term with the fit parameter d_1 describes Q^2 dependent cut-off effects, while the term with d_2 represents lattice artefacts that are independent of the momentum transfer. The choice of the constant factor $4\pi f_K^{\text{exp}}$ does not affect the fit results and is merely used as a typical QCD scale in order to render d_2 dimensionless and of $O(1)$.

In principle it would be possible to take correlations of the data in the Q^2 -dependence on each ensemble into account by using a block diagonal form of the covariance matrix. However, we find that the fits do in many cases not converge and in others result in very poor values for χ^2/dof , due to fluctuations around the general trend of the data caused by the numerical derivative we take to estimate the Adler function. Thus we use only uncorrelated fits in the following analysis.

3.2.2.1 The light-quark contribution

For the light-quark contribution we use the derivatives of the Padé ansätze [2,2], [3,2], [3,3], and [4,3] to describe the Q^2 -dependence. In table 3.1 we list fit ansätze we used and the corresponding uncorrelated χ^2/dof and the degrees of freedom (dof) for both methods. To study systematic effects we impose cuts on the ensembles that enter the combined fit, for lattice artefacts we remove the coarsest lattice spacing ($a < 0.070$ fm), for the pion mass dependence we remove the three ensembles with $m_\pi > 400$ MeV, and we also combine both cuts. The fit interval is limited to $0 < Q^2 < 5.0$ GeV². Due to the bad $\chi_{\text{uncorr}}^2/\text{dof}$ we find very poor p-values, which makes it impossible to use them as weights in the following analysis.

To convince ourselves that these fits still give a good description of the Adler function we investigate the behaviour of the fit ansatz $D_{3,2,4}(Q^2, m_\pi^2, a)$ in some detail. Figure 3.8 shows the result for this ansatz evaluated at $m_\pi = 270$ MeV in the continuum and for the comparison to the data at the respective lattice spacings of ensembles the B6, F7, and O7, which have $m_\pi \approx 270$ MeV using the Plateau of Slopes method. For $Q^2 > 1.0$ GeV² we find a clear separation of the data and the linear ansatz for lattice artefacts in eq. (3.45) describes this behaviour. We observe that for $Q^2 < 1.0$ GeV² this separation diminishes to the point where we can not distinguish the individual curves for the ensembles and the continuum limit itself. In figure 3.9 we show the result of the same fit, where we keep the momentum transfer fixed while we vary the lattice spacing. Again, we observe that the lattice spacing dependence is steeper for larger Q^2 than it is for lower Q^2 .

Figure 3.10 shows the result for the fit ansatz $D_{3,2,4}(Q^2, m_\pi^2, a)$ at the intermediate lattice spacing. This allows us to check the pion mass dependence over the full range in Q^2 . The result of the extrapolation to physical point mass at $a = 0.0658$ fm is shown in gray. A clear separation of the data due to the different pion masses can be observed for 0.5 GeV² $\lesssim Q^2$ and for increasing Q^2 this separation diminishes. Furthermore, we find that the gap between G8 ($m_\pi = 185$ MeV) and the physical pion mass is below the statistical error margin. This behaviour is confirmed in figure 3.11, where we evaluate the fit ansatz at the different lattice spacings at two fixed values of Q^2 while varying the pion mass. For $Q^2 = 4.0$ GeV² we observe a clear separation due to the lattice spacing, while the pion mass dependence is small. At $Q^2 = 1.0$ GeV² on the other hand we do not see the separation due to the lattice spacing as clearly, but the pion mass dependence is much steeper. This indicates that eqs. (3.41 - 3.44) describe the mass dependence correctly and capture the change in Q^2 . The list of results for the Curvature Limit method and the corresponding figures can be found in B.1.

We employ the extended frequentist method (see 1.4.10) to estimate the systematic errors of the result of the Adler function at the physical point. The low Q^2 regime

	Plateau of Slopes method		Curvature Limit method	
Label	χ^2/dof	dof	χ^2/dof	dof
All 11 ensembles				
$D_{2,2,3}$	4.47	678	3.41	672
$D_{3,2,3}$	3.89	677	3.06	671
$D_{2,2,4}$	5.15	680	4.09	674
$D_{3,2,4}$	3.89	679	3.10	673
$D_{3,3,3}$	2.97	676	2.59	670
$D_{4,3,3}$	3.01	675	2.55	669
$D_{3,3,4}$	3.07	678	2.59	672
$D_{4,3,4}$	3.02	677	2.59	671
$m_\pi < 400$ MeV: 8 ensembles				
$D_{2,2,3}$	3.15	543	2.87	529
$D_{3,2,3}$	3.27	542	2.68	528
$D_{2,2,4}$	3.78	545	3.16	531
$D_{3,2,4}$	3.29	544	2.68	530
$D_{3,3,3}$	2.12	541	2.02	527
$D_{4,3,3}$	2.11	540	2.03	526
$D_{3,3,4}$	2.23	543	2.04	529
$D_{4,3,4}$	2.22	542	2.03	528
$a < 0.070$ fm: 7 ensembles				
$D_{2,2,3}$	2.95	469	2.94	471
$D_{3,2,3}$	2.76	468	2.67	470
$D_{2,2,4}$	5.15	471	3.91	473
$D_{3,2,4}$	3.82	470	2.87	472
$D_{3,3,3}$	2.15	467	2.14	469
$D_{4,3,3}$	2.38	466	1.98	468
$D_{3,3,4}$	2.57	469	2.14	471
$D_{4,3,4}$	2.53	468	2.14	470
$m_\pi < 400$ MeV and $a < 0.070$ fm: 5 ensembles				
$D_{2,2,3}$	2.16	382	2.07	380
$D_{3,2,3}$	2.12	381	2.08	379
$D_{2,2,4}$	3.07	384	2.80	382
$D_{3,2,4}$	2.78	383	2.38	381
$D_{3,3,3}$	1.42	380	1.39	378
$D_{4,3,3}$	1.40	379	1.39	377
$D_{3,3,4}$	1.82	382	1.62	380
$D_{4,3,4}$	1.79	381	1.64	379

TABLE 3.1: Details of the fits of the Adler function for the light-quark contribution. We list uncorrelated χ^2/dof and the degrees of freedom (dof).

is sensitive to the number of poles used in the fit ansatz. We found that the higher order Padé ansätze [3,3] and [4,3] show fluctuations in this regime. Thus we remove them from the variations used in the analysis, which reduces the number of variations to 32. We find that the p-values lead to unrealistically small error estimates, since the distribution is dominated by a small number of fits, making it impossible to trust this distribution. To be more conservative we use an unweighted extended frequentist

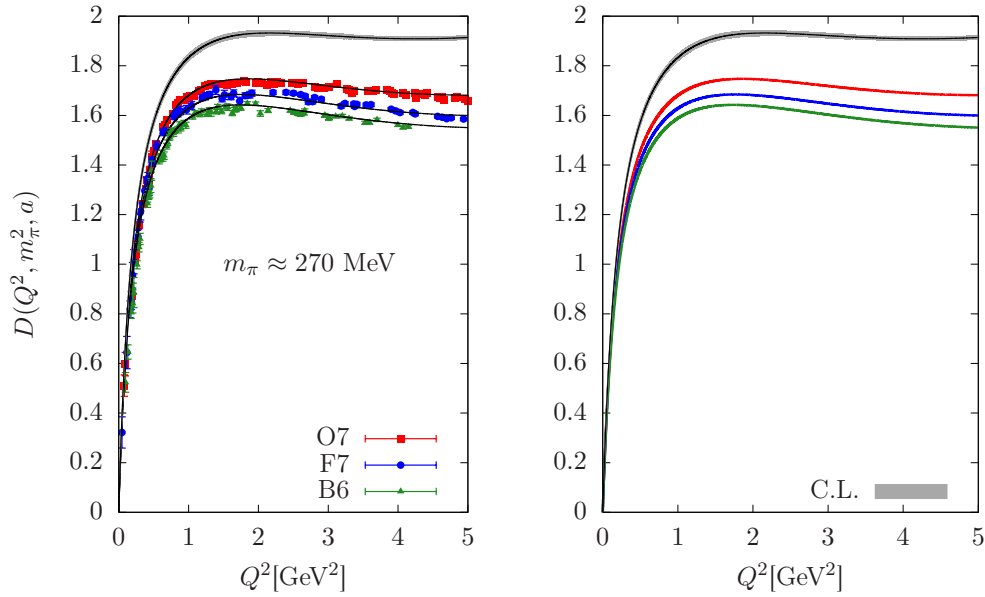


FIGURE 3.8: We study the continuum limit for the light-quark contribution for the fit ansatz $D_{3,2,4}(Q^2, m_\pi^2, a)$ using the ensembles B6 ($a=0.0755$ fm), F7 ($a=0.0658$ fm), and O7 ($a=0.0486$ fm), which are roughly at $m_\pi \approx 270$ MeV. For this ansatz using all 11 ensembles we obtain $\chi^2/\text{dof} = 3.9$. On the left we show the data for the Plateau of Slopes method and the extrapolation in gray to the continuum limit at $m_\pi = 270$ MeV. On the right the corresponding fit results are shown in the respective colours for the parameters of each ensemble. The central values of the fit result are shown as dashed lines in both plots, the bands show the statistical error.

method, i.e. all weights are set to 1. We show the result for the Adler function for the light-quark contribution in figure 3.12. To plot the result we compute the Adler function at the physical point for all ansätze considered in the final analysis with a high density in Q^2 . For each point in Q^2 we then apply the extended frequentist method to estimate the statistical and systematic error. The result is shown as a smooth curve, where the intermediate points are connected. We apply this method of plotting for the other flavours as well. To estimate the contributions to the systematic error we divide the data into subsets and repeat the extended frequentist method. To test lattice artefacts (LA) we divide the variations into the results with and without the cut $a < 0.070$ fm. For the contribution due to the method used for the extraction of the Adler function (AM) we divide the results into two subsets, which are based on the Plateau of Slopes method and the Curvature Limit method, respectively. Furthermore, we also consider the systematic error introduced due to the use of different orders of the Padé approximants, which gives us two subsets, one for each Padé order (PA). The systematic error associated with the chiral extrapolation (χ -ext.) is based on the subsets, which we build from the different orders in the fit ansatz for the pion mass dependence, see equations (3.43, 3.44), and also from the results with and without the cut $m_\pi < 400$ MeV. This gives us four subsets for the chiral extrapolation. We show the the systematic error along with results for

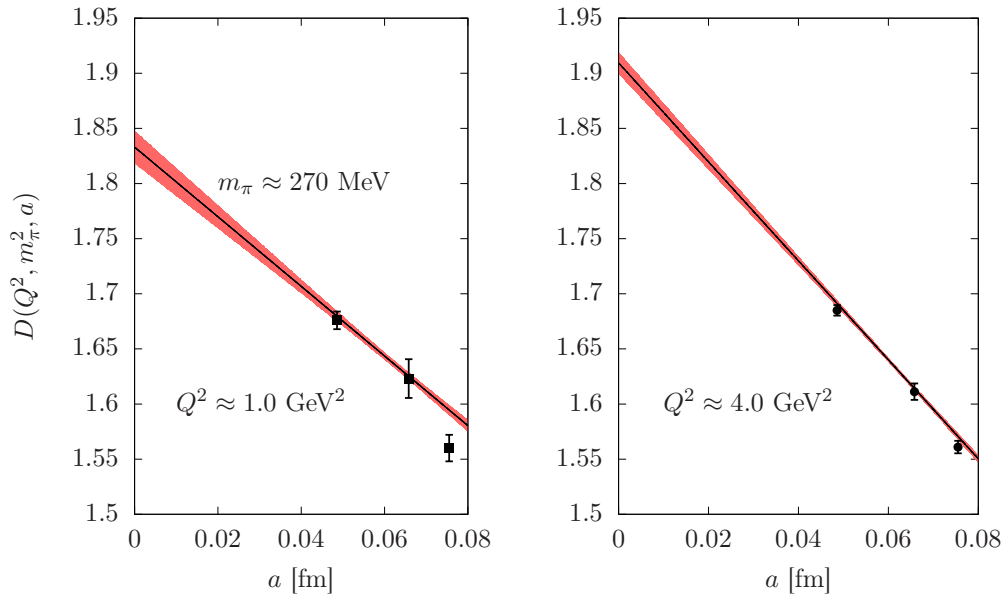


FIGURE 3.9: At fixed momentum transfers $Q^2 = 1.0, 4.0 \text{ GeV}^2$ and fixed pion mass at $m_\pi \approx 270 \text{ MeV}$, we look at the lattice spacing dependence directly. We show the result for the global fit ansatz $D_{3,2,4}(Q^2, m_\pi^2, a)$ ($\chi^2/\text{dof} = 3.9$) using all 11 ensembles evaluated at $Q^2 = 4.5 \text{ GeV}^2$ on the left and at $Q^2 = 1.0 \text{ GeV}^2$ on the right, respectively, for the Plateau of Slopes method for the light-quark contribution. The central values of the fit are shown as dashed lines. The data points shown correspond to the results on the ensembles B6 ($a=0.0755 \text{ fm}$), F7 ($a=0.0658 \text{ fm}$), and O7 ($a=0.0486 \text{ fm}$).

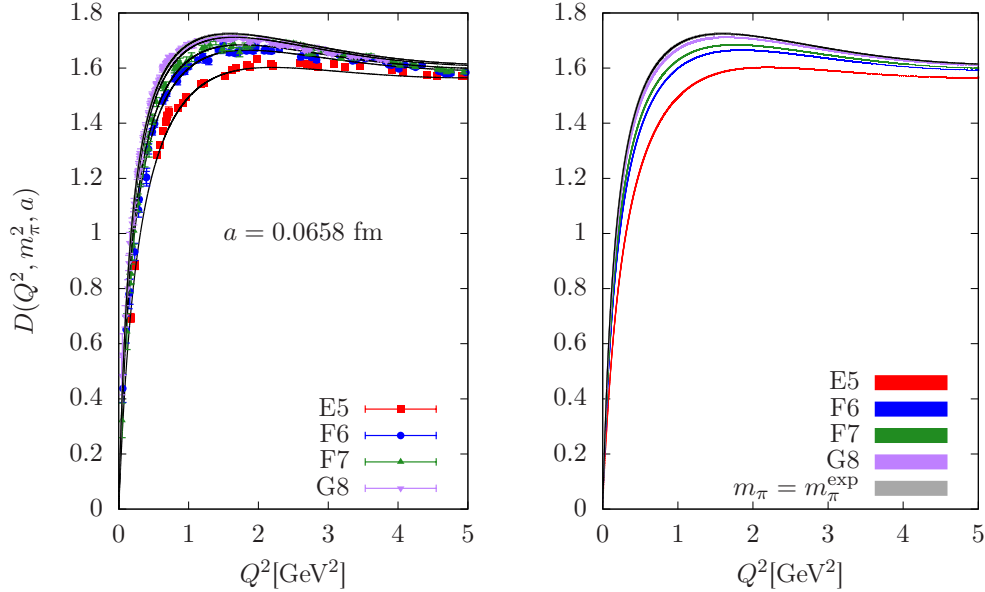


FIGURE 3.10: The pion mass dependence of the light-quark contribution over the considered Q^2 fit interval. We use the data of the intermediate lattice spacing ($a=0.0658 \text{ fm}$) for the fit ansatz $D_{3,2,4}(Q^2, m_\pi^2, a)$ ($\chi^2/\text{dof} = 3.9$) using all 11 ensembles. On the left we show the data for the Plateau of Slopes method and on the right the corresponding fits with the respective colours. The dashed lines correspond to the central values of the fit on both sides. The gray band represents the extrapolation to the physical pion mass for $a = 0.0658 \text{ fm}$.

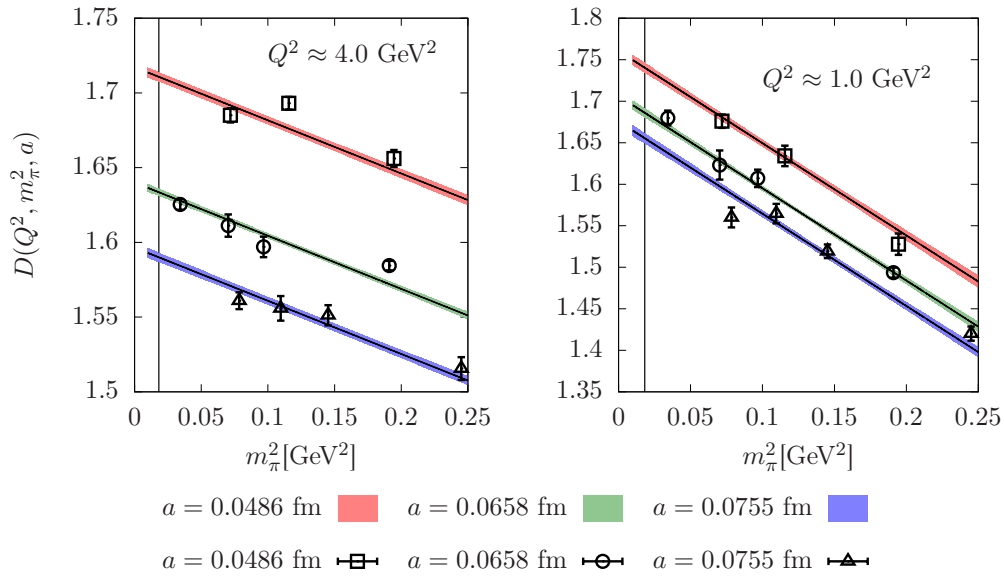


FIGURE 3.11: When we fix the momentum transfer to $Q^2 = 1.0, 4.0 \text{ GeV}^2$ we can study the pion mass dependence across the different lattice spacings. We evaluate the fit ansatz $D_{3,2,4}(Q^2, m_\pi^2, a)$ ($\chi^2/\text{dof} = 3.9$) using all 11 ensembles for the fit to the data obtained via the Plateau of Slopes method for the light-quark contribution at $Q^2 = 4.0 \text{ GeV}^2$ on the left and at $Q^2 = 1.0 \text{ GeV}^2$ on the right, respectively. The vertical line denotes the physical pion mass.

$Q^2[\text{GeV}^2]$	$D(Q^2)$	RP[%]	LA	AM	PA	χ -ext.
0.5	1.644(20)(55)	3.5	58.8	19.8	1.1	20.3
1.0	1.876(18)(52)	2.9	59.0	15.3	2.5	23.1
1.5	1.930(18)(45)	2.5	49.7	21.8	5.1	23.4
2.0	1.946(16)(34)	1.9	48.3	20.0	7.8	23.9
2.5	1.952(14)(23)	1.4	58.7	12.7	5.8	22.8
3.0	1.951(13)(19)	1.2	61.6	5.0	13.5	19.9
3.5	1.948(12)(16)	1.0	35.6	4.2	30.2	30.0
4.0	1.943(11)(13)	0.9	9.3	9.3	30.3	51.0
4.5	1.940(11)(10)	0.8	12.3	19.2	4.4	64.1

TABLE 3.2: The Adler function for the light-quark contribution and the relative overall uncertainty of the Adler function (RP[%]), for which we sum the errors in quadrature. The data shown here correspond to the result shown in figure 3.12 with a reduced number of points in Q^2 . We list the relative contributions to the systematic error in %. We consider lattice artefacts (LA), the method used for the extraction of the Adler function (AM), the order of the Padé ansatz (PA), and the chiral extrapolation (χ -ext.).

the Adler function in table 3.2 at several values of Q^2 . We observe that lattice artefacts dominate the systematic error for $Q^2 < 3.5 \text{ GeV}^2$, while the pion mass dependence is the sub-leading contribution. For $Q^2 > 3.5 \text{ GeV}^2$ the pion mass dependence dominates the systematic error. The choice of the method is relevant for $0.5 < Q^2 < 2.5 \text{ GeV}^2$. The systematic error introduced by the use of different orders of Padé ansätze is only relevant at $3.5 \lesssim Q^2 \lesssim 4.0 \text{ GeV}^2$. We see that the total relative uncertainty of the

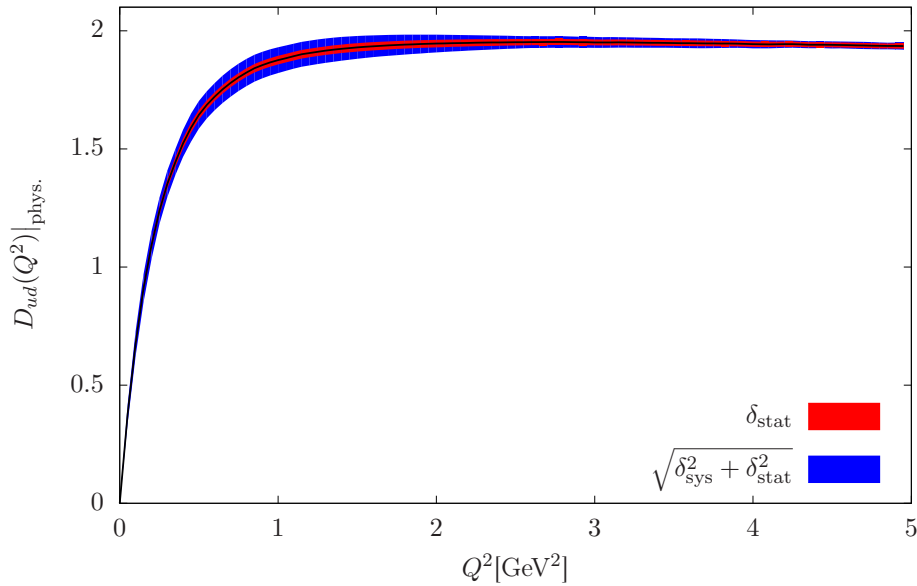


FIGURE 3.12: The Adler function for the light-quark contribution, using 32 variations. Systematic errors dominate for $Q^2 \lesssim 3.5 \text{ GeV}^2$. The errors are summed in quadrature, the full error is shown as a blue band.

result decreases as Q^2 increases. The systematic error dominates the total uncertainty for small Q^2 and is of the same size as the statistical error for larger Q^2 .

3.2.2.2 The strange-quark contribution

For the strange-quark we also use the Padé ansätze [2,2], [3,2], [3,3], and [4,3]. In table 3.3 we collect the uncorrelated χ^2/dof for all fit ansätze with the various cuts we impose. We find that the uncorrelated χ^2/dof is significantly better than it is for the light-quark contribution, but the p-values are still very poor due to the large number of degrees of freedom and the small fluctuations in the data around the general trend.

For the strange-quark we also take a closer look at the fit ansatz $D_{3,2,4}(Q^2, m_\pi^2, a)$ ($\chi^2/\text{dof} = 2.5$) as an example. In figure 3.13 we show the result for this ansatz for the ensembles B6 ($a=0.0755 \text{ fm}$), F7 ($a=0.0658 \text{ fm}$), and O7 ($a=0.0486 \text{ fm}$), for which we have $m_\pi \approx 270 \text{ MeV}$, for the Plateau of Slopes method. We observe a clear separation of the data due to the lattice spacing for $Q^2 \geq 1.0 \text{ GeV}^2$, which is larger than it is for the light-quark contribution, as one would expect for a heavier quark contribution. We also look at the lattice spacing directly at two fixed values of Q^2 and at $m_\pi \approx 270 \text{ MeV}$ in figure 3.14 for the Plateau of Slopes method. We see that the linear ansatz for lattice artefacts yields a good description at both considered momentum transfers.

In figure 3.15 we show the results of the Plateau of Slopes method for the fit ansatz $D_{3,2,4}(Q^2, m_\pi^2, a)$ at fixed lattice spacing ($a=0.0658 \text{ fm}$) to test the pion mass dependence. We observe that the results overlap within errors, but a small residual dependence

	Plateau of Slopes method		Curvature Limit method	
Label	χ^2/dof	dof	χ^2/dof	dof
All 11 ensembles				
$D_{2,2,3}$	2.52	678	2.39	695
$D_{3,2,3}$	2.46	677	2.32	694
$D_{2,2,4}$	2.65	680	2.49	697
$D_{3,2,4}$	2.53	679	2.39	696
$D_{3,3,3}$	2.36	676	-	-
$D_{4,3,3}$	2.36	675	2.21	692
$D_{3,3,4}$	2.37	678	2.24	695
$D_{4,3,4}$	2.33	677	2.33	694
$m_\pi < 400$ MeV: 8 ensembles				
$D_{2,2,3}$	1.34	541	1.55	552
$D_{3,2,3}$	1.30	540	1.55	551
$D_{2,2,4}$	1.66	543	1.76	554
$D_{3,2,4}$	1.56	542	1.73	553
$D_{3,3,3}$	1.33	539	1.55	550
$D_{4,3,3}$	1.30	538	1.55	549
$D_{3,3,4}$	1.44	541	1.61	552
$D_{4,3,4}$	1.40	540	1.61	551
$a < 0.070$ fm: 7 ensembles				
$D_{2,2,3}$	1.58	448	1.67	485
$D_{3,2,3}$	1.58	447	1.67	484
$D_{2,2,4}$	2.01	450	2.22	487
$D_{3,2,4}$	1.97	449	2.15	486
$D_{3,3,3}$	1.56	446	1.61	483
$D_{4,3,3}$	1.56	445	1.62	482
$D_{3,3,4}$	1.84	448	2.01	485
$D_{4,3,4}$	1.97	447	2.02	484
$m_\pi < 400$ MeV and $a < 0.070$ fm: 5 ensembles				
$D_{2,2,3}$	0.84	366	1.14	397
$D_{3,2,3}$	0.83	365	1.14	396
$D_{2,2,4}$	1.03	368	1.26	399
$D_{3,2,4}$	1.01	367	1.26	398
$D_{3,3,3}$	0.83	364	1.15	395
$D_{4,3,3}$	0.82	363	1.15	394
$D_{3,3,4}$	0.98	366	1.23	397
$D_{4,3,4}$	1.01	365	1.24	396

TABLE 3.3: Details of the fits of the Adler function for the strange-quark contribution. We show the result for the uncorrelated χ^2/dof and the degrees of freedom (dof). The fit $D_{3,3,3}$ for Curvature Limit method using all ensembles did not converge within reasonable time.

remains. This can be seen in figure 3.16, where we fix the value of Q^2 to 1.0 and 4.0 GeV^2 , and leave m_π as a free parameter. Note that, although there is a shift between the results for the two values of Q^2 in this figure, the absolute range is the same. Thus it follows that we also observe an increase in the slope for the pion mass dependence for small Q^2 , from which we conclude that the use of eqs. (3.41 - 3.44) for the pion mass

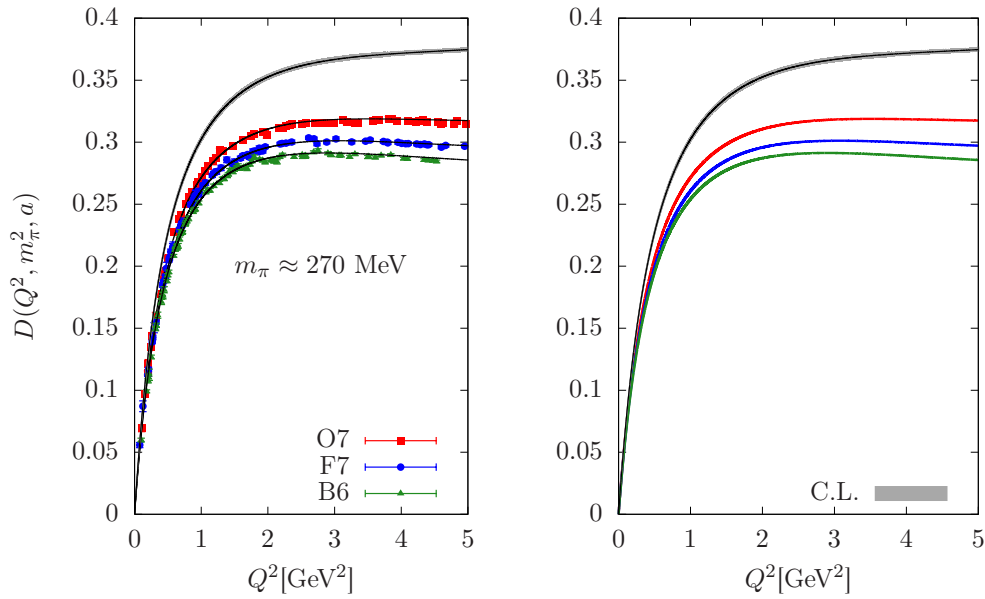


FIGURE 3.13: The continuum limit for the strange-quark contribution for the ansatz $D_{3,2,4}(Q^2, m_\pi^2, a)$. We show the results for the ensembles B6 ($a=0.0755$ fm), F7 ($a=0.0658$ fm), and O7 ($a=0.0486$ fm), which are roughly at $m_\pi \approx 270$ MeV. For the fit using all 11 ensembles we get $\chi^2/\text{dof} = 2.5$. The data for the Plateau of Slopes method are shown on the left including the extrapolation to the continuum limit evaluated at $m_\pi = 270$ MeV in gray. On the right we plot the corresponding fit results with the respective colours at the parameters of the ensembles. The dashed lines mark the central values of the fit result and the bands show the statistical error.

dependence still provides a good description of the data.

For the strange-quark contribution we observe a similar behaviour for higher order Padé ansätze ([3,3] and [4,3]) as for the light-quark contribution. In the small Q^2 -regime these fit ansätze show fluctuations, thus we exclude them from the final estimate for the Adler function at the physical point. We use only the ansätze with two poles in Q^2 [2,2] and [3,2], so that we include 32 variations in the extended frequentist method. Though some p-values are acceptable, we find that the error could be underestimated by using them as weights. We use an unweighted extended frequentist method and set all weights to 1 for the strange-quark contribution as well. The result for the strange-quark contribution to the Adler function at the physical point is shown in figure 3.17. Since we are using the same setup for the strange-quark as for the light-quark contribution, we use the same subsets of data to determine the various contributions to the systematic error. The relative contributions to the systematic error for the strange-quark contribution is shown in table 3.4. We also observe that lattice artefacts are the largest part of the systematic error for $Q^2 < 4.0$ GeV². The systematic error due to the pion mass dependence is the sub-leading effect for $Q^2 < 4.0$ GeV² and dominates the systematic error for $Q^2 \gtrsim 4.0$. Systematic error associated with the method used for the extraction of the Adler function is relevant at small and large Q^2 and is rather small for intermediate

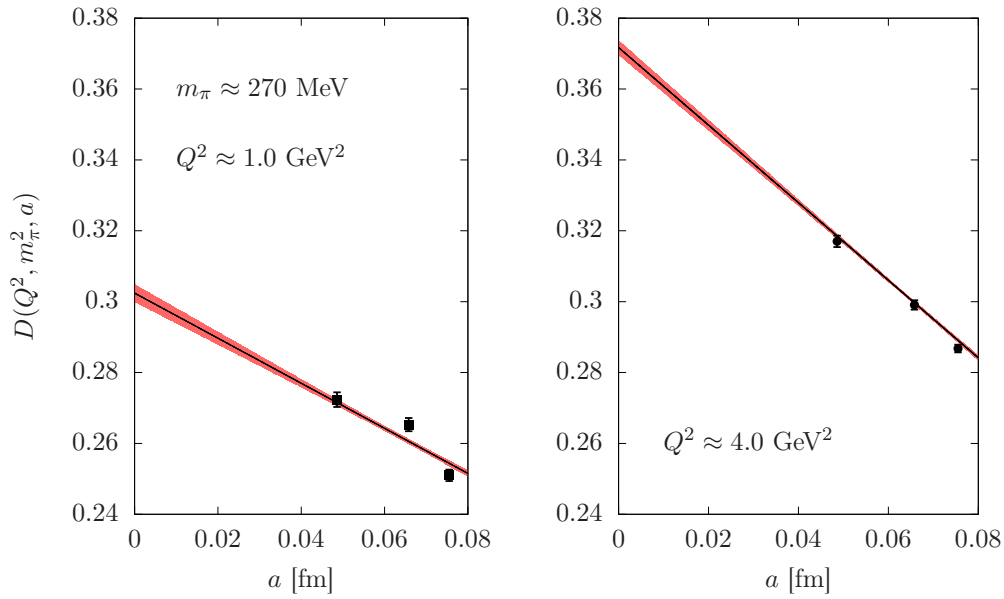


FIGURE 3.14: We keep the pion mass fixed to $m_\pi \approx 270$ MeV and also fix the momentum transfer to $Q^2 = 1.0, 4.0$ GeV², which allows us to look at the lattice spacing dependence directly. The global fit ansatz $D_{3,2,4}(Q^2, m_\pi^2, a)$ ($\chi^2/\text{dof} = 2.5$) using all 11 ensembles evaluated at $Q^2 = 4.0$ GeV² is shown on the left and at $Q^2 = 1.0$ GeV² on the right, respectively, for the Plateau of Slopes method for the strange-quark contribution. Dashed lines represent the central values of the fits, the bands show the statistical error. We show the data points corresponding to the results on the ensembles B6 ($a=0.0755$ fm), F7 ($a=0.0658$ fm), and O7 ($a=0.0486$ fm).

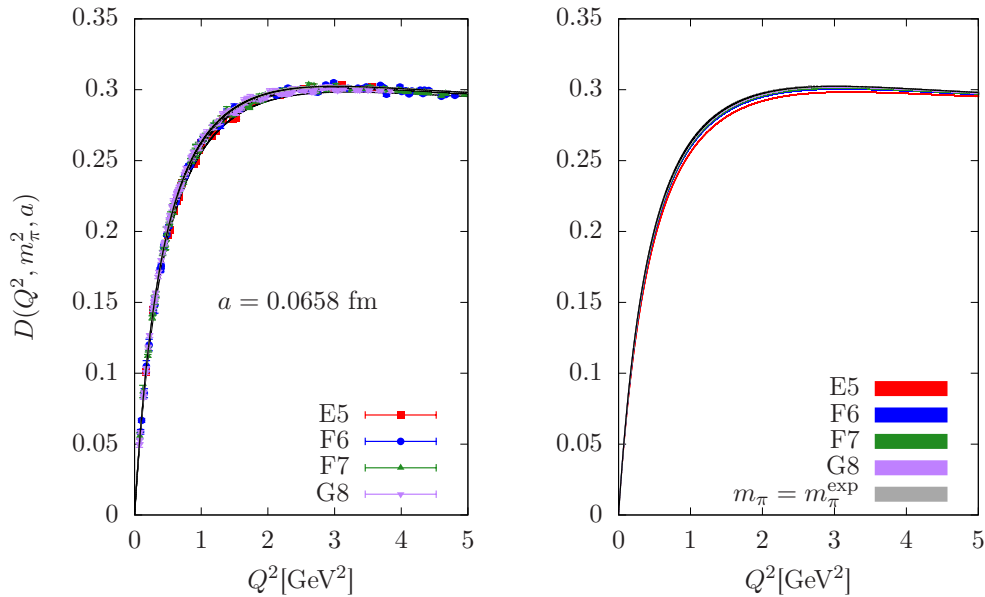


FIGURE 3.15: The pion mass dependence can be studied by looking at the results at a fixed lattice spacing ($a=0.0658$ fm) for the fit ansatz $D_{3,2,4}(Q^2, m_\pi^2, a)$ ($\chi^2/\text{dof} = 2.5$) using all 11 ensembles. The data for the Plateau of Slopes method are shown on the left, while the corresponding fits and their statistical errors as bands are shown on the right. The central values of the fit are shown as dashed lines. The gray band represents the extrapolation to the physical pion mass for $a = 0.0658$ fm.

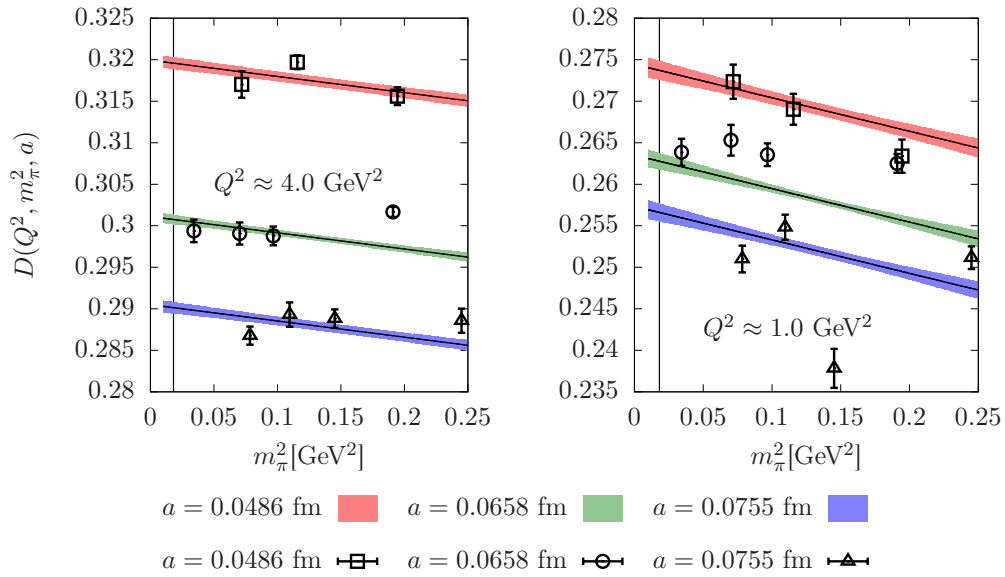


FIGURE 3.16: We fix the momentum transfer to $Q^2 = 1.0 \text{ GeV}^2$ (right) and $Q^2 = 4.0 \text{ GeV}^2$ (left) to study the pion mass dependence across the different lattice spacings. The ansatz $D_{3,2,4}(Q^2, m_\pi^2, a)$ ($\chi^2/\text{dof} = 2.5$) using all 11 ensembles is shown for the fit to the data of the Plateau of Slopes method for the strange-quark contribution. The vertical line denotes the physical pion mass.

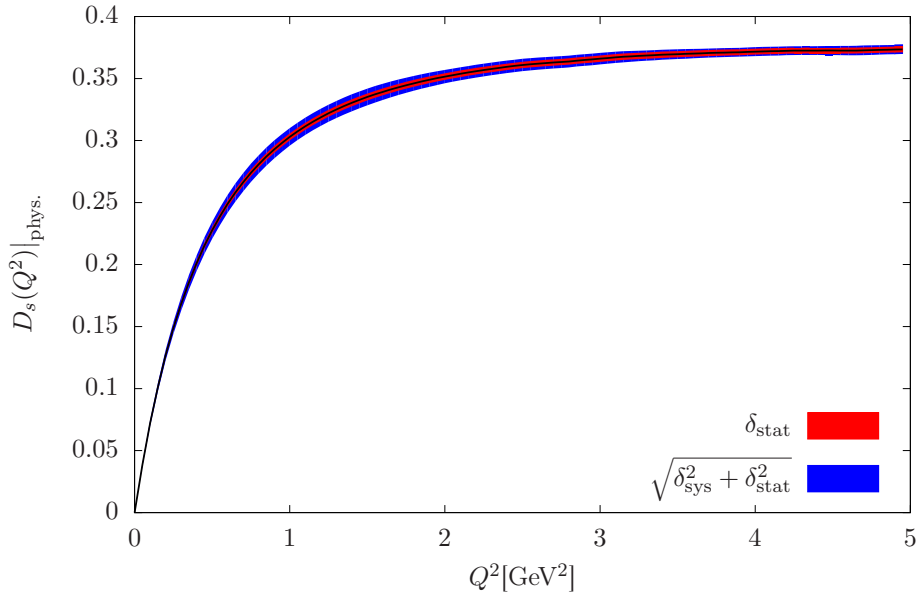


FIGURE 3.17: The result we obtain for the Adler function for the strange-quark contribution, using all 32 variations. We sum the errors in quadrature for the full error band shown in blue.

Q^2 . The order of the Padé ansatz has little influence on the systematic error. We reach a similar precision for the strange-quark contribution as for the light-quark contribution of $\approx 3\text{-}1\%$ depending on the value of Q^2 . The systematic error dominates in the small Q^2 region and is of a similar size as the statistical error for larger Q^2 .

$Q^2[\text{GeV}^2]$	$D(Q^2)$	RP[%]	LA	AM	PA	$\chi\text{-ext.}$
0.5	0.228(2)(6)	3.0	50.8	22.7	1.2	25.2
1.0	0.303(3)(6)	2.3	54.0	18.5	0.5	26.9
1.5	0.335(3)(6)	2.0	52.8	15.1	3.4	28.7
2.0	0.352(3)(5)	1.5	54.9	9.0	5.0	31.1
2.5	0.361(3)(4)	1.4	65.0	0.1	0.3	34.5
3.0	0.366(3)(4)	1.3	52.9	14.5	3.8	28.9
3.5	0.370(3)(3)	1.1	47.3	27.8	3.4	21.5
4.0	0.372(2)(3)	1.0	36.6	26.0	0.3	37.1
4.5	0.373(2)(3)	1.0	19.0	32.1	1.2	47.7

TABLE 3.4: The Adler function for the strange-quark contribution and the relative overall uncertainty of the Adler function (RP[%]), for which we sum the errors in quadrature. We list the relative contributions to the systematic error in %. We consider lattice artefacts (LA), the method used for the extraction of the Adler function (AM), the order of the Padé ansatz (PA), and the chiral extrapolation ($\chi\text{-ext.}$). The data shown here correspond to the data computed for figure 3.17.

3.2.2.3 The charm-quark contribution

The results for the charm-quark behave quite differently, when compared to the results for the strange and the light-quark contribution. We observe that in the momentum range, which is reliably accessible on the lattice, the data show a monotonic increase and do not yet approach the asymptotic regime expected at large Q^2 from perturbation theory. As Q^2 is increased lattice artefacts grow and thus limit the momentum range accessible to lattice calculations. Thus we use lower order Padé ansätze, [1,1] and [2,1], which have only one pole, while we keep the same description for the pion mass dependence. We collect the uncorrelated χ^2/dof and the degrees of freedom for the ansätze we used with the various cuts in table 3.5 for both methods used in the extraction of the Adler function. Similarly as for the light- and strange-quark contributions we find large χ^2/dof for the fit to all 11 ensembles. This is explained by the increased impact of lattice artefacts due to the heavier quark mass and we also observe fluctuations in the data with respect to Q^2 , which, since the data are very precise, have a more severe impact on the χ^2/dof as for the light- and strange-quark contribution. The combined fit can not model these oscillations properly and is not intended to, since we are interested in a description of the general trend of the data in the range of $0 < Q^2 < 5.0 \text{ GeV}^2$. When the coarsest lattice spacing is removed, we find that the χ^2/dof is reduced by roughly a factor of 2. The p-values of the fits to the charm-quark data are again much too small to use them as weights. This is related to the large number of degrees of freedom and the poor χ^2/dof .

As an example we look at the behaviour of the fit ansatz $D_{1,1,4}(Q^2, m_\pi^2, a)$ with $\chi^2/\text{dof} = 6.0$ in more detail. In figure 3.18 we consider the continuum limit for the Plateau of Slopes method at $m_\pi = 270 \text{ MeV}$. As expected we find that the gap between

Charm	Plateau of Slopes method		Curvature Limit method	
Label	χ^2/dof	dof	χ^2/dof	dof
All 11 ensembles				
$D_{1,1,3}$	5.93	754	6.56	848
$D_{2,1,3}$	5.86	752	6.50	846
$D_{1,1,4}$	5.95	755	6.66	849
$D_{2,1,4}$	5.89	754	6.59	848
$m_\pi < 400$ MeV: 8 ensembles				
$D_{1,1,3}$	3.14	583	3.99	634
$D_{2,1,3}$	3.10	581	3.97	632
$D_{1,1,4}$	3.15	584	4.06	635
$D_{2,1,4}$	3.11	583	4.02	634
$a < 0.070$ fm: 7 ensembles				
$D_{1,1,3}$	3.72	448	4.91	522
$D_{2,1,3}$	3.64	446	4.86	520
$D_{1,1,4}$	4.02	449	5.14	523
$D_{2,1,4}$	3.84	448	5.03	522
$m_\pi < 400$ MeV and $a < 0.070$ fm: 5 ensembles				
$D_{1,1,3}$	2.58	340	3.47	375
$D_{2,1,3}$	2.54	338	3.46	373
$D_{1,1,4}$	2.57	341	3.47	376
$D_{2,1,4}$	2.53	340	3.46	375

TABLE 3.5: Details of the fits of the Adler function for the charm-quark contribution. We show the result for the uncorrelated χ^2/dof and the degrees of freedom (dof).

the finest lattice spacing ($a=0.0486$ fm) and the continuum limit is larger than it was for the strange or the light-quark contribution. Figure 3.19 shows the same fit where we fix $Q^2 = 1.0$ GeV² and $Q^2 = 4.0$ GeV² at $m_\pi = 270$ MeV. We observe that the chosen fit ansatz for lattice artefacts works well for small and large values of Q^2 .

We study the pion mass dependence by keeping the lattice spacing fixed to $a=0.0658$ fm in figure 3.20. The pion mass dependence is rather mild and inverted with respect to the behaviour of the light and the strange-quark contribution. This is confirmed in figure 3.21, where we look at the pion mass dependence directly by fixing the momentum to $Q^2 = 1.0$ GeV² and $Q^2 = 4.0$ GeV², respectively, for the lattice spacings considered in this study. We show similar plots for the results of the Curvature Limit method in B.3.

Figure 3.22 shows our result for the charm-quark contribution to the Adler function, where we used all 32 variations listed in table 3.5 for the extended frequentist method. In general the χ^2/dof is larger than we found for the light- and strange-quark contributions, in turn the corresponding p-values are very small. Since considering the weights in this case may lead to underestimated systematic effects, we perform the EFM analysis without weights, i.e. we set all weights to 1.0, and quote the more conservative error estimate for our final results. The statistical error changes little with increasing Q^2 ,

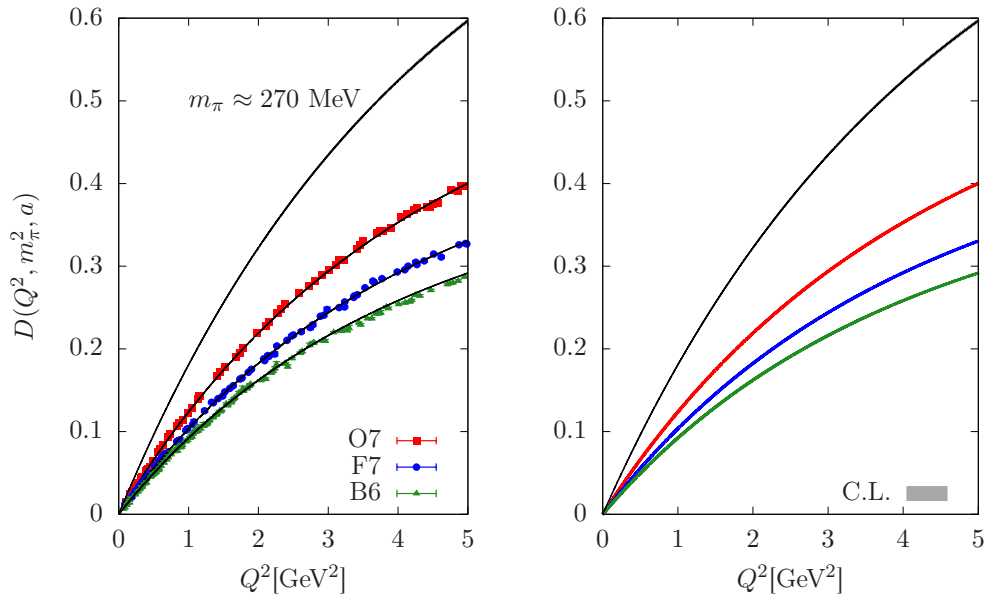


FIGURE 3.18: We take the continuum limit at a fixed pion mass of $m_\pi \approx 270$ MeV for the ensembles B6 ($a=0.0755$ fm), F7 ($a=0.0658$ fm), and O7 ($a=0.0486$ fm) for the charm-quark contribution. We show the data for the Plateau of Slopes method with the extrapolation to the continuum limit in gray at this pion mass on the left, and the corresponding fit with the statistical error bands for the fit ansatz $D_{1,1,4}(Q^2, m_\pi^2, a)$ with $\chi^2/\text{dof} = 6.0$ on the right. The central values of the fit are shown in dashed black lines.

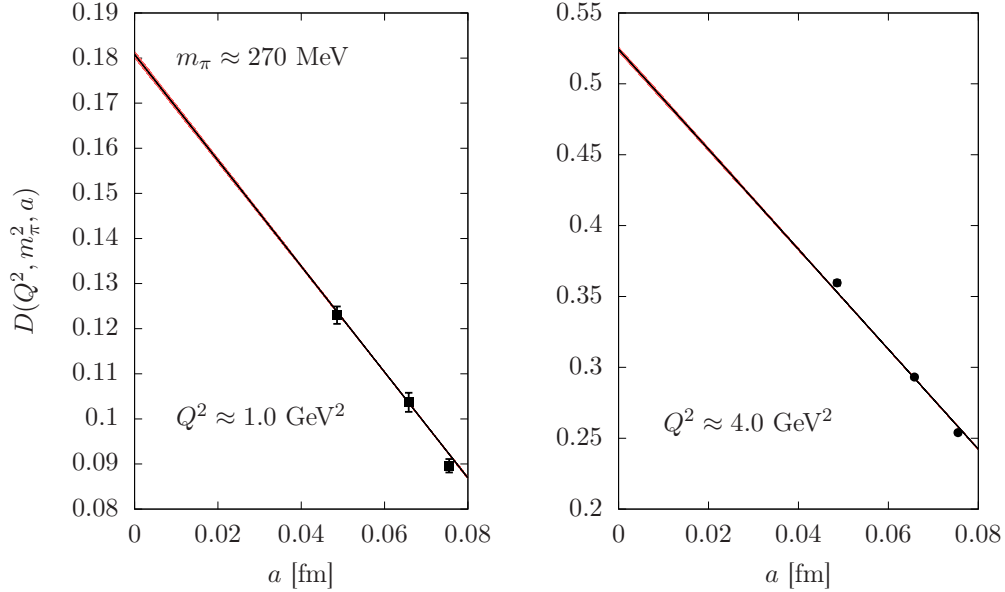


FIGURE 3.19: We fix the momentum to $Q^2 = 1.0$ GeV² (left) and $Q^2 = 4.0$ GeV² (right) for $m_\pi \approx 270$ MeV and vary the lattice spacing to test the linear behaviour of lattice artefacts. We show the global fit ansatz $D_{1,1,4}(Q^2, m_\pi^2, a)$ ($\chi^2/\text{dof} = 6.0$) using all 11 ensembles for the charm-quark contribution based on the data of the Plateau of Slopes method. The data points shown correspond to the results closest to the respective value of Q^2 on the ensembles B6 ($a=0.0755$ fm), F7 ($a=0.0658$ fm), and O7 ($a=0.0486$ fm).

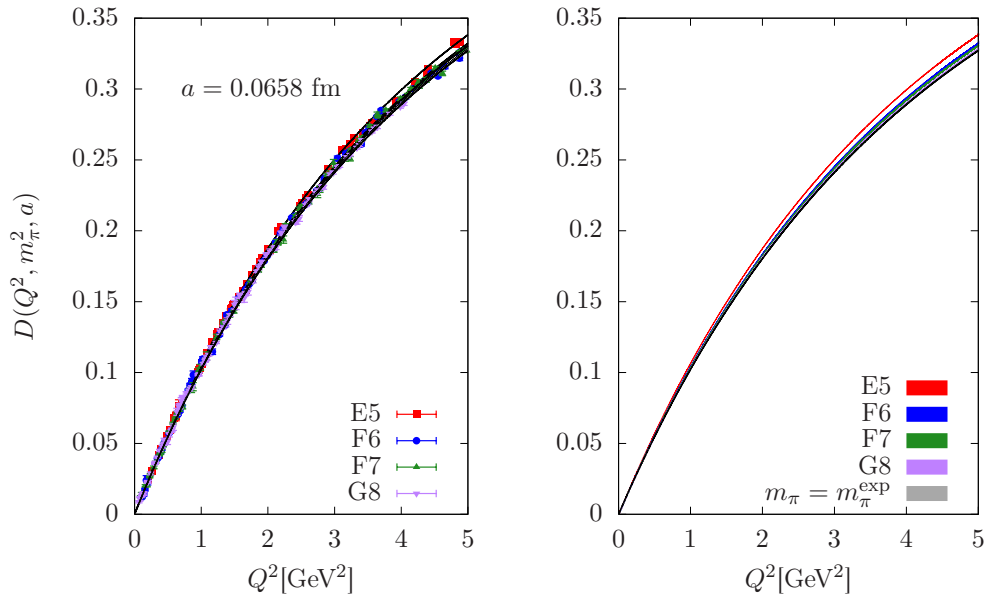


FIGURE 3.20: We study the pion mass dependence by fixing the lattice spacing to $a=0.0658 \text{ fm}$ for the fit ansatz $D_{1,1,4}(Q^2, m_\pi^2, a)$ ($\chi^2/\text{dof} = 6.0$) using all 11 ensembles for the data of the Plateau of Slopes method for the charm-quark contribution (left) and the fit result with the statistical error (right). The dashed black lines denote the central values of the fit. The gray band depicts the extrapolation to the physical pion mass at $a=0.0658 \text{ fm}$.

while the systematic error due to lattice artefacts grows with increasing Q^2 . This is confirmed in table 3.6. We employ similar subsets of the data to estimate the size of the contributions to the systematic error for lattice artefacts, the method for the extraction of the Adler function, and the chiral extrapolation as for the strange- and the light-quark contribution. For the Padé ansätze we adjust the subsets to the orders used for the Padé approximants. For $Q^2 \lesssim 1.5 \text{ GeV}^2$ the systematic error is dominated by the pion mass dependence and for $Q^2 > 1.5$ lattice artefacts and the pion mass dependence give similar contributions to the systematic error. At $Q^2 = 0.5 \text{ GeV}^2$ the order of the Padé is the sub-leading effect, but the contribution quickly diminishes with increasing Q^2 . The method used in the extraction of the Adler function adds a relevant part to the systematic error at intermediate Q^2 . For larger Q^2 the systematic error dominates the total error. We also observe that, while for the light and strange-quark contributions the total relative error diminishes with increasing Q^2 , the total uncertainty increases with growing Q^2 for the charm-quark contribution.

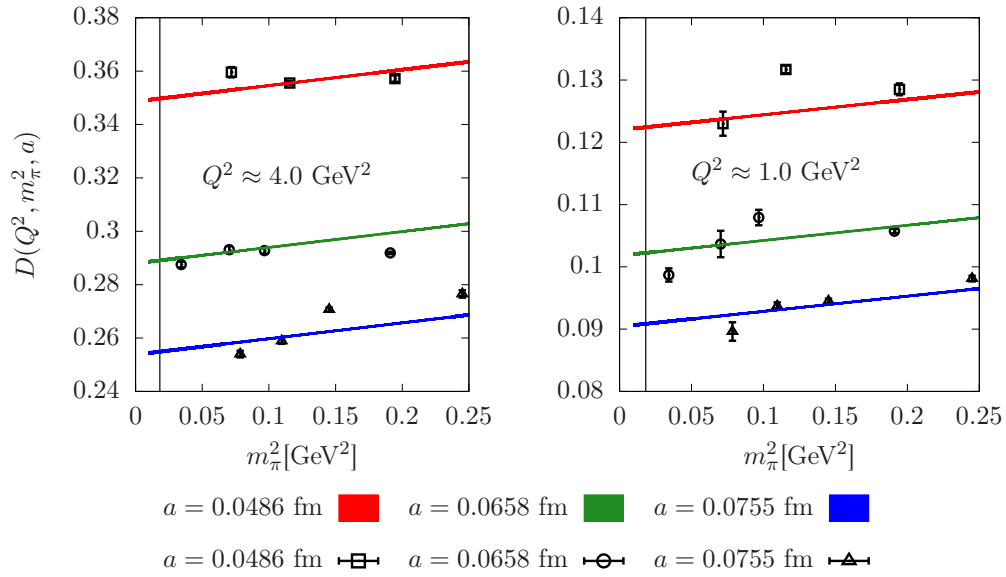


FIGURE 3.21: With the momentum fixed to $Q^2 = 1.0 \text{ GeV}^2$ (right) and $Q^2 = 4.0 \text{ GeV}^2$ (left) we look at the pion mass dependence in more detail for the different lattice spacings. The plots show the result for the fit ansatz $D_{1,1,4}(Q^2, m_\pi^2, a)$ ($\chi^2/\text{dof} = 6.0$) using all 11 ensembles for the charm-quark contribution based on the data of the Plateau of Slopes method. The physical pion mass is shown as a vertical line. The statistical error of the fit is too small to be shown, instead we draw thick lines to show the position of the central value of the fit result. The data show strong fluctuations, which are responsible for the bad χ^2/dof , even though we can extract the general trend of the data with the considered fit ansätze.

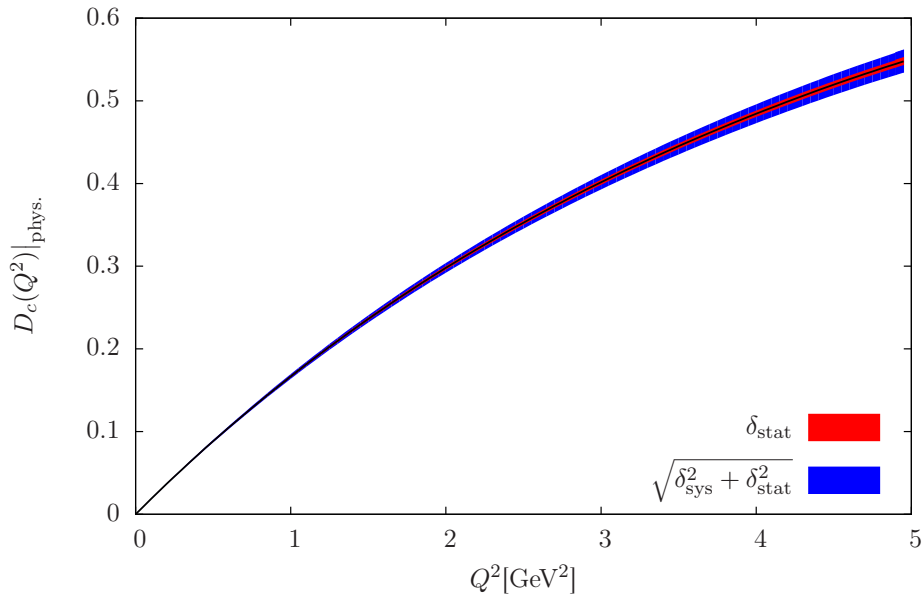


FIGURE 3.22: The result we obtain for the Adler function for the charm-quark contribution, using all 32 variations.

$Q^2[\text{GeV}^2]$	$D(Q^2)$	RP[%]	LA	AM	PA	χ -ext.
0.5	0.096(1)(1)	1.0	9.4	0.2	36.4	54.0
1.0	0.182(1)(1)	0.8	20.7	11.2	14.8	53.3
1.5	0.258(1)(2)	0.8	26.0	23.5	10.8	39.7
2.0	0.326(2)(3)	0.9	32.6	25.0	2.6	39.8
2.5	0.386(2)(3)	1.0	37.1	20.6	4.2	38.1
3.0	0.440(2)(4)	1.1	38.1	19.9	6.2	35.8
3.5	0.488(2)(6)	1.2	39.4	20.4	2.8	37.3
4.0	0.531(2)(7)	1.3	41.9	17.1	1.4	39.6
4.5	0.569(2)(8)	1.4	42.7	14.8	2.8	39.7

TABLE 3.6: The Adler function for the charm-quark contribution and the relative overall uncertainty of the Adler function (RP[%]), for which we sum the errors in quadrature. We list the relative contributions to the systematic error in %. We consider lattice artefacts (LA), the method used for the extraction of the Adler function (AM), the order of the Padé ansatz (PA), and the chiral extrapolation (χ -ext.). The listed data correspond to the data computed for figure 3.22.

3.2.2.4 Summed contributions and comparison to perturbative QCD

We determine the three and four-flavour results by summing the central values and summing the respective errors in quadrature. The three-flavour result is shown in figure 3.23, which is dominated by the light-quark contribution for both the absolute values and the precision. Adding the strange-quark contribution does not change the qualitative behaviour of the curve. We compare our result with perturbative QCD [86] for $Q^2 > 2.0$ GeV^2 . The perturbative result moves closer to our result, when the order is increased, but does not reach agreement. For the three-flavour result the Adler function should approach the limit $D(Q^2 \rightarrow \infty) = 2$, thus we expect the Adler function to drop with increasing Q^2 .

In figure 3.24 we show our four-flavour result, where we see that the charm-quark has

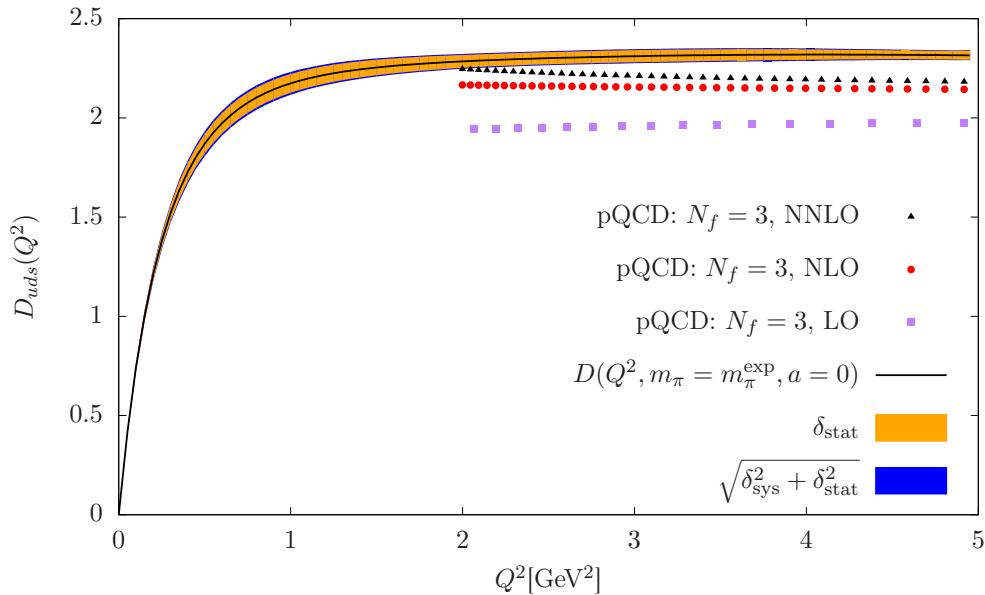


FIGURE 3.23: We sum the contributions for the light and the strange-quark, the respective errors are summed in quadrature. The points refer to the results of perturbative QCD [86] up to NNLO, for which we find no agreement with our results.

an impact on the large Q^2 regime and we no longer observe that the result converges to an asymptotic value, but instead grows monotonously. Here we find agreement of our results with the NNLO result by Jegerlehner for the intermediate Q^2 interval at $2.0 < Q^2 \lesssim 3.5$ GeV^2 . The agreement is lost for larger Q^2 , where presumably lattice artefacts deteriorate the quality of lattice results, especially for the charm-quark contribution. But for increasing order of perturbation theory the result again moves closer to our non-perturbative determination.

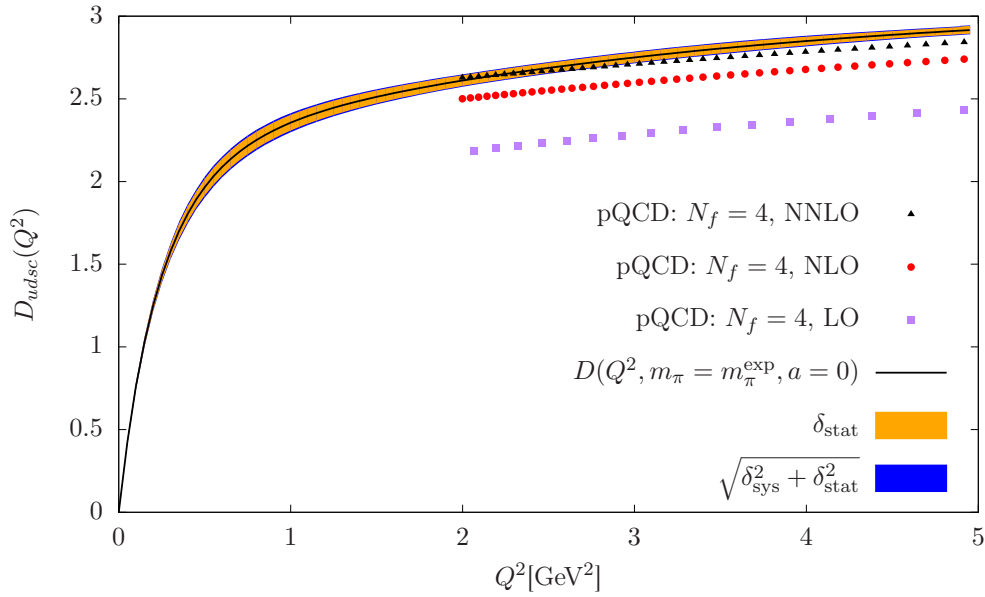


FIGURE 3.24: The four-flavour result is obtained by summing the individual contributions, the respective errors are summed in quadrature. The points refer to the four-flavour result from perturbative QCD [86]. There is agreement with our result for NNLO at intermediate Q^2 .

3.3 Determination of the running of α_{QED} from the Adler function on the lattice

For the determination of the shift in the running of α_{QED} we make use of the relation between the shift and the renormalized vacuum polarization,

$$\Delta\alpha_{\text{QED}}^{\text{had}}(Q^2) = \frac{\alpha_{\text{QED}}^0}{3\pi} \hat{\Pi}(Q^2). \quad (3.46)$$

As we are most interested in the interval $1.0 < Q^2 < 4.0 \text{ GeV}^2$ and a fit to the VPF in this large range might be distorted in the low Q^2 regime and thus yield a misleading $\Pi(Q^2 = 0)$, we use the fit coefficients we determined in the analysis of the previous chapter for the Adler function, see equations (3.36, 3.39, 3.40, 3.43, 3.44, 3.45). Since the Adler function is the derivative of the VPF the additive renormalization drops out. We insert the coefficients a_i, b_j , which we determined with the simultaneous fit to the Adler function data, in eqs. (3.37, 3.38), which gives us the renormalized VPF directly at the physical point.

3.3.1 The light-quark contribution

In order to estimate the light-quark contribution to $\Delta\alpha_{\text{QED}}^{\text{had}}$ we use the same 32 variations we already used to determine the Adler function, see 3.2.2.1, for the extended frequentist

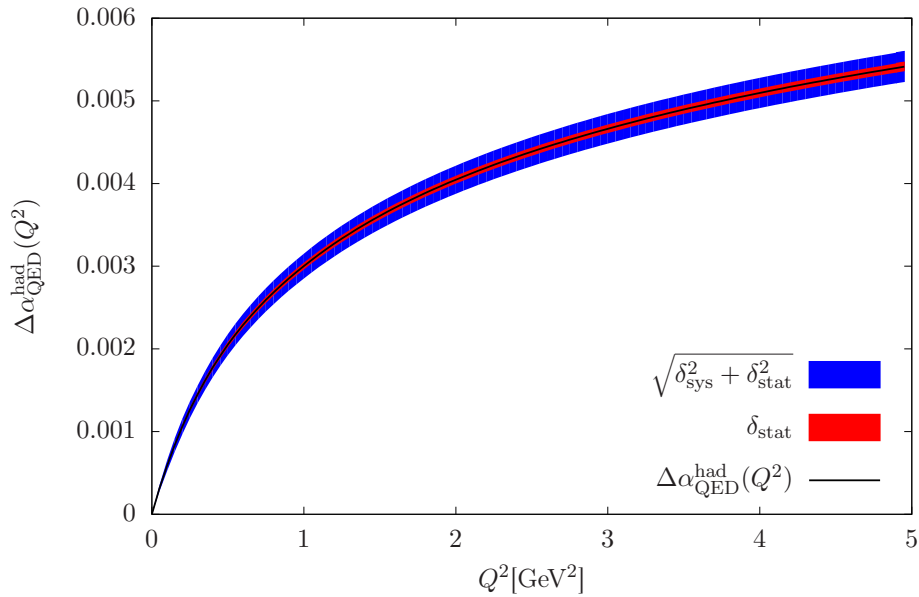


FIGURE 3.25: We use the information provided by the Adler function to evaluate $\Delta\alpha_{\text{QED}}^{\text{had}}$ from the renormalized VPF at the physical point directly for the light-quark sector.

method. Following the analysis of the Adler function we set all weights to 1. The result is shown figure 3.25. To estimate the contributions of the systematic error we use the same subsets as for the Adler function. The normalized results are shown in table 3.7. We observe that the systematic error dominates the total uncertainty. The precision of our result improves with increasing Q^2 from $\sim 6\%$ to 3.5% . Lattice artefacts dominate the systematic error. The choice of the Padé ansatz the sub-leading effect and the pion mass dependence is of a similar size. Both diminish with increasing Q^2 , while lattice artefacts grow. The method of the extraction of the Adler function is a minor effect.

$Q^2[\text{GeV}^2]$	$\Delta\alpha_{\text{QED}}(Q^2) \times 10^5$	%	LA	AM	PA	χ -ext.
0.5	205.3(3.4)(12.2)	6.2	39.0	0.1	35.3	25.5
1.0	300.2(4.1)(14.4)	5.0	50.4	5.9	25.0	18.8
1.5	360.9(4.5)(15.5)	4.5	53.0	8.0	21.7	17.3
2.0	404.6(4.7)(16.3)	4.2	53.8	8.8	20.3	17.1
2.5	438.6(4.9)(16.8)	4.0	54.3	9.1	19.6	17.0
3.0	466.2(5.1)(17.1)	3.8	54.7	9.4	18.9	16.9
3.5	489.5(5.2)(17.3)	3.7	55.1	9.7	18.4	16.8
4.0	509.6(5.4)(17.5)	3.6	55.5	9.8	18.0	16.7
4.5	527.2(5.5)(17.6)	3.5	55.7	9.8	17.9	16.6

TABLE 3.7: Results for $\Delta\alpha_{\text{QED}}^{\text{had}}$ and the relative precision for the light-quark contribution. We consider the same sources for the systematic error as for the Adler function: lattice artefacts (LA), the method for the extraction of the Adler function (AM), the Padé ansatz used for the derivative in the fit to the Adler function (PA), the pion mass dependence (χ -ext.).

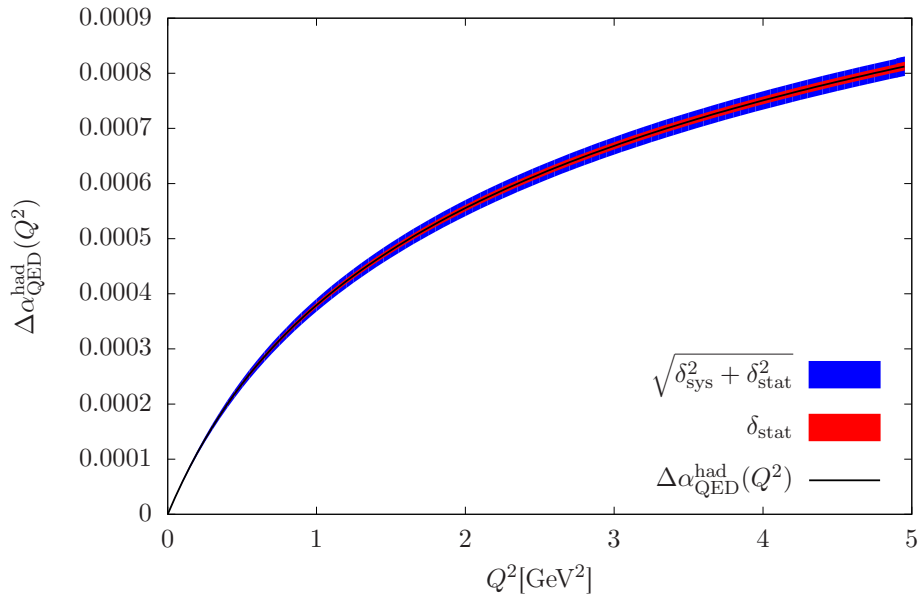


FIGURE 3.26: Estimate of the strange-quark contribution for $\Delta\alpha_{\text{QED}}^{\text{had}}$ from the renormalized VPF.

3.3.2 The strange-quark contribution

We estimate the strange-quark contribution using the extended frequentist method with the same 32 variations we considered for the analysis of the Adler function, cf. 3.2.2.2, with all weights set to 1. We show the result in figure 3.26. Again, we use the same subsets to determine the various contributions to the systematic error as for the Adler function. The estimates are shown in table 3.8. The statistical error dominates the total error. We reach a precision of the order of 3.3% at small Q^2 that improves with increasing Q^2 to 2.2%. We observe that lattice artefacts dominate the systematic error over the whole considered Q^2 region, while the pion mass dependence is the sub-leading effect for $Q^2 \geq 1.0 \text{ GeV}^2$. The method of the extraction of the Adler function is of a similar size as the systematic error associated with the pion mass dependence for small Q^2 . The Padé ansatz gives a minor contribution to the systematic error.

$Q^2[\text{GeV}^2]$	$\Delta\alpha_{\text{QED}}(Q^2) \times 10^5$	%	LA	AM	PA	χ -ext.
0.5	23.7(3)(0.7)	3.3	44.8	23.9	9.2	22.1
1.0	37.9(4)(1.1)	3.0	46.9	23.3	6.4	23.4
1.5	47.9(5)(1.2)	2.8	48.3	22.3	5.7	23.7
2.0	55.5(6)(1.3)	2.6	48.7	21.5	5.6	24.2
2.5	61.7(6)(1.4)	2.5	48.9	20.9	5.6	24.7
3.0	66.8(7)(1.4)	2.4	49.1	20.4	5.5	25.1
3.5	71.2(7)(1.5)	2.3	49.4	19.8	5.3	25.5
4.0	75.1(7)(1.5)	2.2	49.6	19.3	5.2	25.9
4.5	78.5(7)(1.5)	2.2	49.8	18.9	5.1	26.3

TABLE 3.8: Results for $\Delta\alpha_{\text{QED}}^{\text{had}}$ and the relative precision for the strange-quark contribution. We consider the same sources for the systematic error as for the Adler function: lattice artefacts (LA), the method for the extraction of the Adler function (AM), the Padé ansatz used for the derivative in the fit to the Adler function (PA), the pion mass dependence (χ -ext.).

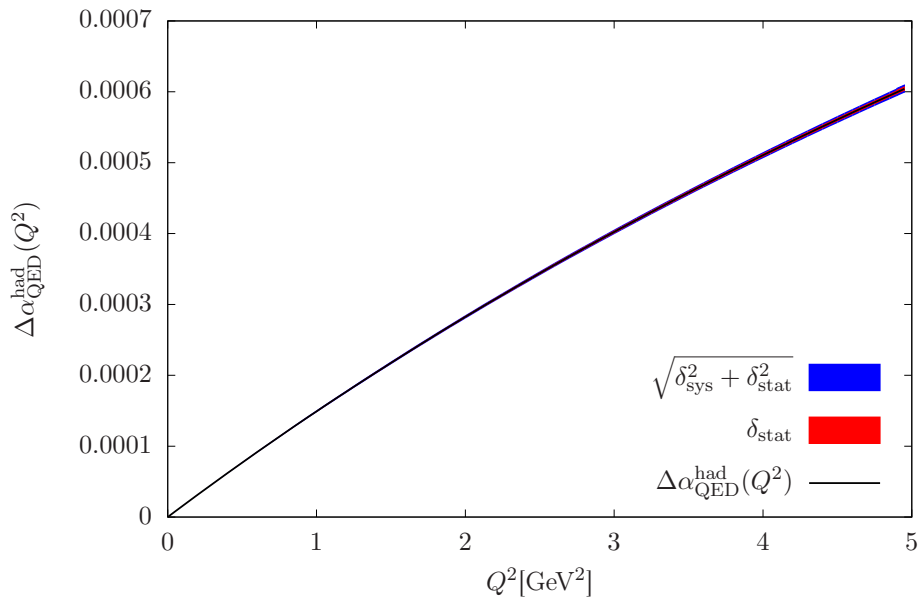


FIGURE 3.27: The error of the charm-quark contribution for $\Delta\alpha_{\text{QED}}^{\text{had}}$ determined via the renormalized VPF is dominated by systematic effects due to lattice artefacts.

3.3.3 The charm-quark contribution

We show the result for the charm-quark in figure 3.27, which is based on the same 32 variations that we already considered for the Adler function in 3.2.2.3. Note that we use the same unweighted procedure as for the charm-quark contribution of the Adler function for the analysis of $\Delta\alpha_{\text{QED}}^{\text{had}}$ here. As before, we use the same subsets to determine the contributions to the systematic error for $\Delta\alpha_{\text{QED}}^{\text{had}}$ as for the Adler function. The results are listed in table 3.9. We obtain a relative precision of $\sim 1\%$. The systematic error is of a similar size as the statistical error. The contribution associated with the pion mass dependence dominates the systematic error. At small Q^2 the Padé ansatz gives a large

contribution to the systematic error, while for larger Q^2 values lattice artefacts and the choice of the method of the extraction of the Adler function matter more. As cut-off effects grow with larger Q^2 this behaviour is expected for lattice artefacts.

$Q^2[\text{GeV}^2]$	$\Delta\alpha_{\text{QED}}(Q^2) \times 10^5$	%	LA	AM	PA	χ -ext.
0.5	7.7(0)(1)	1.0	0.8	5.4	43.7	50.1
1.0	14.9(1)(1)	1.0	8.4	0.5	37.0	54.1
1.5	21.7(1)(2)	0.9	16.6	7.0	25.5	50.9
2.0	28.2(2)(2)	0.9	21.3	8.0	17.0	53.7
2.5	34.4(2)(2)	0.8	21.7	15.1	15.3	47.9
3.0	40.2(2)(3)	0.8	23.4	20.8	14.2	41.7
3.5	45.8(2)(3)	0.8	25.4	23.9	13.7	37.0
4.0	51.1(3)(3)	0.8	27.9	23.0	13.7	35.4
4.5	56.1(3)(4)	0.9	28.8	23.9	11.7	35.6

TABLE 3.9: Results for $\Delta\alpha_{\text{QED}}^{\text{had}}$ and the relative precision for the charm-quark contribution. We consider the same sources for the systematic error as for the Adler function: lattice artefacts (LA), the method for the extraction of the Adler function (AM), the Padé ansatz used for the derivative in the fit to the Adler function (PA), the pion mass dependence (χ -ext.).

3.3.4 Summed contributions and comparison to phenomenology

We estimate the three and four-flavour results by adding the individual flavours, and summing their respective errors in quadrature. The result for three flavours is shown at the top left of figure 3.28 with a comparison to the five flavour result from phenomenology [87, 88]. On the right we show the comparison of the precision we obtain for the statistical error, our full error, and the uncertainty of the result from the dispersive approach. The reason for the discontinuity in our result for the relative uncertainty is that we use the extended frequentist method, which relies on distributions of results at points in Q^2 . When many fits converge to a single point the error is reduced and when Q^2 is increased this convergence may be lost and the fit functions move in different directions. Since only a finite number of points in Q^2 are computed this may result in discontinuities for the relative uncertainty even though we have a continuous result for the absolute value of the function. The three-flavour result agrees with the result from phenomenology only for small Q^2 where the heavy quark flavours are inactive. As we expect, this agreement is lost for larger Q^2 as more flavours become active, but the general behaviour is still comparable.

At the bottom of figure 3.28 we show the four-flavour result on the left with the same comparison to the five flavour result from phenomenology and with a comparison of the uncertainties on the right. The four-flavour result agrees with the result from phenomenology in the considered Q^2 region. From this we conclude that the impact of

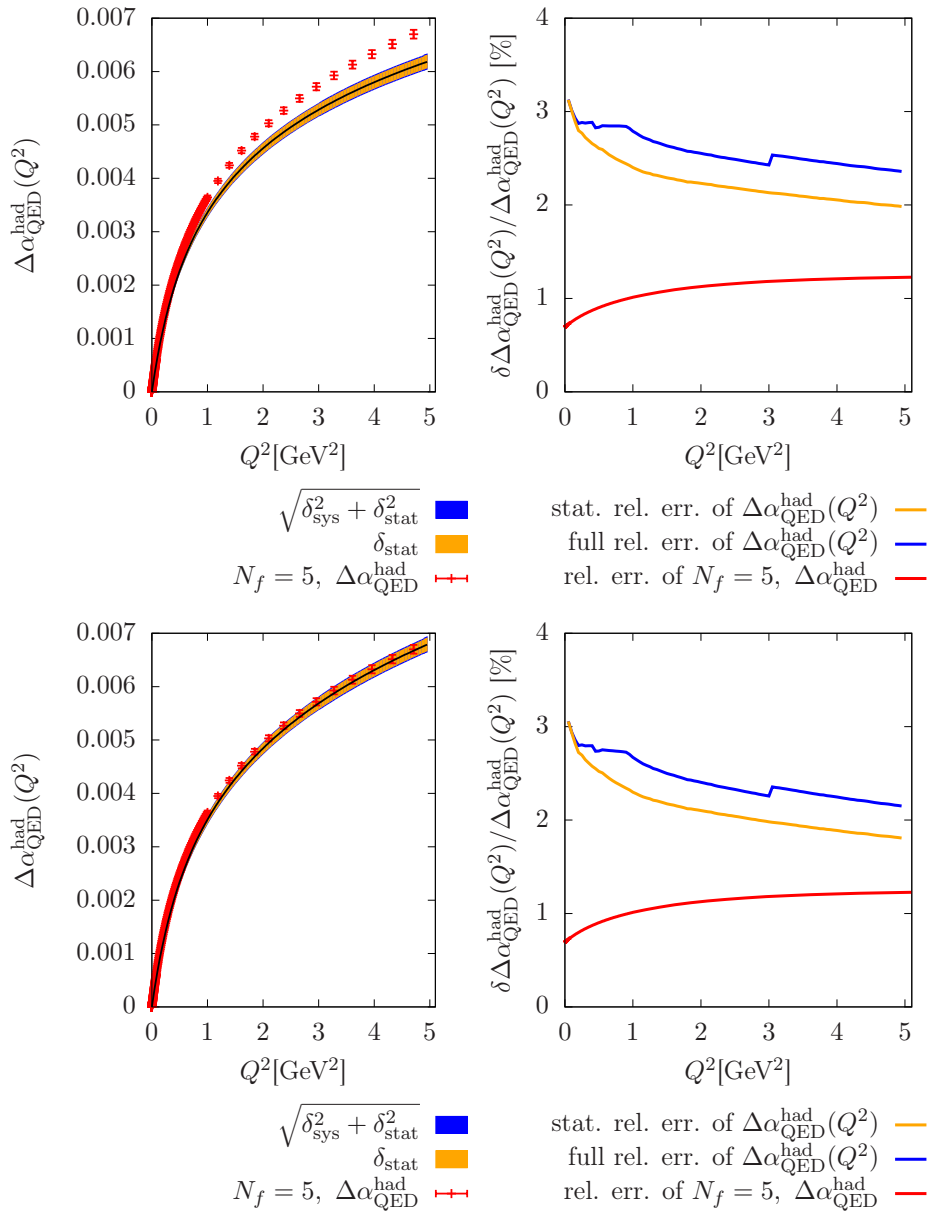


FIGURE 3.28: We sum the central values and the errors in quadrature for three flavours (top) and four flavours (bottom). On the left we show our estimates for $\Delta\alpha_{\text{QED}}^{\text{had}}$ in comparison to the five flavour result by Jegerlehner [87, 88]. On the right we compare the precision of our result for the statistical and the full uncertainty to the one from the dispersive method. From the agreement of our four flavour result and the result by Jegerlehner we conclude that the bottom-quark is too heavy to have a big impact on the result in the considered Q^2 range.

the bottom-quark in this energy range is limited. For $Q^2 > 2.0 \text{ GeV}^2$ we find that the relative precision we reach for the three or four-flavour result is not yet comparable to the precision of phenomenological result. For increasing Q^2 the relative precision of our result improves to $\lesssim 2.5\%$. To improve this situation a better determination of the Adler function in the low Q^2 region is needed, in particular of the low Q^2 regime where the relative precision decreases to up to $> 3\%$.

3.3.5 Conclusions

3.3.5.1 Remarks on the Adler function

We presented two methods to numerically extract the Adler function from the hadronic vacuum polarization. With twisted boundary conditions we are able to estimate a dense set of points on each ensemble. Furthermore, we found that the data obtained this way compares well to a derivative of a fit to the VPF data. The extrapolation to the physical point was performed with a simultaneous fit that models the Q^2 behaviour, the lattice spacing dependence and the pion mass dependence. We found that the different ansätze considered for the light-quark contribution have $\chi^2/\text{dof} \sim 3.9$ for the fits without cuts in the pion mass or the lattice spacing, and with any of these cuts the value of χ^2/dof is further reduced. For the strange-quark contribution we have $\chi^2/\text{dof} \leq 2.5$ without using cuts on the data. The χ^2/dof also improves when cuts on the data are imposed. The charm-quark contribution is more difficult to describe with such a fit using all ensembles, such that we get $\chi^2/\text{dof} \sim 6.0$. Again imposing cuts on the data entering the extrapolation improves the χ^2/dof . The reason for the bad χ^2/dof for all three flavours are small fluctuations of the data around the general trend. These fluctuations are not covered by the statistical error of the points that we get from the two methods for the numerical derivative of the VPF to compute the Adler function. Thus the statistical error of the points from these two numerical procedures may be underestimated. This effect is enhanced for the charm-quark because of the high statistical precision for the points of the VPF. Nevertheless, the fits yield a good description of the general trend of the data and when we include the systematic error determined via the EFM we can cover these fluctuations.

For the light-quark contribution we found that lattice artefacts dominate the systematic error in the small Q^2 region, while the pion mass dependence is dominant at larger Q^2 . This may be counter-intuitive for the light-quark contribution. But when considering figure 3.8, where we discussed the continuum extrapolation, and figure 3.10, where we discussed the extrapolation to physical quark mass, we find that with G8 at $m_\pi = 185$ MeV we are already quite close to the physical quark mass, while the continuum extrapolation is a much larger contribution of the full extrapolation to the physical point. Thus the Adler function is more susceptible to lattice artefacts than it is to the pion mass dependence. The choice of the Padé ansatz is relevant in the intermediate Q^2 range, and the choice of the method for the extraction of the Adler function is important at small Q^2 .

In a similar way lattice artefacts dominate the systematic error at low Q^2 of the strange-quark contribution, while the systematic error associated with the chiral extrapolation dominates at large Q^2 . At larger values of Q^2 the method of the extraction of the Adler

function gives sizeable contribution to the systematic error. The choice of the Padé ansatz has little impact on the systematic error.

The systematic error of the charm-quark contribution is dominated by lattice artefacts for $Q^2 \geq 3.0 \text{ GeV}^2$, while below that the systematic error due to the chiral extrapolation dominates. The choice of the Padé ansatz is relevant at small Q^2 , and the method of the extraction of the Adler function is $\sim 20\%$ for intermediate Q^2 .

In the Q^2 regime considered in this study, the three-flavour determination deviates from the perturbative results. But we expect the Adler function to fall off significantly for $Q^2 \rightarrow \infty$ to approach the limit of $D(Q^2 \rightarrow \infty) = 2$. Our four-flavour result shows a behaviour similar to the NNLO result from perturbative QCD, but does not agree with it for large $Q^2 \gtrsim 3.5 \text{ GeV}^2$. Possible reasons for this disagreement are missing higher order corrections from pQCD, or an underestimated systematic effect from lattice artefacts or cut-off effects of our result.

3.3.5.2 Remarks on the calculation of $\Delta\alpha_{\text{QED}}^{\text{had}}$

We computed $\Delta\alpha_{\text{QED}}^{\text{had}}$ from a simultaneous fit to the Adler function at the physical point using the extended frequentist method. For the light-quark contribution we find a relative precision of $\approx 3.5 - 6.0\%$ depending on the momentum Q^2 . The systematic error dominates the total error. Lattice artefacts are the leading systematic effect, while the choice of the Padé ansatz is the sub-leading effect. The relative precision of the strange-quark contribution varies between $\approx 2.2 - 3.3\%$, it increases with increasing Q^2 as we observed it for the light quark contribution. Systematic error is again dominant. Lattice artefacts are the leading systematic effect and the pion mass dependence as the sub-leading effect for intermediate and large Q^2 . We reach a relative precision of $\sim 1\%$ for the charm-quark contribution. The systematic error and the statistical error are of a similar size. The pion mass dependence is the dominant contribution to the systematic error. At small Q^2 the Padé ansatz gives a sizeable contribution, while for larger Q^2 lattice artefacts grow, as one would expect for a heavy quark.

We attribute the agreement of our data for the four-flavour case with the five flavour result from phenomenology to a small impact of the bottom quark in the considered Q^2 regime. The three and four-flavour results are dominated by the light-quark contribution, thus the relative precision we can reach is limited by the light-quark contribution. For the three and four-flavour results we get a precision of $\approx 2 - 3\%$ for $Q^2 > 1.0 \text{ GeV}^2$. The total relative uncertainty of our result is about a factor of 2 larger than the precision of the result from phenomenology. We discuss possible improvements of the calculation in the conclusions of this work.

Chapter 4

The anomalous magnetic moment of the muon

4.1 a_μ from experiment

The most recent experiment to determine a_μ at Brookhaven (E821) measured the orbital and spin motion of highly polarized muons in a storage ring [89]. A rough sketch of the experiment is shown in figure 4.1. The proton beam hits a target to produce pions which in turn decay into muons which are polarized along the direction of their momentum. After the injection the muons are kept on a ring by a constant magnetic field \vec{B} . The muons oscillate with the cyclotron frequency ω_c in the horizontal plane. This leads due to the magnetic field \vec{B} to a precession of the spin vector \vec{s} with the frequency ω_s , which is described by the Larmor precession. The frequencies are given by

$$\omega_c = \frac{eB}{m_\mu \gamma}, \quad (4.1)$$

$$\omega_s = \frac{eB}{m_\mu \gamma} + \frac{eB}{m_\mu} a_\mu, \quad (4.2)$$

$$\omega_a = \omega_s - \omega_c = \frac{eB}{m_\mu} a_\mu, \quad (4.3)$$

where $\gamma = 1/\sqrt{1 - v^2/c^2}$. The anomalous magnetic moment is then given by

$$a_\mu = \frac{\omega_a}{\omega_L - \omega_c}, \quad (4.4)$$

where ω_L is the Larmor precession frequency of the muon, given by $\omega_L = (a_\mu + 1) \frac{eB}{m_\mu}$. In figure 4.2 we show the weak decay of the muon and the corresponding momentum \vec{p} and spin \vec{s} of the decay products. Due to the small upper bounds of the neutrino masses,

this decay is strongly preferred. The ν_e is left-handed and the $\bar{\nu}_\mu$ is right-handed. The correlation between the directions of the muon spin and the electron momentum allows for a measurement of the muon spin direction as a function of time.

A new experiment was proposed in [2] at Fermilab, which is based on the same principle

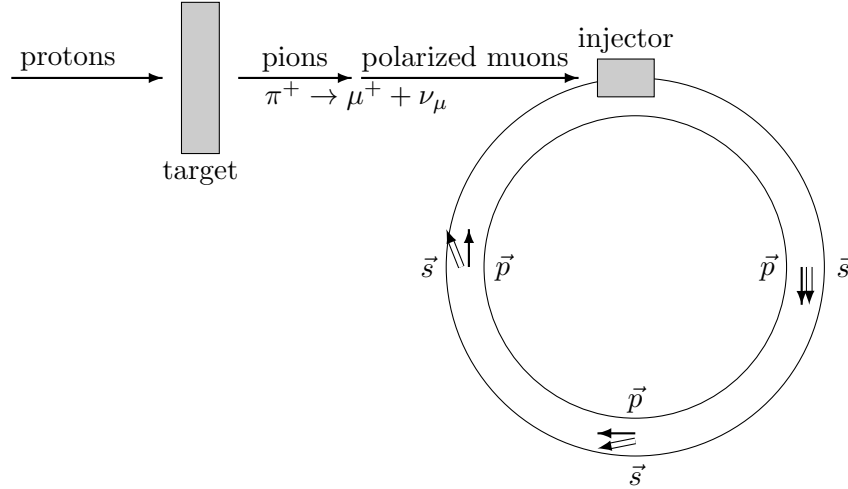


FIGURE 4.1: Sketch of the principal idea to measure a_μ using a μ storage ring, for more elaborate ones see [82, 90]. The precession frequencies of the orbital and spin motion are shown as arrows and double arrows, respectively. As the muons move along the storage ring the polarization is lost, which is given by ω_a , see eq. (4.3).

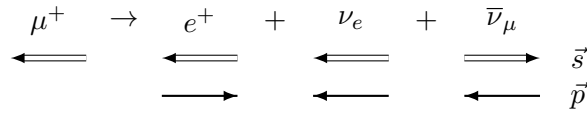


FIGURE 4.2: In this weak decay parity is violated maximally, which leads to a strong correlation between the directions of the muon spin and the emission of the positrons.

and will reuse the storage ring of E821 with the aim to reduce the error on the current result by a factor of 4. For more detailed discussions of experimental setups see [2, 82, 89–92].

4.2 a_μ from theory

The SM prediction can be divided into the contributions from the different interactions,

$$a_\mu^{\text{SM}} = a_\mu^{\text{QED}} + a_\mu^{\text{EW}} + a_\mu^{\text{QCD}}. \quad (4.5)$$

Figure 4.3 shows the leading order Feynman diagrams for the corrections to a_μ . The QED part is known to fifth order in perturbation theory [93–101],

$$a_\mu^{\text{QED}} = 116\,584\,718.95(08) \times 10^{-11}. \quad (4.6)$$

The electro-weak contribution is [102–113]

$$a_\mu^{\text{EW}} = 153.6(1.0) \times 10^{-11}, \quad (4.7)$$

which includes 2-loop corrections, while 3-loop corrections are currently negligible. The leading order hadronic contribution can be estimated with a dispersion integral, cf. chapter 5 of [82],

$$a_\mu^{\text{had,LO}} = \left(\frac{\alpha m_\mu}{3\pi}\right)^2 \left(\int_{m_{\pi^0}^2}^{E_{\text{cut}}^2} \frac{R_\gamma^{\text{data}}(s) \hat{K}(s)}{s^2} ds + \int_{E_{\text{cut}}^2}^{\infty} \frac{R_\gamma^{\text{pQCD}}(s) \hat{K}(s)}{s^2} ds \right), \quad (4.8)$$

where we used the normalized cross section

$$R_\gamma^{\text{had}} = \sigma(e^+e^- \rightarrow \text{hadrons}) / \frac{4\pi\alpha(s)^2}{3s}, \quad (4.9)$$

and $\hat{K}(s)$ is a known analytic function. In the low- Q^2 regime of the dispersion integral experimentally measured cross section of $e^+e^- \rightarrow \text{hadrons}$ is used, since perturbative QCD breaks down in this regime. The result of this approach is [114]

$$a_\mu^{\text{QCD}}[\text{LO}] = 6\,923(42)(3) \times 10^{-11}, \quad (4.10)$$

where the first error is from experimental data input and the second from perturbative QCD. The next-to-leading order hadronic contribution is given by [115]

$$a_\mu^{\text{QCD}}[\text{NLO}] = 7(26) \times 10^{-11}, \quad (4.11)$$

where the error is dominated by the so called hadronic light-by-light (Hlbl) scattering shown in figure 4.4. The uncertainties of the combined result of a_μ^{SM} are dominated by hadronic contributions. The dispersive approach using cross sections measurements of $\sigma(e^+e^- \rightarrow \text{hadrons})$ at low energies and perturbative expressions for higher energies leads to a Standard Model theoretical determination that heavily relies on experimental input. Lattice QCD allows for calculations of the hadronic contributions to a_μ from first principles and thus for a more direct comparison with theory. For Hlbl two approaches have been proposed recently. In [116] non-perturbative lattice QCD was used for a first estimate and in [117] a strategy to compute the Hlbl scattering amplitude by itself was proposed by the Mainz group. In the following we will discuss the extraction of the leading order hadronic contribution to a_μ (a_μ^{HLO}) on the lattice.

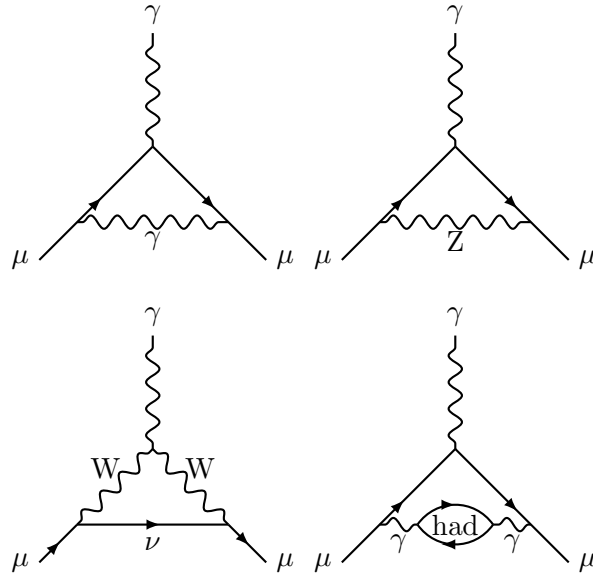


FIGURE 4.3: Diagrams of the leading order contributions to a_μ from QED (top left), weak interactions (top right and bottom left), and QCD (bottom right).

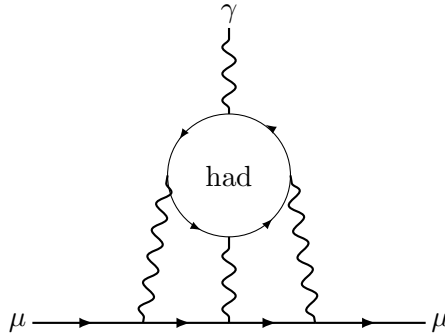


FIGURE 4.4: Diagram of the next-to-leading order hadronic contribution to a_μ , referred to as hadronic light-by-light scattering.

4.3 Extraction of the hadronic anomalous magnetic moment of the muon from lattice data

We can rewrite the equations (1.4, 1.5) in the form

$$a_\mu^{\text{HLO}} = \left(\frac{\alpha}{\pi}\right)^2 \int_0^\infty \frac{dQ^2}{Q^2} w(Q^2/m_\mu^2) \hat{\Pi}(Q^2), \quad (4.12)$$

$$w(r) = 16/\left(r^2 \left(1 + \sqrt{1 + 4/r}\right)^4 \sqrt{1 + 4/r}\right). \quad (4.13)$$

It was shown in [118] that fitting the whole of the accessible Q^2 range of the lattice VPF may lead to a bias of the low Q^2 range of the respective fit function. But this part of the VPF is the most important contribution to the convolution integral of a_μ^{HLO} (eq. 4.12) as it has a peak close to the squared muon mass, which we demonstrate in figure 4.5. Thus

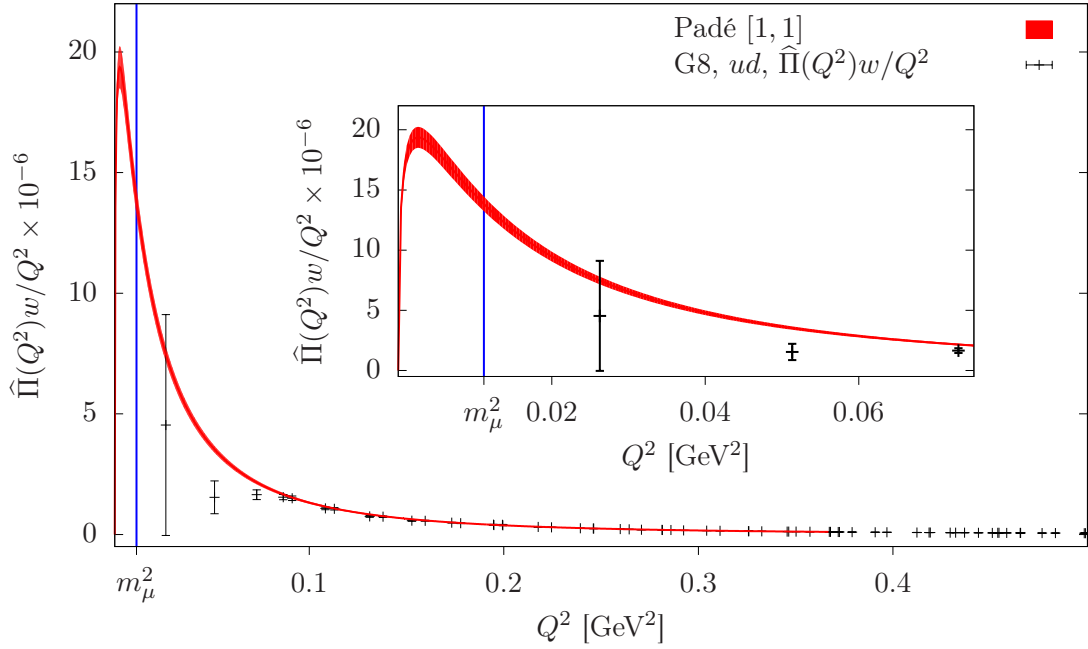


FIGURE 4.5: The low Q^2 regime for the light-quark contribution on G8. The black points refer to the data, where the additive renormalization of the VPF is determined via the extrapolation of the Padé [1,1] fit which is shown as a red band. We used $Q_{\text{cut}}^2 \approx 0.367 \text{ GeV}^2$ and $\chi_{\text{corr}}^2/\text{dof}=1.32$. The fit in comparison to the VPF data without the multiplication of the weight function of the convolution integral is shown in figure 4.7.

one would ideally map the peaked region very precisely while the large Q^2 range can be estimated by a less accurate numerical procedure, that only relies on the respective method used in the low Q^2 regime for the additive renormalization of the VPF. Following the equations (4.12, 4.13) and the strategy of [118], we split the integral into two parts, where we use a continuous description for the first part (I) with $Q^2 \in [0, Q_{\text{cut}}^2]$, and for the second part (II) the trapezoidal rule to integrate the interval $Q^2 \in [Q_{\text{cut}}^2, Q_{\text{max}}^2]$. The renormalization of part II depends on the method used for part I.

$$a_\mu^{\text{I}} = 4\alpha^2 Z_V \int_0^{Q_{\text{cut}}^2} \frac{dQ^2}{Q^2} w(Q^2/m_\mu^2) \left[\Pi_{[n,m]}^{\text{fit}}(Q^2) - \Pi_{[n,m]}^{\text{fit}}(Q=0) \right], \quad (4.14)$$

$$a_\mu^{\text{II}} = 4\alpha^2 Z_V \int_{Q_{\text{cut}}^2}^{Q_{\text{max}}^2} \frac{dQ^2}{Q^2} w(Q^2/m_\mu^2) \left[\Pi^{\text{data}}(Q^2) - \Pi_{[n,m]}^{\text{fit}}(Q=0) \right], \quad (4.15)$$

$$\Rightarrow a_\mu^{\text{HLO}} = a_\mu^{\text{I}} + a_\mu^{\text{II}}. \quad (4.16)$$

We fix the value of Q_{max}^2 to 4.0 GeV^2 . Though one should in principle add the result from perturbation theory for $Q_{\text{max}}^2 < Q^2 < \infty$ we find that this contribution is below 0.1% of the size of the statistical uncertainty and thus we neglect this part entirely.

In [119] it was suggested to rescale the kernel of the integral by a ratio of the vector

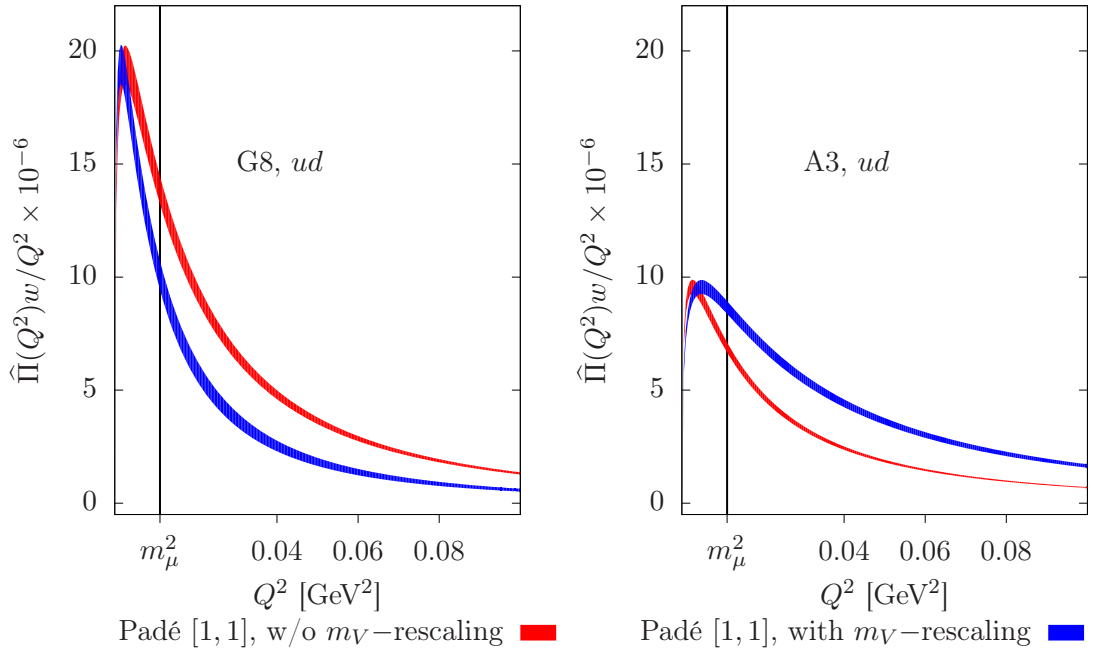


FIGURE 4.6: Illustration of the shift in the convolution integral due to m_V -rescaling on G8 and on A3 for the light-quark contribution.

mass on the lattice and the physical ρ -mass,

$$w\left(\frac{Q^2}{m_\mu^2}\right) \rightarrow w\left(\frac{Q^2}{m_\mu^2} \frac{(m_\rho^{\text{phys}})^2}{m_V^2}\right), \quad (4.17)$$

with the aim to reduce the strong quark mass dependence, such that we may use a linear ansatz in m_π^2 for the chiral extrapolation. The original weight function is recovered at the physical point. This shifts the bulk of the contribution to the integral in the low Q^2 region to slightly larger Q^2 , which in theory can help reduce the uncertainty on the result for a_μ^{HLO} . We will refer to this type of analysis as “ m_V -rescaled”. We use the vector masses listed in table 4.6. In figure 4.6 we show the effect of m_V -rescaling for fits on G8 and A3. On G8 the ρ is no longer a stable particle, thus it can decay into a two pion state. In principle one would need more elaborate methods to extract the ρ -mass reliably, but this is beyond the scope of this thesis. We find, due the fact that the vector mass on G8 is smaller than the physical ρ mass, that m_V -rescaling actually shifts the peak of the convolution integral to slightly smaller Q^2 . For ensembles with heavier pion mass the ρ is stable and $m_\rho > m_\rho^{\text{phys}}$. Here the peak is shifted slightly towards larger Q^2 and the area below the curve is increased, thus leading to a less steep chiral extrapolation.

In the following subsections we discuss two methods to obtain the continuous description for the low Q^2 range of the renormalized VPF and compute a_μ^{HLO} from it.

4.3.1 The extraction of a_μ^{HLO} with the hybrid method

For the hybrid method we use a fit for the description of the low Q^2 range. We employ the Padé approximants written in the form¹ [84, 85],

$$P_{[i+1,i]}(Q^2) = Q^2 \left(a_0 + \sum_{j=1}^i \frac{a_j}{b_j + Q^2} \right), \quad (4.18)$$

$$P_{[i,i]}(Q^2) = Q^2 \left(\sum_{j=1}^i \frac{a_j}{b_j + Q^2} \right), \quad (4.19)$$

as fit ansätze. The coefficients then obey

$$a_{i>0} > 0, \quad \text{and} \quad b_n > b_{n-1} > \dots > b_1 > 4m_\pi^2. \quad (4.20)$$

The Padé approximants are guaranteed to converge to the exact result of the VPF [85]. We impose these conditions by rewriting the fit functions as

$$P_{[i+1,i]}(Q^2) = Q^2 \left(a_0 + \sum_{j=1}^i \frac{e^{\tilde{a}_j}}{e^{\tilde{b}_j} + 4m_\pi^2 + Q^2} \right), \quad (4.21)$$

$$P_{[i,i]}(Q^2) = Q^2 \left(\sum_{j=1}^i \frac{e^{\tilde{a}_j}}{e^{\tilde{b}_j} + 4m_\pi^2 + Q^2} \right). \quad (4.22)$$

The fit function for the VPF then reads

$$\Pi_{[n,m]}^{\text{fit}}(Q^2) = \Pi(Q^2 = 0) + \tilde{P}_{[n,m]}(Q^2), \quad (4.23)$$

where $\Pi(Q^2 = 0)$ is a fit parameter, that is the result of an extrapolation to vanishing Q^2 where no data are available. Note that at this stage of the calculation the renormalization coefficient Z_V required by the use of the local vector current shown in section 2.1.1 is not applied. We renormalize the result of the convolution integral in eq. (4.12) and include the error of the renormalization by including the bootstrap samples of the determination of Z_V . The use of twisted boundary conditions allows us to perform a fine scan of Q_{cut}^2 . We then look for results that are stable for all ensembles. Writing the fit functions as in equations (4.21, 4.22) helps to obtain stable results down to very low Q_{cut}^2 , but has little to no effect for $Q_{\text{cut}}^2 > 0.3 \text{ GeV}^2$. The Q^2 behaviour of the VPF data is highly correlated, thus a correlated fit is used to take the correlations into account, which also

¹Eqs. (4.18, 4.19) are the same as eqs. (3.37, 3.38). We repeat them here for the readers convenience.

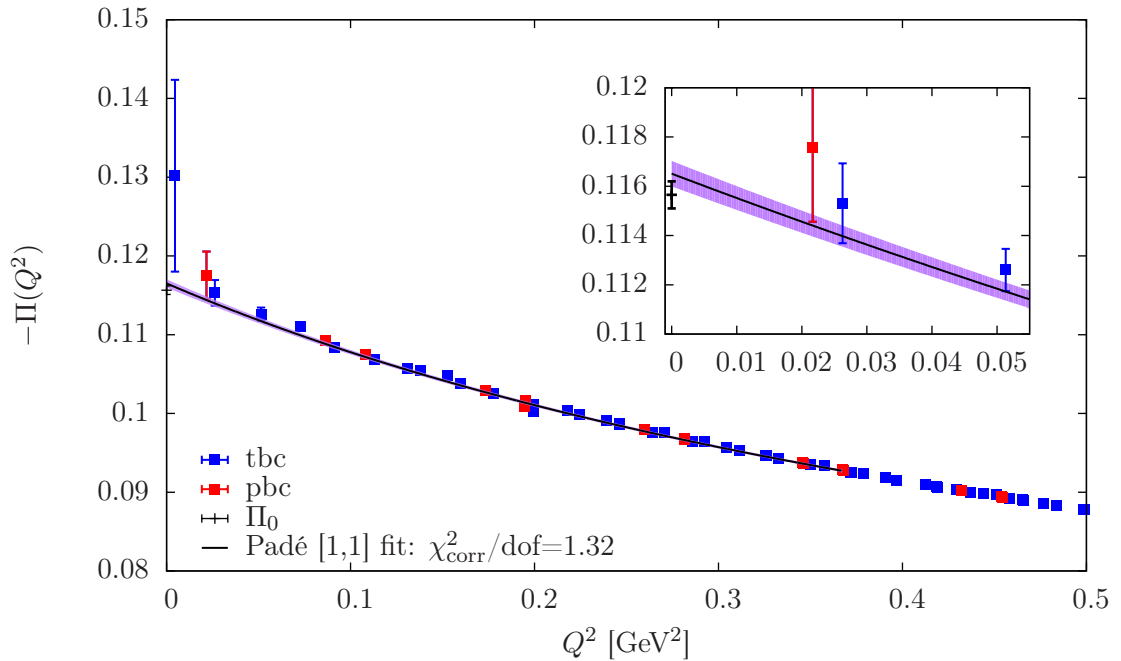


FIGURE 4.7: Illustration of a fit to the VPF on G8 for the light-quark contribution using a Padé [1,1] ansatz. The points obtained with periodic boundary conditions (pbc) are shown in red, twisted boundary conditions (tbc) results are shown in blue. The statistical error of the fit is shown as a purple band. As a reference we also show the result for Π_0 which we get from time moments, see 4.3.2 for the details of the computation. Note that Π_0 does not enter in the fit.

helps to reduce the statistical error significantly. To invert the correlated covariance matrix we use a singular value decomposition (SVD) and remove singular eigenvalues that are 10^{-5} smaller than the largest singular eigenvalue. We find that we can not go to the very low Q_{cut}^2 as proposed in [118] of $Q_{\text{cut}}^2 \lesssim 0.2 \text{ GeV}^2$ due to instabilities of the fits. Furthermore, we stick to low order Padé ansätze of [1,1] and [2,1] which are stable for $0 < Q_{\text{cut}}^2 \lesssim 0.6 \text{ GeV}^2$. Higher orders are poorly constrained by the data, such that a fit using two poles frequently tries to model small fluctuations in the data rather than the general trend. We show as an example the result of a scan in Q_{cut}^2 in table 4.1 using the Padé [1,1] as a fit ansatz with the renormalization factor Z_V . We list the scans we performed for all flavours and fit ansätze in C.1. In figure 4.7 we show an example of a fit to the data on G8 for the light-quark contribution with $Q_{\text{cut}}^2 = 0.367 \text{ GeV}^2$ and $\chi_{\text{corr}}^2/\text{dof}=1.32$ for 41 points. We observe that the time moment Π_0 , which is only shown as a reference and is not used in the fit, agrees within errors with the extrapolated value of $\Pi(Q^2 = 0)$ from the fit.

For the selection of Q_{cut}^2 we make two choices where possible to monitor systematic effects due to the choice of this cut. The first is based on kinematic reasons, we look for a roughly similar value on all considered ensembles, where the fit is stable. We choose $Q_{\text{cut},1}^2 \approx 0.5 \text{ GeV}^2$. The second choice is based on parameters of the fit. We select Q_{cut}^2

Q_{cut}^2 [GeV ²]	a_{μ}^{I}	a_{μ}^{II}	a_{μ}^{HLO}	$\chi_{\text{corr}}^2/\text{dof}$	N
0.3574	499.41(18.53)	21.42(0.37)	520.83(18.82)	1.36	40
0.3673	501.44(18.66)	20.65(0.35)	522.08(18.99)	1.32	41
0.3679	502.54(18.72)	20.63(0.35)	523.18(18.99)	1.28	42
0.3719	503.92(18.48)	20.35(0.34)	524.27(18.80)	1.33	43
0.3725	501.63(17.63)	20.27(0.33)	521.90(17.94)	1.28	44
0.3791	500.54(17.55)	19.76(0.32)	520.30(17.81)	1.25	45
0.3909	502.67(17.62)	18.95(0.30)	521.62(17.91)	1.23	46
0.3969	502.69(17.35)	18.55(0.29)	521.23(17.63)	1.29	47
0.4123	501.97(16.98)	17.54(0.27)	519.51(17.22)	1.26	48
0.4186	500.69(16.40)	17.15(0.26)	517.84(16.62)	1.21	49
0.4192	497.40(15.87)	17.08(0.25)	514.48(16.11)	1.19	50
0.4295	497.66(15.95)	16.49(0.24)	514.16(16.18)	1.18	51
0.4322	494.48(15.97)	16.30(0.24)	510.79(16.22)	1.16	52
0.4368	494.67(15.47)	16.06(0.23)	510.73(15.66)	1.14	53
0.4440	491.50(13.50)	15.64(0.21)	507.14(13.68)	1.12	54
0.4511	492.45(13.33)	15.29(0.20)	507.75(13.47)	1.10	55
0.4539	490.79(12.60)	15.14(0.19)	505.93(12.74)	1.08	56
0.4545	493.52(12.16)	15.14(0.19)	508.66(12.33)	1.06	57
0.4585	492.86(11.99)	14.94(0.19)	507.80(12.15)	1.04	58
0.4655	492.82(11.90)	14.61(0.18)	507.43(12.05)	0.99	59
0.4657	491.94(12.09)	14.59(0.18)	506.53(12.23)	0.98	60
0.4767	492.06(12.05)	14.10(0.17)	506.16(12.19)	0.96	61
0.4835	491.99(12.10)	13.80(0.17)	505.79(12.24)	0.94	62
0.4983	491.59(11.76)	13.19(0.16)	504.79(11.87)	0.93	63
0.4989	491.86(11.62)	13.17(0.16)	505.03(11.75)	0.91	64
0.5052	491.26(11.42)	12.92(0.15)	504.18(11.55)	0.90	65
0.5161	491.58(11.23)	12.52(0.14)	504.10(11.35)	0.88	66
0.5188	491.48(11.13)	12.42(0.14)	503.90(11.24)	0.87	67
0.5234	490.64(10.98)	12.25(0.14)	502.88(11.09)	0.85	68
0.5306	488.91(10.78)	11.98(0.13)	500.89(10.90)	0.84	69

TABLE 4.1: Scan of fit windows on G8 for the ud contribution using Padé [1,1]. The results we used for the extrapolation to the physical point are marked in red.

such that we have $N \leq 20$ points contributing to the fit, while the fit still yields a stable result. We observe that the fits on G8 suffer from numerical instabilities for $N \lesssim 40$, such that we have to make an exception here and pick the lowest number of points where we get a robust result for a_{μ}^{HLO} .

4.3.1.1 The light-quark contribution

We collect the results for the light-quark contribution in table 4.2 and in table 4.3 we show the corresponding results using m_V -rescaling. We observe that for a given Q_{cut}^2 the result from the Padé [2,1] does not add new information and tends to be less precise. We illustrate this effect in figure 4.8, where we find that only the result on G8 yields

different results for the two Padé ansätze. Technically the same applies to E5 for Padé [2,1], but the fit is unstable and gives an unphysically large result. We choose to use only the results from Padé [1,1] in the extrapolation to the physical point. Furthermore, we find that the E5 and N6 ensembles suffer from particularly large $\chi_{\text{corr}}^2/\text{dof}$. We attribute this effect to the high precision of the data and small fluctuations around the general trend, that cannot be described by the fit ansätze. For the E5 ensemble we find that for $Q_{\text{cut}}^2=0.52 \text{ GeV}^2$ the points with $Q^2 < 0.2 \text{ GeV}^2$ are above the fit curve and thus lead to a large $\chi_{\text{corr}}^2/\text{dof}$. We find a similar behaviour for the fit on the N6 ensemble with $Q_{\text{cut}}^2 \approx 0.5 \text{ GeV}^2$ for the points with $Q^2 < 0.1 \text{ GeV}^2$. These fluctuations may be caused by a combination of effects, such as finite volume effects and hyper cubic lattice artefacts. We exclude the results on E5 and N6 from the extrapolation to the physical point.

Although in principle one would expect the statistical precision for the m_V -rescaled results to be equal to the results without rescaling via the vector mass, we find that including the statistical error of the vector mass leads to a reduction in the statistical precision. This may be related to the fact that, though the measurements for the vector masses were taken on the same ensembles, we can not take correlations of the measurements for the VPF and the vector mass directly into account, because different configurations were used. Unfortunately using only the subset of measurements where the two calculations were performed on the same configurations would decrease statistics so far that a test of this is pointless. This effect is more pronounced for ensembles with smaller pion masses.

4.3.1.2 The strange-quark contribution

The results for the strange-quark contribution are shown in table 4.4 for Padé [1,1] and [2,1]. We find that for the strange-quark we can reduce Q_{cut}^2 and still get stable fit results. In figure 4.9 we show a comparison of the results from Padé [1,1] and [2,1] for fixed $Q_{\text{cut}}^2 \approx 0.5 \text{ GeV}^2$. We only use the results from Padé [1,1] for the extrapolation to the physical point, since, similar to the light-quark contribution, the additional term deteriorates the precision of the fits and they are in general less stable. As expected we find that the pion mass dependence is reduced with increasing quark mass, while lattice artefacts grow. Again, the $\chi_{\text{corr}}^2/\text{dof}$ for the result on the E5 ensemble is too large, thus we remove this result from the extrapolation to the physical point.

Ens.	Q_{cut}^2	N	Padé [1,1]			Padé [2,1]		
			$\chi_{\text{corr}}^2/\text{dof}$	a_{μ}^{HLO}	%	$\chi_{\text{corr}}^2/\text{dof}$	a_{μ}^{HLO}	%
A3	0.4840	13	0.83	268.12(7.76)	2.9	0.92	270.84(20.77)	7.7
A4	0.4840	13	2.13	343.99(14.65)	4.3	2.31	367.72(39.98)	10.9
A5	0.4840	13	0.85	330.02(25.92)	7.9	0.89	381.60(102.48)	26.9
B6	0.5010	43	0.60	379.40(10.81)	2.8	0.62	376.99(22.07)	5.9
E5	0.5223	10	6.78	324.13(11.00)	3.4	6.19	1009.94(226.71)	22.4
F6	0.5001	29	0.65	397.59(9.90)	2.5	0.62	425.03(27.33)	6.4
F7	0.5001	29	0.61	442.02(18.06)	4.1	0.63	437.08(47.76)	10.9
G8	0.4989	64	0.91	504.79(11.87)	2.4	0.80	587.76(39.02)	6.6
N5	0.4973	12	1.60	316.54(16.32)	5.2	1.71	337.40(34.65)	10.3
N6	0.4973	12	6.72	399.29(22.92)	5.7	7.35	457.34(75.18)	16.4
O7	0.4964	27	0.92	425.30(11.70)	2.8	0.95	437.23(30.08)	6.9
B6	0.2937	20	1.06	385.09(18.63)	4.8			
F6	0.3866	20	0.89	406.33(12.75)	3.1			
F7	0.3866	20	0.87	430.95(24.14)	5.6			
G8	0.3673	41	1.32	520.84(18.82)	3.6			
O7	0.3990	20	1.14	418.76(15.68)	3.7			

TABLE 4.2: Collection of results for a_{μ}^{HLO} for the light-quark contribution using the hybrid method. We show Q_{cut}^2 in units of GeV^2 , the number of points contributing to the fit N, and $a_{\mu}^{\text{HLO}} \times 10^{10}$ for Padé [1,1] and [2,1] for $Q_{\text{cut}}^2 \approx 0.5 \text{ GeV}^2$ and for Padé [1,1] for $N \leq 20$ where possible. We show the relative precision in %.

Ens.	Q_{cut}^2	N	Padé [1,1]			Padé [2,1]		
			$\chi_{\text{corr}}^2/\text{dof}$	a_{μ}^{HLO}	%	$\chi_{\text{corr}}^2/\text{dof}$	a_{μ}^{HLO}	%
A3	0.4840	13	0.83	454.31(13.96)	3.1	0.92	458.55(33.09)	7.2
A4	0.4840	13	2.13	496.94(22.04)	4.4	2.31	529.27(55.14)	10.4
A5	0.4840	13	0.85	447.04(36.01)	8.1	0.89	513.55(132.61)	25.8
B6	0.5010	43	0.60	452.98(24.28)	5.4	0.62	450.18(33.31)	7.4
E5	0.5223	10	6.78	483.75(17.53)	3.6	6.19	1403.29(299.83)	21.4
F6	0.5001	29	0.65	500.66(17.05)	3.4	0.62	534.00(35.57)	6.7
F7	0.5001	29	0.61	505.45(26.19)	5.2	0.63	499.90(55.85)	11.2
G8	0.4989	64	0.91	502.61(18.55)	3.7	0.80	585.28(41.91)	7.2
N5	0.4973	12	1.60	458.69(24.59)	5.4	1.71	486.87(48.50)	10.0
N6	0.4973	12	6.72	538.15(32.30)	6.0	7.35	612.19(97.42)	15.9
O7	0.4964	27	0.92	539.96(37.86)	7.0	0.95	554.58(50.85)	9.2
B6	0.2937	20	1.06	459.55(30.73)	6.7			
F6	0.3866	20	0.89	511.35(20.04)	3.9			
F7	0.3866	20	0.87	492.97(31.71)	6.4			
G8	0.3673	41	1.32	518.61(23.66)	4.6			
O7	0.3990	20	1.14	531.79(39.58)	7.4			

TABLE 4.3: Results for the light-quark contribution for a_{μ}^{HLO} with m_V -rescaling for the hybrid method. Q_{cut}^2 is shown in units of GeV^2 and a_{μ}^{HLO} in units of 10^{10} . We show the results for Padé [1,1] and [2,1] for $Q_{\text{cut}}^2 \approx 0.5 \text{ GeV}^2$ and for Padé [1,1] for $N \leq 20$ where applicable.

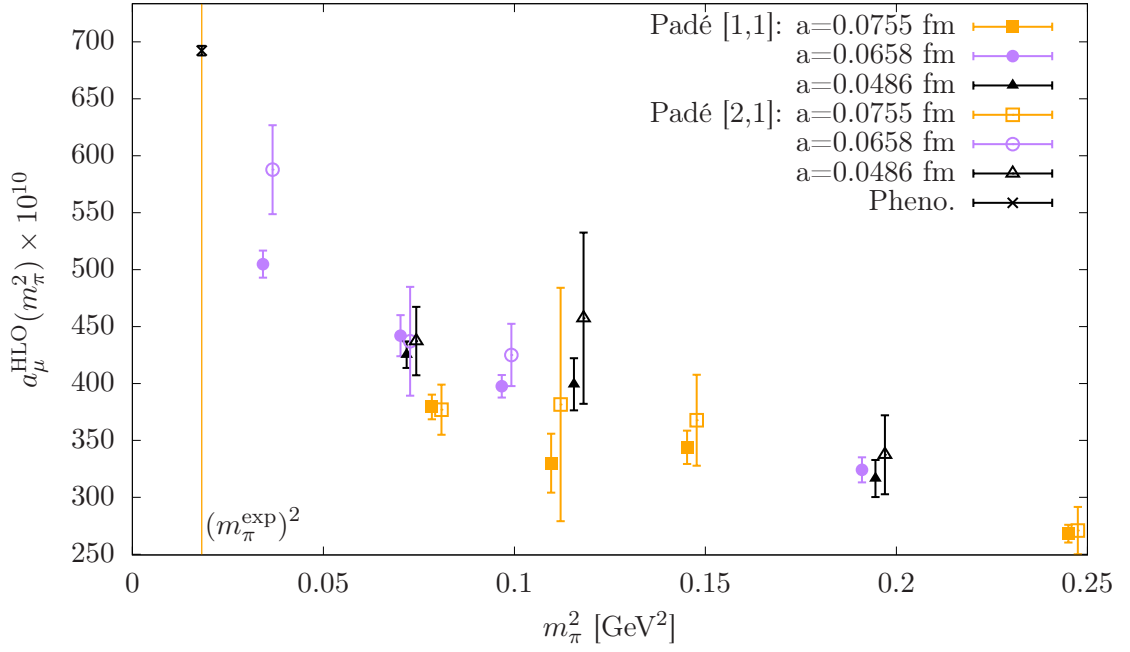


FIGURE 4.8: Results for a_μ^{HLO} for the light-quark contribution for $Q_{\text{cut}}^2 \approx 0.5$ GeV² for Padé [1,1] and [2,1], the latter are shifted to the right to improve visibility. As a reference we show the leading order hadronic contribution determined via phenomenology, note that this calculation is for $N_f = 5$, [1].

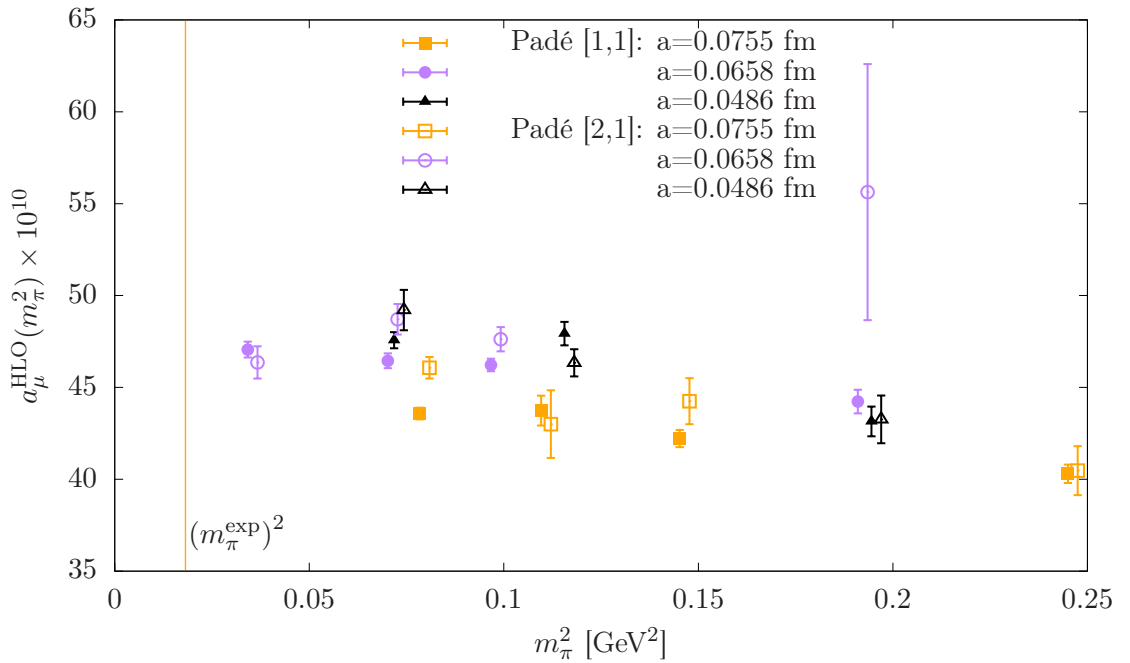


FIGURE 4.9: Results for a_μ^{HLO} for the strange-quark contribution at $Q_{\text{cut}}^2 \approx 0.5$ GeV² for the Padé ansätze [1,1] and [2,1].

4.3.1.3 The charm-quark contribution

For the charm-quark contribution we use the Padé [1,1] and a polynomial fit ansatz of $O(Q^2)$,

$$\Pi_c^{\text{fit}}(Q^2) = \Pi_c(Q^2 = 0) + bQ^2, \quad (4.24)$$

Ens.	Q_{cut}^2	N	Padé [1,1]			Padé [2,1]		
			$\chi_{\text{corr}}^2/\text{dof}$	a_{μ}^{HLO}	%	$\chi_{\text{corr}}^2/\text{dof}$	a_{μ}^{HLO}	%
A3	0.4840	13	1.16	40.30(50)	1.2	1.29	40.47(1.33)	3.3
A4	0.4840	13	3.41	42.22(47)	1.1	3.41	44.25(1.25)	2.8
A5	0.4840	13	1.04	43.74(81)	1.9	1.13	43.00(1.84)	4.3
B6	0.5010	43	1.23	43.58(32)	0.7	0.43	46.07(59)	1.3
E5	0.5223	10	6.97	44.23(64)	1.4	6.71	55.63(6.97)	12.5
F6	0.5001	29	0.76	46.22(34)	0.7	0.47	47.62(66)	1.4
F7	0.5001	29	0.98	46.45(40)	0.9	0.57	48.71(83)	1.7
G8	0.4989	64	0.33	47.06(43)	0.9	0.32	46.36(88)	1.9
N5	0.4973	12	1.07	43.15(81)	1.9	1.20	43.26(1.30)	3.0
N6	0.4973	12	2.13	47.93(64)	1.3	1.48	46.34(74)	1.6
O7	0.4964	27	0.90	47.57(44)	0.9	0.82	49.21(1.10)	2.2
A3	0.3423	9	1.50	38.96(1.30)	3.3			
A4	0.3423	9	1.98	43.33(1.14)	2.6			
A5	0.3423	9	1.14	45.76(1.42)	3.1			
B6	0.2060	12	0.29	44.76(68)	1.5			
F6	0.3078	14	0.89	46.47(47)	1.0			
F7	0.3078	14	1.18	47.50(54)	1.1			
G8	0.1379	11	0.80	47.08(82)	1.7			
N5	0.4493	11	1.20	43.18(83)	1.9			
N6	0.3676	9	1.95	47.44(83)	1.7			
O7	0.2926	13	1.24	50.17(93)	1.9			

TABLE 4.4: Results for a_{μ}^{HLO} in units of 10^{10} for the strange-quark contribution for Padé [1,1] and [2,1]. Q_{cut}^2 is in GeV^2 . The data of the strange-quark allows us to reduce the number of points contributing to the fit to smaller Q_{cut}^2 when compared to the light-quark contribution.

where $\Pi_c(Q^2 = 0)$ and b are fit parameters. As an example we show the fit we use on G8 in figure 4.10, where we see that for the short range in Q^2 required for the fit the data can be approximated with a linear ansatz in Q^2 . We found that the Padé ansatz [2,1] and higher orders suffer from numerical instabilities and in turn a_{μ}^{HLO} fluctuates with the choice of Q_{cut}^2 . The results for all ensembles are used in the extrapolation to the physical point and collected in table 4.5. In figure 4.11 we plot the data with respect to the pion mass dependence. The pion mass dependence diminishes further for the charm-quark and lattice artefacts are even more pronounced.

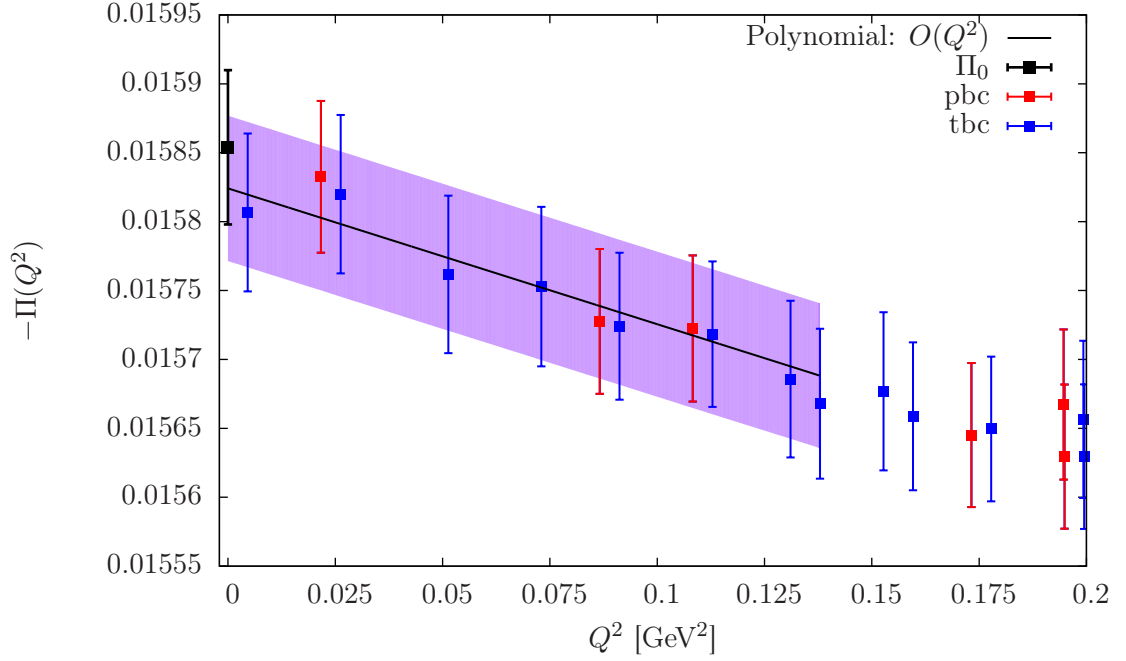


FIGURE 4.10: We use polynomials of $O(Q^2)$ to describe the momentum dependence of the VPF for the charm-quark contribution, cf. eq. (4.24). The example shows the fit we use on G8 with $Q_{\text{cut}}^2 \approx 0.14 \text{ GeV}^2$, and $\chi_{\text{corr}}^2/\text{dof}=1.1$. The time moment Π_0 is shown as a reference only and not included in the fit.

Ens.	Q_{cut}^2	N	poly. $O(Q^2)$			Padé [1,1]		
			$\chi_{\text{corr}}^2/\text{dof}$	a_{μ}^{HLO}	%	$\chi_{\text{corr}}^2/\text{dof}$	a_{μ}^{HLO}	%
A3	0.2215	5	0.25	7.58(35)	4.6	0.38	7.58(35)	4.6
A4	0.2215	5	0.05	7.08(28)	4.0	0.08	7.08(28)	4.0
A5	0.3967	10	1.22	6.71(12)	1.8	1.30	7.20(57)	7.9
B6	0.1461	8	0.83	7.16(34)	4.7	0.99	7.16(34)	4.7
E5	0.3640	7	0.83	7.94(10)	1.3	1.04	7.94(10)	1.3
F6	0.1924	8	0.93	7.82(18)	2.3	1.12	7.82(18)	2.3
F7	0.2451	11	1.35	8.10(14)	1.7	1.36	8.65(51)	5.9
G8	0.1379	11	1.11	8.10(28)	3.5	1.23	8.50(73)	8.6
N5	0.2821	6	0.54	9.37(24)	2.6	0.72	9.37(24)	2.6
N6	0.3527	8	0.86	9.41(09)	1.0	0.87	9.92(54)	5.4
O7	0.2528	11	0.38	9.35(21)	2.2	0.40	9.73(61)	6.3

TABLE 4.5: For the charm-quark contribution we use a polynomial of $O(Q^2)$ to describe the momentum dependence of the VPF as we found that fits with the Padé ansatz [2,1] suffer from numerical instabilities. We show a_{μ}^{HLO} in units of 10^{10} and Q_{cut}^2 in GeV^2 .

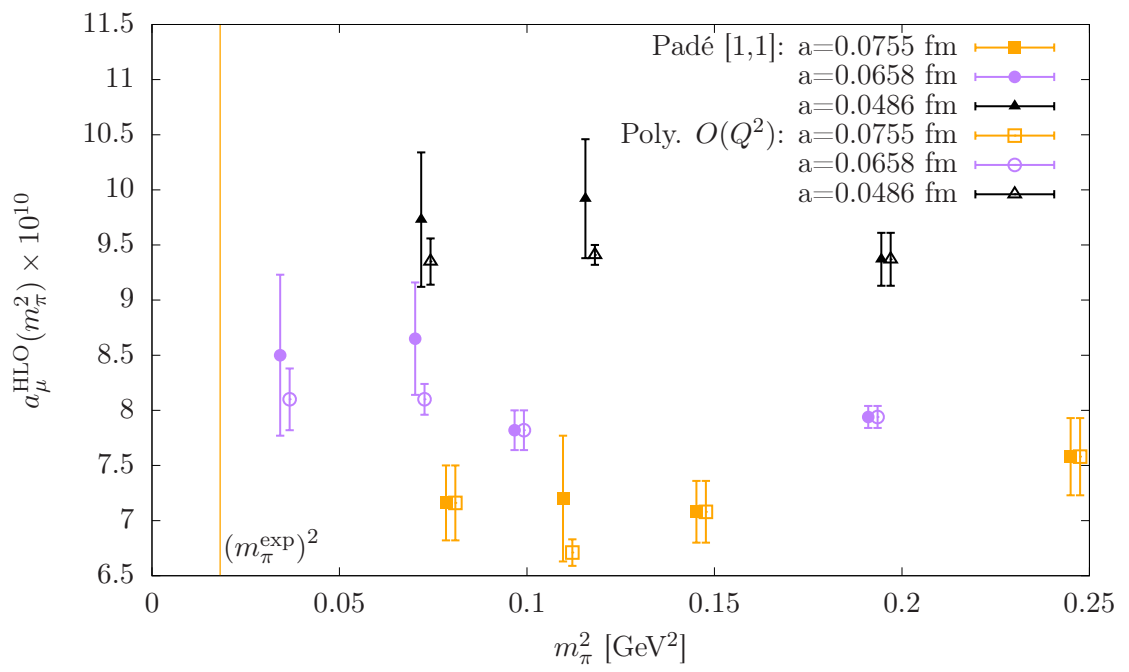


FIGURE 4.11: For the charm-quark we compare the results for a_μ^{HLO} from a polynomial fit ansatz of $O(Q^2)$ (open symbols, shifted to the right) and Padé [1,1] (filled symbols) with $Q_{\text{cut}}^2 < 0.5$ GeV².

4.3.2 The extraction of a_μ^{HLO} via time moments

For the second method we investigated the use of time moments to describe the VPF in the low Q^2 regime [120]. The VPF can be described by a Taylor expansion in the vicinity of $Q^2 = 0$,

$$\Pi(Q^2) = \Pi_0 + \sum_{j=1}^{\infty} Q^{2j} \Pi_j. \quad (4.25)$$

Restricting the VPF to the spatial vector-currents and using only momenta with $Q = (\omega, \vec{0})$ modifies eq. (2.1) to

$$\Pi_{kk}(\omega^2) = a^4 \sum_t e^{i\omega t} \sum_{\vec{x}} \langle V_k(t, \vec{x}) V_k(0) \rangle, \quad (4.26)$$

where we also switched from continuous coordinates to discrete lattice coordinates. Furthermore, we observe that for this special case eq. (2.15) is reduced to

$$\Pi_{kk}(\omega^2) = -\omega^2 \Pi(\omega^2). \quad (4.27)$$

Thus the spatially summed vector-correlator,

$$G(t) = -a^3 \sum_{\vec{x}} \langle V_k(t, \vec{x}) V_k(0) \rangle, \quad (4.28)$$

can be related to the derivative of the renormalized VPF,

$$G_{2n} = a \sum_t t^{2n} G(t) = (-1)^n \frac{\partial^{2n}}{\partial \omega^{2n}} \left\{ \omega^2 \hat{\Pi}(\omega^2) \right\}_{\omega=0}. \quad (4.29)$$

With this relation we find the expansion coefficients

$$\Pi(Q^2 = 0) = \Pi_0 = -\frac{1}{2} G_2, \quad \Pi_j = (-1)^{j+1} \frac{G_{2j+2}}{(2+j)!}, \quad (4.30)$$

of the Taylor expansion in eq. (4.25). In this work we use time-reflection in the sum of the spatial-vector correlator and we average over the three spatial components. With these changes the definition in eq. (4.29) changes to

$$G_{2n} = \frac{a^4}{3} \sum_{i=1}^3 \sum_{t=0}^{T/2} \sum_{\vec{x}} t^{2n} \left(\left\langle V_i(\vec{x}, t) V_i(\vec{0}, 0) \right\rangle + \left\langle V_i(\vec{x}, T-t) V_i(\vec{0}, 0) \right\rangle \right). \quad (4.31)$$

For the light-quark contribution we observe that sum over t adds only noise to the result after a short extent in lattice time. On our most chiral ensemble (G8) this effect is particularly severe, such that for $j \geq 2$ the time moments loose precision rapidly as the

sum runs to larger t . We can improve the precision by truncating the sum in eq. (4.31) and replacing the correlator data by the amplitude of the correlation function and the mass of the vector channel for $t > t_{\text{trunc}}$ [121] to model the asymptotic behaviour. From eq. (1.86) we know that we can use the vector mass m_V and amplitude A of the ground state to approximate the vector correlation function for sufficiently large times, where excited states are suppressed.

In our calculation we use the upper bound of the fit range used in [122] for the amplitude as t_{trunc} . In [122] we used fits with a single exponential to determine the vector mass m_V and the amplitude A from the respective correlation functions. For the light-quark contribution the vector mass was determined using a correlation function with standard Gaussian smearing [53] for the quark propagators and the link variables were APE-smearred in the spatial directions. Smearing was applied at the source and the sink of the correlation functions. For the vector masses of the strange- and charm-quark contribution and the amplitudes for all three flavours we use the data of the mixed vector correlator for which we listed the statistics in table 2.3.

The expression in eq. (4.31) including the approximation for $t > t_{\text{trunc}}$ for the summation then reads

$$\begin{aligned} \tilde{G}_{2n} = & \frac{a^4}{3} \sum_{i=1}^3 \sum_{t=0}^{t_{\text{trunc}}} \sum_{\vec{x}} t^{2n} \left(\langle V_i(\vec{x}, t) V_i(\vec{0}, 0) \rangle + \langle V_i(\vec{x}, T-t) V_i(\vec{0}, 0) \rangle \right) \\ & + a^4 \int_{t_{\text{trunc}}}^{\infty} 2t^{2n} A e^{-m_V t} dt, \end{aligned} \quad (4.32)$$

with this definition we redefine the time moments as

$$\Pi_0 = -\frac{1}{2} \tilde{G}_2, \quad \Pi_j = (-1)^{j+1} \frac{\tilde{G}_{2j+2}}{(2j+2)!}. \quad (4.33)$$

In table 4.6 we collect m_V and A for all ensembles and flavours, as well as the values for t_{trunc} used in this calculation. We vary the choice of $t_{\text{trunc}/a}$ by ± 1 to study systematic effects. In figure 4.12 we show the behaviour of the vector masses for the light-quark contribution with respect to the pion mass. As a reference the physical ρ mass is shown in purple.

In table 4.7 we collect the results for the first 5 time moments in lattice units for the light-quark contribution. The results for the strange and the charm-quark contribution are listed in the tables C.70, C.71. We find that with increasing t_{trunc} the error on the moments grow, as expected, and that the central values shift by small amounts within the statistical errors. To test if the sums in equations (4.31,4.32) are convergent we plot a part of the sum up to a t_{cut} which we then run from 0 to T of the lattice for eq. (4.31) and from $t_{\text{cut}} = t_{\text{trunc}}$ to $t_{\text{cut}}/a = 200$ for eq. (4.32). We show the results for Π_0 , Π_1 , and Π_2 in figures 4.13 and 4.14 for G8 for the light-quark contribution. The higher

Ens.	t_{trunc}/a	ud		s		c	
		am_V	A	am_V	A	am_V	A
A3	15	0.3937(29)	0.00272(14)	0.4399(22)	0.00345(8)	1.1719(6)	0.01146(10)
A4	15	0.3620(31)	0.00229(12)	0.4291(15)	0.00317(5)	1.1816(5)	0.01125(7)
A5	15	0.3491(41)	0.00189(19)	0.4259(26)	0.00300(9)	1.1848(7)	0.01102(11)
B6	15	0.3263(82)	0.00154(19)	0.4133(22)	0.00263(8)	1.1831(8)	0.01013(12)
E5	21	0.3208(29)	0.00139(9)	0.3704(13)	0.00198(3)	1.0264(3)	0.00766(4)
F6	21	0.2928(38)	0.00112(10)	0.3624(17)	0.00187(5)	1.0295(5)	0.00753(7)
F7	21	0.2780(49)	0.00114(13)	0.3546(18)	0.00170(4)	1.0272(5)	0.00742(7)
G8	20	0.2579(39)	0.00075(7)	0.3503(20)	0.00163(4)	1.0280(6)	0.00743(7)
N5	24	0.2331(27)	0.00052(3)	0.2727(15)	0.00074(2)	0.7628(3)	0.00360(3)
N6	24	0.2244(28)	0.00051(4)	0.2710(9)	0.00078(1)	0.7611(3)	0.00365(2)
O7	24	0.2173(77)	0.00051(9)	0.2664(17)	0.00073(2)	0.7621(5)	0.00355(4)

TABLE 4.6: Vector masses and amplitudes for the light-, strange-, and charm-quark contribution and the t_{trunc} used in the estimate for the time moments, all in lattice units. A does not include Z_V .

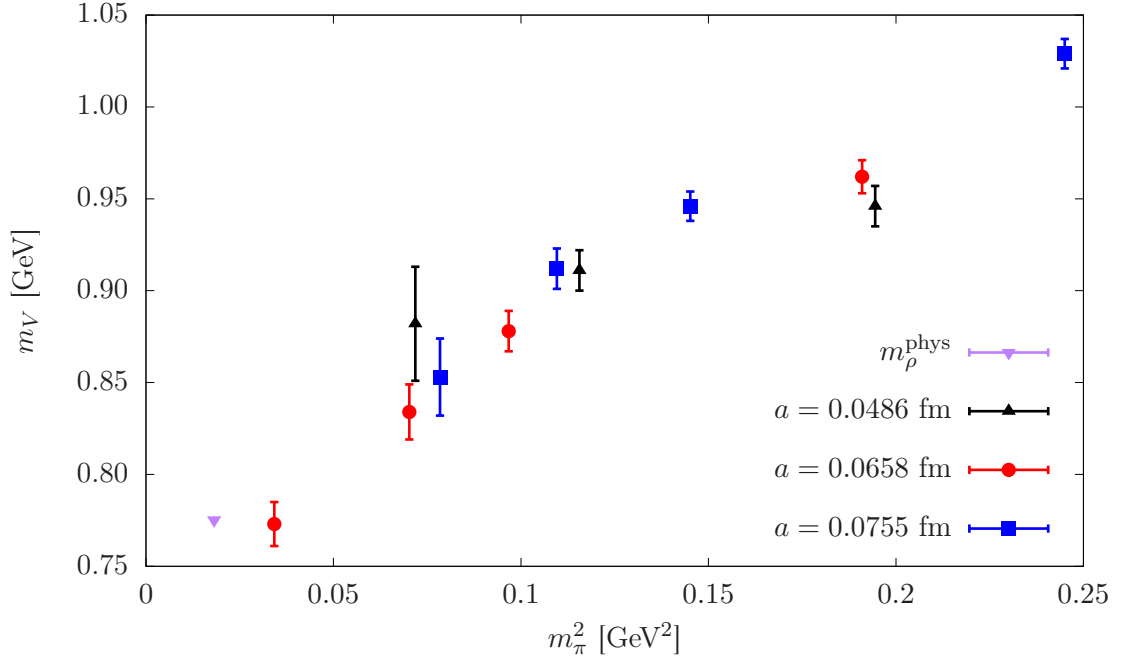


FIGURE 4.12: Plot of the chiral behaviour of the light vector masses. In purple we show the physical ρ mass as a reference.

moments for the light-quark contribution are shown in figures C.1, C.2. The results of this test for the strange and the charm-quark contribution are collected in C.2.2 and C.2.3, respectively. These tests show that within statistical errors the asymptotic behaviour is well described by a single exponential ansatz for the correlation function in the sum and yields a convergent result. The black points, referring to eq. (4.31), show that for this approach we add only noise for $\Pi_{i \geq 2}$ for the light-quark contribution above $t/a \gtrsim 30$. The exponential ansatz improves the statistical error for all considered moments by a large margin for the light-quark contribution. For the strange-quark

Ens.	t/a	Π_0	Π_1	Π_2	Π_3	Π_4
A3	$t_{\text{trunc}} - 1$	-0.09507(44)	0.3667(23)	-2.155(17)	13.53(24)	-86.3(2.7)
	$t_{\text{trunc}} \pm 0$	-0.09489(46)	0.3654(28)	-2.156(20)	13.56(24)	-86.4(2.7)
	$t_{\text{trunc}} + 1$	-0.09477(48)	0.3645(32)	-2.159(23)	13.61(25)	-86.6(2.7)
A4	$t_{\text{trunc}} - 1$	-0.10131(45)	0.4595(31)	-3.229(36)	24.14(60)	-182.8(7.6)
	$t_{\text{trunc}} \pm 0$	-0.10112(48)	0.4585(38)	-3.235(39)	24.19(61)	-183.0(7.6)
	$t_{\text{trunc}} + 1$	-0.10098(51)	0.4577(44)	-3.241(43)	24.26(61)	-183.3(7.6)
A5	$t_{\text{trunc}} - 1$	-0.10217(83)	0.4718(81)	-3.460(43)	27.56(15)	-224.2(5.6)
	$t_{\text{trunc}} \pm 0$	-0.10199(89)	0.4709(89)	-3.466(47)	27.62(19)	-224.4(5.7)
	$t_{\text{trunc}} + 1$	-0.10186(98)	0.4703(107)	-3.473(59)	27.69(27)	-224.7(5.8)
B6	$t_{\text{trunc}} - 1$	-0.10590(50)	0.5420(108)	-4.509(255)	41.04(4.25)	-382.4(58.9)
	$t_{\text{trunc}} \pm 0$	-0.10571(55)	0.5413(114)	-4.517(257)	41.11(4.26)	-382.7(58.8)
	$t_{\text{trunc}} + 1$	-0.10554(59)	0.5400(119)	-4.521(258)	41.18(4.27)	-382.9(58.8)
E5	$t_{\text{trunc}} - 1$	-0.10242(29)	0.5332(38)	-4.649(47)	43.85(88)	-419.9(14.9)
	$t_{\text{trunc}} \pm 0$	-0.10236(30)	0.5320(43)	-4.644(53)	43.90(90)	-420.4(15.0)
	$t_{\text{trunc}} + 1$	-0.10230(31)	0.5308(48)	-4.637(60)	43.92(93)	-420.9(15.1)
F6	$t_{\text{trunc}} - 1$	-0.10947(51)	0.6742(70)	-7.039(93)	79.68(2.23)	-918.3(46.6)
	$t_{\text{trunc}} \pm 0$	-0.10939(53)	0.6727(83)	-7.035(109)	79.76(2.29)	-919.1(46.9)
	$t_{\text{trunc}} + 1$	-0.10932(55)	0.6716(97)	-7.035(128)	79.87(2.36)	-920.2(46.9)
F7	$t_{\text{trunc}} - 1$	-0.11409(76)	0.8218(121)	-10.027(223)	128.56(6.03)	-1654.4(130.6)
	$t_{\text{trunc}} \pm 0$	-0.11403(81)	0.8215(144)	-10.046(247)	128.84(6.14)	-1656.2(130.9)
	$t_{\text{trunc}} + 1$	-0.11394(86)	0.8200(168)	-10.045(273)	128.99(6.20)	-1657.7(131.6)
G8	$t_{\text{trunc}} - 1$	-0.11576(51)	0.8626(90)	-11.408(265)	165.97(8.04)	-2472.9(194.1)
	$t_{\text{trunc}} \pm 0$	-0.11565(55)	0.8613(107)	-11.413(276)	166.14(8.10)	-2474.0(194.1)
	$t_{\text{trunc}} + 1$	-0.11551(60)	0.8583(125)	-11.394(291)	166.15(8.15)	-2474.6(193.9)
N5	$t_{\text{trunc}} - 1$	-0.11269(45)	0.9755(83)	-15.957(295)	286.15(10.72)	-5225.4(310.8)
	$t_{\text{trunc}} \pm 0$	-0.11263(46)	0.9745(90)	-15.964(303)	286.44(10.73)	-5228.3(311.0)
	$t_{\text{trunc}} + 1$	-0.11259(47)	0.9738(97)	-15.975(310)	286.79(10.73)	-5231.9(311.3)
N6	$t_{\text{trunc}} - 1$	-0.11759(42)	1.1350(111)	-20.379(463)	395.93(17.50)	-7808.9(536.0)
	$t_{\text{trunc}} \pm 0$	-0.11753(44)	1.1340(120)	-20.391(471)	396.30(17.55)	-7812.5(536.3)
	$t_{\text{trunc}} + 1$	-0.11747(45)	1.1330(131)	-20.401(478)	396.70(17.57)	-7816.8(536.1)
O7	$t_{\text{trunc}} - 1$	-0.12147(52)	1.2948(384)	-25.341(2.013)	529.25(76.67)	-11161.3(2412.6)
	$t_{\text{trunc}} \pm 0$	-0.12139(54)	1.2931(387)	-25.346(2.010)	529.61(76.60)	-11165.1(2412.4)
	$t_{\text{trunc}} + 1$	-0.12132(55)	1.2918(388)	-25.355(2.006)	530.04(76.49)	-11169.9(2412.2)

TABLE 4.7: Results for the time moments of equations (4.32, 4.33) for the light-quark contribution in lattice units. The precision for each time moment is shown as percentage. t_{trunc} refers to the values listed in table 4.6.

contribution we find that there is still an improvement for $\Pi_{i \geq 2}$. In the case of the charm-quark we do not find a difference between the two approaches with respect to the statistical error, though we observe a small shift within errors for the central values. For convenience we treat all flavours the same way and use eq. (4.32) to estimate the time moments in this study.

We can improve the radius of convergence of eq. (4.25) by using Padé approximants,

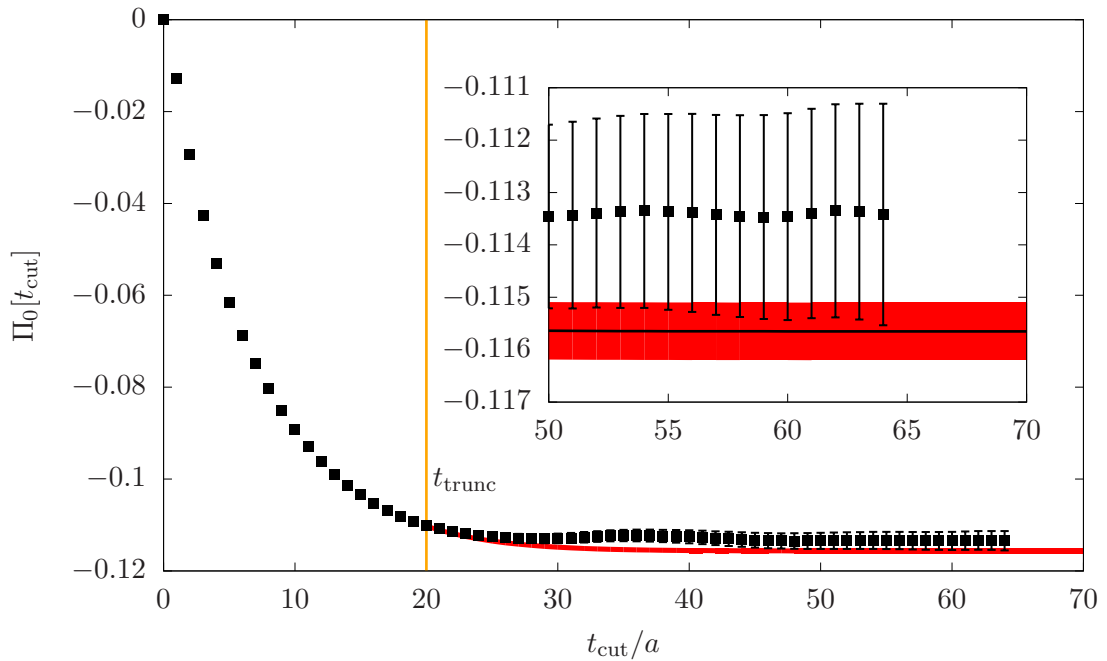


FIGURE 4.13: We test the convergence of equations (4.31, 4.32) by cutting the sum at t_{cut} for Π_0 on G8 ($T/a=128$) for the light-quark contribution. We show the result of eq. (4.31) as black points, the result of eq. (4.32) is shown as a red curve.

which read with inserted time moments:

$$\hat{\Pi}_{[1,1]}^{\text{mom}} = \frac{\Pi_1^2 Q^2}{\Pi_1 - \Pi_2 Q^2}, \quad (4.34)$$

$$\hat{\Pi}_{[2,1]}^{\text{mom}} = \frac{\Pi_1 \Pi_2 Q^2 + (\Pi_2^2 - \Pi_1 \Pi_3) Q^4}{\Pi_2 - \Pi_3 Q^2}. \quad (4.35)$$

This serves as an alternative for determining $\Pi(Q^2)$ in the low Q^2 regime from a direct fit to the VPF data, as discussed in section 4.3.1. We use the first time moment $\Pi_0 = \Pi(Q^2 = 0)$ to renormalize the data to perform the numerical integration for $Q^2 > Q_{\text{cut}}^2$. We determine Q_{cut}^2 for this method by minimizing the difference of the respective Padé approximant with the data,

$$Q_{\text{cut}}^2 = \min_{0.1 < Q^2 < 0.5 \text{ GeV}^2} \left| \hat{\Pi}_{[n,m]}^{\text{mom}} - \left(\Pi^{\text{data}}(Q^2) - \Pi_0 \right) \right|. \quad (4.36)$$

The lower bound of the interval for the search of the Q_{cut}^2 has to be sufficiently large enough to have a sufficient number of accurate measurements. The upper bound of this interval has to be small enough to ensure that the time moments still give a reliable estimate of the VPF. As a reference only we also compute the correlated χ^2/dof for the Padé ansatz with time moments. Although this could in principle also be used as a selection criterion for Q_{cut}^2 , we find that $\chi_{\text{corr}}^2/\text{dof}$ fluctuates while Q_{cut}^2 is varied due to strong correlations in the data. Thus the smoothness criterion in eq. (4.36) yields

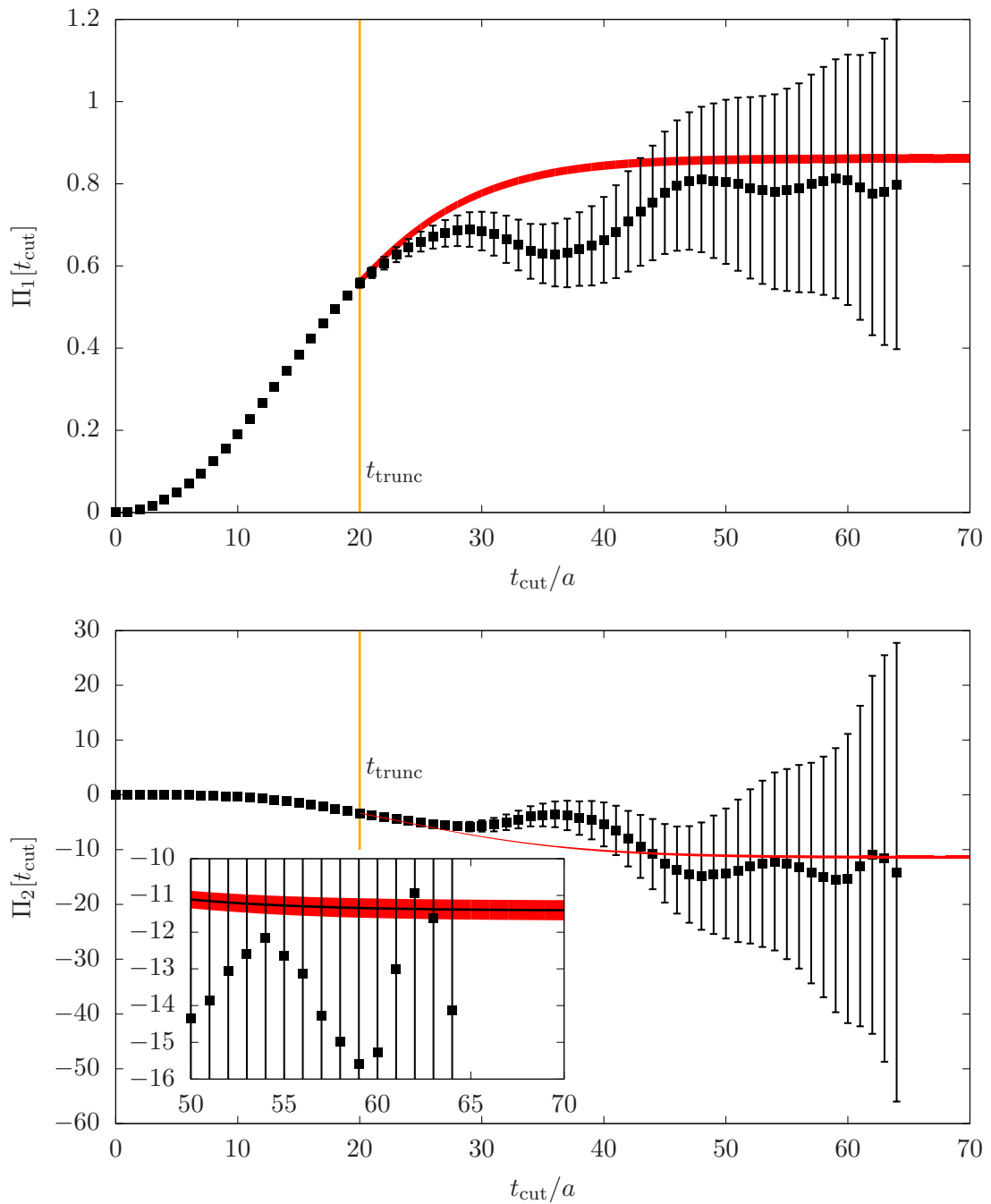


FIGURE 4.14: Test of the convergence for equations (4.31, 4.32), where we cut the sum at t_{cut} for Π_1 (top) and Π_2 (bottom) on G8 ($T/a=128$) for the light-quark contribution. The results of eq. (4.31) are shown as black points, the results for (4.32) are shown as a red curve.

more stable results. As an example we show the result for Padé [1,1] for the light-quark contribution on G8 in figure 4.15.

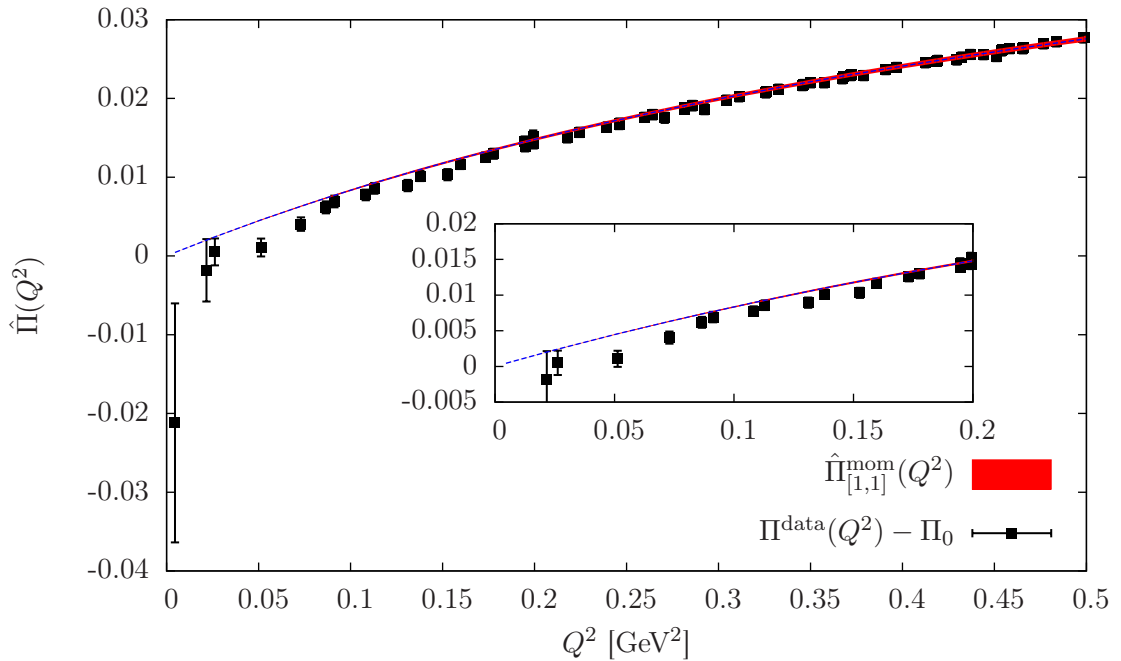


FIGURE 4.15: Example of the renormalized VPF on G8 for the light-quark contribution. The data are renormalized by the time moment Π_0 and the function shown is the Padé [1,1], where the red band indicates the statistical error and the dashed blue line refers to the central value. The vertical dispersion between the data points and the Padé curve at low Q^2 signals a difference in the value of the additive renormalization constant $\Pi(0)$ among these two methods. We stress that this behaviour is not observed on all ensembles. We find $Q_{\text{cut}}^2 = 0.1947 \text{ GeV}^2$ and $\chi_{\text{corr}}^2/\text{dof}=1.54$, note that the latter is only computed as a reference and is not the result of any minimization.

4.3.2.1 The light-quark contribution

In the tables 4.8 and 4.9 we show the results for a_μ^{HLO} computed from time moments for the light-quark contribution for Padé [1,1] and [2,1], respectively. We observe that the difference between Padé [1,1] and [2,1] are negligible. For the E5, N5, and N6 ensembles we find that the $\chi_{\text{corr}}^2/\text{dof}$ is relatively large, which is explained by an offset between Π_0 and the lowest Q^2 -points. The results for Q_{cut}^2 shown refer to the minimization in eq. (4.36). We reach a precision of 1-3%. The m_V -rescaled data show, as expected, a much milder pion mass dependence. Because of the inclusion of the error of the vector mass, the precision of the m_V -rescaled results deteriorates to ~ 1.5 -4%. Results for the different values of t_{trunc} are compared in figure 4.16. We observe that the central values shift monotonously down with increasing t_{trunc} . But this shift is well within the statistical errors, which grow with growing t_{trunc} . In figure 4.17 we show the pion mass dependence of the results without rescaling.

Ens.	Q_{cut}^2	$\chi_{\text{corr}}^2/\text{dof}$	N	a_{μ}^{HLO}	%	$a_{\mu}^{\text{HLO}}(m_V\text{-rescaled})$	%
$t_{\text{trunc}} - 1$							
A3	0.4625	2.96	11	286.69(1.96)	0.7	484.90(7.17)	1.5
A4	0.1557	8.11	3	355.48(3.64)	1.0	514.29(9.49)	1.8
A5	0.2765	1.19	6	361.08(6.72)	1.9	487.73(17.81)	3.7
B6	0.4963	0.84	41	411.20(7.28)	1.8	490.34(14.77)	3.0
E5	0.4506	7.18	8	319.43(2.27)	0.7	476.53(8.14)	1.7
F6	0.4698	0.72	25	397.82(4.21)	1.1	500.78(12.74)	2.5
F7	0.4804	0.79	26	478.57(7.14)	1.5	546.86(17.59)	3.2
G8	0.4186	1.40	48	498.51(5.10)	1.0	496.37(12.77)	2.6
N5	0.2378	4.68	4	327.57(3.11)	0.9	473.96(9.13)	1.9
N6	0.4973	8.94	11	377.59(3.53)	0.9	508.87(9.43)	1.9
O7	0.3653	0.91	17	427.59(11.30)	2.6	542.61(21.82)	4.0
$t_{\text{trunc}} \pm 0$							
A3	0.2625	2.31	5	285.69(2.56)	0.9	483.22(7.67)	1.6
A4	0.2215	4.45	4	353.55(3.40)	1.0	511.11(8.67)	1.7
A5	0.2765	1.24	6	360.17(7.45)	2.1	486.42(17.46)	3.6
B6	0.1523	1.93	8	410.16(8.47)	2.1	489.00(14.84)	3.0
E5	0.4506	7.18	8	318.69(2.55)	0.8	475.41(8.15)	1.7
F6	0.4698	0.76	25	396.86(4.92)	1.2	499.55(12.79)	2.6
F7	0.3456	1.11	15	478.42(8.51)	1.8	546.68(17.94)	3.3
G8	0.1947	1.54	15	496.98(6.53)	1.3	494.84(12.99)	2.6
N5	0.2378	4.67	4	327.16(3.34)	1.0	473.32(9.20)	1.9
N6	0.4973	9.08	11	377.20(3.87)	1.0	508.33(9.55)	1.9
O7	0.3653	0.90	17	426.97(11.41)	2.7	541.81(21.86)	4.0
$t_{\text{trunc}} + 1$							
A3	0.3423	1.61	8	284.86(2.72)	1.0	481.68(7.51)	1.6
A4	0.4840	2.70	12	352.35(3.49)	1.0	509.10(8.32)	1.6
A5	0.2765	1.27	6	359.58(8.75)	2.4	485.56(17.97)	3.7
B6	0.3942	1.04	30	409.37(8.22)	2.0	488.10(14.79)	3.0
E5	0.4506	7.20	8	317.92(2.83)	0.9	474.26(8.28)	1.7
F6	0.4698	0.79	25	396.18(5.71)	1.4	498.69(13.05)	2.6
F7	0.3456	1.07	15	477.43(9.87)	2.1	545.55(18.47)	3.4
G8	0.4192	1.64	49	495.84(7.14)	1.4	493.70(13.14)	2.7
N5	0.2378	4.67	4	326.86(3.57)	1.1	472.86(9.30)	2.0
N6	0.4973	9.23	11	376.84(4.20)	1.1	507.83(9.74)	1.9
O7	0.3653	0.89	17	426.47(11.46)	2.7	541.16(22.07)	4.1

TABLE 4.8: Results for a_{μ}^{HLO} in units of 10^{10} for Padé [1,1] for the light-quark contribution. Q_{cut}^2 is shown in GeV^2 and $\chi_{\text{corr}}^2/\text{dof}$ is computed as a reference but is not the result of any minimization.

4.3.2.2 The strange-quark contribution

We collect the results for a_{μ}^{HLO} for the strange-quark contribution in table 4.10. We observe a similar offset $\Pi(Q^2 = 0)$ on the ensembles B6, E5, N5, and N6 as for the light-quark contribution, which leads to a larger $\chi_{\text{corr}}^2/\text{dof}$. For the strange-quark we reach a precision of 0.8-1.6%. The pion mass dependence is, as expected, milder than for the

Ens.	Q_{cut}^2	$\chi_{\text{corr}}^2/\text{dof}$	N	a_{μ}^{HLO}	%	$a_{\mu}^{\text{HLO}}(m_V\text{-rescaled})$	%
$t_{\text{trunc}} - 1$							
A3	0.3283	2.23	7	286.86(2.09)	0.7	485.31(7.33)	1.5
A4	0.1557	-	3	355.53(3.64)	1.0	514.37(9.48)	1.8
A5	0.2765	1.53	6	361.23(6.71)	1.9	487.97(17.78)	3.6
B6	0.1461	2.26	7	411.43(8.04)	2.0	490.64(15.01)	3.1
E5	0.3640	12.64	6	319.47(2.30)	0.7	476.58(8.13)	1.7
F6	0.3538	1.06	17	397.99(4.28)	1.1	501.02(12.76)	2.5
F7	0.3078	1.03	13	478.90(7.34)	1.5	547.28(17.68)	3.2
G8	0.1947	1.55	15	498.23(5.59)	1.1	496.09(12.86)	2.6
N5	0.2378	9.46	4	327.68(3.11)	0.9	474.16(9.13)	1.9
N6	0.2971	12.77	6	377.27(3.69)	1.0	508.26(9.47)	1.9
O7	0.3653	1.43	17	427.81(11.36)	2.7	542.94(21.76)	4.0
$t_{\text{trunc}} \pm 0$							
A3	0.3423	2.58	8	285.69(2.38)	0.8	483.22(7.33)	1.5
A4	0.4182	4.22	10	353.26(3.02)	0.9	510.54(8.19)	1.6
A5	0.2765	1.59	6	360.32(7.44)	2.1	486.66(17.43)	3.6
B6	0.1523	2.28	8	410.27(8.49)	2.1	489.14(14.82)	3.0
E5	0.4506	10.74	8	318.87(2.55)	0.8	475.77(8.13)	1.7
F6	0.3538	1.05	17	397.01(4.96)	1.2	499.78(12.78)	2.6
F7	0.3463	1.36	16	478.63(8.50)	1.8	546.96(17.88)	3.3
G8	0.1947	1.58	15	497.26(6.54)	1.3	495.12(12.97)	2.6
N5	0.2378	9.44	4	327.27(3.35)	1.0	473.52(9.19)	1.9
N6	0.2971	12.82	6	376.85(4.02)	1.1	507.68(9.60)	1.9
O7	0.3653	1.37	17	427.19(11.50)	2.7	542.14(21.80)	4.0
$t_{\text{trunc}} + 1$							
A3	0.2215	3.98	4	285.00(3.07)	1.1	482.00(8.15)	1.7
A4	0.3423	4.56	8	352.53(3.59)	1.0	509.44(8.45)	1.7
A5	0.2765	1.62	6	359.72(8.74)	2.4	485.79(17.93)	3.7
B6	0.2687	1.75	17	409.38(8.37)	2.0	488.10(14.82)	3.0
E5	0.4506	10.55	8	318.10(2.82)	0.9	474.63(8.26)	1.7
F6	0.3538	1.04	17	396.33(5.74)	1.4	498.91(13.07)	2.6
F7	0.4251	1.42	21	477.64(9.78)	2.0	545.81(18.34)	3.4
G8	0.1947	1.63	15	495.33(7.62)	1.5	493.20(13.31)	2.7
N5	0.2378	9.43	4	326.97(3.58)	1.1	473.05(9.28)	2.0
N6	0.2971	12.85	6	376.47(4.36)	1.2	507.14(9.81)	1.9
O7	0.3653	1.32	17	426.69(11.54)	2.7	541.49(22.01)	4.1

TABLE 4.9: Results for a_{μ}^{HLO} in units of 10^{10} for Padé [2,1] for the light-quark contribution. Q_{cut}^2 is shown in GeV^2 and $\chi_{\text{corr}}^2/\text{dof}$ is computed as a reference but is not the result of any minimization.

light-quark contribution. Lattice artefacts lead to a clearer separation of the results for the coarsest lattice spacing from the results for the intermediate and the finest lattice spacing. Figure 4.18 shows a comparison of the results for the different t_{trunc} used in the analysis. We observe that the variation has only some influence on the error, while the central values are compatible within errors. In figure 4.19 we show a_{μ}^{HLO} plotted versus the squared pion mass. Again, we observe that the difference between the results for

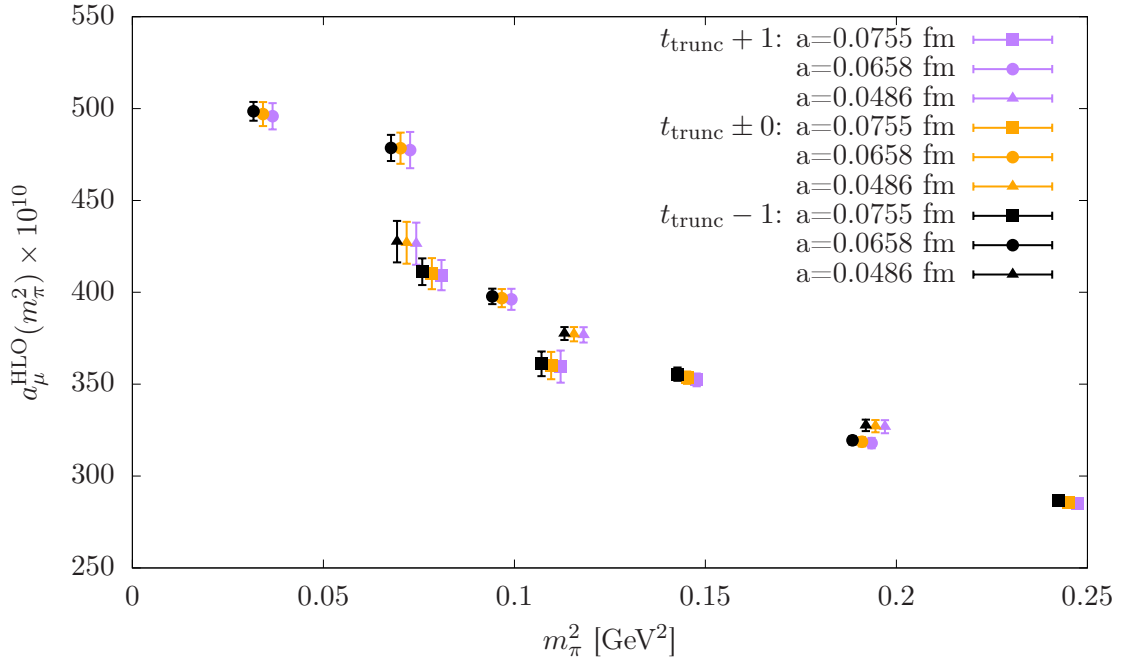


FIGURE 4.16: Results for a_μ^{HLO} for the light-quark contribution for Padé [1,1] at $t_{\text{trunc}} \pm \{0, 1\}$. To improve visibility of the different results we shift the results with $t_{\text{trunc}} - 1$ to the left and those with $t_{\text{trunc}} + 1$ to the right.

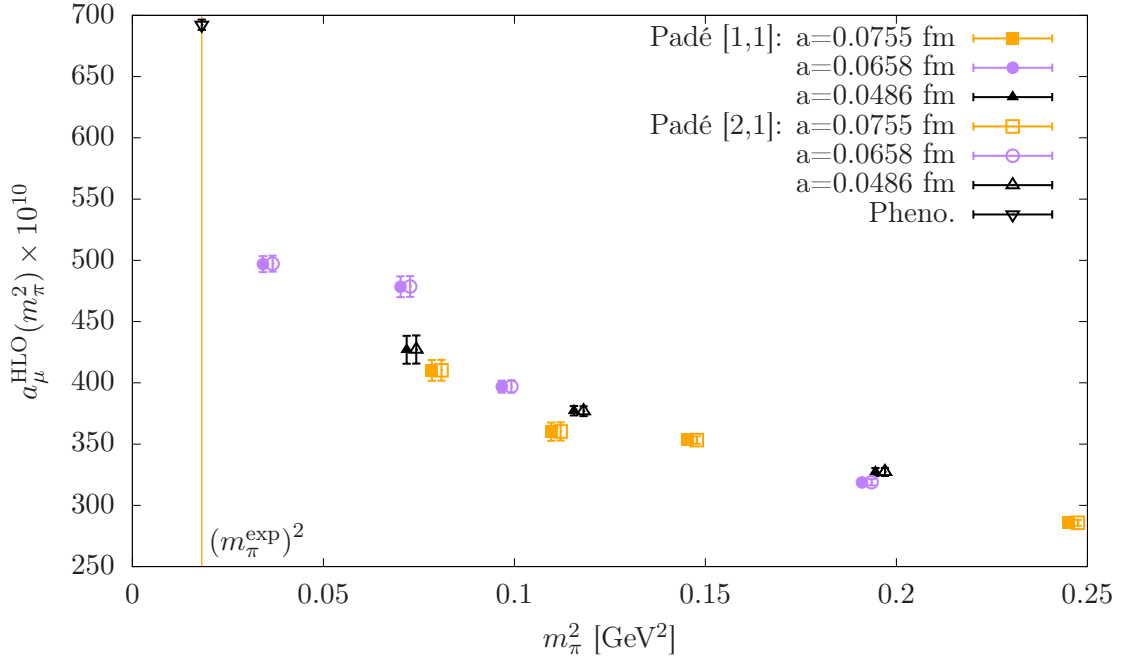


FIGURE 4.17: Results for a_μ^{HLO} from time moments for the light-quark contribution. The results for Padé [2,1] are shifted to the right for visibility due to the large overlap. The result from phenomenology is shown as a reference [1].

the different Padé ansätze is negligible.

Ens.	Padé [1,1]					Padé [2,1]				
	Q_{cut}^2	$\chi_{\text{corr}}^2/\text{dof}$	N	a_{μ}^{HLO}	%	Q_{cut}^2	$\chi_{\text{corr}}^2/\text{dof}$	N	a_{μ}^{HLO}	%
$t_{\text{trunc}} - 1$										
A3	0.4625	8.76	11	43.02(29)	0.7	0.3967	6.55	9	43.03(30)	0.7
A4	0.3967	10.56	9	44.87(25)	0.6	0.4182	16.06	10	44.88(24)	0.5
A5	0.2625	2.41	5	44.91(37)	0.8	0.1557	-	3	44.98(54)	1.2
B6	0.4487	2.81	35	46.73(25)	0.5	0.3942	5.11	30	46.75(26)	0.6
E5	0.4506	8.01	8	45.20(18)	0.4	0.3640	13.50	6	45.20(19)	0.4
F6	0.2328	1.24	9	47.53(36)	0.8	0.2328	1.66	9	47.54(36)	0.8
F7	0.2836	2.74	12	48.54(39)	0.8	0.2713	4.22	11	48.56(40)	0.8
G8	0.4655	0.61	58	49.63(39)	0.8	0.1995	3.47	18	49.64(51)	1.0
N5	0.1672	6.27	3	45.32(43)	0.9	0.1672	-	3	45.33(44)	1.0
N6	0.4267	1.79	9	47.57(23)	0.5	0.2378	7.18	4	47.57(27)	0.6
O7	0.3653	1.06	17	48.85(41)	0.8	0.3990	1.96	19	48.86(40)	0.8
$t_{\text{trunc}} \pm 0$										
A3	0.3283	3.76	7	42.84(32)	0.7	0.3423	6.58	8	42.84(32)	0.7
A4	0.3283	4.53	7	44.69(27)	0.6	0.2215	3.80	4	44.73(31)	0.7
A5	0.2625	2.20	5	44.72(39)	0.9	0.2625	3.57	5	44.73(39)	0.9
B6	0.3942	3.15	30	46.57(28)	0.6	0.2625	9.19	15	46.58(31)	0.7
E5	0.4506	7.72	8	45.10(19)	0.4	0.3640	13.28	6	45.10(19)	0.4
F6	0.2328	1.14	9	47.42(36)	0.8	0.1297	0.95	4	47.43(57)	1.2
F7	0.2451	2.78	10	48.44(42)	0.9	0.1924	2.10	7	48.45(48)	1.0
G8	0.1379	4.48	10	49.53(70)	1.4	0.2708	2.29	26	49.53(45)	0.9
N5	0.4973	2.07	11	45.14(28)	0.6	0.2378	6.29	4	45.16(34)	0.8
N6	0.4267	1.86	9	47.50(23)	0.5	0.2378	7.34	4	47.49(28)	0.6
O7	0.4509	0.97	22	48.77(40)	0.8	0.2528	1.28	10	48.79(47)	1.0
$t_{\text{trunc}} + 1$										
A3	0.2765	4.33	6	42.69(35)	0.8	0.2765	6.14	6	42.70(35)	0.8
A4	0.1557	2.56	3	44.65(43)	1.0	0.1557	-	3	44.65(43)	1.0
A5	0.2625	2.06	5	44.56(40)	0.9	0.2625	3.33	5	44.57(40)	0.9
B6	0.3318	3.66	22	46.40(31)	0.7	0.2154	8.67	12	46.41(36)	0.8
E5	0.4506	7.52	8	45.02(19)	0.4	0.3640	13.13	6	45.02(20)	0.4
F6	0.1297	0.49	4	47.32(57)	1.2	0.1297	0.98	4	47.33(57)	1.2
F7	0.1924	1.63	7	48.35(49)	1.0	0.2006	4.14	8	48.36(48)	1.0
G8	0.1732	3.10	13	49.40(59)	1.2	0.1732	3.74	13	49.40(59)	1.2
N5	0.4973	1.91	11	45.08(29)	0.6	0.2378	6.26	4	45.09(35)	0.8
N6	0.4267	1.93	9	47.44(24)	0.5	0.2378	7.49	4	47.42(28)	0.6
O7	0.2528	1.04	10	48.71(48)	1.0	0.2799	1.67	11	48.71(46)	0.9

TABLE 4.10: Results for a_{μ}^{HLO} in units of 10^{10} for Padé [1,1] and [2,1] for the strange quark contribution. Q_{cut}^2 is shown in GeV^2 and $\chi_{\text{corr}}^2/\text{dof}$ is computed as a reference but is not the result of any minimization.

4.3.2.3 The charm-quark contribution

The results for the charm-quark contribution are collected in table 4.11. The larger $\chi_{\text{corr}}^2/\text{dof}$ on A5 for Padé [1,1] and on N5 for Padé [2,1] are explained by the fact that the respective curves are systematically above the central values of the data. For the

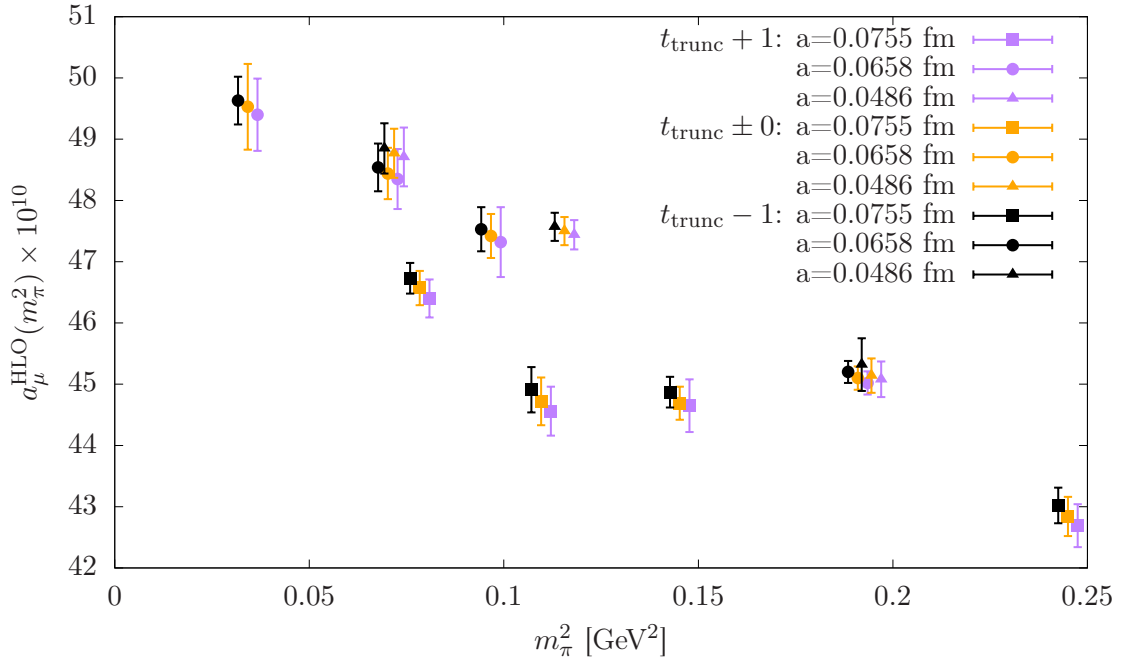


FIGURE 4.18: Results for a_μ^{HLO} for the strange-quark contribution for Padé [1,1] at $t_{\text{trunc}} \pm \{0, 1\}$. The results for $t_{\text{trunc}} - 1$ are shifted to the left, and $t_{\text{trunc}} + 1$ are shifted to the right for better visibility.

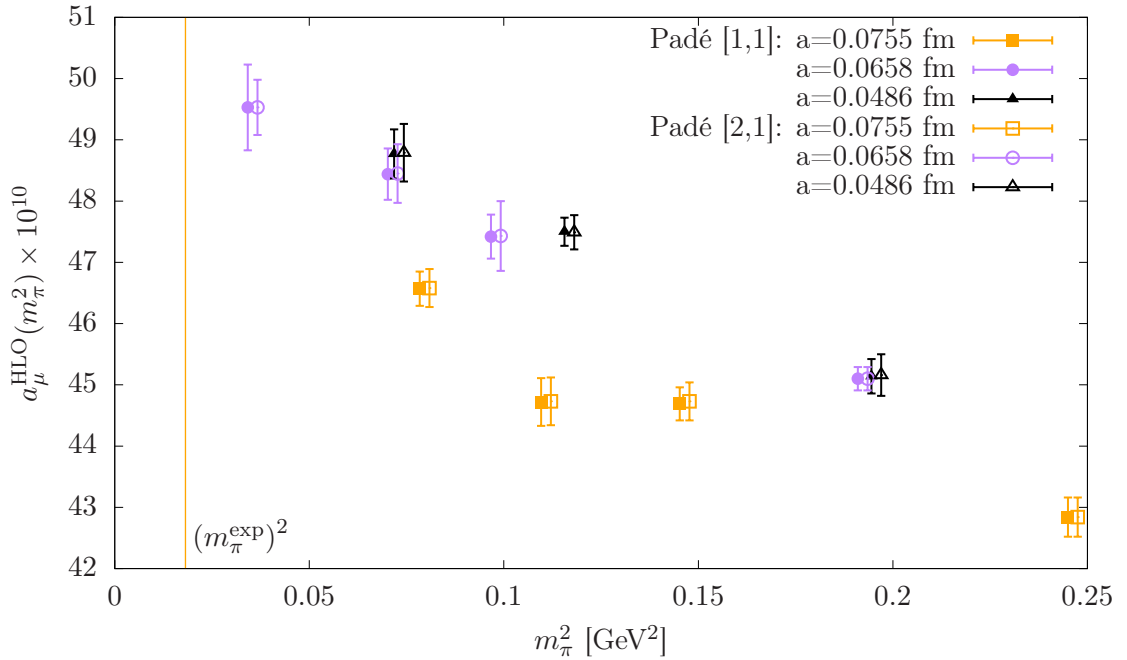


FIGURE 4.19: Results for a_μ^{HLO} for the strange-quark contribution for Padé [1,1] (filled symbols) and [2,1] (open symbols), the latter are shifted to the right.

results on E5 for both Padé ansätze and for A3, A4, and A5 for Padé [2,1] the Q_{cut}^2 chosen by the minimization of eq. (4.36) is too small to compute the corresponding $\chi_{\text{corr}}^2/\text{dof}$. We compare the results for the different t_{trunc} in figure 4.20 and find that this variation

has no impact on the results. In figure 4.21 we show a_μ^{HLO} plotted versus the pion mass squared. We observe that the pion mass dependence and the differences between the two Padé ansätze can be neglected. Lattice artefacts, on the other hand, are clearly visible since the data computed at different lattice spacings differ significantly.

Ens.	Padé [1,1]					Padé [2,1]				
	Q_{cut}^2	$\chi_{\text{corr}}^2/\text{dof}$	N	a_μ^{HLO}	%	Q_{cut}^2	$\chi_{\text{corr}}^2/\text{dof}$	N	a_μ^{HLO}	%
$t_{\text{trunc}} - 1$										
A3	0.1557	1.94	3	8.68(31)	3.6	0.1557	-	3	8.68(31)	3.6
A4	0.1557	0.99	3	8.30(25)	3.0	0.1557	-	3	8.30(25)	3.0
A5	0.1557	7.88	3	8.06(35)	4.3	0.1557	-	3	8.06(35)	4.3
B6	0.1231	2.75	6	7.93(57)	7.2	0.1231	3.66	6	7.93(57)	7.2
E5	0.1050	-	2	9.03(41)	4.5	0.1050	-	2	9.03(41)	4.5
F6	0.1297	0.55	4	8.75(41)	4.7	0.1297	1.10	4	8.75(41)	4.7
F7	0.1539	0.14	5	9.00(35)	3.9	0.1539	0.21	5	9.00(35)	3.9
G8	0.3043	0.95	31	9.08(13)	1.4	0.3043	0.99	31	9.08(13)	1.4
N5	0.2821	3.97	5	10.34(12)	1.2	0.2821	5.96	5	10.34(12)	1.2
N6	0.2378	1.26	4	10.41(13)	1.2	0.2378	2.52	4	10.41(13)	1.2
O7	0.1672	0.76	6	10.24(43)	4.2	0.1672	1.01	6	10.24(43)	4.2
$t_{\text{trunc}} \pm 0$										
A3	0.1557	1.94	3	8.68(31)	3.6	0.1557	-	3	8.68(31)	3.6
A4	0.1557	0.99	3	8.30(25)	3.0	0.1557	-	3	8.30(25)	3.0
A5	0.1557	7.87	3	8.06(35)	4.3	0.1557	-	3	8.06(35)	4.3
B6	0.1231	2.75	6	7.93(57)	7.2	0.1231	3.66	6	7.93(57)	7.2
E5	0.1050	-	2	9.03(41)	4.5	0.1050	-	2	9.03(41)	4.5
F6	0.1297	0.55	4	8.75(41)	4.7	0.1297	1.10	4	8.75(41)	4.7
F7	0.1539	0.14	5	9.00(35)	3.9	0.1539	0.21	5	9.00(35)	3.9
G8	0.3043	0.95	31	9.08(13)	1.4	0.3043	0.99	31	9.08(13)	1.4
N5	0.2821	3.97	5	10.34(12)	1.2	0.2821	5.96	5	10.34(12)	1.2
N6	0.2378	1.26	4	10.41(13)	1.2	0.2378	2.52	4	10.41(13)	1.2
O7	0.1672	0.76	6	10.24(43)	4.2	0.1672	1.01	6	10.24(43)	4.2
$t_{\text{trunc}} + 1$										
A3	0.1557	1.94	3	8.68(31)	3.6	0.1557	-	3	8.68(31)	3.6
A4	0.1557	0.99	3	8.30(25)	3.0	0.1557	-	3	8.30(25)	3.0
A5	0.1557	7.87	3	8.06(35)	4.3	0.1557	-	3	8.06(35)	4.3
B6	0.1231	2.75	6	7.93(57)	7.2	0.1231	3.66	6	7.93(57)	7.2
E5	0.1050	-	2	9.03(41)	4.5	0.1050	-	2	9.03(41)	4.5
F6	0.1297	0.55	4	8.75(41)	4.7	0.1297	1.10	4	8.75(41)	4.7
F7	0.1539	0.14	5	9.00(35)	3.9	0.1539	0.21	5	9.00(35)	3.9
G8	0.3043	0.95	31	9.08(13)	1.4	0.3043	0.99	31	9.08(13)	1.4
N5	0.2821	3.97	5	10.34(12)	1.2	0.2821	5.96	5	10.34(12)	1.2
N6	0.2378	1.26	4	10.41(13)	1.2	0.2378	2.52	4	10.41(13)	1.2
O7	0.1672	0.76	6	10.24(43)	4.2	0.1672	1.01	6	10.24(43)	4.2

TABLE 4.11: Results for a_μ^{HLO} in units of 10^{10} for Padé [1,1] and [2,1] for the charm-quark contribution. Q_{cut}^2 is shown in GeV^2 and $\chi_{\text{corr}}^2/\text{dof}$ is computed as a reference but is not the result of any minimization.

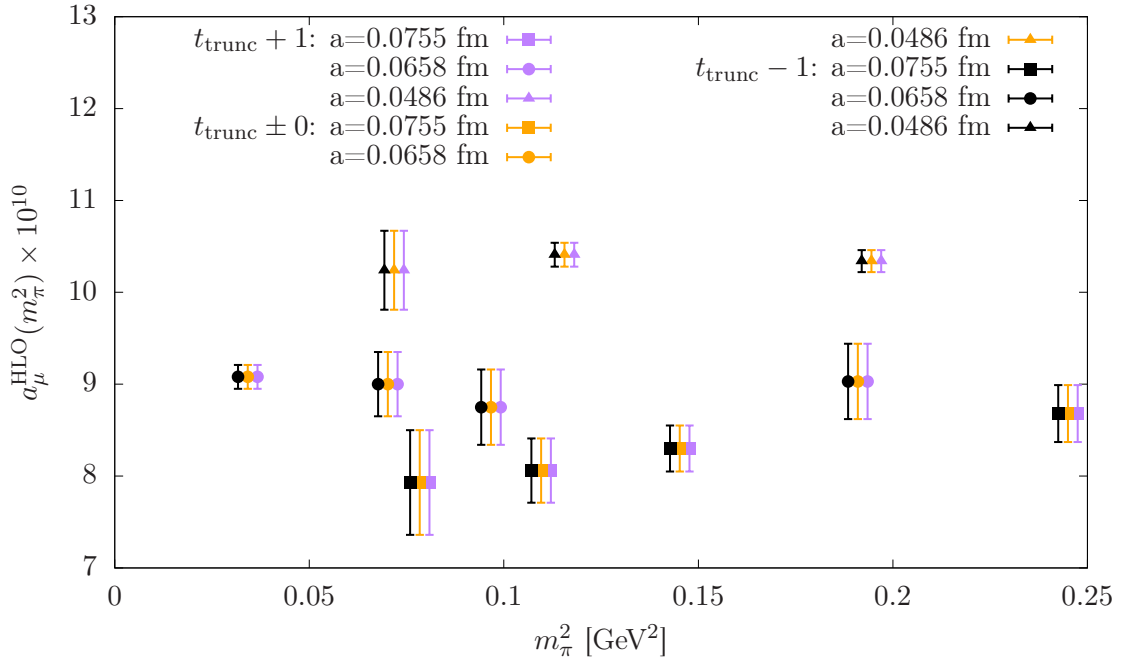


FIGURE 4.20: Results for a_μ^{HLO} for the charm-quark contribution for Padé [1,1] at $t_{\text{trunc}} \pm \{0, 1\}$. We shift the results with $t_{\text{trunc}} - 1$ to the left and the results with $t_{\text{trunc}} + 1$ to the right to improve visibility.

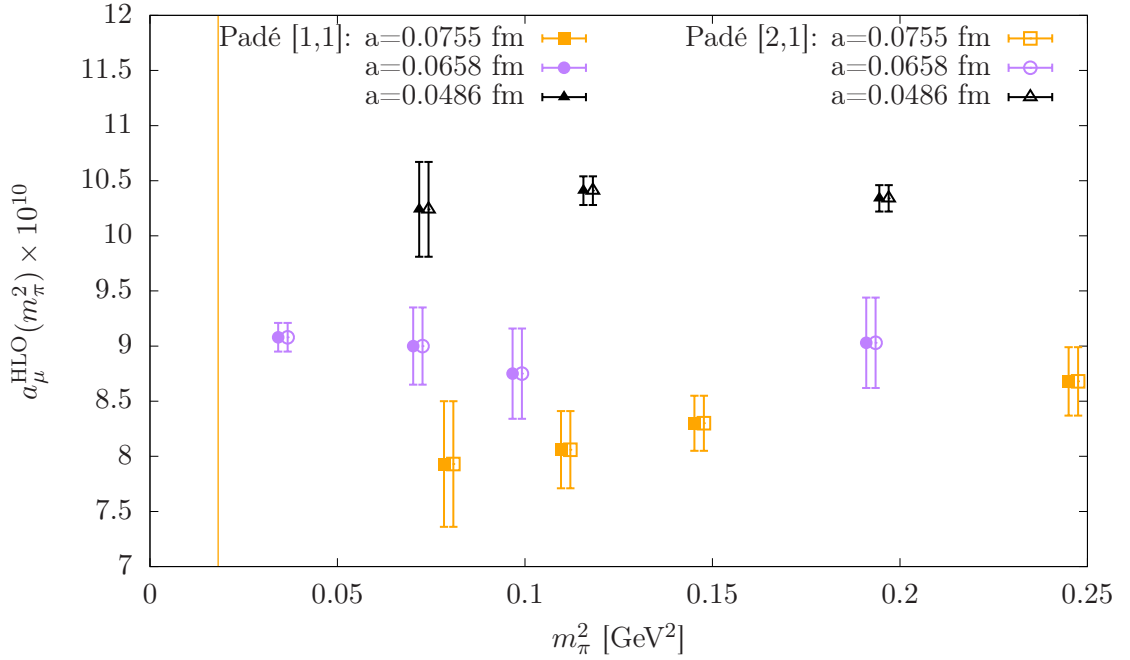


FIGURE 4.21: Results for a_μ^{HLO} for the charm-quark contribution for Padé [1,1] (filled symbols) and [2,1] (open symbols). The results for Padé [2,1] are shifted to the right.

4.3.3 The extrapolation to the physical point for a_μ^{HLO}

We extrapolate to the physical point of a_μ^{HLO} using uncorrelated fits, for which we use several ansätze. Which ansatz is used depends on the flavour, since the pion mass dependence varies with the flavour. The ansätze are

$$a_\mu^{\text{A},O(a)}(m_\pi^2, a) = b_0 + b_1 m_\pi^2 + b_2 m_\pi^2 \log(m_\pi^2) + b_3 a, \quad (4.37)$$

$$a_\mu^{\text{A}}(m_\pi^2) = b_0 + b_1 m_\pi^2 + b_2 m_\pi^2 \log(m_\pi^2), \quad (4.38)$$

$$a_\mu^{\text{B},O(a)}(m_\pi^2, a) = b_0 + b_1 m_\pi^2 + b_2 m_\pi^4 + b_3 a, \quad (4.39)$$

$$a_\mu^{\text{B}}(m_\pi^2) = b_0 + b_1 m_\pi^2 + b_2 m_\pi^4, \quad (4.40)$$

$$a_\mu^{\text{C},O(a)}(m_\pi^2, a) = b_0 + b_1 m_\pi^2 + b_2 a, \quad (4.41)$$

$$a_\mu^{\text{C}}(m_\pi^2) = b_0 + b_1 m_\pi^2, \quad (4.42)$$

$$a_\mu^{\text{D},O(a)}(m_\pi^2, a) = b_0 + b_1 a. \quad (4.43)$$

A -type fits are inspired by chiral perturbation theory, B -, C -, and D -type fits are based on an expansion of a_μ^{HLO} with decreasing order in m_π^2 . The fits which model lattice artefacts are implemented as simultaneous fits of the pion mass depending coefficients and the ones depending on lattice artefacts. In addition to the different fit ansätze we also use cuts on the data that enter the fit. The cuts we use are $m_\pi < 400$ MeV, which removes 3 ensembles, $a < 0.070$ fm, which removes 4 ensembles, and the conjunction of both cuts, which removes 5 ensembles. These cuts allow us to study the systematic effects the pion mass dependence and lattice artefacts have on the final result.

4.3.3.1 The light-quark contribution

For the light-quark contribution we observed for the results without m_V -rescaling a curvature of the data with respect to the pion mass, see figures 4.8 and 4.17. Thus we use the fit ansätze of type A and B . As an example for an A -type fit we show the fit without cuts to the results of the hybrid method in figure 4.22. The data we use for the fits are the results for Padé [1,1] shown in table 4.2 for the hybrid method without the results on E5 and N6 due to the large $\chi_{\text{corr}}^2/\text{dof}$. For the results determined via time moments we use all ensembles shown in table 4.8 for Padé [1,1]. We show an example of a B -type fit in figure 4.23 to the time moments results without cuts. For the fits with the cut $a < 0.070$ fm we drop lattice artefacts from the fit function, because the data of the intermediate and the finest lattice spacing are not distinguished from each other.

For the results with m_V -rescaling we use C -type fits for both the results from the hybrid method and the results from time moments. As an example we show a fit to the m_V -rescaled data of the hybrid method in figure 4.24. We collect the individual

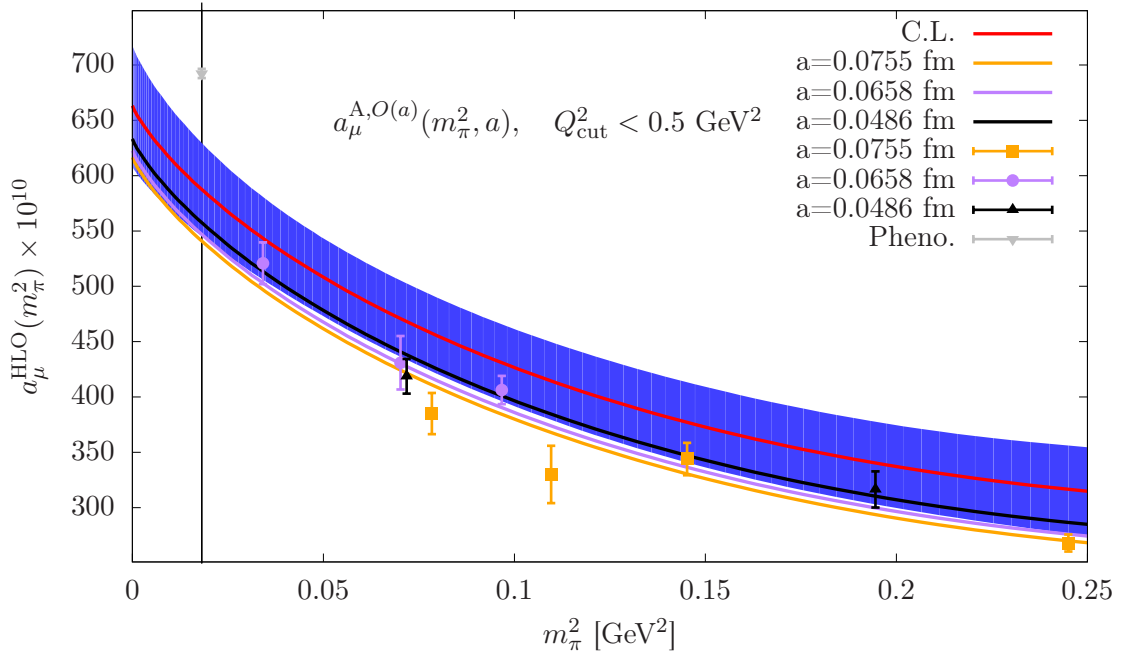


FIGURE 4.22: Example of an A -type fit, cf. eq. (4.37), including lattice artefacts of $O(a)$ for the results of the hybrid method for the light-quark contribution with $Q_{\text{cut}}^2 < 0.5 \text{ GeV}^2$. For this fit without any cuts we have $\chi_{\text{uncorr}}^2/\text{dof}=1.7$ and get $a_{\mu}^{\text{HLO}}=587.56(42.87)\times 10^{-10}$ which corresponds to a precision of $\approx 7\%$. We show the result of the fit evaluated at the different lattice spacings in the respective colours of the points. The continuum result is shown in red with the corresponding blue band for the statistical error. As a reference we show the result from phenomenology at the physical point [1].

results that enter the extended frequentist method for the light-quark contribution for the hybrid method in table 4.12, for the time moments in the tables C.73 and C.74, where the latter contains the results with m_V -rescaling. We observe that for the hybrid method without m_V -rescaling the $\chi_{\text{uncorr}}^2/\text{dof}$ improves with cuts on the lattice spacing. The reason for this is the non-monotonicity of the data with respect to the lattice spacing, such that the lattice spacing dependence cannot be distinguished. The fits to the m_V -rescaled data of the hybrid method have a good $\chi_{\text{uncorr}}^2/\text{dof}$ for all considered variations, due to the larger errors. For the results from time moments we find that $\chi_{\text{uncorr}}^2/\text{dof} > 4$, which we attribute to fluctuations in the data and the higher statistical precision. Again, for the m_V -rescaled results $\chi_{\text{uncorr}}^2/\text{dof}$ improves due to the larger errors.

For the light-quark contribution we can also fit the results from the data with and

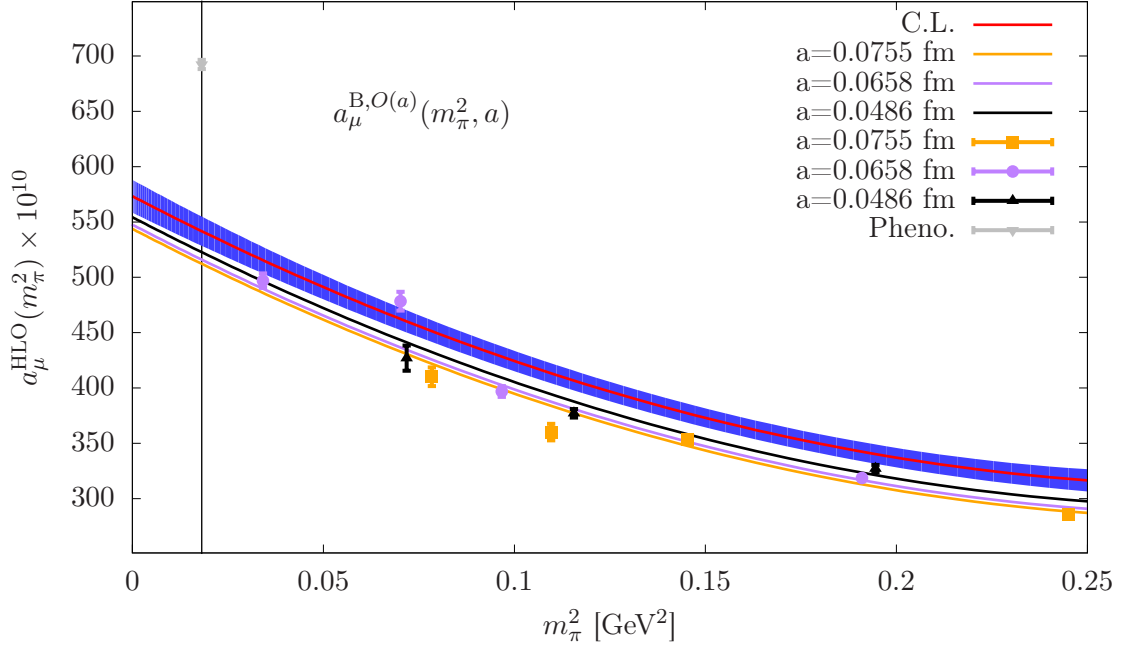


FIGURE 4.23: Example of a B -type fit for the results determined with time moments for the light-quark contribution. We get $\chi_{\text{uncorr}}^2/\text{dof}=8.0$ and $a_{\mu}^{\text{HLO}}=550.15(13.67)\times 10^{-10}$, which corresponds to a precision of 2.5%. We show the fit evaluated at the different lattice spacings with the respective colours. The continuum limit is shown in red with the blue band for the statistical error. The results shown here refer to $t_{\text{trunc}} \pm 0$. The result from phenomenology is shown in gray as a reference [1].

without m_V -rescaling simultaneously. To this end we define the following fit functions,

$$a_{\mu}^{\text{E},O(a)}(\Delta m^2, a) = \begin{cases} b_0 + b_1 \Delta m^2 + b_2 \Delta m^2 \log(\Delta m^2) + b_3 a & \text{data w/o rescaling,} \\ b_0 + b_4 \Delta m^2 + b_5 a & m_V\text{-rescaled data,} \end{cases} \quad (4.44)$$

$$a_{\mu}^{\text{E}}(\Delta m^2) = \begin{cases} b_0 + b_1 \Delta m^2 + b_2 \Delta m^2 \log(\Delta m^2) & \text{data w/o rescaling,} \\ b_0 + b_3 \Delta m^2 & m_V\text{-rescaled data,} \end{cases} \quad (4.45)$$

$$a_{\mu}^{\text{F},O(a)}(\Delta m^2, a) = \begin{cases} b_0 + b_1 \Delta m^2 + b_2 \Delta m^4 + b_3 a & \text{data w/o rescaling,} \\ b_0 + b_4 \Delta m^2 + b_5 a & m_V\text{-rescaled data,} \end{cases} \quad (4.46)$$

$$a_{\mu}^{\text{F}}(\Delta m^2) = \begin{cases} b_0 + b_1 \Delta m^2 + b_2 \Delta m^4 & \text{data w/o rescaling,} \\ b_0 + b_3 \Delta m^2 & m_V\text{-rescaled data,} \end{cases} \quad (4.47)$$

where we introduced $\Delta m^2 = m_{\pi}^2 - (m_{\pi}^{\text{exp}})^2$, with the pion mass on each ensemble as m_{π} and the physical pion mass m_{π}^{exp} . This notation ensures that both fit functions approach the same limit at the physical point, which is given by b_0 . The results on each ensemble are uncorrelated, but the results of the two strategies are not. Thus we define

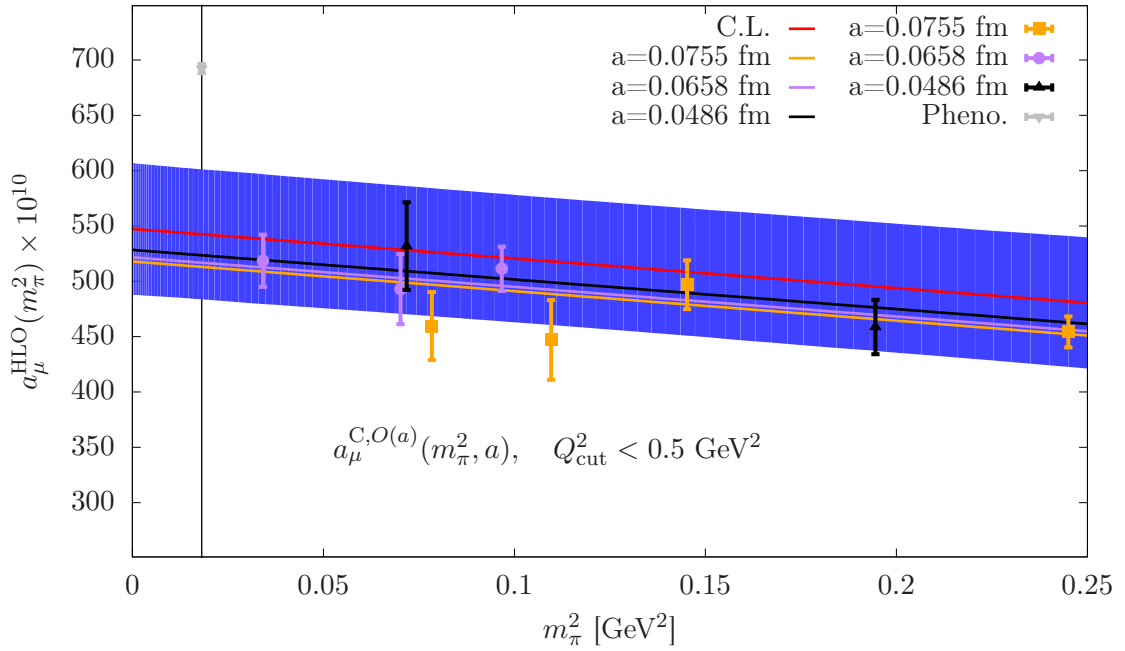


FIGURE 4.24: Example of a C -type fit for the light-quark contribution determined with the hybrid method and m_V -rescaling for $Q_{\text{cut}}^2 < 0.5 \text{ GeV}^2$. Without cuts we obtain $\chi_{\text{uncorr}}^2/\text{dof}=0.8$ and $a_{\mu}^{\text{HLO}}=538.90(59.43)\times 10^{-10}$ which corresponds to a precision of 11.0%. The fit is also evaluated at the different lattice spacings and shown in the corresponding colours. The red line and the blue band refer to the continuum limit with the statistical error. As a reference we show the result from phenomenology [1].

the following covariance matrix:

$$M = \begin{pmatrix} \alpha & \beta \\ \beta & \gamma \end{pmatrix}, \quad (4.48)$$

where the blocks α, β , and γ are diagonal matrices. α and γ contain the uncorrelated covariance matrices for the data of the results without and with m_V -rescaling, respectively. β contains the correlations between the two data sets. We show an example of an E -type fit in figure 4.25 for the hybrid method. We collect the results for all variations we consider for the hybrid method in table C.72, and for the results determined via time moments in C.75.

a_μ^{HLO}	%	p-val.	$\chi_{\text{uncorr}}^2/\text{dof}$	cuts	fit ansatz
$Q_{\text{cut}}^2 \approx 0.5 \text{ GeV}^2$, without m_V -rescaling					
604.15(33.61)	5.6	0.06	2.32	-	$a_\mu^{A,O(a)}(m_\pi^2, a)$
586.38(33.06)	5.6	0.02	2.64	-	$a_\mu^{B,O(a)}(m_\pi^2, a)$
652.30(47.64)	7.3	0.07	2.39	$m_\pi < 400 \text{ MeV}$	$a_\mu^{A,O(a)}(m_\pi^2, a)$
631.49(43.59)	6.9	0.05	2.57	$m_\pi < 400 \text{ MeV}$	$a_\mu^{B,O(a)}(m_\pi^2, a)$
556.61(20.11)	3.6	0.71	0.35	$a < 0.070 \text{ fm}$	$a_\mu^A(m_\pi^2)$
546.78(17.45)	3.2	0.65	0.43	$a < 0.070 \text{ fm}$	$a_\mu^B(m_\pi^2)$
565.52(30.52)	5.4	0.45	0.58	$m_\pi < 400 \text{ MeV}, a < 0.070 \text{ fm}$	$a_\mu^A(m_\pi^2)$
557.74(26.32)	4.7	0.45	0.57	$m_\pi < 400 \text{ MeV}, a < 0.070 \text{ fm}$	$a_\mu^B(m_\pi^2)$
$Q_{\text{cut}}^2 < 0.5 \text{ GeV}^2$, without m_V -rescaling					
587.56(42.87)	7.3	0.13	1.70	-	$a_\mu^{A,O(a)}(m_\pi^2, a)$
567.41(40.40)	7.1	0.07	2.07	-	$a_\mu^{B,O(a)}(m_\pi^2, a)$
632.42(67.22)	10.6	0.11	2.03	$m_\pi < 400 \text{ MeV}$	$a_\mu^{A,O(a)}(m_\pi^2, a)$
606.42(61.94)	10.2	0.09	2.19	$m_\pi < 400 \text{ MeV}$	$a_\mu^{B,O(a)}(m_\pi^2, a)$
571.94(30.52)	5.3	0.39	0.96	$a < 0.070 \text{ fm}$	$a_\mu^A(m_\pi^2)$
557.95(26.51)	4.8	0.30	1.22	$a < 0.070 \text{ fm}$	$a_\mu^B(m_\pi^2)$
622.75(48.95)	7.9	0.67	0.18	$m_\pi < 400 \text{ MeV}, a < 0.070 \text{ fm}$	$a_\mu^A(m_\pi^2)$
602.50(39.99)	6.6	0.68	0.18	$m_\pi < 400 \text{ MeV}, a < 0.070 \text{ fm}$	$a_\mu^B(m_\pi^2)$
$Q_{\text{cut}}^2 \approx 0.5 \text{ GeV}^2$, with m_V -rescaling					
549.49(56.25)	10.2	0.44	0.97	-	$a_\mu^{C,O(a)}(m_\pi^2, a)$
695.70(71.95)	10.3	0.74	0.50	$a < 0.070 \text{ fm}$	$a_\mu^{C,O(a)}(m_\pi^2, a)$
527.00(21.73)	4.1	0.71	0.47	$a < 0.070$	$a_\mu^C(m_\pi^2)$
514.14(23.18)	4.5	0.68	0.39	$m_\pi < 400 \text{ MeV}, a < 0.070 \text{ fm}$	$a_\mu^C(m_\pi^2)$
$Q_{\text{cut}}^2 < 0.5 \text{ GeV}^2$, with m_V -rescaling					
538.90(59.43)	11.0	0.56	0.81	-	$a_\mu^{C,O(a)}(m_\pi^2, a)$
671.17(86.16)	12.8	0.65	0.61	$m_\pi < 400 \text{ MeV}$	$a_\mu^{C,O(a)}(m_\pi^2, a)$
539.78(25.15)	4.7	0.82	0.31	$a < 0.070 \text{ fm}$	$a_\mu^C(m_\pi^2)$
526.47(29.58)	5.6	0.76	0.28	$m_\pi < 400 \text{ MeV}, a < 0.070 \text{ fm}$	$a_\mu^C(m_\pi^2)$

TABLE 4.12: We show the results for the extrapolation to the physical point for a_μ^{HLO} for the light-quark contribution in units of 10^{10} for the analysis without m_V -rescaling at the top and with m_V -rescaling at the bottom. The p-value is used as the weight in the extended frequentist method. The fits are based on the results for the Padé [1,1] in table 4.2.

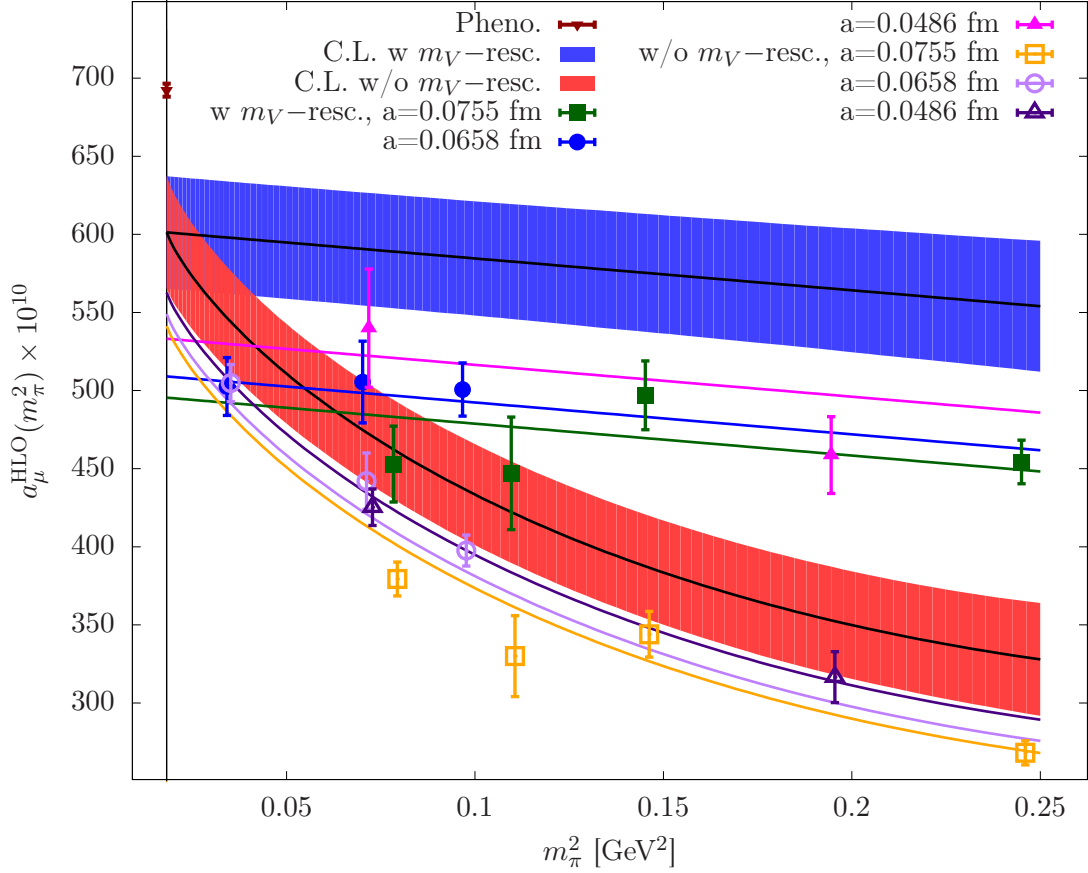


FIGURE 4.25: We fit the data with and without m_V -rescaling simultaneously with an E -type fit to extrapolate a_μ^{HLO} to the physical point for the light-quark contribution using the data determined via the hybrid method at $Q_{\text{cut}}^2 \approx 0.5 \text{ GeV}^2$. We get $\chi_{\text{uncorr}}^2/\text{dof}=1.5$ and $a_\mu^{\text{HLO}}=601.26(35.90)$, which corresponds to a precision of 6.0%. The data without m_V -rescaling are shown as open symbols and the dashed lines in the corresponding colours refer to the fit evaluated at the different lattice spacings. The continuum limit is shown as a black dashed line with the red band for the statistical error. The m_V -rescaled results are shown as filled symbols and the lines in the corresponding colours refer to the fit evaluated at the different lattice spacings. The continuum limit in this case is the black line with the statistical error shown in blue.

The result from phenomenology is shown as a reference [1].

a_μ^{HLO}	%	p-val.	$\chi_{\text{uncorr}}^2/\text{dof}$	cuts	fit ansatz
Hybrid method: $Q_{\text{cut}}^2 \approx 0.5 \text{ GeV}^2$					
56.42(1.00)	1.8	3.84e-04	3.81	-	$a_\mu^{\text{C},O(a)}(m_\pi^2, a)$
57.12(1.16)	2.0	4.70e-02	2.25	$m_\pi < 400\text{MeV}$	$a_\mu^{\text{C},O(a)}(m_\pi^2, a)$
52.90(1.78)	3.4	6.00e-02	2.47	$a < 0.070\text{fm}$	$a_\mu^{\text{C},O(a)}(m_\pi^2, a)$
51.86(1.80)	3.5	6.30e-01	0.46	$m_\pi < 400\text{MeV} a < 0.070\text{fm}$	$a_\mu^{\text{C},O(a)}(m_\pi^2, a)$
Hybrid method: $Q_{\text{cut}}^2 < 0.5 \text{ GeV}^2$					
57.12(1.88)	3.3	3.01e-01	1.20	-	$a_\mu^{\text{C},O(a)}(m_\pi^2, a)$
57.55(2.17)	3.8	4.90e-01	0.88	$m_\pi < 400\text{MeV}$	$a_\mu^{\text{C},O(a)}(m_\pi^2, a)$
57.65(3.07)	5.3	1.14e-01	1.98	$a < 0.070\text{fm}$	$a_\mu^{\text{C},O(a)}(m_\pi^2, a)$
56.60(3.11)	5.5	2.25e-01	1.49	$m_\pi < 400\text{MeV} a < 0.070\text{fm}$	$a_\mu^{\text{C},O(a)}(m_\pi^2, a)$
Time moments: $t_{\text{trunc}} - 1$					
53.38(0.66)	1.2	4.70e-02	1.96	-	$a_\mu^{\text{C},O(a)}(m_\pi^2, a)$
54.53(0.71)	1.3	2.07e-01	1.44	$m_\pi < 400\text{MeV}$	$a_\mu^{\text{C},O(a)}(m_\pi^2, a)$
51.03(0.86)	1.7	9.86e-01	0.09	$a < 0.070\text{fm}$	$a_\mu^{\text{C},O(a)}(m_\pi^2, a)$
51.92(1.56)	3.0	9.52e-01	0.05	$m_\pi < 400\text{MeV} a < 0.070\text{fm}$	$a_\mu^{\text{C},O(a)}(m_\pi^2, a)$
Time moments: $t_{\text{trunc}} \pm 0$					
53.16(0.64)	1.2	5.28e-02	1.92	-	$a_\mu^{\text{C},O(a)}(m_\pi^2, a)$
54.61(0.75)	1.4	2.20e-01	1.40	$m_\pi < 400\text{MeV}$	$a_\mu^{\text{C},O(a)}(m_\pi^2, a)$
50.99(0.85)	1.7	9.81e-01	0.10	$a < 0.070\text{fm}$	$a_\mu^{\text{C},O(a)}(m_\pi^2, a)$
52.00(1.65)	3.2	9.51e-01	0.05	$m_\pi < 400\text{MeV} a < 0.070\text{fm}$	$a_\mu^{\text{C},O(a)}(m_\pi^2, a)$
Time moments: $t_{\text{trunc}} + 1$					
53.14(0.70)	1.3	6.65e-02	1.83	-	$a_\mu^{\text{C},O(a)}(m_\pi^2, a)$
54.88(0.90)	1.6	2.69e-01	1.28	$m_\pi < 400\text{MeV}$	$a_\mu^{\text{C},O(a)}(m_\pi^2, a)$
50.84(0.90)	1.8	9.90e-01	0.07	$a < 0.070\text{fm}$	$a_\mu^{\text{C},O(a)}(m_\pi^2, a)$
51.85(2.14)	4.1	9.63e-01	0.04	$m_\pi < 400\text{MeV} a < 0.070\text{fm}$	$a_\mu^{\text{C},O(a)}(m_\pi^2, a)$

TABLE 4.13: Collection of all results for the strange-quark contribution for a_μ^{HLO} at the physical point in units of 10^{10} . The results for the hybrid method are based on the data shown in table 4.4 for Padé [1,1] and for the time moments on the data presented in table 4.10 also for Padé [1,1].

4.3.3.2 The strange-quark contribution

For the strange-quark contribution we use the fit ansatz $a_\mu^{\text{C},O(a)}(m_\pi^2, a)$. To investigate lattice artefacts we also use the cut $a < 0.070 \text{ fm}$, but as we observe a gap between the data of the intermediate and the finest lattice spacing we do not drop lattice artefacts for this fit. The pion mass dependence is studied by applying the cut $m_\pi < 400 \text{ MeV}$. And, as before, we study all combinations of different cuts. The individual results are listed in table 4.13. Note that E5 was removed from the data that enters the fit due to the poor $\chi_{\text{corr}}^2/\text{dof}$ for the fit to the HVP with the hybrid method. We show an example of a fit to the strange-quark contribution in figure 4.26.

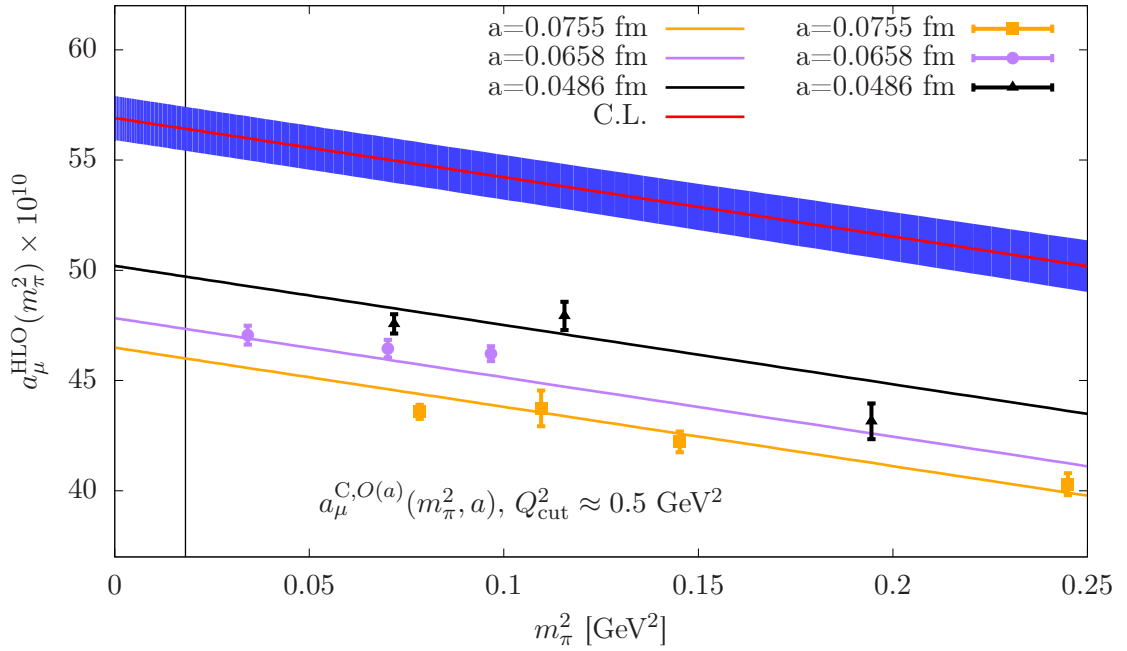


FIGURE 4.26: We fit the data for the strange quark contribution with $Q_{\text{cut}}^2 \approx 0.5 \text{ GeV}^2$ with C -type fits such as the result shown here without cuts on the contributing ensembles for the hybrid method. The result at the physical point for a_μ^{HLO} for this example is $a_\mu^{\text{HLO}} = 56.42(1.00) \times 10^{-10}$, which corresponds to a precision of 1.8%, and we get $\chi_{\text{uncorr}}^2/\text{dof} = 3.8$. We evaluate the fit result at the lattice spacings considered and show the result in the corresponding colours. The continuum result is shown in red with the blue band as the statistical error.

4.3.3.3 The charm-quark contribution

For the charm-quark mass the pion mass dependence diminishes further thus we use, in addition to the fit ansatz the $a_\mu^{C,O(a)}(m_\pi^2, a)$, the ansatz $a_\mu^{D,O(a)}(m_\pi^2, a)$. We use the cut $a < 0.070 \text{ fm}$ again to study lattice artefacts but, as these effects are even stronger as they are for the strange-quark, the term for lattice artefacts is not dropped from the fit. The effect of the pion mass dependence is considered by using the cut $m_\pi < 400 \text{ MeV}$, and we also the combination of both cuts. For the charm-quark contribution we consider the results from all ensembles for the hybrid method. The results for the hybrid method and the time moments are collected in the tables 4.14 and 4.15, respectively. In figure 4.27 we show an example of a fit to the data determined with the hybrid method using a polynomial ansatz of $O(Q^2)$. For the charm-quark contribution corrections due to lattice artefacts are about $O(50\%)$ of the result at the physical point. Thus the extrapolation to the physical point for the charm-quark contribution has to be well controlled for calculations aiming at $< 1\%$ relative precision for the four-flavour result.

a_μ^{HLO}	%	p-val.	$\chi_{\text{uncorr}}^2/\text{dof}$	cuts	fit ansatz
Hybrid method: Polynomial $O(Q^2)$					
13.87(0.29)	2.1	1.77e-01	1.41	-	$a_\mu^{\text{D},O(a)}(m_\pi^2, a)$
13.87(0.31)	2.2	1.32e-01	1.56	-	$a_\mu^{\text{C},O(a)}(m_\pi^2, a)$
14.05(0.31)	2.2	1.89e-01	1.46	$m_\pi < 400\text{MeV}$	$a_\mu^{\text{D},O(a)}(m_\pi^2, a)$
14.38(0.38)	2.6	3.11e-01	1.19	$m_\pi < 400\text{MeV}$	$a_\mu^{\text{C},O(a)}(m_\pi^2, a)$
13.40(0.38)	2.8	8.59e-01	0.39	$a < 0.070\text{fm}$	$a_\mu^{\text{D},O(a)}(m_\pi^2, a)$
13.43(0.38)	2.8	8.14e-01	0.39	$a < 0.070\text{fm}$	$a_\mu^{\text{C},O(a)}(m_\pi^2, a)$
13.34(0.44)	3.3	6.32e-01	0.57	$m_\pi < 400\text{MeV} a < 0.070\text{fm}$	$a_\mu^{\text{D},O(a)}(m_\pi^2, a)$
13.74(0.82)	6.0	4.90e-01	0.71	$m_\pi < 400\text{MeV} a < 0.070\text{fm}$	$a_\mu^{\text{C},O(a)}(m_\pi^2, a)$
Hybrid method: Padé [1,1]					
13.56(0.65)	4.8	7.55e-01	0.65	-	$a_\mu^{\text{D},O(a)}(m_\pi^2, a)$
13.56(0.70)	5.2	6.65e-01	0.73	-	$a_\mu^{\text{C},O(a)}(m_\pi^2, a)$
14.48(1.08)	7.5	7.42e-01	0.59	$m_\pi < 400\text{MeV}$	$a_\mu^{\text{D},O(a)}(m_\pi^2, a)$
14.47(1.08)	7.5	6.61e-01	0.65	$m_\pi < 400\text{MeV}$	$a_\mu^{\text{C},O(a)}(m_\pi^2, a)$
13.91(0.83)	6.0	5.46e-01	0.81	$a < 0.070\text{fm}$	$a_\mu^{\text{D},O(a)}(m_\pi^2, a)$
14.00(0.88)	6.3	4.48e-01	0.92	$a < 0.070\text{fm}$	$a_\mu^{\text{C},O(a)}(m_\pi^2, a)$
15.16(1.62)	10.7	3.82e-01	1.02	$m_\pi < 400\text{MeV} a < 0.070\text{fm}$	$a_\mu^{\text{D},O(a)}(m_\pi^2, a)$
16.44(1.83)	11.1	4.20e-01	0.87	$m_\pi < 400\text{MeV} a < 0.070\text{fm}$	$a_\mu^{\text{C},O(a)}(m_\pi^2, a)$

TABLE 4.14: Collection of all results for the charm-quark contribution for a_μ^{HLO} at the physical point in units of 10^{10} for the hybrid method, which are based on the data shown in table 4.5 with $Q_{\text{cut}}^2 < 0.5 \text{ GeV}^2$.

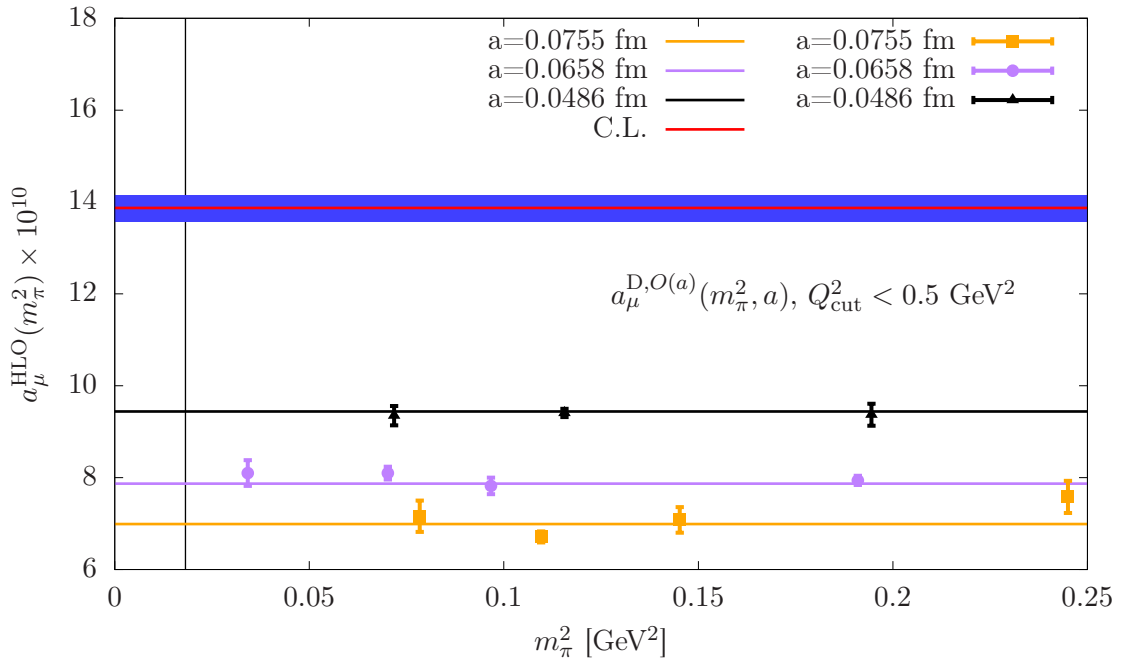


FIGURE 4.27: Example of a D -type fit to the charm-quark data determined with the hybrid method using a polynomial ansatz with $O(Q^2)$. We get $\chi_{\text{uncorr}}^2/\text{dof} = 1.4$ and $a_\mu^{\text{HLO}} = 13.87(0.29) \times 10^{-10}$, with a precision of 2.1%. We show the fit result evaluated at the different lattice spacings in the corresponding colours as lines. The continuum limit is shown as a red line with the statistical error shown as a blue band.

a_μ^{HLO}	%	p-val.	$\chi_{\text{uncorr}}^2/\text{dof}$	cuts	fit ansatz
Time moments: $t_{\text{trunc}} - 1$					
14.00(0.34)	2.4	9.44e-01	0.38	-	$a_\mu^{\text{D},O(a)}(m_\pi^2, a)$
14.03(0.42)	3.0	9.16e-01	0.41	-	$a_\mu^{\text{C},O(a)}(m_\pi^2, a)$
14.31(0.46)	3.2	9.56e-01	0.26	$m_\pi < 400\text{MeV}$	$a_\mu^{\text{D},O(a)}(m_\pi^2, a)$
14.43(0.53)	3.7	9.23e-01	0.28	$m_\pi < 400\text{MeV}$	$a_\mu^{\text{C},O(a)}(m_\pi^2, a)$
14.09(0.46)	3.3	9.70e-01	0.18	$a < 0.070\text{fm}$	$a_\mu^{\text{D},O(a)}(m_\pi^2, a)$
14.45(0.81)	5.6	9.46e-01	0.18	$a < 0.070\text{fm}$	$a_\mu^{\text{C},O(a)}(m_\pi^2, a)$
14.22(0.58)	4.1	8.50e-01	0.27	$m_\pi < 400\text{MeV} a < 0.070\text{fm}$	$a_\mu^{\text{D},O(a)}(m_\pi^2, a)$
14.91(1.57)	10.5	7.44e-01	0.30	$m_\pi < 400\text{MeV} a < 0.070\text{fm}$	$a_\mu^{\text{C},O(a)}(m_\pi^2, a)$
Time moments: $t_{\text{trunc}} \pm 0$					
14.10(0.34)	2.4	9.45e-01	0.38	-	$a_\mu^{\text{D},O(a)}(m_\pi^2, a)$
14.10(0.41)	2.9	9.27e-01	0.39	-	$a_\mu^{\text{C},O(a)}(m_\pi^2, a)$
14.36(0.46)	3.2	9.56e-01	0.26	$m_\pi < 400\text{MeV}$	$a_\mu^{\text{D},O(a)}(m_\pi^2, a)$
14.44(0.53)	3.7	9.23e-01	0.28	$m_\pi < 400\text{MeV}$	$a_\mu^{\text{C},O(a)}(m_\pi^2, a)$
14.09(0.46)	3.3	9.70e-01	0.18	$a < 0.070\text{fm}$	$a_\mu^{\text{D},O(a)}(m_\pi^2, a)$
14.45(0.81)	5.6	9.46e-01	0.18	$a < 0.070\text{fm}$	$a_\mu^{\text{C},O(a)}(m_\pi^2, a)$
14.22(0.58)	4.1	8.50e-01	0.27	$m_\pi < 400\text{MeV} a < 0.070\text{fm}$	$a_\mu^{\text{D},O(a)}(m_\pi^2, a)$
14.91(1.57)	10.5	7.44e-01	0.30	$m_\pi < 400\text{MeV} a < 0.070\text{fm}$	$a_\mu^{\text{C},O(a)}(m_\pi^2, a)$
Time moments: $t_{\text{trunc}} + 1$					
14.10(0.34)	2.4	9.45e-01	0.38	-	$a_\mu^{\text{D},O(a)}(m_\pi^2, a)$
13.97(0.42)	3.0	9.18e-01	0.41	-	$a_\mu^{\text{C},O(a)}(m_\pi^2, a)$
14.36(0.46)	3.2	9.56e-01	0.26	$m_\pi < 400\text{MeV}$	$a_\mu^{\text{D},O(a)}(m_\pi^2, a)$
14.44(0.53)	3.7	9.23e-01	0.28	$m_\pi < 400\text{MeV}$	$a_\mu^{\text{C},O(a)}(m_\pi^2, a)$
14.09(0.46)	3.3	9.70e-01	0.18	$a < 0.070\text{fm}$	$a_\mu^{\text{D},O(a)}(m_\pi^2, a)$
14.45(0.81)	5.6	9.46e-01	0.18	$a < 0.070\text{fm}$	$a_\mu^{\text{C},O(a)}(m_\pi^2, a)$
14.22(0.58)	4.1	8.50e-01	0.27	$m_\pi < 400\text{MeV} a < 0.070\text{fm}$	$a_\mu^{\text{D},O(a)}(m_\pi^2, a)$
14.91(1.57)	10.5	7.44e-01	0.30	$m_\pi < 400\text{MeV} a < 0.070\text{fm}$	$a_\mu^{\text{C},O(a)}(m_\pi^2, a)$

TABLE 4.15: Collection of all results for the charm-quark contribution for a_μ^{HLO} at the physical point in units of 10^{10} for the time moments, which were presented in table 4.11 for Padé [1,1].

4.3.4 Results at the physical point for a_μ^{HLO}

We collect the results for a_μ^{HLO} obtained with the extended frequentist method in table 4.16 for the hybrid method and the time moments. Though the precision of the results from the time moments is, for the dominant light-quark contribution, better than the ones from the hybrid method, we show the results of the time moments only for a comparison due to the large values of $\chi_{\text{uncorr}}^2/\text{dof}$. The chiral behaviour of the results for the time moments fluctuates too much to give reliable fit results. We find $\chi_{\text{uncorr}}^2/\text{dof} \gtrsim 4.5$ for the extrapolations to the physical point without m_V -rescaling, cf. table C.73, and $\chi_{\text{uncorr}}^2/\text{dof} \gtrsim 3.7$ for the simultaneous fit to the data with and without m_V -rescaling, see table C.75. For the results with m_V -rescaling the $\chi_{\text{uncorr}}^2/\text{dof}$ is improved, but we find that the relative precision deteriorates slightly.

We observe that the results we get for the hybrid method agree with each other within errors for the different approaches presented for the light-quark contribution. Since the light-quark contribution dominates the full result, this also holds for the three and four-flavour results. The results determined via the hybrid method and those using the time moments agree for the light and charm-quark contributions within errors for the considered approaches for the extrapolation. For the strange-quark contribution we find a difference of $\sim 1.1\sigma$ between the results from the hybrid method and the time moments.

In table 4.17 we show the contributions to the systematic error for the various approaches. For the hybrid method we use the following subsets to estimate the contributions to the systematic error. To study lattice artefacts (LA) we build subsets of the data, that enter the extended frequentist method, with and without the cut $a < 0.070$ fm. For the pion mass dependence we use similar subsets with the cut $m_\pi < 400$ MeV. We investigate the Q^2 -dependence by building subsets consisting of the different values used for Q_{cut}^2 for the light and strange-quark contribution, and for the charm-quark contribution we use the different fit ansätze, i.e. the polynomial and the Padé [1,1]. For the light-quark contribution we find that the considered systematic effects contribute about the same amount each for the analysis without m_V -rescaling. For the analysis with m_V -rescaling lattice artefacts dominate the systematic error, the same holds for the analysis based on the simultaneous fit to data with and without m_V -rescaling. For the analysis using the combination of the fits to the data with and without m_V -rescaling we find that lattice artefacts dominate and the pion mass dependence is the sub-leading effect. For the strange-quark contribution lattice artefacts and the Q^2 -dependence are the main sources of systematic effects. The systematic error of the charm-quark contribution is dominated by the Q^2 -dependence, while lattice artefacts and the pion mass dependence give a similar contribution to the systematic error. This does not necessarily mean that lattice artefacts are small, but that the part of the fits describing lattice artefacts varies little when the cut $a < 0.070$ fm is applied. It should be noted that there are

flavour	Hybrid method				Time moments			
	N_{var}	$a_{\mu}^{\text{HLO}} \times 10^{10}$	$\sqrt{\Sigma \delta_i^2}$	%	N_{var}	$a_{\mu}^{\text{HLO}} \times 10^{10}$	$\sqrt{\Sigma \delta_i^2}$	%
Analysis without m_V -rescaling								
ud	16	565.5(31.2)(33.1)	45.5	8.0	24	533.3(13.5)(9.8)	16.7	3.1
s	8	57.1(3.2)(2.9)	4.3	7.5	12	51.9(1.6)(0.5)	1.6	3.2
c	16	13.74(0.68)(0.54)	0.87	6.3	24	14.22(0.52)(0.18)	0.55	3.9
uds	-	622.6(31.3)(33.2)	45.6	7.3	-	585.2(13.6)(9.8)	16.8	2.9
$udsc$	-	636.4(31.3)(33.2)	45.7	7.2	-	599.4(13.6)(9.8)	16.8	2.8
Analysis with m_V -rescaling								
ud	8	538.9(40.9)(72.4)	83.1	15.4	12	528.5(18.3)(9.1)	20.4	3.9
uds	-	596.0(41.0)(72.4)	83.2	14.0	-	580.4(18.3)(9.1)	20.5	3.5
$udsc$	-	609.8(41.0)(72.4)	83.2	13.7	-	594.6(18.4)(9.1)	20.5	3.4
Analysis of the combination of data w and w/o m_V -rescaling								
ud	24	556.6(27.9)(47.9)	55.4	10.0	36	528.5(17.9)(9.1)	20.1	3.8
uds	-	613.7(28.1)(48.0)	55.6	9.1	-	580.4(18.0)(9.1)	20.2	3.5
$udsc$	-	627.5(28.1)(48.0)	55.6	8.9	-	594.6(18.0)(9.1)	20.2	3.4
Analysis of simultaneous fits to data w and w/o m_V -rescaling								
ud	16	539.2(24.8)(50.4)	56.1	10.4	24	520.1(13.7)(8.1)	15.9	3.0
uds	-	596.3(25.0)(50.4)	56.3	9.4	-	572.0(13.7)(8.1)	15.9	2.8
$udsc$	-	610.0(25.0)(50.4)	56.3	9.2	-	586.2(13.7)(8.1)	15.9	2.7

TABLE 4.16: We combine the various results for a_{μ}^{HLO} from the fits for the two considered methods with the extended frequentist method separately to determine the systematic and statistical errors. The column N_{var} refers to the number of variations used in the extended frequentist method and in $\sqrt{\Sigma \delta_i^2}$ the statistical and systematic errors are summed in quadrature. For the three and four-flavour results we sum the individual contributions and the errors are summed in quadrature.

severe cut off effects for this heavy mass and systematic error due to the extrapolation with respect to the lattice spacing may be underestimated.

For the time moments we look at lattice artefacts, the pion mass dependence, and the effect of changing t_{trunc} in the sum of the moments. We use similar subsets for the first two effects, which correspond to the cuts in the lattice spacing a and the pion mass m_{π} . For the estimate of the contribution to the systematic error due to the variation of t_{trunc} we have a subset for each value of t_{trunc} . We find that for the analysis without m_V -rescaling the systematic effects are dominated by lattice artefacts, while the pion mass dependence is the sub-leading effect. For the analysis based on m_V -rescaling alone we observe that the pion mass dependence dominates the systematic error, while lattice artefacts and variations in t_{trunc} add a smaller but relevant part to the systematic error. For the simultaneous fit to data with and without m_V -rescaling lattice artefacts dominate the error and the pion mass dependence is the sub-leading effect. For the combined analysis of data extracted with and without m_V -rescaling the systematic error is dominated by the pion mass dependence, and lattice artefacts are the sub-leading effect. The agreement with the analysis based on the data with m_V -rescaling is accidental. For the strange-quark lattice artefacts dominate the systematic error. For the charm-quark

contribution the systematic error is dominated by the pion mass dependence. Naively this would be unexpected, but this is explained by the fact that the result at the physical point for the charm-quark changes very little when we apply the cut $a < 0.070$ fm, while the change of the result due to the cut $m_\pi < 400$ MeV is much larger, even though the data show very little dependence on the pion-mass. For the heavier quarks, the effects due to variations in the truncation t_{trunc} of the sum for the determinations of the time moments is negligible.

	Hybrid method			Time moments		
	LA	Q^2	m_π	LA	m_π	Δt_{trunc}
ud						
w/o m_V -rescaling	30.8	34.6	34.6	51.1	39.6	9.3
w m_V -rescaling	85.1	7.5	7.3	29.7	52.9	17.4
Simultaneous fit to data w and w/o m_V -rescaling	81.8	12.4	5.8	58.0	32.2	9.9
Combined analysis of data w and w/o m_V -rescaling	51.6	10.4	37.9	29.7	52.9	17.4
s	44.9	44.9	10.2	77.2	20.1	2.7
c	29.4	43.6	27.0	26.6	73.4	0.0

TABLE 4.17: Estimated contributions to the systematic error normalized such that the two methods in each line sum up to 100% up to rounding errors. LA refers to lattice artefacts, m_π to the pion mass dependence, Q^2 to the effects due to changing Q^2_{cut} (light and strange) or the fit function applied to the HVP (charm), and Δt_{trunc} to the variation of the cut of the sum for the time moments, where the correlation function is inserted as an approximation.

4.3.5 Determination of a_μ^{HLO} via the Adler function

The Adler function can also be used to compute a_μ^{HLO} using the integral [123, 124],

$$a_\mu^{\text{HLO}} = \int_0^1 g(x) D\left(\frac{x^2 m_\mu^2}{1-x}\right) dx, \quad g(x) = \frac{\alpha^2}{6\pi^2} \frac{(1-x)(2-x)}{x}, \quad (4.49)$$

where we replaced $Q^2 \rightarrow \frac{x^2 m_\mu^2}{1-x}$. This approach has the advantage over eq. (4.12) since the determination of the additive renormalization $\Pi(Q^2 = 0)$ is not necessary. We show the kernel of the convolution integral in eq. 4.49 for the light-quark contribution on G8 in figure 4.28. The bulk of contribution to the convolution integral for a_μ^{HLO} is at $Q^2 \approx m_\mu^2$ which corresponds to $x \approx 0.62$. To highlight this fact we show the muon mass as a vertical orange line. While we know that $\lim_{x \rightarrow 0} g(x) D\left(\frac{x^2 m_\mu^2}{1-x}\right) = 0$, we observe that a large part of the convolution integral is still unconstrained by data, which only has an impact for $x \gtrsim 0.85$ in the example shown here.

Since we quote the results from the hybrid method introduced in 4.3.1 as our final result for a_μ^{HLO} , we could in principle treat the Adler function data similarly as the VPF data. But this type of analysis is beyond the scope of this thesis, instead we make use of the

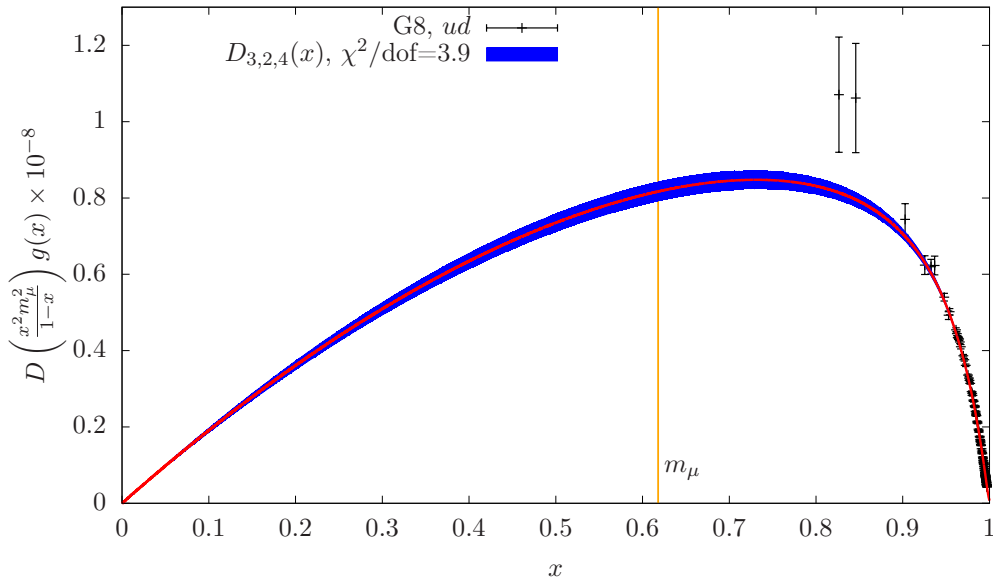


FIGURE 4.28: We show the kernel of the integral in eq. (4.49) for the fit ansatz $D_{3,2,4}$, shown as the blue band, to the data obtained with the Plateau of Slopes method on G8 for the light-quark contribution, depicted in black. The vertical orange line shows the position of the muon mass.

flavour	N_{var}	$a_{\mu}^{\text{HLO}} \times 10^{10}$	$\sqrt{\Sigma \delta_i^2}$	%
ud	32	518.1(11.3)(61.9)	62.9	12.2
s	32	51.6(0.7)(1.6)	1.8	3.4
c	32	13.5(1)(1)	0.1	1.0
uds	-	569.7(11.4)(61.9)	63.0	11.1
$udsc$	-	583.2(11.4)(61.9)	63.0	10.8

TABLE 4.18: Results for a_{μ}^{HLO} from the Adler function. For the three and four-flavour result the central values are summed and the errors are summed in quadrature. N_{var} represents the number of variations used in the extended frequentist method, and $\sqrt{\Sigma \delta_i^2}$ sum in quadrature of the systematic and statistical uncertainties.

combined fits we already performed for the calculations in 3.2.2. Since these combined fits model a larger range in Q^2 higher Padé orders were used.

In the tables B.1, B.2, and B.3 we list the results for a_{μ}^{HLO} determined via the Adler function for the light-, strange-, and charm-quark contribution, respectively. We find that results for a_{μ}^{HLO} for the light-quark contribution fluctuate for Padés [3,3] and [4,3]. For the strange-quark contribution this effect is reduced, but not negligible. For the charm-quark contribution we only use the Padé approximants [1,1] and [2,1], where this does not occur. We use the extended frequentist method to estimate the systematic and statistical uncertainties with the same variations we already included in the estimate of the Adler function for each flavour. The result of this analysis is shown in table 4.18. In table 4.19 we show the contributions to the systematic error for the estimate of a_{μ}^{HLO} via the Adler function. We find that for the light and charm-quark contributions

flavour	LA	PA	χ -ext.	AM
ud	16.7	39.3	39.6	4.4
s	43.1	17.9	18.5	20.4
c	8.6	40.8	38.3	12.3

TABLE 4.19: Contributions to the systematic error for a_μ^{HLO} from the Adler function. We study lattice artefacts (LA), the influence of the Padé ansatz chosen in the global fit to the Adler function (PA), the pion mass dependence χ -ext., and the impact of the choice of the method for the extraction of the Adler function. All contributions are normalized for each flavour separately.

the systematic errors associated with the Padé ansätze and the chiral extrapolation give the largest part of the systematic error. For the strange-quark contribution lattice artefacts dominate the systematic error, while the other sources are of a similar size.

4.3.6 Comparison of a_μ^{HLO} from different methods

In figure 4.29 we compare the results determined from the HVP directly with the results from the Adler function for each flavour separately. For the time moments and the hybrid method we plot the result from the analysis without including m_V -rescaling. We find that the three methods agree within errors for the light- and strange-quark contributions. The result from time moments is the most precise in this case with a relative precision of 3.1%, while the hybrid method reaches a relative precision of $\sim 8\%$. The result from the Adler function is the least precise with a relative precision of 12.2%. The central value of the result for the Adler function is lower than the result from the hybrid method and the time moments. We attribute this to the fact that we used fits modeling a much larger range in Q^2 for the Adler function, since we observed similar effects in earlier calculations using fits to the VPF with fit ranges of $0 < Q^2 < 4 \text{ GeV}^2$. The strategy of fitting the VPF with a large Q^2 range was abandoned because points at large Q^2 are much more precise and thus dominate the fit, which introduces a bias of the fit result, while they contribute little to the convolution integral in eq. (4.12).

For the strange-quark contribution we get a relative precision of 3.2% for the time moments, for the Adler function we get 3.4% and for the hybrid method we get a relative precision of 7.5%.

For the charm-quark contribution we find that the hybrid method agrees within errors with the results from the time moments and the Adler function, while there is a difference of $\sim 1.3\sigma$ between the results of the Adler function and the time moments. For the heaviest flavour we find that the result from Adler function is the most precise with a relative precision of 1%. The time moments reach a precision of 3.9% and the hybrid method a precision of 6.3%.

We find that we do not gain an increase in precision by including the m_V -rescaling in our

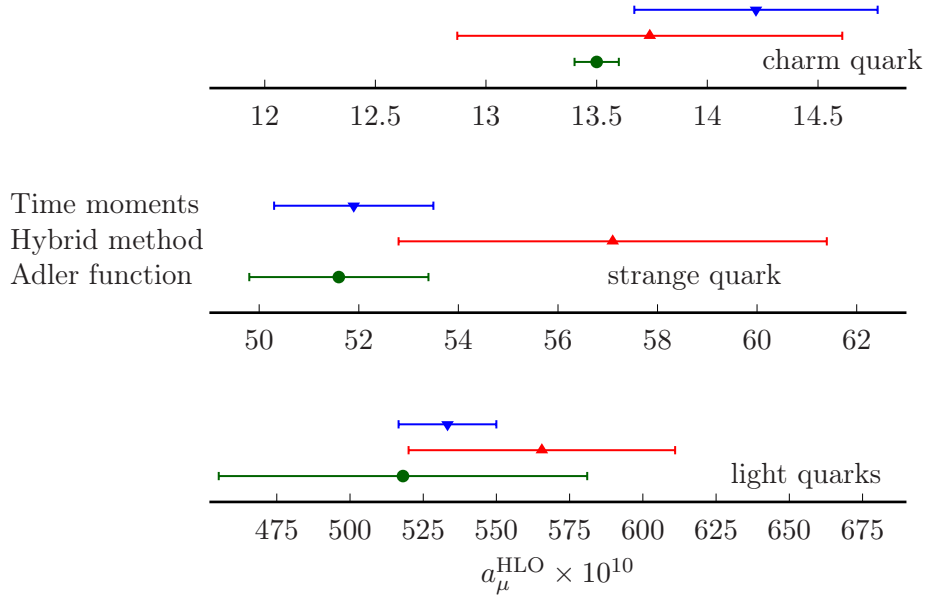


FIGURE 4.29: We compare the results for a_μ^{HLO} for the different methods studied in this work for each flavour separately. The results for a_μ^{HLO} using time moments are shown in blue, we use red for the hybrid method, and green for the results determined via the Adler function, discussed in 4.3.5. Systematic and statistical errors are summed in quadrature.

analysis. Though the determination of a_μ^{HLO} via the Adler function has the advantage that it does not rely on the accuracy of the estimate of $\Pi(Q^2 = 0)$ the precision we get for our result is worse than for the hybrid method or the time moments, since the light-quark contribution dominates the four-flavour result. Due to the difficulties to fit the results obtained with time moments we quote as our final result the analysis based on the hybrid method without including m_V -rescaling. The corresponding area is highlighted in red in table 4.16.

4.3.7 Conclusions

We discussed two strategies to extract a_μ^{HLO} from HVP lattice data, the hybrid method and the use of time moments, and a third strategy was used to compute a_μ^{HLO} from the Adler function. For the hybrid method we found that for the ensembles E5 and N6 the fits have difficulties to describe the data for the light-quark contribution of the HVP due to fluctuations in the low Q^2 regime, which is the dominant part of the convolution integral for a_μ^{HLO} . The time moments allow to circumvent this problem, as long as precise measurements of the vector mass and amplitude are available to approximate the correlation function for $t \rightarrow \infty$, and give more precise results. But this increased precision leads to a bad $\chi_{\text{uncorr}}^2/\text{dof}$ for the extrapolations to the physical point, because

of fluctuations in the chiral behaviour of the results of a_μ^{HLO} on the ensembles we considered in this study. Due to this issue, we choose the more conservative estimate computed with the hybrid method, where larger errors allow for a better $\chi_{\text{uncorr}}^2/\text{dof}$ in the extrapolations. We investigated several methods to extract the light-quark contribution with both strategies at the physical point. We found that for our data m_V -rescaling deteriorates the statistical error and thus does not lead to an improvement for the result at the physical point. This also applies to the estimates where we incorporated both data sets (with and without m_V -rescaling) in one analysis. For the determination of a_μ^{HLO} via the Adler function we observe that the accuracy is lower than for the approaches using the HVP data directly. Thus the choice falls to the results from the hybrid method without m_V -rescaling for all flavours,

$$a_\mu^{\text{HLO},ud} = 565.5(31.2)(33.1), \quad (4.50)$$

$$a_\mu^{\text{HLO},uds} = 622.6(31.3)(33.2), \quad (4.51)$$

$$a_\mu^{\text{HLO},udsc} = 636.4(31.3)(33.2). \quad (4.52)$$

We show a comparison of the results of this work and previous results by the group, which are based on a subset of the ensembles with lower statistics and different analysis methods, with the results of other collaborations in figure 4.30. We achieved an improvement of the error with respect to the previous results and added the charm-quark contribution. Our four-flavour result shows a $\sim 1.2\sigma$ difference with the result from the dispersive approach, shown at the top of the figure and as the yellow band and we do not yet reach a comparable precision. Our results are in agreement with the results by most other collaborations for the two-, three-, and four-flavour cases. But we find that our error estimates are more conservative than the recent results by other groups, and in particular those by the HPQCD collaboration, who accumulated higher statistics than the calculations used in this work.

In figure 4.31 we compare our results for the strange and the charm-quark contribution,

$$a_\mu^{\text{HLO},s} = 57.1(3.2)(2.9), \quad (4.53)$$

$$a_\mu^{\text{HLO},c} = 13.74(68)(54), \quad (4.54)$$

to results by other collaborations. We observe that our results agree within errors with the results by other collaborations but the relative error of our results are more conservative. Concerning the relative precision of our four-flavour result the accuracy of the strange- and charm-quark contributions are not yet an issue, because the error of the light-quark contribution dominates the total error of the four-flavour result by a large margin.

Though we improved the precision of our calculation with new methods and increased

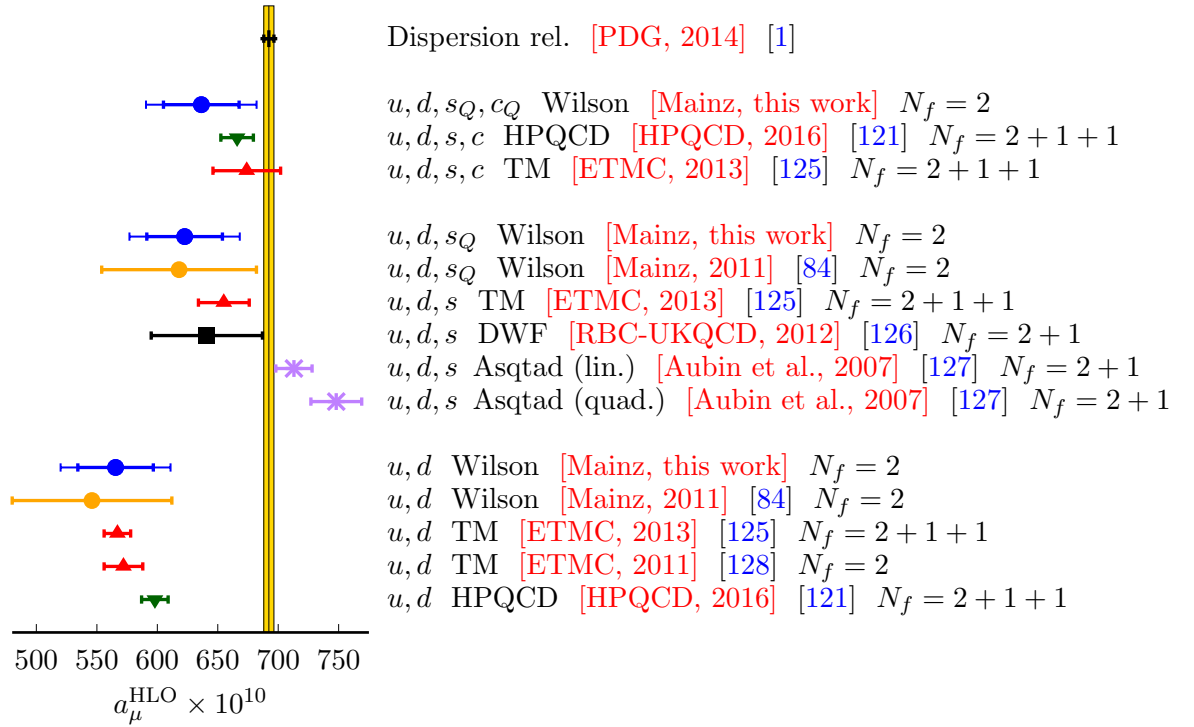


FIGURE 4.30: Comparison of our the previous results (orange) and the new results (blue), cf. eqs. (4.50, 4.51, 4.52), where the inner error bar depicts the statistical error and the full error bar includes the systematic error in quadrature, with results from other collaborations. The data are ordered by valence quark contribution, which is noted on the left of the panel on the right. The sea quark content is noted on the right of the panel on the right.

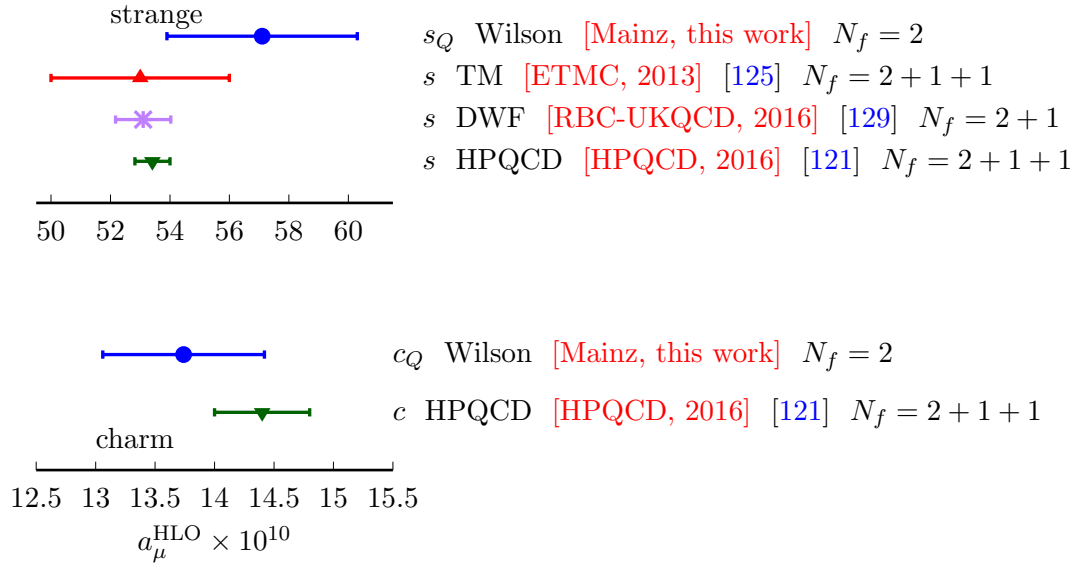


FIGURE 4.31: We compare our results (blue), cf. eqs. (4.53, 4.54), for the strange at the top and the charm-quark contribution at the bottom to results by other collaborations.

statistics, further improvements are still needed to reach a precision compatible to the result from dispersive methods.

Chapter 5

Conclusions and Outlook

In order to discard or verify theoretical models beyond the Standard Model through observables in the low energy regime precise measurements from experiment and calculations from theory are needed. Lattice QCD allows for the calculation of hadronic observables, which are in many cases the dominant source of error, from first principle in the low energy regime, where perturbation theory breaks down. As computer power increases and the employed algorithms improve the precision of lattice QCD calculations is improved.

In this work we focused on the hadronic vacuum polarization contribution to the anomalous magnetic moment of the muon and the running of α_{QED} . We used twisted boundary conditions to improve the momentum resolution. The violation of the Ward Identity of the HVP due to twisted boundary conditions is at the current precision negligible. We presented two numerical procedures to compute the Adler function from the HVP. Our result of the Adler function at the physical point agrees with the result from perturbation theory in the intermediate region of $Q^2 \sim 2.5 \text{ GeV}^2$. The methods we described for the numerical extraction of the Adler function work reasonably well down to $Q^2 > 0.5 \text{ GeV}^2$ on the considered ensembles. For $Q^2 < 0.5 \text{ GeV}^2$ the results could be supplemented by using time moments to compute additional points. The precision of the time moments deteriorates too fast to add helpful information above that region. One could use the time moments in the derivatives of the Padé ansätze to obtain the Adler function in the low- Q^2 regime. Furthermore, it is also possible to obtain the Adler function directly using spatial derivatives on the Fourier transform of the current-current correlator as suggested in [130]. The potential drawback of this method are finite volume effects, which would be introduced by higher moments that can amplify long distance contributions. A third method to extract the Adler function is the time-momentum representation presented first in [63]. This method does not rely on a 4-dim. Fourier transform and thus will have to be used for measurements on the next generation of

CLS ensembles, which have open boundary conditions in time.

From the Adler function we computed $\Delta\alpha_{\text{QED}}^{\text{had}}$ at the physical point directly. Our result is dominated by systematic effects and the precision we reach is not yet comparable to the result from phenomenology. Naturally, all improvements we make in the calculation of the HVP and the extraction of the Adler function from it would reflect on the estimate of $\Delta\alpha_{\text{QED}}^{\text{had}}$ in turn.

We discussed two methods to compute a_{μ}^{HLO} from the HVP directly and one to estimate a_{μ}^{HLO} from the Adler function. We observed that the results from time moments have the highest statistical precision, but suffer from fluctuations in their chiral behaviour. The results from the hybrid method have a reduced precision, but the extrapolations to the physical point are more reliable, due to smaller χ^2/dof . Results for a_{μ}^{HLO} determined via the Adler function are less accurate.

In order to improve the presented calculations higher statistics are needed. The extrapolation to the physical point can be improved by measurements on more chiral ensembles, more lattice spacings, and an increase in the number of sea quarks. The next generation of CLS ensembles include the strange-quark in the sea, and ensembles at physical pion mass will soon be available. Furthermore, a number of ensembles at four different lattice spacings have been generated. Thus the improvement of the extrapolation to the physical point can be achieved in the short-term.

In this study we neglected finite volume effects, which may have an impact on all results, in particular on the estimate for a_{μ}^{HLO} [131]. A direct numerical estimate of these effects was not possible in this work. The next generation of CLS ensembles will enable us to study these effects numerically. For these ensembles the extraction of the HVP also has to rely on the time-momentum representation, which we only briefly presented in 2.1.1. For the time-momentum representation there is an analytic formula to compute finite volume effects exists [132] based on Poisson-resummation of the spatial vector correlator for small t and the fact that the vector correlator can be related to low-lying energy eigenstates on a torus for large t . This approach requires the time-like pion form factor $F_{\pi}(\omega)$ as an input [63, 133]

Since the new experiment at Fermilab [2] aims to reduce the current precision of the determination of a_{μ}^{exp} , cf. eq. (1.2), by a factor of 4, the leading order hadronic contribution to a_{μ} has to reach sub-percent precision to match the accuracy of the experimental result. To reach this precision with lattice calculations quark-disconnected contributions and iso-spin symmetry breaking have to be taken into account, which we neglected in this work. An upper bound for the quark-disconnected contribution was published in [64] using the time momentum representation [63]. The work on the formalism and the code for the inclusion of iso-spin symmetry breaking effects was started recently. To reduce the total error on a_{μ}^{HLO} due to hadronic contributions a more precise estimate of light-by-light scattering is needed. The strategy for this calculation using lattice QCD was

presented in [117].

Appendix A

Definitions

A.1 Generators of $SU(3)$

The generators T^a of $SU(3)$ can be written in the form of $T^a = \lambda^a/2$, where the λ^a are the Gell-Mann matrices defined as

$$\lambda^1 = \begin{pmatrix} 0 & 1 & 0 \\ 1 & 0 & 0 \\ 0 & 0 & 0 \end{pmatrix}, \quad \lambda^2 = \begin{pmatrix} 0 & -i & 0 \\ i & 0 & 0 \\ 0 & 0 & 0 \end{pmatrix}, \quad \lambda^3 = \begin{pmatrix} 1 & 0 & 0 \\ 0 & -1 & 0 \\ 0 & 0 & 0 \end{pmatrix}, \quad (\text{A.1})$$

$$\lambda^4 = \begin{pmatrix} 0 & 0 & 1 \\ 0 & 0 & 0 \\ 1 & 0 & 0 \end{pmatrix}, \quad \lambda^5 = \begin{pmatrix} 0 & 0 & -i \\ 0 & 0 & 0 \\ i & 0 & 0 \end{pmatrix}, \quad \lambda^6 = \begin{pmatrix} 0 & 0 & 0 \\ 0 & 0 & 1 \\ 0 & 1 & 0 \end{pmatrix}, \quad (\text{A.2})$$

$$\lambda^7 = \begin{pmatrix} 0 & 0 & 0 \\ 0 & 0 & -i \\ 0 & -i & 0 \end{pmatrix}, \quad \lambda^8 = \frac{1}{\sqrt{3}} \begin{pmatrix} 1 & 0 & 0 \\ 0 & 1 & 0 \\ 0 & 0 & -2 \end{pmatrix}. \quad (\text{A.3})$$

The obey the relations

$$[T^a, T^b] = i \sum_{c=1}^8 f^{abc} T^c, \quad (\text{A.4})$$

where f^{abc} are the structure constants of the Lie algebra:

$$f^{123} = 1, \quad (\text{A.5})$$

$$f^{147} = -f^{156} = f^{246} = f^{257} = f^{345} = -f^{367} = \frac{1}{2}, \quad (\text{A.6})$$

$$f^{458} = f^{678} = \frac{3}{2}. \quad (\text{A.7})$$

A.2 Link differential operator

The Link differential operator that acts on a function $f(U)$ depending on the gauge field U is defined as [42]

$$\partial_{x,\mu}^a f(U) = \left. \frac{d}{ds} f(e^{-sX} U) \right|_{s=0}, \quad X(y, \nu) = \begin{cases} T^a & \text{if } (y, \nu) = (x, \mu), \\ 0 & \text{otherwise,} \end{cases} \quad (\text{A.8})$$

where T^a is a generator of $SU(3)$. This would depend on the choice of the basis for the generators, but it can be shown that

$$\partial_{x,\mu} f(U) = T^a \partial_{x,\mu}^a f(U) \quad (\text{A.9})$$

is independent of this choice.

A.3 Euclidean gamma matrices

The Euclidean gamma matrices fulfill the anti-commutation relations

$$\{\gamma_\mu, \gamma_\nu\} = 2\delta_{\mu\nu}\mathbb{1}, \quad (\text{A.10})$$

where $\mu = 1, 2, 3, 4$ and with respect to the gamma matrices in Minkowski space the metric tensor $g_{\mu\nu} = \text{diag}(1, -1, -1, -1)$ was replaced by the metric tensor in Euclidean space. In addition to the 4 matrices defined by eq. (A.10) it is often convenient to define there product as

$$\gamma_5 = \gamma_1 \gamma_2 \gamma_3 \gamma_4, \quad (\text{A.11})$$

which fulfills $\{\gamma_5, \gamma_\mu\} = 0$ and $\gamma_5^2 = \mathbb{1}$. The matrices defined by these relations obey

$$\gamma_\mu = \gamma_\mu^\dagger = \gamma_\mu^{-1} \quad (\text{A.12})$$

where $\mu = 1, 2, 3, 4, 5$. An explicit representation of the gamma matrices reads:

$$\gamma_1 = \begin{pmatrix} 0 & 0 & 0 & -i \\ 0 & 0 & -i & 0 \\ 0 & i & 0 & 0 \\ i & 0 & 0 & 0 \end{pmatrix}, \quad \gamma_2 = \begin{pmatrix} 0 & 0 & 0 & -1 \\ 0 & 0 & 1 & 0 \\ 0 & 1 & 0 & 0 \\ -1 & 0 & 0 & 0 \end{pmatrix}, \quad \gamma_3 = \begin{pmatrix} 0 & 0 & -i & 0 \\ 0 & 0 & 0 & i \\ i & 0 & 0 & 0 \\ 0 & -i & 0 & 0 \end{pmatrix}, \quad (\text{A.13})$$

$$\gamma_4 = \begin{pmatrix} 0 & 0 & 1 & 0 \\ 0 & 0 & 0 & 1 \\ 1 & 0 & 0 & 0 \\ 0 & 1 & 0 & 0 \end{pmatrix}, \quad \gamma_5 = \begin{pmatrix} 1 & 0 & 0 & 0 \\ 0 & 1 & 0 & 0 \\ 0 & 0 & -1 & 0 \\ 0 & 0 & 0 & -1 \end{pmatrix}. \quad (\text{A.14})$$

A.4 Derivation of the hadronic vacuum polarization

To obtain the hadronic vacuum polarization in terms of propagators we start from the definitions of eqs. (2.21, 2.22) and include all Dirac (α, β, \dots) and color indices (a, b, \dots),

$$\begin{aligned} \langle V_\mu^{(f,c)}(n) V_\nu^{(f,l)}(m) \rangle &= \langle \frac{q_f}{2} \left\{ \bar{\psi}_a^\alpha(n + a\hat{\mu})(1 + \gamma_\mu)^{\alpha\beta} (U_\mu^\dagger)_{ab}(n) \psi_b^\beta(n) \right. \\ &\quad \left. - \bar{\psi}_a^\alpha(n)(1 - \gamma_\mu)^{\alpha\beta} (U_\mu)_{ab}(n) \psi_b^\beta(n + a\hat{\mu}) \right\} \\ &\quad \left. Z_V q_f \bar{\psi}_c^\gamma(m) (\gamma_\nu)^{\gamma\delta} \psi_c^\delta(m) \right\rangle. \end{aligned} \quad (\text{A.15})$$

Contracting the fermions and switching to propagator notation ($S_{ab}^{\alpha\beta}(n, m) = \psi_a^\alpha(n) \bar{\psi}_b^\beta(m)$) we obtain

$$\begin{aligned} &= \frac{q_f^2 Z_V}{2} \langle -(\gamma_\nu)^{\gamma\delta} S_{ca}^{\delta\alpha}(m, n + a\hat{\mu})(1 + \gamma_\mu)^{\alpha\beta} (U_\mu^\dagger)_{ab}(n) S_{bc}^{\beta\gamma}(n, m) \\ &\quad + (\gamma_\nu)^{\gamma\delta} S_{ca}^{\delta\alpha}(m, n)(1 - \gamma_\mu)^{\alpha\beta} (U_\mu)_{ab}(n) S_{bc}^{\beta\gamma}(n + a\hat{\mu}, m) \\ &\quad + (\gamma_\nu)^{\gamma\delta} S_{cc}^{\delta\gamma}(m, m)(1 + \gamma_\mu)^{\alpha\beta} (U_\mu^\dagger)_{ab}(n) S_{ba}^{\beta\alpha}(n, n + a\hat{\mu}) \\ &\quad - (\gamma_\nu)^{\gamma\delta} S_{cc}^{\delta\gamma}(m, m)(1 - \gamma_\mu)^{\alpha\beta} (U_\mu)_{ab}(n) S_{ba}^{\beta\alpha}(n, n + a\hat{\mu}) \rangle, \end{aligned} \quad (\text{A.16})$$

which we can rewrite in terms of traces taken over Dirac and colour space,

$$\begin{aligned} &= \frac{q_f^2 Z_V}{2} \langle \text{Tr} \left[-\gamma_\nu S(m, n + a\hat{\mu})(1 + \gamma_\mu) U_\mu^\dagger(n) S(n, m) \right. \\ &\quad \left. + \gamma_\nu S(m, n)(1 - \gamma_\mu) U_\mu(n) S(n + a\hat{\mu}, m) \right] \\ &\quad \left. + \text{Tr} [\gamma_\nu S(m, m)] \text{Tr} \left[(1 + \gamma_\mu) U_\mu^\dagger(n) S(n, n + a\hat{\mu}) \right] \right. \\ &\quad \left. - \text{Tr} [\gamma_\nu S(m, m)] \text{Tr} \left[(1 - \gamma_\mu) U_\mu(n) S(n, n + a\hat{\mu}) \right] \right\rangle. \end{aligned} \quad (\text{A.17})$$

Terms involving propagators of the type $S(m, m)$ are called quark-disconnected contributions. We discuss these contributions briefly in chapter 2.1.1. From now on we drop the disconnected contributions. Using translational invariance we can set $m = 0$, and with γ_5 -hermiticity ($S(a, b) = \gamma_5 S^\dagger(b, a) \gamma_5$) we can rewrite this to

$$= \frac{q_f^2 Z_V}{2} \left\langle -\text{Tr} \left[\gamma_\nu \gamma_5 S^\dagger(n + a\hat{\mu}, 0) \gamma_5 (1 + \gamma_\mu) U_\mu^\dagger(n) S(n, 0) \right] \right. \\ \left. + \text{Tr} \left[\gamma_\nu \gamma_5 S^\dagger(n, 0) \gamma_5 (1 - \gamma_\mu) U_\mu(n) S(n + a\hat{\mu}, 0) \right] \right\rangle, \quad (\text{A.18})$$

where we now find that only one inversion is required to compute the quark-connected part of the leading order hadronic vacuum polarization tensor.

Appendix B

Fit results for the extrapolation of the Adler function to the continuum

B.1 The light quark contribution: the Curvature Limit method.

In the following we show plots for the light quark contribution based on the Curvature Limit method similar to those already shown for the Plateau of Slopes method in [3.2.2.1](#).

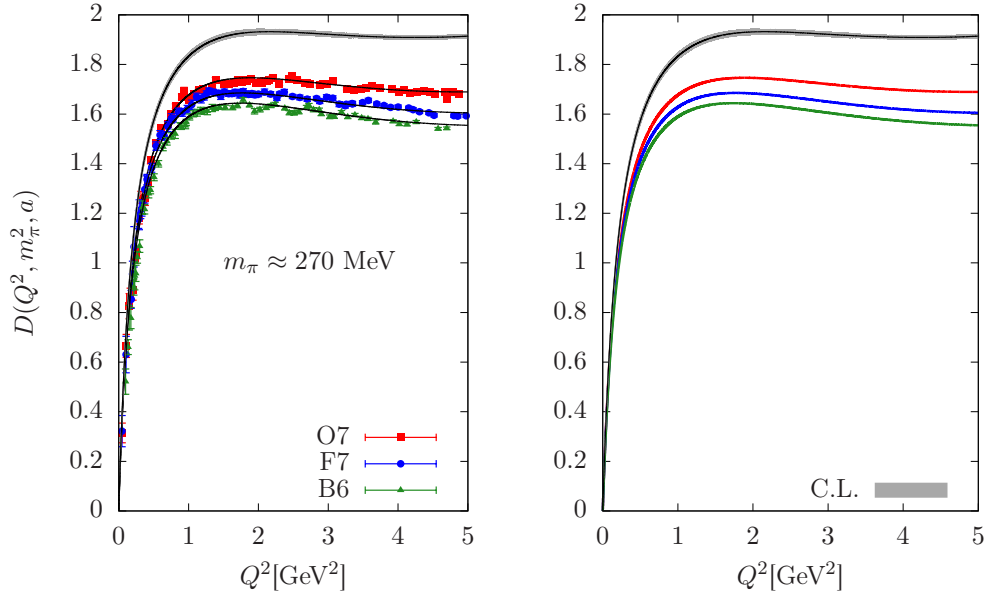


FIGURE B.1: We study the continuum limit for the light quark contribution for the fit ansatz $D_{3,2,4}(Q^2, m_\pi^2, a)$ using the ensembles B6 ($a=0.0755$ fm), F7 ($a=0.0658$ fm), and O7 ($a=0.0486$ fm), which are roughly at $m_\pi \approx 270$ MeV. For this ansatz using all 11 ensembles we obtain $\chi^2/\text{dof} = 1.3$. On the left we show the data for the Curvature Limit method and the extrapolation in gray to the continuum limit at $m_\pi = 270$ MeV. On the right the corresponding fit results are shown in the respective colors for the parameters of each ensemble. The central values of the fit result are shown as dashed lines in both plots, the bands show the statistical error.

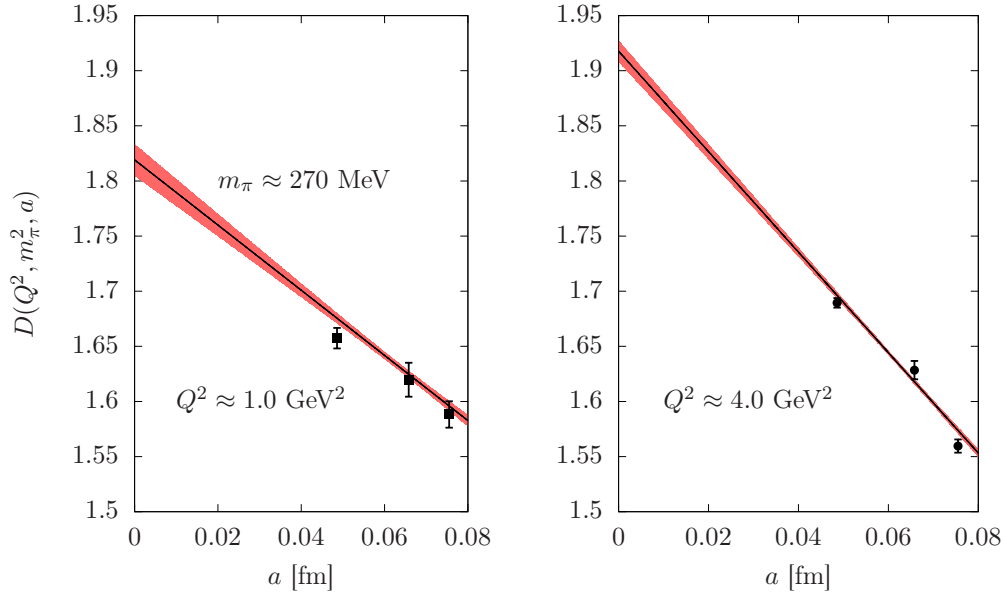


FIGURE B.2: At fixed momentum transfers $Q^2 = 1.0, 4.0$ GeV² and fixed pion mass at $m_\pi \approx 270$ MeV, we can look at the lattice spacing dependence directly. We show the result for the fit ansatz $D_{3,2,4}(Q^2, m_\pi^2, a)$ ($\chi^2/\text{dof} = 1.3$) using all 11 ensembles evaluated at $Q^2 = 4.0$ GeV² on the left and at $Q^2 = 1.0$ GeV² on the right, respectively, for the Curvature Limit method for the light quark contribution. The central values of the fit are shown as dashed lines. The data points shown correspond to the results on the ensembles B6 ($a=0.0755$ fm), F7 ($a=0.0658$ fm), and O7 ($a=0.0486$ fm).

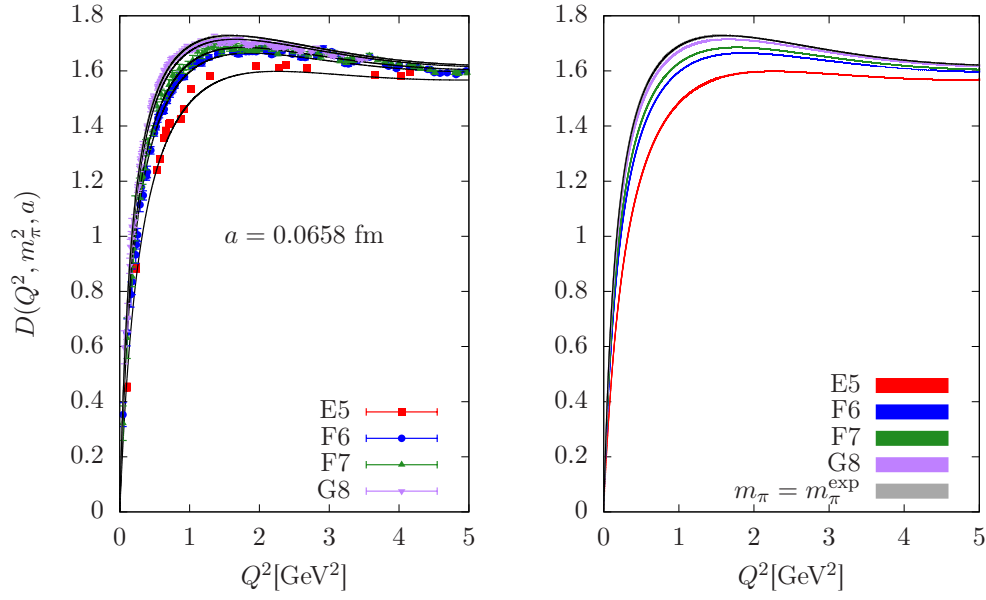


FIGURE B.3: To study the pion mass dependence of the light quark contribution over the considered Q^2 fit interval, we use the data of the intermediate lattice spacing ($a=0.0658$ fm) for the fit ansatz $D_{3,2,4}(Q^2, m_\pi^2, a)$ ($\chi^2/\text{dof} = 1.3$) using all 11 ensembles. On the left we show the data for the Curvature Limit method and on the right the corresponding fits with the respective colors. The dashed lines correspond to the central values of the fit on both sides. The gray band represents the extrapolation to the physical pion mass for $a = 0.0658$ fm.

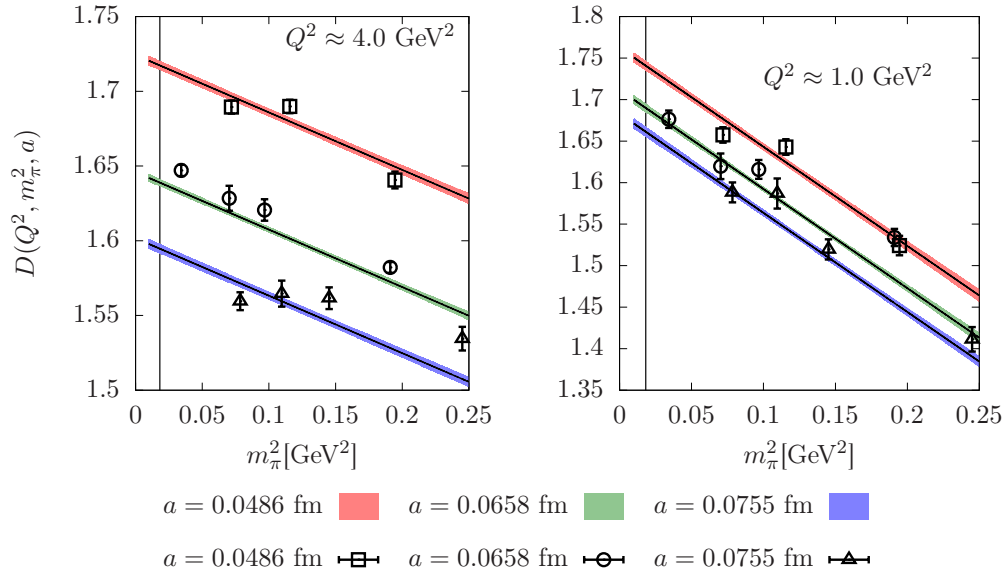


FIGURE B.4: When we fix the momentum transfer to $Q^2 = 1.0, 4.0$ GeV^2 we can study the pion mass dependence across the different lattice spacings. We evaluate the fit ansatz $D_{3,2,4}(Q^2, m_\pi^2, a)$ ($\chi^2/\text{dof} = 1.3$) using all 11 ensembles for the fit to the data obtained via the Curvature Limit method for the light quark contribution at $Q^2 = 4.0$ GeV^2 on the left and at $Q^2 = 1.0$ GeV^2 on the right, respectively. The vertical line denotes the physical pion mass.

B.2 The strange quark contribution: the Curvature Limit method.

In the following we show plots of the Adler function determined via the Curvature Limit method similar to the plots shown in 3.2.2.2.

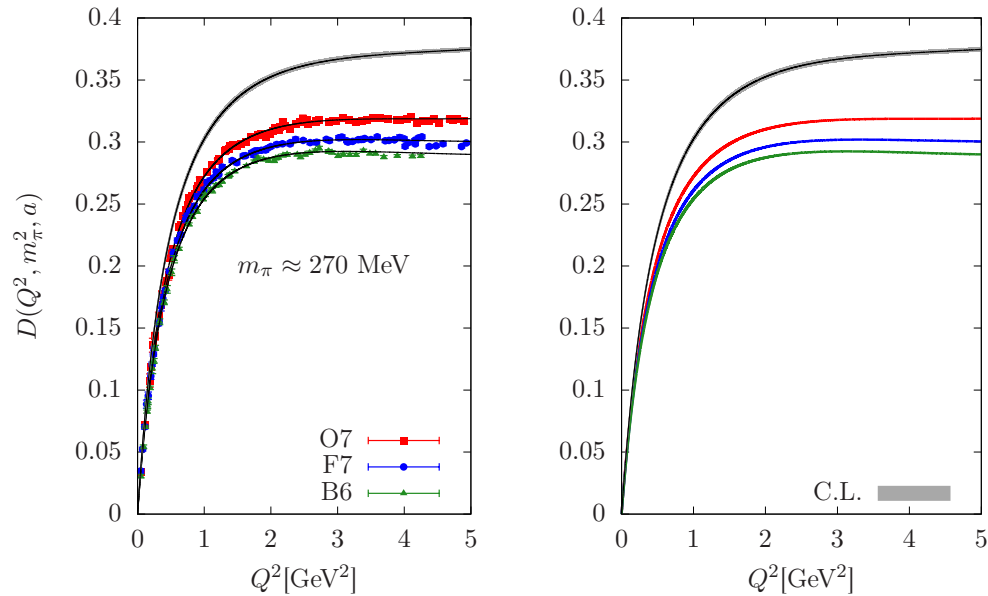


FIGURE B.5: We study the continuum limit for the strange quark contribution for the fit ansatz $D_{3,2,4}(Q^2, m_\pi^2, a)$ using the ensembles B6 ($a=0.0755$ fm), F7 ($a=0.0658$ fm), and O7 ($a=0.0486$ fm), which are roughly at $m_\pi \approx 270$ MeV. For this ansatz using all 11 ensembles we obtain $\chi^2/\text{dof} = 1.0$. On the left we show the data for the Curvature Limit method and the extrapolation in gray to the continuum limit at $m_\pi = 270$ MeV. On the right the corresponding fit results are shown in the respective colors for the parameters of each ensemble. The central values of the fit result are shown as dashed lines in both plots, the bands show the statistical error.

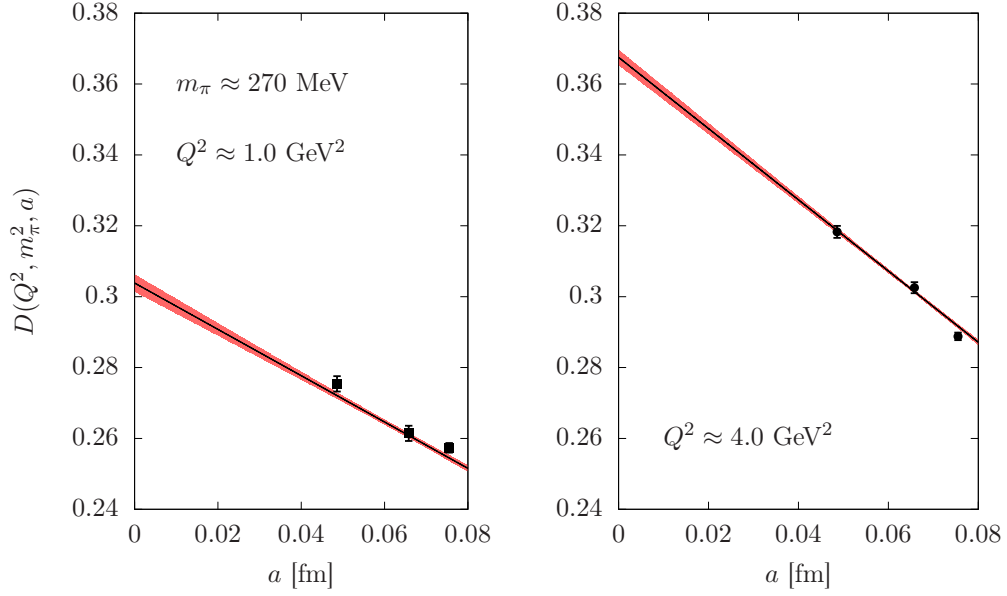


FIGURE B.6: At fixed momentum transfers $Q^2 = 1.0, 4.0 \text{ GeV}^2$ and fixed pion mass at $m_\pi \approx 270 \text{ MeV}$, we can look at the lattice spacing dependence directly. We show the result for the fit ansatz $D_{3,2,4}(Q^2, m_\pi^2, a)$ ($\chi^2/\text{dof} = 0.9$) using all 11 ensembles evaluated at $Q^2 = 4.0 \text{ GeV}^2$ on the left and at $Q^2 = 1.0 \text{ GeV}^2$ on the right, respectively, for the Curvature Limit method for the strange quark contribution. The central values of the fit are shown as dashed lines. The data points shown correspond to the results on the ensembles B6 ($a=0.0755 \text{ fm}$), F7 ($a=0.0658 \text{ fm}$), and O7 ($a=0.0486 \text{ fm}$).

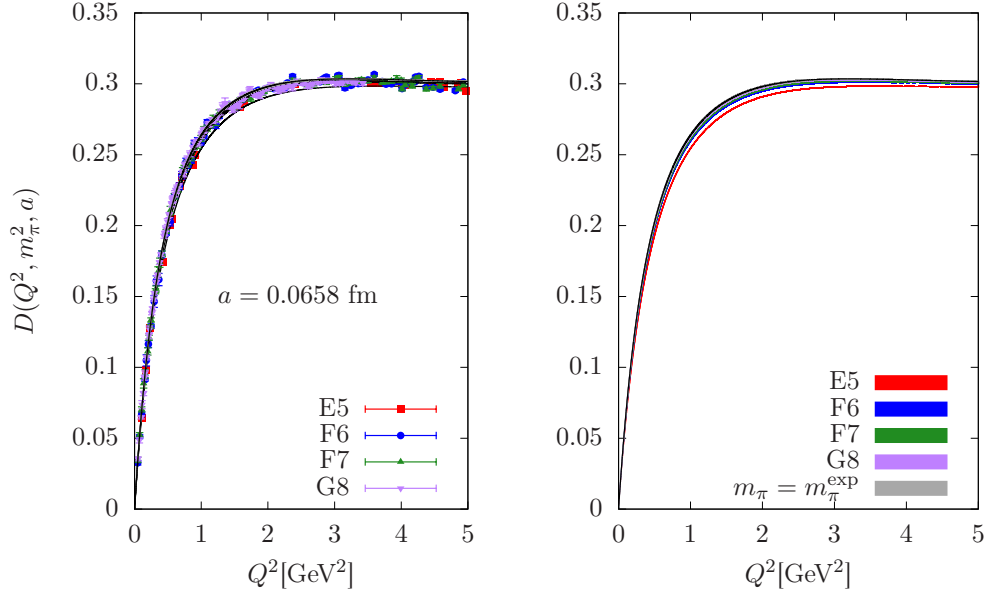


FIGURE B.7: To study the pion mass dependence of the strange quark contribution over the considered Q^2 fit interval, we use the data of the intermediate lattice spacing ($a=0.0658 \text{ fm}$) for the fit ansatz $D_{3,2,4}(Q^2, m_\pi^2, a)$ ($\chi^2/\text{dof} = 1.0$) using all 11 ensembles. On the left we show the data for the Curvature Limit method and on the right the corresponding fits with the respective colors. The dashed lines correspond to the central values of the fit on both sides. The gray band represents the extrapolation to the physical pion mass for $a = 0.0658 \text{ fm}$.

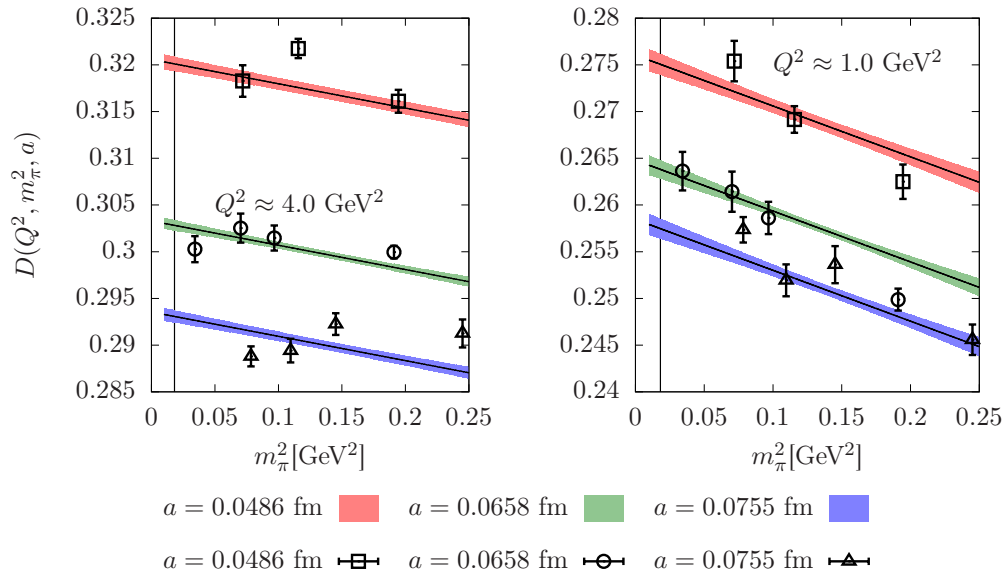


FIGURE B.8: When we fix the momentum transfer to $Q^2 = 1.0, 4.0 \text{ GeV}^2$ we can study the pion mass dependence across the different lattice spacings. We evaluate the fit ansatz $D_{3,2,4}(Q^2, m_\pi^2, a)$ ($\chi^2/\text{dof} = 1.0$) using all 11 ensembles for the fit to the data obtained via the Curvature Limit method for the strange quark contribution at $Q^2 = 4.0 \text{ GeV}^2$ on the left and at $Q^2 = 1.0 \text{ GeV}^2$ on the right, respectively. The vertical line denotes the physical pion mass.

B.3 The charm quark contribution: the Curvature Limit method.

The following plots show the results for the data obtained via the Curvature Limit method for the charm quark contribution. We find a similar behaviour to the example discussed in more detail in [3.2.2.3](#).

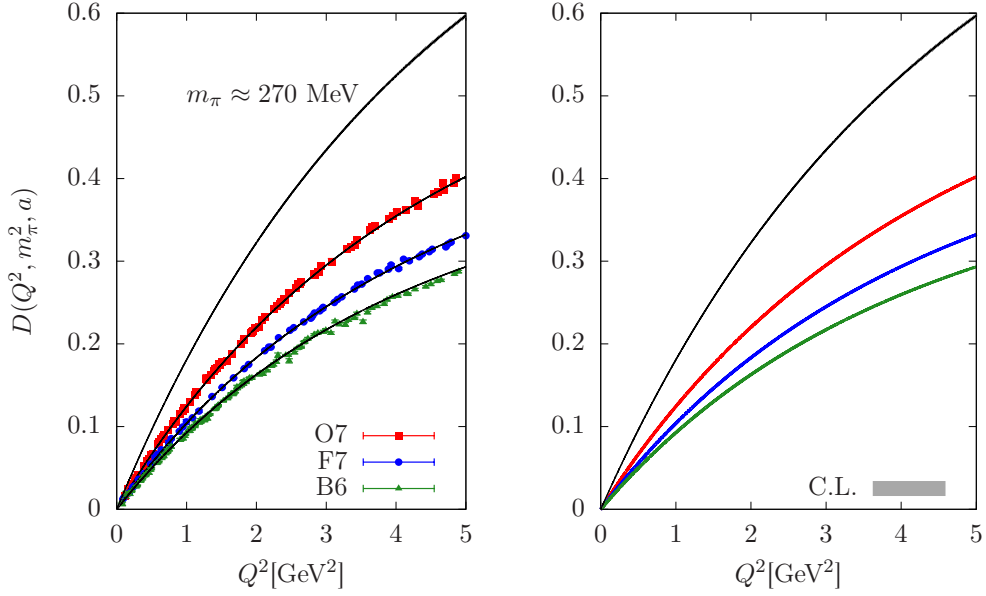


FIGURE B.9: We take the continuum limit at a fixed pion mass of $m_\pi \approx 270$ MeV for the ensembles B6 ($a=0.0755$ fm), F7 ($a=0.0658$ fm), and O7 ($a=0.0486$ fm) for the charm quark contribution. We show the data for the Curvature Limit method with the extrapolation to the continuum limit in gray at this pion mass on the left, and the corresponding fit with the statistical error bands for the fit ansatz $D_{1,1,4}(Q^2, m_\pi^2, a)$ with $\chi^2/\text{dof} = 3.0$ on the right. The central values of the fit are shown in dashed black lines.

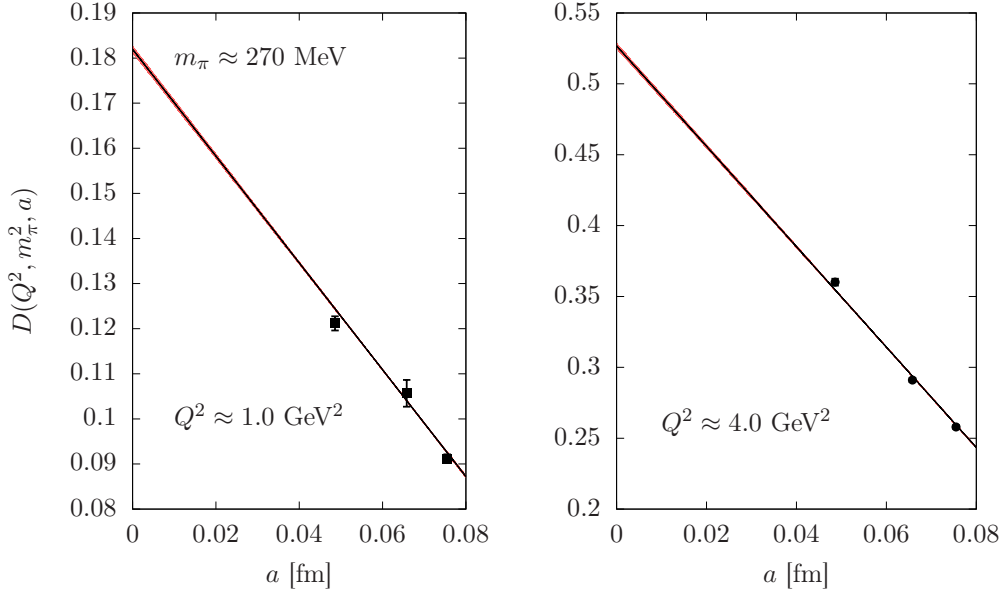


FIGURE B.10: We fix the momentum to $Q^2 = 1.0$ GeV² (left) and $Q^2 = 4.0$ GeV² (right) for $m_\pi \approx 270$ MeV and vary the lattice spacing to test the linear behaviour of lattice artifacts. We show the fit ansatz $D_{1,1,4}(Q^2, m_\pi^2, a)$ ($\chi^2/\text{dof} = 3.0$) using all 11 ensembles for the charm quark contribution based on the data of the Curvature Limit method. The data points shown correspond to the results closest to the respective values of Q^2 on the ensembles B6 ($a=0.0755$ fm), F7 ($a=0.0658$ fm), and O7 ($a=0.0486$ fm).

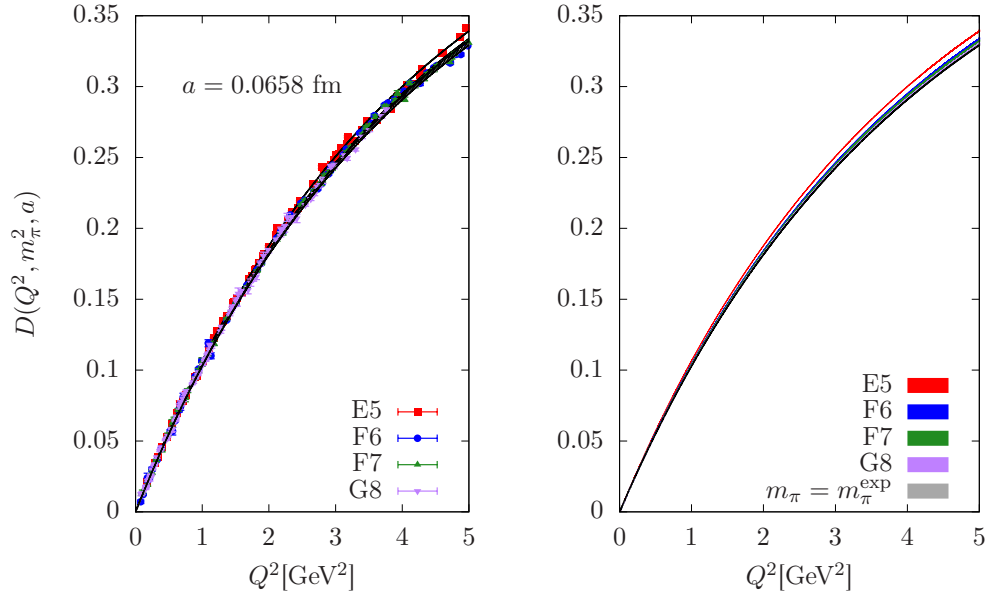


FIGURE B.11: We study the pion mass dependence by fixing the lattice spacing to $a=0.0658$ fm for the fit ansatz $D_{1,1,4}(Q^2, m_\pi^2, a)$ ($\chi^2/\text{dof} = 3.0$) using all 11 ensembles for the data of the Curvature Limit method for the charm quark contribution (left) and the fit result with the statistical error (right). The dashed black lines denote the central values of the fit. The gray band depicts the extrapolation to the physical pion mass at $a=0.0658$ fm.

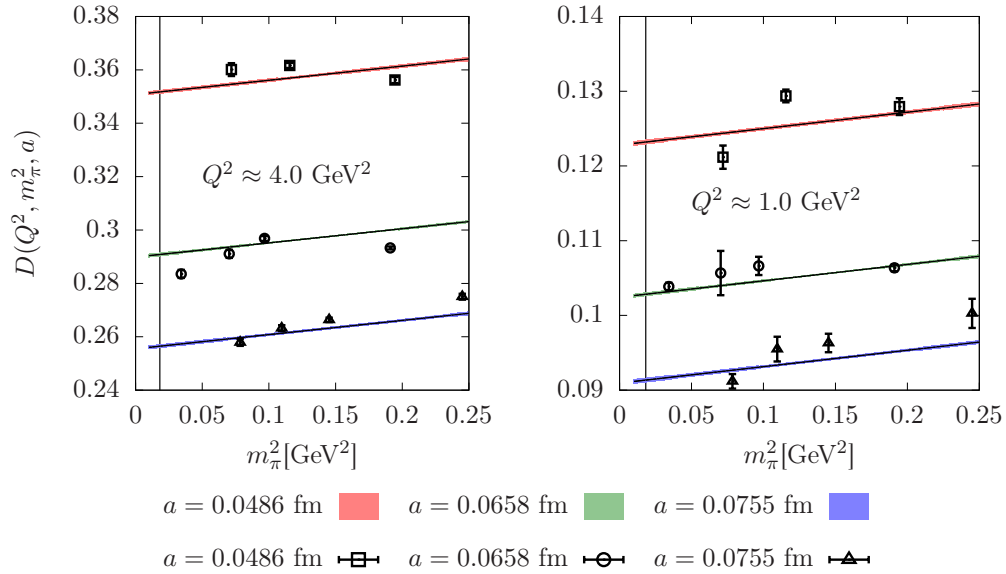


FIGURE B.12: With the momentum fixed to $Q^2 = 1.0$ GeV² (right) and $Q^2 = 4.0$ GeV² (left) we look at the pion mass dependence in more detail for the different lattice spacings. The plots show the result for the fit ansatz $D_{1,1,4}(Q^2, m_\pi^2, a)$ ($\chi^2/\text{dof} = 3.0$) using all 11 ensembles for the charm quark contribution based on the data of the Curvature Limit method. The physical pion mass is shown as a vertical line.

B.4 a_μ^{HLO} determined via the Adler function

Label	Plateau of Slopes method			Curvature Limit method		
	$a_\mu^{\text{HLO}} \times 10^{10}$	%	χ^2/dof	$a_\mu^{\text{HLO}} \times 10^{10}$	%	χ^2/dof
All 11 ensembles						
$D_{2,2,3}$	524.15(9.47)	1.8	4.47	531.52(9.65)	1.8	3.41
$D_{3,2,3}$	650.32(26.41)	4.1	3.89	657.41(24.77)	3.8	3.06
$D_{2,2,4}$	510.81(7.91)	1.5	5.15	515.76(8.26)	1.6	4.09
$D_{3,2,4}$	644.43(20.34)	3.2	3.89	645.87(21.57)	3.3	3.10
$D_{3,3,3}$	660.74(41.33)	6.3	2.97	687.90(32.15)	4.7	2.59
$D_{4,3,3}$	666.55(42.32)	6.3	3.01	635.44(27.91)	4.4	2.55
$D_{3,3,4}$	728.21(42.33)	5.8	3.07	681.30(29.01)	4.3	2.59
$D_{4,3,4}$	664.51(49.11)	7.4	3.02	670.80(37.99)	5.7	2.59
$m_\pi < 400$ MeV: 8 ensembles						
$D_{2,2,3}$	540.85(13.45)	2.5	3.15	497.66(8.23)	1.7	2.87
$D_{3,2,3}$	594.69(41.46)	7.0	3.27	534.36(14.12)	2.6	2.68
$D_{2,2,4}$	515.74(9.43)	1.8	3.78	527.43(9.47)	1.8	3.16
$D_{3,2,4}$	595.11(22.20)	3.7	3.29	611.17(21.39)	3.5	2.68
$D_{3,3,3}$	780.77(127.67)	16.4	2.12	883.47(135.05)	15.3	2.02
$D_{4,3,3}$	746.92(95.97)	12.8	2.11	786.56(139.09)	17.7	2.03
$D_{3,3,4}$	1105.71(233.61)	21.1	2.23	889.01(110.81)	12.5	2.04
$D_{4,3,4}$	1068.08(240.02)	22.5	2.22	861.99(106.59)	12.4	2.03
$a < 0.070$ fm: 7 ensembles						
$D_{2,2,3}$	453.71(8.57)	1.9	2.95	456.94(8.49)	1.9	2.94
$D_{3,2,3}$	479.66(12.28)	2.6	2.76	496.17(14.99)	3.0	2.67
$D_{2,2,4}$	496.73(9.89)	2.0	5.15	501.51(10.37)	2.1	3.91
$D_{3,2,4}$	620.00(21.79)	3.5	3.82	627.78(24.85)	4.0	2.87
$D_{3,3,3}$	704.91(92.21)	13.1	2.15	724.63(66.70)	9.2	2.14
$D_{4,3,3}$	1026.93(12746.72)	1241.2	2.38	685.88(56.40)	8.2	1.98
$D_{3,3,4}$	797.00(72.93)	9.2	2.57	711.62(44.06)	6.2	2.14
$D_{4,3,4}$	744.18(73.41)	9.9	2.53	691.38(44.73)	6.5	2.14
$m_\pi < 400$ MeV and $a < 0.070$ fm: 5 ensembles						
$D_{2,2,3}$	510.54(17.54)	3.4	2.16	514.57(17.73)	3.4	2.07
$D_{3,2,3}$	504.95(18.45)	3.7	2.12	515.47(17.90)	3.5	2.08
$D_{2,2,4}$	476.00(16.03)	3.4	3.07	491.98(16.43)	3.3	2.80
$D_{3,2,4}$	518.06(22.20)	4.3	2.78	555.46(25.99)	4.7	2.38
$D_{3,3,3}$	682.98(128.53)	18.8	1.42	704.26(115.79)	16.4	1.39
$D_{4,3,3}$	616.62(96.52)	15.7	1.40	700.59(117.84)	16.8	1.39
$D_{3,3,4}$	1695.37(904.57)	53.4	1.82	1226.60(379.16)	30.9	1.62
$D_{4,3,4}$	2033.86($7 \cdot 10^{13}$)	-	1.79	1134.58(308.74)	27.2	1.64

TABLE B.1: Results for the determination of a_μ^{HLO} via the Adler function for the light-quark contribution. We show a_μ^{HLO} in units of 10^{10} , the relative precision in %, and the corresponding uncorrelated χ^2/dof . Due to large fluctuations in the low Q^2 regime we drop the higher order Padé ansätze [3,3] and [4,3] from the analysis.

Label	Plateau of Slopes method			Curvature Limit method		
	$a_\mu^{\text{HLO}} \times 10^{10}$	%	χ^2/dof	$a_\mu^{\text{HLO}} \times 10^{10}$	%	χ^2/dof
All 11 ensembles						
$D_{2,2,3}$	51.13(59)	1.2	2.52	53.18(72)	1.4	2.39
$D_{3,2,3}$	52.23(76)	1.5	2.46	52.49(69)	1.3	2.32
$D_{2,2,4}$	51.59(62)	1.2	2.65	52.64(58)	1.1	2.49
$D_{3,2,4}$	53.22(75)	1.4	2.53	54.14(66)	1.2	2.39
$D_{3,3,3}$	55.12(1.02)	1.8	2.36	-	-	-
$D_{4,3,3}$	54.71(85)	1.6	2.36	55.01(75)	1.4	2.21
$D_{3,3,4}$	55.94(1.84)	3.3	2.37	55.39(78)	1.4	2.24
$D_{4,3,4}$	55.66(1.47)	2.6	2.33	54.84(92)	1.7	2.33
$m_\pi < 400$ MeV: 8 ensembles						
$D_{2,2,3}$	52.41(72)	1.4	1.34	53.06(67)	1.3	1.55
$D_{3,2,3}$	53.23(88)	1.7	1.30	53.25(73)	1.4	1.55
$D_{2,2,4}$	52.76(78)	1.5	1.66	53.81(72)	1.3	1.76
$D_{3,2,4}$	54.26(94)	1.7	1.56	54.51(77)	1.4	1.73
$D_{3,3,3}$	52.53(88)	1.7	1.33	53.06(85)	1.6	1.55
$D_{4,3,3}$	53.23(87)	1.6	1.30	53.36(79)	1.5	1.55
$D_{3,3,4}$	57.61(2.00)	3.5	1.44	56.97(1.72)	3.0	1.61
$D_{4,3,4}$	56.54(1.96)	3.5	1.40	56.88(1.26)	2.2	1.61
$a < 0.070$ fm: 7 ensembles						
$D_{2,2,3}$	48.52(71)	1.5	1.58	50.14(77)	1.5	1.67
$D_{3,2,3}$	48.81(73)	1.5	1.58	50.39(78)	1.5	1.67
$D_{2,2,4}$	48.80(74)	1.5	2.01	51.12(83)	1.6	2.22
$D_{3,2,4}$	49.62(81)	1.6	1.97	52.32(89)	1.7	2.15
$D_{3,3,3}$	48.31(99)	2.1	1.56	50.16(93)	1.8	1.61
$D_{4,3,3}$	48.67(89)	1.8	1.56	50.13(91)	1.8	1.62
$D_{3,3,4}$	51.12(1.11)	2.2	1.84	53.52(94)	1.7	2.01
$D_{4,3,4}$	49.70(91)	1.8	1.97	53.51(1.03)	1.9	2.02
$m_\pi < 400$ MeV and $a < 0.070$ fm: 5 ensembles						
$D_{2,2,3}$	50.33(1.33)	2.6	0.84	50.82(1.35)	2.7	1.14
$D_{3,2,3}$	50.65(1.38)	2.7	0.83	50.96(1.38)	2.7	1.14
$D_{2,2,4}$	49.39(1.52)	3.1	1.03	50.05(1.49)	3.0	1.26
$D_{3,2,4}$	49.99(1.61)	3.2	1.01	50.32(1.56)	3.1	1.26
$D_{3,3,3}$	50.58(1.35)	2.7	0.83	51.08(1.36)	2.7	1.15
$D_{4,3,3}$	50.76(1.39)	2.7	0.82	51.02(1.37)	2.7	1.15
$D_{3,3,4}$	52.19(3.10)	5.9	0.98	52.35(2.65)	5.1	1.23
$D_{4,3,4}$	50.00(1.62)	3.2	1.01	52.72(2.67)	5.1	1.24

TABLE B.2: Results for the determination of a_μ^{HLO} via the Adler function for the strange-quark contribution. We show a_μ^{HLO} in units of 10^{10} , the relative precision in %, and the corresponding uncorrelated χ^2/dof . Due to large fluctuations in the low Q^2 regime we drop the higher order Padé ansätze [3,3] and [4,3] from the analysis.

Charm	Plateau of Slopes method			Curvature Limit method		
Label	$a_\mu^{\text{HLO}} \times 10^{10}$	%	χ^2/dof	$a_\mu^{\text{HLO}} \times 10^{10}$	%	χ^2/dof
All 11 ensembles						
$D_{1,1,3}$	13.33(6)	0.4	5.93	13.43(6)	0.4	6.56
$D_{2,1,3}$	13.45(6)	0.5	5.86	13.56(6)	0.5	6.50
$D_{1,1,4}$	13.32(6)	0.4	5.95	13.41(6)	0.4	6.66
$D_{2,1,4}$	13.44(6)	0.5	5.89	13.55(6)	0.5	6.59
$m_\pi < 400$ MeV: 8 ensembles						
$D_{1,1,3}$	13.52(8)	0.6	3.14	13.68(8)	0.6	3.99
$D_{2,1,3}$	13.61(8)	0.6	3.10	13.78(8)	0.6	3.97
$D_{1,1,4}$	13.51(7)	0.5	3.15	13.64(7)	0.5	4.06
$D_{2,1,4}$	13.60(8)	0.6	3.11	13.75(7)	0.5	4.02
$a < 0.070$ fm: 7 ensembles						
$D_{1,1,3}$	13.44(8)	0.6	3.72	13.39(8)	0.6	4.91
$D_{2,1,3}$	13.62(9)	0.7	3.64	13.54(9)	0.6	4.86
$D_{1,1,4}$	13.53(8)	0.6	4.02	13.49(8)	0.6	5.14
$D_{2,1,4}$	13.74(9)	0.6	3.84	13.66(8)	0.6	5.03
$m_\pi < 400$ MeV and $a < 0.070$ fm: 5 ensembles						
$D_{1,1,3}$	13.46(18)	1.3	2.58	13.45(19)	1.4	3.47
$D_{2,1,3}$	13.56(19)	1.4	2.54	13.52(19)	1.4	3.46
$D_{1,1,4}$	13.48(14)	1.0	2.57	13.49(15)	1.1	3.47
$D_{2,1,4}$	13.58(15)	1.1	2.53	13.56(16)	1.1	3.46

TABLE B.3: Results for the determination of a_μ^{HLO} via the Adler function for the light-quark contribution. We show a_μ^{HLO} in units of 10^{10} , the relative precision in %, and the corresponding uncorrelated χ^2/dof .

Appendix C

Fit results for the extraction of

$$a_{\mu}^{\text{HLO}}$$

C.1 Fits to the VPF for the hybrid method

In this section we list the scans we performed to determine Q_{cut}^2 for the various flavors and the two Padé ansätze [1,1] and [2,1] for the hybrid method. For convenience we show $a_{\mu}^{\text{HLO}} \times 10^{10}$. We discussed the hybrid method in detail in [4.3.1](#).

C.1.1 The light-quark contribution

C.1.1.1 Fit ansatz: Padé [1,1]

Q_{cut}^2 [GeV ²]	a_μ^{I}	a_μ^{II}	a_μ^{HLO}	$\chi_{\text{corr}}^2/\text{dof}$	N
0.3283	242.96(15.25)	15.10(0.34)	258.06(15.56)	0.86	8
0.3423	242.89(15.04)	11.84(0.24)	254.73(15.27)	0.98	9
0.3967	256.05(13.30)	11.16(0.20)	267.22(13.49)	0.90	10
0.4182	257.46(13.33)	9.76(0.17)	267.22(13.50)	1.01	11
0.4625	258.37(7.66)	9.75(0.12)	268.12(7.76)	0.92	12
0.4840	258.22(6.59)	9.15(0.10)	267.38(6.69)	0.83	13
0.5250	259.51(6.63)	8.17(0.09)	267.69(6.70)	0.75	14
0.5390	259.96(6.38)	6.95(0.07)	266.91(6.45)	0.68	15
0.5883	259.25(5.73)	6.89(0.07)	266.15(5.79)	0.63	16
0.5908	260.22(5.66)	6.90(0.07)	267.11(5.72)	0.58	17
0.6022	260.14(5.62)	6.66(0.06)	266.80(5.67)	0.61	18
0.6048	256.44(4.08)	6.63(0.06)	263.08(4.14)	0.58	19
0.6592	257.51(4.09)	5.57(0.05)	263.08(4.13)	0.60	20
0.6807	257.10(3.92)	5.56(0.05)	262.66(3.96)	0.56	21
0.7250	257.76(3.89)	5.05(0.04)	262.81(3.93)	0.64	22
0.7440	259.08(3.91)	4.87(0.04)	263.94(3.95)	0.60	23
0.7465	259.13(3.79)	4.84(0.04)	263.97(3.83)	0.57	24

TABLE C.1: Scan of fit windows on A3 for the ud contribution using Padé [1,1].

Q_{cut}^2 [GeV ²]	a_μ^{I}	a_μ^{II}	a_μ^{HLO}	$\chi_{\text{corr}}^2/\text{dof}$	N
0.3283	329.30(24.26)	17.94(0.49)	347.24(24.72)	2.55	8
0.3423	324.07(23.12)	13.97(0.34)	338.04(23.46)	2.23	9
0.3967	328.42(20.39)	13.02(0.29)	341.44(20.65)	2.43	10
0.4182	325.80(20.75)	11.29(0.25)	337.09(21.00)	2.13	11
0.4625	332.64(14.45)	11.34(0.19)	343.98(14.65)	2.35	12
0.4840	327.68(11.11)	10.57(0.15)	338.25(11.26)	2.13	13
0.5250	332.43(11.80)	9.44(0.14)	341.87(11.91)	1.97	14
0.5390	329.16(11.15)	7.96(0.11)	337.12(11.25)	1.77	15
0.5883	324.06(9.37)	7.86(0.09)	331.91(9.46)	1.71	16
0.5908	322.62(9.18)	7.84(0.09)	330.45(9.27)	1.68	17
0.6022	322.02(9.09)	7.57(0.09)	329.59(9.16)	1.61	18
0.6048	315.72(7.07)	7.52(0.08)	323.24(7.13)	1.52	19
0.6592	317.43(7.15)	6.29(0.06)	323.72(7.20)	1.51	20
0.6807	315.91(6.19)	6.28(0.06)	322.20(6.24)	1.40	21
0.7250	315.56(6.09)	5.69(0.05)	321.25(6.13)	1.34	22
0.7440	313.43(5.91)	5.46(0.05)	318.89(5.96)	1.30	23
0.7465	312.65(5.77)	5.42(0.05)	318.07(5.80)	1.31	24

TABLE C.2: Scan of fit windows on A4 for the ud contribution using Padé [1,1].

Q_{cut}^2 [GeV ²]	a_μ^{I}	a_μ^{II}	a_μ^{HLO}	$\chi_{\text{corr}}^2/\text{dof}$	N
0.3283	351.77(45.31)	19.17(0.97)	370.94(46.27)	1.01	8
0.3423	357.09(46.44)	14.79(0.68)	371.88(47.12)	0.95	9
0.3967	360.18(44.79)	13.76(0.60)	373.95(45.37)	0.89	10
0.4182	363.76(44.13)	11.97(0.49)	375.73(44.60)	0.78	11
0.4625	318.55(25.62)	11.46(0.34)	330.01(25.93)	0.72	12
0.4840	335.33(32.80)	10.92(0.37)	346.25(33.23)	0.85	13
0.5250	317.70(20.70)	9.56(0.24)	327.26(20.93)	0.71	14
0.5390	318.69(20.91)	8.12(0.19)	326.81(21.08)	0.72	15
0.5883	320.62(19.06)	8.07(0.18)	328.69(19.23)	0.71	16
0.5908	314.41(18.44)	7.98(0.17)	322.39(18.61)	0.64	17
0.6022	317.17(17.80)	7.73(0.16)	324.90(17.95)	0.78	18
0.6048	324.12(19.85)	7.77(0.17)	331.90(20.02)	0.71	19
0.6592	324.30(19.67)	6.50(0.14)	330.80(19.80)	0.64	20
0.6807	315.96(12.97)	6.45(0.11)	322.41(13.07)	0.61	21
0.7250	316.98(12.40)	5.86(0.10)	322.84(12.50)	0.60	22
0.7440	317.77(13.37)	5.63(0.09)	323.40(13.46)	0.57	23
0.7465	317.52(11.83)	5.60(0.09)	323.12(11.91)	0.55	24

TABLE C.3: Scan of fit windows on A5 for the ud contribution using Padé [1,1].

Q_{cut}^2 [GeV ²]	a_μ^{I}	a_μ^{II}	a_μ^{HLO}	$\chi_{\text{corr}}^2/\text{dof}$	N
0.1768	282.59(32.92)	40.12(1.48)	322.71(34.36)	1.66	10
0.1862	295.62(38.12)	38.03(1.47)	333.65(39.56)	1.69	11
0.2060	326.85(30.82)	34.74(1.12)	361.59(31.75)	1.62	12
0.2154	334.05(27.68)	33.10(0.99)	367.15(28.55)	1.50	13
0.2338	337.04(28.02)	30.06(0.85)	367.10(28.84)	1.38	14
0.2400	344.80(28.41)	26.29(0.70)	371.09(29.01)	1.26	15
0.2625	361.32(25.21)	26.49(0.66)	387.81(25.90)	1.29	16
0.2630	360.76(24.63)	26.40(0.63)	387.15(25.21)	1.26	17
0.2687	357.21(24.29)	25.61(0.60)	382.82(24.85)	1.17	18
0.2692	359.47(18.21)	25.59(0.53)	385.06(18.62)	1.13	19
0.2937	359.13(17.29)	22.89(0.44)	382.02(17.68)	1.06	20
0.3030	362.64(16.71)	22.04(0.41)	384.69(17.08)	1.02	21
0.3229	365.00(16.61)	20.31(0.36)	385.31(16.95)	0.97	22
0.3318	364.80(15.97)	19.56(0.34)	384.36(16.28)	0.92	23
0.3323	366.38(15.89)	18.26(0.31)	384.64(16.17)	0.87	24
0.3506	357.01(14.32)	18.12(0.30)	375.13(14.58)	0.80	25
0.3568	357.55(14.32)	17.19(0.28)	374.74(14.56)	0.87	26
0.3649	352.89(13.42)	17.12(0.27)	370.01(13.66)	0.83	27
0.3794	355.33(13.29)	16.23(0.26)	371.57(13.54)	0.85	28
0.3799	356.44(13.16)	15.94(0.24)	372.38(13.38)	0.82	29
0.3856	357.99(12.85)	15.49(0.23)	373.48(13.08)	0.79	30
0.3942	360.53(12.89)	14.67(0.22)	375.20(13.09)	0.77	31
0.4105	362.23(12.60)	14.22(0.21)	376.45(12.80)	0.74	32
0.4199	363.76(11.51)	14.22(0.20)	377.98(11.68)	0.68	33
0.4393	363.69(11.31)	13.32(0.18)	377.01(11.50)	0.66	34
0.4398	364.66(11.49)	13.34(0.18)	378.00(11.65)	0.67	35
0.4487	365.25(11.06)	12.32(0.16)	377.56(11.21)	0.65	36
0.4655	365.73(11.00)	12.24(0.16)	377.97(11.13)	0.64	37
0.4675	367.26(11.06)	12.25(0.16)	379.50(11.21)	0.62	38
0.4717	369.25(10.89)	11.76(0.15)	381.01(11.04)	0.64	39
0.4818	369.27(10.57)	11.75(0.15)	381.02(10.70)	0.66	40
0.4948	368.90(10.69)	11.26(0.14)	380.16(10.79)	0.64	41
0.4963	368.20(10.66)	11.10(0.14)	379.30(10.80)	0.63	42
0.5010	368.21(10.57)	11.05(0.14)	379.27(10.70)	0.60	43
0.5025	367.51(10.15)	11.05(0.14)	378.56(10.27)	0.61	44
0.5111	365.78(10.16)	10.27(0.13)	376.06(10.26)	0.59	45
0.5274	369.26(10.16)	10.27(0.12)	379.52(10.27)	0.57	46
0.5348	368.36(8.96)	10.05(0.12)	378.41(9.08)	0.68	47
0.5562	368.41(8.92)	9.50(0.11)	377.91(9.02)	0.66	48
0.5640	368.72(8.73)	9.31(0.10)	378.02(8.82)	0.60	49

TABLE C.4: Scan of fit windows on B6 for the ud contribution using Padé [1,1].

Q_{cut}^2 [GeV ²]	a_μ^{I}	a_μ^{II}	a_μ^{HLO}	$\chi_{\text{corr}}^2/\text{dof}$	N
0.2916	296.39(37.88)	20.42(0.79)	316.81(38.71)	15.53	5
0.3456	283.37(28.63)	16.19(0.44)	299.57(29.05)	10.97	6
0.3640	329.18(13.30)	15.68(0.25)	344.86(13.53)	8.41	7
0.4322	313.73(11.05)	12.16(0.16)	325.89(11.20)	7.22	8
0.4506	312.65(10.86)	11.51(0.15)	324.16(11.00)	7.41	9
0.5223	314.57(9.73)	9.33(0.10)	323.89(9.83)	6.78	10
0.5506	315.34(9.74)	8.65(0.09)	323.98(9.82)	5.93	11
0.6089	299.79(5.64)	7.34(0.06)	307.12(5.69)	5.28	12
0.6372	298.52(4.78)	6.85(0.05)	305.37(4.83)	5.25	13
0.6912	300.32(4.84)	6.06(0.04)	306.38(4.88)	4.80	14
0.7096	301.98(4.86)	5.83(0.04)	307.81(4.89)	4.32	15
0.7745	300.00(4.36)	5.08(0.03)	305.07(4.39)	4.39	16
0.7778	300.56(4.36)	5.04(0.03)	305.60(4.39)	4.19	17
0.7929	300.36(4.15)	4.89(0.03)	305.25(4.18)	3.94	18
0.7962	295.93(3.38)	4.84(0.03)	300.77(3.41)	3.70	19
0.8679	295.70(3.25)	4.21(0.02)	299.91(3.27)	3.70	20
0.8962	293.70(2.81)	3.99(0.02)	297.69(2.83)	3.54	21
0.9545	294.45(2.78)	3.59(0.02)	298.04(2.80)	3.48	22
0.9795	293.07(2.60)	3.44(0.02)	296.51(2.62)	3.33	23
0.9828	292.79(2.57)	3.42(0.02)	296.20(2.59)	3.31	24

TABLE C.5: Scan of fit windows on E5 for the ud contribution using Padé [1,1].

Q_{cut}^2 [GeV ²]	a_μ^{I}	a_μ^{II}	a_μ^{HLO}	$\chi_{\text{corr}}^2/\text{dof}$	N
0.3159	381.74(22.75)	21.57(0.47)	403.31(23.19)	1.17	15
0.3456	382.03(18.19)	19.12(0.35)	401.15(18.52)	1.10	16
0.3463	381.40(17.73)	19.05(0.34)	400.45(18.06)	1.01	17
0.3538	379.05(17.44)	18.45(0.32)	397.50(17.76)	0.95	18
0.3544	387.80(12.51)	18.52(0.28)	406.32(12.75)	0.94	19
0.3866	387.45(12.08)	16.43(0.24)	403.88(12.29)	0.89	20
0.3990	387.69(11.47)	15.73(0.22)	403.43(11.67)	0.85	21
0.4251	389.87(11.45)	14.40(0.20)	404.27(11.64)	0.81	22
0.4368	390.26(10.98)	13.87(0.18)	404.12(11.16)	0.78	23
0.4375	390.68(11.04)	13.84(0.18)	404.52(11.19)	0.74	24
0.4616	388.47(10.56)	12.81(0.16)	401.28(10.72)	0.69	25
0.4698	388.15(10.41)	12.48(0.16)	400.63(10.54)	0.70	26
0.4804	386.15(10.01)	12.08(0.15)	398.23(10.14)	0.68	27
0.4995	386.17(9.77)	11.41(0.14)	397.59(9.90)	0.69	28
0.5001	386.23(9.83)	11.39(0.14)	397.63(9.96)	0.65	29
0.5077	384.54(9.68)	11.15(0.14)	395.69(9.80)	0.62	30
0.5190	385.81(9.56)	10.80(0.13)	396.62(9.67)	0.69	31
0.5405	385.71(9.41)	10.17(0.12)	395.88(9.50)	0.62	32
0.5528	378.05(8.32)	9.77(0.11)	387.82(8.42)	0.60	33
0.5784	379.82(8.35)	9.15(0.10)	388.97(8.43)	0.71	34
0.5790	380.28(8.28)	9.14(0.10)	389.41(8.37)	0.65	35
0.5907	377.03(8.12)	8.84(0.10)	385.87(8.22)	0.60	36
0.6129	378.07(8.12)	8.37(0.09)	386.44(8.20)	0.69	37
0.6155	381.37(8.27)	8.37(0.09)	389.74(8.35)	0.65	38
0.6211	381.78(8.20)	8.25(0.09)	390.04(8.28)	0.69	39
0.6343	375.78(7.85)	7.93(0.08)	383.71(7.92)	0.63	40
0.6514	376.63(7.70)	7.62(0.08)	384.25(7.77)	0.77	41
0.6534	373.60(7.55)	7.55(0.08)	381.15(7.63)	0.75	42
0.6596	376.22(7.54)	7.46(0.08)	383.68(7.62)	0.86	43
0.6615	376.79(7.43)	7.43(0.08)	384.22(7.50)	0.74	44
0.6728	377.62(7.42)	7.24(0.07)	384.86(7.48)	0.72	45
0.6944	379.82(7.77)	6.91(0.07)	386.74(7.84)	0.69	46
0.7041	379.35(7.55)	6.76(0.07)	386.11(7.62)	0.66	47
0.7322	375.49(6.99)	6.32(0.06)	381.81(7.05)	0.65	48
0.7426	375.24(6.94)	6.19(0.06)	381.44(7.00)	0.68	49

TABLE C.6: Scan of fit windows on F6 for the ud contribution using Padé [1,1].

Q_{cut}^2 [GeV ²]	a_μ^{I}	a_μ^{II}	a_μ^{HLO}	$\chi_{\text{corr}}^2/\text{dof}$	N
0.3159	414.61(38.66)	23.10(0.77)	437.71(39.34)	0.91	15
0.3456	416.48(33.50)	20.50(0.61)	436.98(34.06)	0.85	16
0.3463	413.71(33.50)	20.37(0.61)	434.08(34.07)	0.79	17
0.3538	415.43(32.70)	19.79(0.57)	435.22(33.33)	0.99	18
0.3544	411.25(23.67)	19.69(0.49)	430.94(24.13)	0.93	19
0.3866	425.92(21.94)	17.63(0.39)	443.55(22.31)	0.87	20
0.3990	420.25(21.45)	16.78(0.37)	437.04(21.78)	0.90	21
0.4251	422.56(20.92)	15.37(0.32)	437.92(21.24)	0.78	22
0.4368	422.85(19.95)	14.80(0.30)	437.64(20.28)	0.75	23
0.4375	424.33(20.22)	14.78(0.30)	439.11(20.50)	0.69	24
0.4616	425.69(18.79)	13.69(0.27)	439.38(19.04)	0.68	25
0.4698	427.98(18.86)	13.37(0.26)	441.35(19.10)	0.65	26
0.4804	429.17(18.16)	12.95(0.24)	442.12(18.39)	0.66	27
0.4995	429.79(17.83)	12.23(0.22)	442.02(18.06)	0.63	28
0.5001	431.57(17.73)	12.22(0.22)	443.79(17.93)	0.61	29
0.5077	428.73(17.30)	11.93(0.21)	440.66(17.49)	0.59	30
0.5190	429.06(17.41)	11.55(0.21)	440.61(17.59)	0.60	31
0.5405	427.18(16.76)	10.85(0.19)	438.03(16.92)	0.58	32
0.5528	429.82(15.93)	10.50(0.18)	440.33(16.09)	0.56	33
0.5784	429.92(15.70)	9.80(0.16)	439.73(15.84)	0.55	34
0.5790	429.63(15.44)	9.79(0.16)	439.41(15.60)	0.53	35
0.5907	409.39(13.95)	9.33(0.15)	418.73(14.09)	0.54	36
0.6129	412.16(14.27)	8.84(0.14)	421.00(14.41)	0.87	37
0.6155	426.66(15.50)	8.88(0.15)	435.55(15.64)	0.85	38
0.6211	426.19(15.49)	8.76(0.14)	434.95(15.63)	0.62	39
0.6343	418.04(14.76)	8.42(0.13)	426.46(14.88)	0.61	40
0.6514	417.44(14.73)	8.07(0.13)	425.51(14.84)	0.68	41
0.6534	416.39(14.73)	8.02(0.13)	424.41(14.85)	0.66	42
0.6596	414.77(14.41)	7.90(0.12)	422.67(14.51)	0.69	43
0.6615	412.95(14.06)	7.85(0.12)	420.80(14.18)	0.68	44
0.6728	417.06(14.19)	7.67(0.12)	424.73(14.30)	0.65	45
0.6944	418.58(14.02)	7.31(0.11)	425.89(14.12)	0.63	46
0.7041	420.30(13.90)	7.16(0.11)	427.46(14.00)	0.60	47
0.7322	418.50(13.67)	6.72(0.10)	425.22(13.76)	0.58	48
0.7426	418.57(13.35)	6.57(0.10)	425.14(13.43)	0.60	49

TABLE C.7: Scan of fit windows on F7 for the ud contribution using Padé [1,1].

Q_{cut}^2 [GeV ²]	a_μ^{I}	a_μ^{II}	a_μ^{HLO}	$\chi_{\text{corr}}^2/\text{dof}$	N
0.3527	310.77(18.52)	16.02(0.36)	326.80(18.87)	2.00	8
0.3676	307.23(17.91)	15.21(0.33)	322.44(18.21)	1.81	9
0.4267	304.23(15.93)	12.37(0.23)	316.60(16.17)	1.95	10
0.4493	305.02(16.13)	11.53(0.21)	316.56(16.32)	1.77	11
0.4973	310.18(9.13)	10.04(0.12)	320.21(9.26)	1.60	12
0.5199	307.27(7.94)	9.39(0.11)	316.66(8.05)	1.45	13
0.5641	308.16(7.93)	8.35(0.09)	316.51(8.01)	1.37	14
0.5791	310.12(7.93)	8.05(0.09)	318.17(8.02)	1.26	15
0.6335	309.61(7.26)	7.04(0.07)	316.65(7.33)	1.37	16
0.6347	310.07(7.10)	7.02(0.07)	317.09(7.16)	1.26	17
0.6485	309.89(6.91)	6.79(0.07)	316.69(6.97)	1.18	18
0.6497	302.35(6.11)	6.74(0.07)	309.10(6.17)	1.11	19
0.7087	300.83(5.80)	5.90(0.06)	306.73(5.85)	1.39	20
0.7313	301.17(5.18)	5.62(0.05)	306.79(5.23)	1.35	21
0.7793	301.15(5.13)	5.09(0.05)	306.23(5.17)	1.27	22
0.8007	299.03(5.04)	4.86(0.04)	303.88(5.08)	1.19	23
0.8019	297.79(4.92)	4.84(0.04)	302.63(4.96)	1.46	24
0.8462	300.37(4.94)	4.45(0.04)	304.82(4.97)	1.45	25
0.8612	300.29(4.93)	4.33(0.04)	304.62(4.97)	1.17	26
0.8807	299.14(4.88)	4.18(0.04)	303.32(4.92)	1.14	27
0.9156	297.86(4.72)	3.91(0.03)	301.77(4.75)	1.20	28
0.9168	297.27(4.73)	3.90(0.03)	301.17(4.76)	1.23	29
0.9306	297.16(4.46)	3.81(0.03)	300.97(4.50)	1.24	30
0.9513	296.44(4.39)	3.67(0.03)	300.11(4.42)	1.19	31
0.9908	294.11(4.24)	3.42(0.03)	297.52(4.26)	1.19	32
1.0134	295.73(4.23)	3.30(0.03)	299.03(4.26)	1.31	33
1.0602	294.70(4.16)	3.05(0.02)	297.75(4.19)	1.12	34

TABLE C.8: Scan of fit windows on N5 for the ud contribution using Padé [1,1].

Q_{cut}^2 [GeV ²]	a_μ^{I}	a_μ^{II}	a_μ^{HLO}	$\chi_{\text{corr}}^2/\text{dof}$	N
0.3527	382.77(26.59)	18.59(0.49)	401.36(27.02)	7.95	8
0.3676	368.60(24.76)	17.56(0.45)	386.17(25.19)	7.39	9
0.4267	387.60(22.64)	14.47(0.31)	402.07(22.92)	8.27	10
0.4493	385.83(22.67)	13.45(0.28)	399.28(22.92)	7.47	11
0.4973	395.89(15.43)	11.71(0.18)	407.61(15.61)	6.72	12
0.5199	394.60(13.13)	10.97(0.15)	405.57(13.26)	6.07	13
0.5641	397.65(13.49)	9.74(0.13)	407.39(13.62)	5.52	14
0.5791	400.16(13.62)	9.38(0.13)	409.54(13.75)	5.02	15
0.6335	396.53(12.39)	8.16(0.10)	404.69(12.49)	5.08	16
0.6347	397.73(12.19)	8.15(0.10)	405.87(12.27)	4.67	17
0.6485	385.85(11.45)	7.80(0.09)	393.65(11.54)	4.40	18
0.6497	394.22(12.85)	7.83(0.10)	402.05(12.93)	4.75	19
0.7087	400.41(11.45)	6.87(0.08)	407.28(11.53)	4.34	20
0.7313	371.16(7.46)	6.38(0.06)	377.54(7.52)	3.71	21
0.7793	371.96(7.47)	5.77(0.05)	377.74(7.51)	4.20	22
0.8007	368.43(6.39)	5.51(0.05)	373.94(6.44)	3.98	23
0.8019	368.29(6.32)	5.49(0.05)	373.79(6.36)	3.86	24
0.8462	367.97(6.15)	5.04(0.04)	373.01(6.18)	3.63	25
0.8612	368.65(6.09)	4.89(0.04)	373.54(6.13)	3.43	26
0.8807	378.25(7.07)	4.76(0.04)	383.01(7.11)	3.32	27
0.9156	375.70(6.68)	4.45(0.04)	380.15(6.71)	2.81	28
0.9168	366.67(5.61)	4.41(0.03)	371.07(5.64)	2.74	29
0.9306	374.06(6.41)	4.32(0.03)	378.38(6.43)	2.94	30
0.9513	366.27(5.51)	4.14(0.03)	370.41(5.53)	2.58	31
0.9908	365.02(5.37)	3.86(0.03)	368.88(5.39)	2.75	32
1.0134	362.55(5.28)	3.70(0.03)	366.25(5.30)	2.70	33
1.0602	361.37(5.21)	3.42(0.02)	364.79(5.23)	2.84	34

TABLE C.9: Scan of fit windows on N6 for the ud contribution using Padé [1,1].

Q_{cut}^2 [GeV ²]	a_μ^{I}	a_μ^{II}	a_μ^{HLO}	$\chi_{\text{corr}}^2/\text{dof}$	N
0.2402	383.07(37.57)	31.80(1.07)	414.87(38.68)	0.70	10
0.2528	379.36(37.34)	29.75(0.97)	409.11(38.28)	0.67	11
0.2799	426.48(28.54)	26.97(0.67)	453.45(29.23)	0.63	12
0.2926	407.58(23.67)	25.23(0.58)	432.80(24.20)	0.83	13
0.3175	407.47(23.48)	22.63(0.49)	430.09(23.94)	0.95	14
0.3260	410.38(23.75)	21.92(0.47)	432.30(24.22)	0.93	15
0.3569	423.99(22.06)	19.55(0.38)	443.54(22.42)	0.96	16
0.3572	432.03(21.49)	19.68(0.37)	451.71(21.85)	0.90	17
0.3653	429.29(21.16)	19.03(0.35)	448.31(21.48)	0.94	18
0.3657	400.13(15.39)	18.63(0.30)	418.76(15.68)	0.91	19
0.3990	407.64(15.77)	16.62(0.26)	424.26(16.03)	1.14	20
0.4116	406.81(14.80)	15.91(0.24)	422.72(15.05)	1.06	21
0.4387	408.35(14.91)	14.56(0.21)	422.91(15.10)	0.99	22
0.4509	421.10(15.09)	14.16(0.20)	435.25(15.29)	0.97	23
0.4513	417.26(12.68)	14.10(0.18)	431.35(12.83)	0.98	24
0.4763	411.97(11.83)	12.99(0.16)	424.96(11.98)	0.93	25
0.4847	412.63(11.57)	12.67(0.15)	425.30(11.70)	0.96	26
0.4964	421.72(13.02)	12.35(0.15)	434.07(13.18)	0.92	27
0.5156	425.58(12.66)	11.71(0.14)	437.29(12.79)	0.88	28
0.5160	407.82(10.69)	11.52(0.13)	419.34(10.81)	0.87	29
0.5241	409.55(10.64)	11.28(0.12)	420.83(10.76)	1.10	30
0.5361	412.21(10.89)	10.93(0.12)	423.15(11.02)	1.09	31
0.5578	412.40(10.18)	10.30(0.11)	422.71(10.27)	1.04	32
0.5704	412.19(10.63)	9.97(0.11)	422.16(10.73)	0.98	33
0.5971	414.21(10.24)	9.32(0.10)	423.53(10.33)	1.01	34
0.5975	413.27(10.07)	9.30(0.09)	422.57(10.15)	0.97	35
0.6097	412.65(9.85)	9.02(0.09)	421.66(9.94)	0.94	36
0.6335	413.17(9.62)	8.50(0.08)	421.67(9.69)	0.91	37
0.6351	412.66(9.52)	8.46(0.08)	421.13(9.60)	0.88	38
0.6420	412.31(9.61)	8.32(0.08)	420.63(9.69)	0.85	39
0.6551	408.58(9.79)	8.03(0.08)	416.62(9.86)	0.83	40
0.6732	396.75(7.58)	7.61(0.06)	404.36(7.65)	0.92	41
0.6744	398.45(9.69)	7.61(0.08)	406.06(9.76)	0.99	42
0.6817	398.50(9.37)	7.48(0.07)	405.98(9.45)	1.25	43
0.6828	397.70(9.45)	7.45(0.07)	405.15(9.52)	1.20	44

TABLE C.10: Scan of fit windows on O7 for the ud contribution using Padé [1,1].

C.1.1.2 Fit ansatz: Padé [2,1]

Q_{cut}^2 [GeV ²]	a_μ^{I}	a_μ^{II}	a_μ^{HLO}	$\chi_{\text{corr}}^2/\text{dof}$	N
0.3283	352.49(131.62)	16.14(1.11)	368.63(132.68)	1.08	8
0.3423	362.32(127.34)	12.61(0.74)	374.93(128.13)	1.05	9
0.3967	245.02(33.55)	11.08(0.31)	256.10(33.80)	0.89	10
0.4182	261.62(25.67)	9.78(0.20)	271.40(25.87)	1.14	11
0.4625	261.07(20.58)	9.77(0.19)	270.84(20.78)	1.03	12
0.4840	262.05(20.22)	9.18(0.18)	271.23(20.38)	0.92	13
0.5250	262.93(20.05)	8.20(0.15)	271.13(20.21)	0.82	14
0.5390	263.24(17.69)	6.96(0.11)	270.21(17.81)	0.74	15
0.5883	264.22(16.08)	6.92(0.11)	271.14(16.17)	0.68	16
0.5908	268.60(15.77)	6.94(0.10)	275.54(15.86)	0.62	17
0.6022	270.04(16.25)	6.71(0.10)	276.75(16.33)	0.63	18
0.6048	271.76(14.43)	6.72(0.09)	278.48(14.51)	0.59	19
0.6592	273.37(14.83)	5.64(0.08)	279.01(14.90)	0.55	20
0.6807	271.41(13.29)	5.63(0.07)	277.04(13.36)	0.52	21
0.7250	265.66(12.40)	5.08(0.06)	270.74(12.47)	0.60	22
0.7440	258.90(10.78)	4.87(0.06)	263.77(10.84)	0.60	23
0.7465	257.44(10.06)	4.83(0.05)	262.27(10.11)	0.60	24

TABLE C.11: Scan of fit windows on A3 for the ud contribution using Padé [2,1].

Q_{cut}^2 [GeV ²]	a_μ^{I}	a_μ^{II}	a_μ^{HLO}	$\chi_{\text{corr}}^2/\text{dof}$	N
0.3283	301.44(15.67)	17.65(0.41)	319.08(16.06)	3.00	8
0.3423	327.34(57.90)	14.00(0.55)	341.34(58.32)	2.45	9
0.3967	326.93(45.81)	13.01(0.41)	339.94(46.23)	2.84	10
0.4182	401.02(89.85)	11.70(0.50)	412.72(90.41)	2.43	11
0.4625	356.21(39.70)	11.51(0.32)	367.72(39.99)	2.31	12
0.4840	358.78(38.80)	10.79(0.29)	369.57(39.07)	2.31	13
0.5250	356.93(37.82)	9.59(0.24)	366.51(38.03)	2.08	14
0.5390	337.58(31.40)	8.00(0.17)	345.57(31.54)	1.88	15
0.5883	347.76(28.75)	7.98(0.16)	355.74(28.92)	1.85	16
0.5908	340.12(26.50)	7.93(0.15)	348.05(26.66)	1.74	17
0.6022	337.98(21.64)	7.65(0.13)	345.63(21.75)	1.68	18
0.6048	344.26(22.22)	7.68(0.13)	351.94(22.37)	1.57	19
0.6592	352.96(28.77)	6.44(0.12)	359.40(28.88)	1.45	20
0.6807	338.15(19.82)	6.38(0.10)	344.54(19.92)	1.36	21
0.7250	339.15(18.42)	5.79(0.09)	344.94(18.49)	1.32	22
0.7440	343.48(17.35)	5.58(0.08)	349.05(17.41)	1.25	23
0.7465	343.01(16.70)	5.54(0.08)	348.55(16.78)	1.16	24

TABLE C.12: Scan of fit windows on A4 for the ud contribution using Padé [2,1].

Q_{cut}^2 [GeV ²]	a_μ^{I}	a_μ^{II}	a_μ^{HLO}	$\chi_{\text{corr}}^2/\text{dof}$	N
0.3283	325.51(32.64)	18.89(0.88)	344.40(33.52)	1.23	8
0.3423	328.00(34.91)	14.62(0.64)	342.62(35.55)	1.08	9
0.3967	325.59(67.17)	13.54(0.76)	339.13(68.05)	0.95	10
0.4182	331.36(49.36)	11.80(0.51)	343.16(49.93)	0.84	11
0.4625	369.75(101.82)	11.84(0.73)	381.59(102.48)	0.74	12
0.4840	354.56(85.10)	11.05(0.60)	365.61(85.67)	0.89	13
0.5250	369.33(94.91)	9.87(0.55)	379.21(95.36)	0.78	14
0.5390	383.15(89.74)	8.41(0.41)	391.56(90.21)	0.73	15
0.5883	390.62(83.04)	8.41(0.39)	399.03(83.36)	0.68	16
0.5908	365.34(76.37)	8.22(0.37)	373.57(76.79)	0.59	17
0.6022	371.11(74.47)	7.98(0.35)	379.09(74.72)	0.78	18
0.6048	344.10(64.80)	7.87(0.32)	351.97(65.07)	0.70	19
0.6592	360.11(77.32)	6.63(0.28)	366.74(77.62)	0.67	20
0.6807	347.47(48.98)	6.58(0.22)	354.05(49.19)	0.62	21
0.7250	340.14(43.16)	5.94(0.18)	346.08(43.35)	0.60	22
0.7440	336.63(43.29)	5.70(0.17)	342.34(43.44)	0.58	23
0.7465	329.37(32.89)	5.65(0.15)	335.02(33.03)	0.56	24

TABLE C.13: Scan of fit windows on A5 for the ud contribution using Padé [2,1].

Q_{cut}^2 [GeV ²]	a_μ^{I}	a_μ^{II}	a_μ^{HLO}	$\chi_{\text{corr}}^2/\text{dof}$	N
0.1768	283.56(30.13)	40.16(1.43)	323.72(31.40)	1.94	10
0.1862	299.28(39.35)	38.19(1.58)	337.47(40.88)	1.93	11
0.2060	321.75(25.75)	34.67(1.05)	356.42(26.70)	1.81	12
0.2154	326.26(22.94)	32.98(0.92)	359.24(23.78)	1.63	13
0.2338	329.22(23.25)	29.96(0.80)	359.18(24.04)	1.48	14
0.2400	334.66(27.42)	26.17(0.71)	360.82(28.07)	1.34	15
0.2625	344.38(20.60)	26.28(0.61)	370.67(21.18)	1.38	16
0.2630	344.18(21.28)	26.21(0.61)	370.39(21.83)	1.30	17
0.2687	340.33(26.25)	25.39(0.62)	365.72(26.85)	1.20	18
0.2692	342.03(26.76)	25.35(0.60)	367.38(27.35)	1.19	19
0.2937	353.64(32.33)	22.83(0.55)	376.47(32.86)	1.11	20
0.3030	345.47(29.12)	21.84(0.50)	367.31(29.57)	1.07	21
0.3229	346.73(27.86)	20.12(0.44)	366.85(28.26)	1.01	22
0.3318	358.41(30.82)	19.50(0.43)	377.91(31.15)	0.96	23
0.3323	354.45(27.81)	18.17(0.37)	372.62(28.14)	0.91	24
0.3506	382.40(34.01)	18.34(0.41)	400.75(34.40)	0.83	25
0.3568	382.48(34.06)	17.39(0.38)	399.87(34.45)	0.88	26
0.3649	390.16(35.45)	17.44(0.39)	407.60(35.80)	0.84	27
0.3794	385.30(34.73)	16.46(0.36)	401.76(35.10)	0.83	28
0.3799	387.34(35.07)	16.17(0.35)	403.51(35.44)	0.82	29
0.3856	387.47(35.54)	15.71(0.34)	403.18(35.81)	0.78	30
0.3942	379.35(37.57)	14.79(0.32)	394.15(37.83)	0.76	31
0.4105	380.57(31.45)	14.34(0.28)	394.91(31.72)	0.76	32
0.4199	378.38(29.82)	14.31(0.28)	392.70(30.11)	0.69	33
0.4393	373.74(31.13)	13.38(0.26)	387.12(31.36)	0.67	34
0.4398	369.26(29.92)	13.37(0.25)	382.62(30.13)	0.68	35
0.4487	366.74(24.06)	12.33(0.21)	379.07(24.23)	0.67	36
0.4655	368.22(24.27)	12.26(0.21)	380.48(24.42)	0.65	37
0.4675	366.43(24.05)	12.24(0.21)	378.67(24.22)	0.63	38
0.4717	358.64(21.70)	11.69(0.19)	370.33(21.88)	0.66	39
0.4818	361.08(21.12)	11.70(0.19)	372.79(21.28)	0.67	40
0.4948	363.45(21.62)	11.23(0.18)	374.68(21.76)	0.65	41
0.4963	365.80(21.93)	11.09(0.18)	376.89(22.07)	0.64	42
0.5010	368.72(21.87)	11.06(0.17)	379.78(22.03)	0.62	43
0.5025	369.09(20.97)	11.06(0.17)	380.15(21.11)	0.63	44
0.5111	373.93(21.60)	10.31(0.16)	384.24(21.75)	0.61	45
0.5274	355.57(17.93)	10.20(0.15)	365.77(18.05)	0.58	46
0.5348	357.80(18.54)	10.00(0.15)	367.80(18.67)	0.67	47
0.5562	361.44(17.69)	9.47(0.13)	370.91(17.77)	0.67	48
0.5640	363.22(17.37)	9.28(0.13)	372.49(17.48)	0.61	49

TABLE C.14: Scan of fit windows on B6 for the ud contribution using Padé [2,1].

Q_{cut}^2 [GeV ²]	a_μ^{I}	a_μ^{II}	a_μ^{HLO}	$\chi_{\text{corr}}^2/\text{dof}$	N
0.2916	726.08(132.57)	25.09(1.69)	751.16(134.28)	26.43	5
0.3456	714.79(123.60)	19.67(1.12)	734.47(124.66)	13.50	6
0.3640	752.64(375.97)	19.08(2.82)	771.71(378.71)	9.03	7
0.4322	975.28(245.06)	15.72(1.18)	990.99(246.12)	8.80	8
0.4506	995.14(225.71)	14.85(0.99)	1009.98(226.71)	7.41	9
0.5223	422.76(201.25)	9.87(0.83)	432.63(202.14)	6.19	10
0.5506	330.89(21.24)	8.71(0.13)	339.60(21.36)	6.24	11
0.6089	335.43(18.16)	7.52(0.10)	342.95(18.25)	5.81	12
0.6372	334.46(17.71)	7.02(0.09)	341.48(17.80)	5.17	13
0.6912	334.27(17.63)	6.20(0.08)	340.47(17.71)	4.67	14
0.7096	342.52(16.54)	5.99(0.07)	348.51(16.59)	4.22	15
0.7745	338.45(14.57)	5.21(0.05)	343.66(14.61)	3.97	16
0.7778	338.37(14.13)	5.17(0.05)	343.54(14.16)	3.71	17
0.7929	322.18(10.63)	4.97(0.04)	327.15(10.67)	3.45	18
0.7962	335.03(12.67)	4.98(0.05)	340.01(12.72)	3.51	19
0.8679	333.25(11.76)	4.32(0.04)	337.57(11.80)	3.05	20
0.8962	330.04(10.53)	4.10(0.03)	334.14(10.56)	2.88	21
0.9545	320.35(9.35)	3.66(0.03)	324.02(9.38)	2.74	22
0.9795	315.83(7.62)	3.50(0.02)	319.32(7.64)	2.95	23
0.9828	315.58(7.43)	3.48(0.02)	319.06(7.46)	2.85	24

TABLE C.15: Scan of fit windows on E5 for the ud contribution using Padé [2,1].

Q_{cut}^2 [GeV ²]	a_μ^{I}	a_μ^{II}	a_μ^{HLO}	$\chi_{\text{corr}}^2/\text{dof}$	N
0.3159	530.13(163.76)	22.99(1.33)	553.12(164.99)	1.08	15
0.3456	460.74(99.37)	19.86(0.88)	480.60(100.16)	1.01	16
0.3463	448.83(90.62)	19.68(0.81)	468.51(91.44)	0.98	17
0.3538	450.81(82.10)	19.12(0.73)	469.93(82.74)	0.93	18
0.3544	406.59(48.22)	18.72(0.55)	425.31(48.77)	0.88	19
0.3866	416.93(44.33)	16.69(0.44)	433.62(44.77)	0.93	20
0.3990	423.75(45.28)	16.03(0.41)	439.79(45.70)	0.87	21
0.4251	408.68(39.18)	14.54(0.34)	423.22(39.52)	0.80	22
0.4368	408.36(32.04)	13.99(0.28)	422.35(32.25)	0.81	23
0.4375	405.26(30.71)	13.94(0.27)	419.20(30.95)	0.75	24
0.4616	413.17(29.79)	12.96(0.24)	426.13(30.03)	0.71	25
0.4698	414.04(29.74)	12.64(0.24)	426.68(30.01)	0.69	26
0.4804	416.91(27.91)	12.26(0.22)	429.16(28.10)	0.66	27
0.4995	413.46(27.14)	11.57(0.20)	425.03(27.33)	0.64	28
0.5001	415.18(28.21)	11.55(0.20)	426.73(28.39)	0.62	29
0.5077	418.26(27.29)	11.33(0.19)	429.59(27.50)	0.59	30
0.5190	409.45(27.87)	10.93(0.19)	420.38(28.04)	0.64	31
0.5405	407.91(24.52)	10.28(0.16)	418.18(24.64)	0.61	32
0.5528	415.99(22.20)	9.97(0.15)	425.95(22.36)	0.59	33
0.5784	414.18(23.41)	9.31(0.14)	423.49(23.53)	0.58	34
0.5790	411.01(21.82)	9.28(0.14)	420.29(21.93)	0.57	35
0.5907	413.28(18.24)	9.01(0.12)	422.29(18.32)	0.53	36
0.6129	412.96(18.53)	8.52(0.12)	421.48(18.64)	0.52	37
0.6155	419.71(20.39)	8.51(0.12)	428.22(20.50)	0.51	38
0.6211	413.54(20.52)	8.37(0.11)	421.91(20.65)	0.55	39
0.6343	420.17(18.33)	8.12(0.11)	428.29(18.43)	0.55	40
0.6514	422.37(19.06)	7.80(0.10)	430.17(19.15)	0.53	41
0.6534	425.40(19.25)	7.75(0.10)	433.16(19.34)	0.52	42
0.6596	414.75(19.19)	7.61(0.10)	422.35(19.28)	0.57	43
0.6615	405.70(18.12)	7.54(0.10)	413.24(18.20)	0.61	44
0.6728	404.90(18.96)	7.35(0.10)	412.25(19.05)	0.65	45
0.6944	401.18(15.80)	6.99(0.09)	408.17(15.87)	0.64	46
0.7041	407.24(18.66)	6.86(0.09)	414.10(18.77)	0.61	47
0.7322	405.56(15.65)	6.44(0.08)	412.01(15.71)	0.59	48
0.7426	408.79(15.16)	6.32(0.08)	415.10(15.21)	0.57	49

TABLE C.16: Scan of fit windows on F6 for the ud contribution using Padé [2,1].

Q_{cut}^2 [GeV 2]	a_μ^{I}	a_μ^{II}	a_μ^{HLO}	$\chi_{\text{corr}}^2/\text{dof}$	N
0.3159	414.44(184.92)	23.10(1.76)	437.54(186.49)	0.98	15
0.3456	447.45(158.60)	20.81(1.41)	468.26(160.14)	0.92	16
0.3463	507.64(205.26)	21.26(1.60)	528.90(206.66)	0.85	17
0.3538	465.20(174.17)	20.28(1.44)	485.48(175.67)	1.02	18
0.3544	450.23(112.84)	20.10(1.14)	470.33(113.97)	0.97	19
0.3866	395.07(47.40)	17.32(0.57)	412.39(47.95)	0.91	20
0.3990	442.88(72.45)	16.98(0.68)	459.86(73.11)	0.94	21
0.4251	439.56(70.24)	15.50(0.60)	455.07(70.78)	0.82	22
0.4368	427.72(63.21)	14.83(0.54)	442.55(63.73)	0.78	23
0.4375	412.09(59.36)	14.68(0.52)	426.77(59.89)	0.72	24
0.4616	419.93(42.36)	13.65(0.38)	433.58(42.69)	0.71	25
0.4698	422.73(43.89)	13.33(0.38)	436.06(44.28)	0.68	26
0.4804	423.05(45.33)	12.91(0.38)	435.95(45.72)	0.68	27
0.4995	424.87(47.40)	12.20(0.36)	437.07(47.76)	0.66	28
0.5001	422.04(46.32)	12.16(0.35)	434.20(46.66)	0.63	29
0.5077	431.18(45.31)	11.94(0.34)	443.13(45.57)	0.61	30
0.5190	434.62(52.50)	11.58(0.35)	446.20(52.86)	0.62	31
0.5405	442.82(47.77)	10.93(0.30)	453.75(48.04)	0.60	32
0.5528	428.88(36.61)	10.50(0.25)	439.38(36.84)	0.58	33
0.5784	438.40(42.20)	9.84(0.25)	448.24(42.45)	0.57	34
0.5790	440.02(40.22)	9.84(0.24)	449.85(40.39)	0.54	35
0.5907	490.64(40.11)	9.73(0.23)	500.36(40.36)	0.56	36
0.6129	490.11(40.57)	9.18(0.21)	499.30(40.77)	0.68	37
0.6155	468.97(37.37)	9.06(0.20)	478.03(37.60)	0.69	38
0.6211	473.67(39.13)	8.95(0.20)	482.62(39.27)	0.58	39
0.6343	485.17(37.40)	8.70(0.19)	493.87(37.54)	0.56	40
0.6514	486.11(37.23)	8.34(0.18)	494.45(37.38)	0.54	41
0.6534	490.10(36.56)	8.32(0.18)	498.41(36.74)	0.51	42
0.6596	486.23(34.30)	8.18(0.17)	494.41(34.44)	0.51	43
0.6615	485.64(34.45)	8.15(0.17)	493.78(34.57)	0.50	44
0.6728	487.49(35.87)	7.94(0.17)	495.43(36.05)	0.47	45
0.6944	478.13(33.74)	7.53(0.15)	485.65(33.87)	0.48	46
0.7041	477.11(34.70)	7.36(0.15)	484.47(34.87)	0.49	47
0.7322	471.68(31.87)	6.89(0.13)	478.57(31.99)	0.49	48
0.7426	469.46(31.81)	6.73(0.13)	476.19(31.95)	0.50	49

TABLE C.17: Scan of fit windows on F7 for the ud contribution using Padé [2,1].

Q_{cut}^2 [GeV ²]	a_μ^{I}	a_μ^{II}	a_μ^{HLO}	$\chi_{\text{corr}}^2/\text{dof}$	N
0.3574	622.55(77.40)	22.47(0.68)	645.01(77.96)	1.18	40
0.3673	628.52(80.95)	21.66(0.66)	650.18(81.51)	1.20	41
0.3679	635.36(81.86)	21.68(0.66)	657.04(82.55)	1.16	42
0.3719	630.63(84.35)	21.32(0.65)	651.95(84.89)	1.20	43
0.3725	608.73(71.48)	21.13(0.61)	629.86(71.98)	1.18	44
0.3791	644.31(81.83)	20.83(0.62)	665.14(82.35)	1.17	45
0.3909	658.74(77.07)	20.03(0.54)	678.78(77.64)	1.10	46
0.3969	695.52(86.03)	19.79(0.56)	715.31(86.44)	1.08	47
0.4123	651.10(73.44)	18.47(0.48)	669.57(73.83)	1.02	48
0.4186	650.18(72.53)	18.07(0.46)	668.25(72.97)	1.02	49
0.4192	641.38(68.93)	17.99(0.45)	659.37(69.38)	1.00	50
0.4295	642.14(69.27)	17.37(0.43)	659.51(69.63)	0.98	51
0.4322	662.45(69.04)	17.28(0.42)	679.73(69.39)	0.96	52
0.4368	654.71(64.65)	16.99(0.40)	671.70(64.96)	0.87	53
0.4440	629.58(55.60)	16.51(0.37)	646.09(55.85)	0.86	54
0.4511	613.77(51.23)	16.05(0.34)	629.82(51.50)	0.88	55
0.4539	602.97(47.55)	15.86(0.33)	618.84(47.88)	0.89	56
0.4545	565.51(41.70)	15.64(0.32)	581.15(41.99)	0.89	57
0.4585	566.97(38.68)	15.44(0.30)	582.41(38.95)	0.96	58
0.4655	571.26(40.03)	15.13(0.30)	586.39(40.27)	0.90	59
0.4657	575.68(40.95)	15.13(0.29)	590.81(41.29)	0.88	60
0.4767	576.20(40.28)	14.62(0.28)	590.82(40.54)	0.85	61
0.4835	574.56(39.62)	14.30(0.27)	588.86(39.89)	0.83	62
0.4983	574.10(38.80)	13.66(0.25)	587.76(39.02)	0.81	63
0.4989	563.88(36.51)	13.59(0.24)	577.47(36.78)	0.80	64
0.5052	561.90(36.45)	13.33(0.24)	575.22(36.65)	0.81	65
0.5161	557.85(35.30)	12.89(0.23)	570.74(35.56)	0.80	66
0.5188	554.10(34.74)	12.77(0.22)	566.86(34.97)	0.79	67
0.5234	548.04(31.52)	12.57(0.21)	560.60(31.69)	0.78	68
0.5306	544.84(30.25)	12.29(0.20)	557.13(30.44)	0.77	69

TABLE C.18: Scan of fit windows on G8 for the ud contribution using Padé [2,1].

Q_{cut}^2 [GeV ²]	a_μ^{I}	a_μ^{II}	a_μ^{HLO}	$\chi_{\text{corr}}^2/\text{dof}$	N
0.3527	285.44(40.91)	15.76(0.51)	301.20(41.45)	2.48	8
0.3676	338.91(72.38)	15.48(0.66)	354.39(72.97)	2.11	9
0.4267	350.44(74.77)	12.69(0.51)	363.13(75.28)	2.23	10
0.4493	325.76(34.46)	11.66(0.28)	337.42(34.65)	1.92	11
0.4973	315.81(24.81)	10.08(0.21)	325.88(25.02)	1.71	12
0.5199	318.18(24.77)	9.46(0.19)	327.64(24.94)	1.60	13
0.5641	319.36(24.84)	8.41(0.16)	327.77(24.99)	1.49	14
0.5791	334.52(23.99)	8.18(0.14)	342.69(24.15)	1.35	15
0.6335	326.26(20.64)	7.12(0.11)	333.38(20.74)	1.37	16
0.6347	325.72(18.66)	7.09(0.11)	332.82(18.77)	1.28	17
0.6485	321.37(14.88)	6.85(0.09)	328.22(14.97)	1.19	18
0.6497	340.85(19.11)	6.91(0.10)	347.76(19.20)	1.13	19
0.7087	339.65(18.35)	6.04(0.08)	345.69(18.40)	1.10	20
0.7313	329.37(15.46)	5.73(0.07)	335.10(15.53)	1.05	21
0.7793	327.13(14.84)	5.17(0.06)	332.31(14.90)	1.09	22
0.8007	333.46(13.81)	4.97(0.06)	338.44(13.85)	1.02	23
0.8019	334.70(13.28)	4.97(0.06)	339.67(13.32)	1.06	24
0.8462	333.78(15.91)	4.55(0.06)	338.33(15.96)	0.95	25
0.8612	333.81(15.57)	4.43(0.05)	338.24(15.62)	0.95	26
0.8807	321.60(10.42)	4.23(0.04)	325.83(10.46)	0.90	27
0.9156	327.40(11.20)	3.98(0.04)	331.38(11.23)	0.92	28
0.9168	327.32(10.79)	3.98(0.04)	331.30(10.82)	0.80	29
0.9306	326.79(10.75)	3.89(0.04)	330.67(10.78)	0.77	30
0.9513	332.34(11.51)	3.76(0.04)	336.10(11.53)	0.77	31
0.9908	329.01(9.98)	3.50(0.03)	332.51(10.01)	0.69	32
1.0134	331.66(11.39)	3.37(0.03)	335.03(11.41)	0.67	33
1.0602	330.52(10.71)	3.12(0.03)	333.64(10.73)	0.66	34

TABLE C.19: Scan of fit windows on N5 for the ud contribution using Padé [2,1].

Q_{cut}^2 [GeV ²]	a_μ^{I}	a_μ^{II}	a_μ^{HLO}	$\chi_{\text{corr}}^2/\text{dof}$	N
0.3527	981.55(92.76)	22.84(0.90)	1004.39(93.64)	9.88	8
0.3676	930.87(90.22)	21.30(0.83)	952.17(91.01)	8.48	9
0.4267	492.37(318.00)	15.16(1.60)	507.53(319.65)	8.61	10
0.4493	443.53(74.60)	13.80(0.50)	457.32(75.18)	8.38	11
0.4973	406.05(38.88)	11.78(0.29)	417.83(39.19)	7.35	12
0.5199	407.48(37.86)	11.05(0.27)	418.53(38.13)	6.73	13
0.5641	405.74(37.05)	9.78(0.23)	415.52(37.28)	6.06	14
0.5791	441.35(37.13)	9.58(0.20)	450.93(37.31)	5.47	15
0.6335	431.96(34.45)	8.31(0.17)	440.27(34.61)	5.36	16
0.6347	436.17(33.67)	8.31(0.16)	444.48(33.85)	4.91	17
0.6485	461.66(32.40)	8.12(0.15)	469.77(32.57)	4.57	18
0.6497	470.87(37.44)	8.12(0.16)	479.00(37.59)	4.44	19
0.7087	418.41(34.89)	6.93(0.14)	425.35(35.03)	4.15	20
0.7313	447.68(28.22)	6.68(0.11)	454.36(28.34)	3.91	21
0.7793	441.37(26.75)	6.01(0.10)	447.38(26.85)	3.81	22
0.8007	430.72(24.45)	5.72(0.09)	436.44(24.54)	3.65	23
0.8019	421.63(24.01)	5.68(0.09)	427.31(24.09)	3.58	24
0.8462	438.24(24.41)	5.25(0.08)	443.49(24.48)	3.45	25
0.8612	433.56(24.33)	5.09(0.08)	438.65(24.40)	3.05	26
0.8807	403.10(16.40)	4.83(0.06)	407.92(16.46)	3.02	27
0.9156	406.15(18.35)	4.53(0.06)	410.69(18.42)	2.78	28
0.9168	409.22(17.15)	4.52(0.06)	413.74(17.20)	2.68	29
0.9306	405.24(15.82)	4.41(0.05)	409.65(15.87)	2.70	30
0.9513	412.88(18.56)	4.26(0.05)	417.14(18.60)	2.47	31
0.9908	411.95(17.06)	3.97(0.05)	415.92(17.11)	2.53	32
1.0134	427.77(18.56)	3.85(0.05)	431.62(18.61)	2.42	33
1.0602	430.32(18.50)	3.56(0.04)	433.89(18.54)	2.35	34

TABLE C.20: Scan of fit windows on N6 for the ud contribution using Padé [2,1].

Q_{cut}^2 [GeV ²]	a_μ^{I}	a_μ^{II}	a_μ^{HLO}	$\chi_{\text{corr}}^2/\text{dof}$	N
0.2402	597.55(94.49)	34.39(1.68)	631.94(96.17)	0.81	10
0.2528	462.28(131.79)	30.87(1.70)	493.16(133.37)	0.72	11
0.2799	386.58(36.98)	26.37(0.73)	412.96(37.59)	0.64	12
0.2926	405.01(54.91)	25.19(0.84)	430.21(55.72)	0.85	13
0.3175	406.19(53.48)	22.61(0.71)	428.80(54.06)	1.04	14
0.3260	435.11(60.56)	22.17(0.72)	457.28(61.23)	1.02	15
0.3569	384.65(30.99)	19.16(0.43)	403.81(31.36)	1.02	16
0.3572	417.97(41.35)	19.56(0.48)	437.53(41.82)	0.90	17
0.3653	436.00(40.87)	19.09(0.47)	455.09(41.29)	1.00	18
0.3657	458.07(46.08)	19.20(0.49)	477.27(46.60)	0.97	19
0.3990	457.38(52.02)	17.01(0.45)	474.39(52.41)	1.05	20
0.4116	445.65(47.37)	16.21(0.41)	461.86(47.78)	1.04	21
0.4387	449.94(42.45)	14.84(0.33)	464.78(42.81)	0.99	22
0.4509	408.18(32.43)	14.07(0.28)	422.25(32.71)	0.94	23
0.4513	414.66(30.49)	14.08(0.28)	428.74(30.76)	1.02	24
0.4763	425.65(30.25)	13.09(0.25)	438.74(30.48)	0.98	25
0.4847	424.47(29.86)	12.75(0.24)	437.22(30.08)	0.99	26
0.4964	420.93(26.79)	12.34(0.21)	433.28(26.98)	0.95	27
0.5156	407.02(26.01)	11.60(0.19)	418.62(26.21)	0.92	28
0.5160	444.18(27.81)	11.75(0.20)	455.93(28.00)	0.88	29
0.5241	439.82(27.89)	11.47(0.20)	451.29(28.07)	1.06	30
0.5361	437.46(30.27)	11.08(0.20)	448.53(30.47)	1.07	31
0.5578	428.39(28.46)	10.40(0.18)	438.78(28.64)	1.04	32
0.5704	439.86(28.81)	10.11(0.17)	449.97(28.96)	1.00	33
0.5971	425.11(28.08)	9.37(0.16)	434.48(28.24)	1.00	34
0.5975	425.21(28.25)	9.36(0.16)	434.57(28.42)	0.99	35
0.6097	423.59(27.37)	9.07(0.15)	432.66(27.51)	0.96	36
0.6335	421.44(26.64)	8.54(0.14)	429.98(26.76)	0.93	37
0.6351	424.24(21.08)	8.52(0.12)	432.75(21.21)	0.90	38
0.6420	426.90(21.41)	8.39(0.12)	435.29(21.54)	0.86	39
0.6551	449.23(25.63)	8.20(0.12)	457.42(25.74)	0.83	40
0.6732	443.08(20.15)	7.84(0.10)	450.92(20.24)	0.84	41
0.6744	472.98(24.28)	7.90(0.11)	480.88(24.37)	0.81	42
0.6817	483.93(25.13)	7.81(0.11)	491.74(25.24)	0.83	43
0.6828	481.27(25.38)	7.77(0.11)	489.04(25.49)	0.72	44

TABLE C.21: Scan of fit windows on O7 for the ud contribution using Padé [2,1].

C.1.2 The strange-quark contribution

C.1.2.1 Fit ansatz: Padé [1,1]

Q_{cut}^2 [GeV ²]	a_μ^{I}	a_μ^{II}	a_μ^{HLO}	$\chi_{\text{corr}}^2/\text{dof}$	N
0.2215	32.96(3.49)	3.12(0.07)	36.07(3.56)	2.30	5
0.2625	35.73(3.04)	3.15(0.06)	38.88(3.10)	2.07	6
0.2765	37.14(1.53)	2.99(0.05)	40.12(1.57)	1.69	7
0.3283	36.55(1.27)	2.41(0.03)	38.96(1.30)	1.39	8
0.3423	36.55(1.24)	1.90(0.02)	38.45(1.26)	1.50	9
0.3967	38.18(0.93)	1.79(0.02)	39.97(0.95)	1.32	10
0.4182	38.46(0.90)	1.57(0.01)	40.03(0.91)	1.41	11
0.4625	38.72(0.49)	1.57(0.01)	40.30(0.50)	1.29	12
0.4840	38.62(0.52)	1.48(0.01)	40.09(0.53)	1.16	13
0.5250	38.76(0.51)	1.32(0.01)	40.08(0.52)	1.07	14
0.5390	39.22(0.49)	1.13(0.01)	40.35(0.50)	0.97	15
0.5883	39.18(0.38)	1.12(0.01)	40.30(0.39)	1.29	16
0.5908	39.19(0.38)	1.12(0.01)	40.31(0.39)	1.23	17
0.6022	39.25(0.39)	1.09(0.01)	40.33(0.40)	1.15	18
0.6048	38.84(0.39)	1.08(0.01)	39.93(0.40)	1.07	19
0.6592	38.89(0.37)	0.91(0.01)	39.80(0.37)	1.33	20
0.6807	38.79(0.32)	0.91(0.01)	39.70(0.32)	1.36	21
0.7250	38.86(0.31)	0.83(0.01)	39.69(0.32)	1.28	22
0.7440	38.96(0.31)	0.80(0.01)	39.76(0.32)	1.20	23
0.7465	39.00(0.31)	0.80(0.00)	39.80(0.31)	1.12	24

TABLE C.22: Scan of fit windows on A3 for the s contribution using Padé [1,1].

Q_{cut}^2 [GeV ²]	a_μ^{I}	a_μ^{II}	a_μ^{HLO}	$\chi_{\text{corr}}^2/\text{dof}$	N
0.2215	31.54(0.42)	3.16(0.03)	34.71(0.45)	1.01	5
0.2625	35.45(2.15)	3.24(0.04)	38.69(2.18)	1.17	6
0.2765	40.53(1.26)	3.11(0.04)	43.64(1.29)	1.59	7
0.3283	40.81(1.12)	2.52(0.03)	43.33(1.14)	2.31	8
0.3423	39.93(1.04)	1.97(0.02)	41.90(1.05)	1.98	9
0.3967	41.32(0.74)	1.85(0.01)	43.17(0.76)	4.06	10
0.4182	41.48(0.74)	1.62(0.01)	43.10(0.75)	3.76	11
0.4625	40.61(0.46)	1.61(0.01)	42.22(0.47)	3.39	12
0.4840	41.02(0.39)	1.52(0.01)	42.53(0.40)	3.41	13
0.5250	41.16(0.40)	1.36(0.01)	42.52(0.40)	3.25	14
0.5390	41.35(0.39)	1.16(0.01)	42.50(0.40)	2.97	15
0.5883	41.25(0.36)	1.15(0.01)	42.40(0.37)	3.14	16
0.5908	41.25(0.36)	1.15(0.01)	42.40(0.37)	3.09	17
0.6022	41.29(0.36)	1.11(0.01)	42.40(0.37)	2.89	18
0.6048	40.34(0.28)	1.10(0.01)	41.44(0.28)	2.70	19
0.6592	40.48(0.28)	0.93(0.00)	41.41(0.28)	3.69	20
0.6807	40.44(0.27)	0.93(0.00)	41.36(0.28)	3.47	21
0.7250	40.43(0.26)	0.84(0.00)	41.27(0.27)	3.36	22
0.7440	40.56(0.27)	0.81(0.00)	41.37(0.28)	3.29	23
0.7465	40.51(0.27)	0.81(0.00)	41.32(0.27)	2.99	24

TABLE C.23: Scan of fit windows on A4 for the s contribution using Padé [1,1].

Q_{cut}^2 [GeV ²]	a_μ^{I}	a_μ^{II}	a_μ^{HLO}	$\chi_{\text{corr}}^2/\text{dof}$	N
0.2215	39.40(4.61)	3.34(0.09)	42.74(4.69)	0.57	5
0.2625	39.58(3.42)	3.33(0.07)	42.91(3.49)	1.98	6
0.2765	42.06(1.66)	3.16(0.05)	45.21(1.70)	1.49	7
0.3283	43.19(1.39)	2.56(0.03)	45.76(1.42)	1.30	8
0.3423	42.82(1.30)	2.01(0.02)	44.84(1.32)	1.14	9
0.3967	42.68(1.09)	1.88(0.02)	44.55(1.10)	1.16	10
0.4182	42.50(1.03)	1.64(0.02)	44.14(1.05)	1.09	11
0.4625	42.11(0.80)	1.63(0.02)	43.74(0.82)	1.09	12
0.4840	41.90(0.60)	1.53(0.01)	43.43(0.61)	1.04	13
0.5250	42.08(0.58)	1.37(0.01)	43.45(0.59)	0.99	14
0.5390	42.40(0.57)	1.17(0.01)	43.57(0.57)	0.91	15
0.5883	41.77(0.46)	1.16(0.01)	42.93(0.47)	1.08	16
0.5908	41.78(0.46)	1.16(0.01)	42.94(0.47)	1.43	17
0.6022	41.87(0.45)	1.13(0.01)	42.99(0.46)	1.34	18
0.6048	41.16(0.46)	1.12(0.01)	42.27(0.47)	1.28	19
0.6592	41.58(0.47)	0.94(0.01)	42.52(0.48)	2.48	20
0.6807	40.70(0.37)	0.94(0.01)	41.64(0.38)	2.15	21
0.7250	40.78(0.36)	0.86(0.01)	41.64(0.36)	2.59	22
0.7440	41.00(0.36)	0.83(0.01)	41.83(0.37)	2.45	23
0.7465	40.96(0.36)	0.82(0.01)	41.78(0.37)	2.11	24

TABLE C.24: Scan of fit windows on A5 for the s contribution using Padé [1,1].

Q_{cut}^2 [GeV ²]	a_μ^{I}	a_μ^{II}	a_μ^{HLO}	$\chi_{\text{corr}}^2/\text{dof}$	N
0.0985	34.40(3.59)	8.04(0.16)	42.44(3.73)	0.38	5
0.1169	37.45(3.19)	8.12(0.13)	45.57(3.29)	0.30	6
0.1231	36.64(1.45)	6.49(0.08)	43.14(1.52)	0.30	7
0.1461	37.44(1.45)	6.48(0.08)	43.92(1.52)	0.28	8
0.1523	37.36(1.22)	6.20(0.07)	43.56(1.28)	0.44	9
0.1768	39.44(0.71)	5.34(0.04)	44.78(0.75)	0.41	10
0.1862	39.71(0.65)	5.05(0.04)	44.77(0.68)	0.33	11
0.2060	40.18(0.55)	4.52(0.03)	44.70(0.58)	0.29	12
0.2154	40.37(0.43)	4.29(0.03)	44.66(0.45)	0.23	13
0.2338	40.70(0.42)	3.91(0.03)	44.61(0.44)	0.21	14
0.2400	40.80(0.40)	3.42(0.02)	44.21(0.42)	0.19	15
0.2625	41.16(0.38)	3.42(0.02)	44.57(0.40)	0.18	16
0.2630	41.20(0.38)	3.40(0.02)	44.60(0.40)	0.16	17
0.2687	41.29(0.39)	3.32(0.02)	44.60(0.41)	0.37	18
0.2692	41.37(0.41)	3.31(0.02)	44.69(0.43)	0.34	19
0.2937	41.62(0.39)	2.99(0.02)	44.60(0.41)	0.30	20
0.3030	41.78(0.39)	2.88(0.02)	44.66(0.40)	0.28	21
0.3229	41.77(0.34)	2.66(0.02)	44.43(0.36)	0.23	22
0.3318	41.86(0.34)	2.57(0.02)	44.43(0.35)	0.30	23
0.3323	41.87(0.34)	2.40(0.01)	44.27(0.35)	0.27	24
0.3506	41.98(0.33)	2.40(0.01)	44.38(0.34)	0.25	25
0.3568	41.97(0.35)	2.28(0.01)	44.25(0.36)	0.24	26
0.3649	41.81(0.32)	2.28(0.01)	44.09(0.33)	0.31	27
0.3794	41.97(0.33)	2.16(0.01)	44.13(0.34)	0.41	28
0.3799	41.92(0.33)	2.12(0.01)	44.05(0.34)	0.40	29
0.3856	42.23(0.39)	2.07(0.01)	44.30(0.39)	0.45	30
0.3942	42.33(0.38)	1.96(0.01)	44.29(0.39)	0.38	31
0.4105	42.36(0.38)	1.90(0.01)	44.26(0.39)	0.35	32
0.4199	42.36(0.36)	1.90(0.01)	44.27(0.37)	0.40	33
0.4393	42.66(0.36)	1.79(0.01)	44.45(0.37)	0.40	34
0.4398	42.55(0.35)	1.79(0.01)	44.34(0.36)	0.28	35
0.4487	41.71(0.30)	1.65(0.01)	43.36(0.31)	0.32	36
0.4655	41.82(0.31)	1.64(0.01)	43.46(0.31)	1.20	37
0.4675	41.73(0.31)	1.63(0.01)	43.36(0.31)	1.22	38
0.4717	42.01(0.32)	1.57(0.01)	43.57(0.32)	1.31	39
0.4818	42.04(0.31)	1.57(0.01)	43.61(0.32)	1.31	40
0.4948	42.12(0.31)	1.50(0.01)	43.63(0.32)	1.26	41
0.4963	42.08(0.31)	1.49(0.01)	43.56(0.32)	1.26	42
0.5010	42.19(0.30)	1.48(0.01)	43.68(0.31)	1.23	43
0.5025	42.30(0.30)	1.48(0.01)	43.79(0.30)	1.20	44
0.5111	42.37(0.30)	1.39(0.01)	43.76(0.30)	1.16	45
0.5274	42.30(0.31)	1.38(0.01)	43.68(0.32)	1.14	46
0.5348	42.41(0.31)	1.36(0.01)	43.77(0.31)	1.20	47
0.5562	42.46(0.31)	1.29(0.01)	43.75(0.31)	1.16	48
0.5640	42.51(0.31)	1.26(0.01)	43.77(0.32)	1.14	49

TABLE C.25: Scan of fit windows on B6 for the s contribution using Padé [1,1].

Q_{cut}^2 [GeV ²]	a_μ^{I}	a_μ^{II}	a_μ^{HLO}	$\chi_{\text{corr}}^2/\text{dof}$	N
0.2916	39.89(2.10)	3.03(0.04)	42.92(2.13)	13.15	5
0.3456	40.04(1.58)	2.45(0.02)	42.50(1.60)	11.86	6
0.3640	43.11(0.76)	2.33(0.02)	45.44(0.78)	8.92	7
0.4322	42.43(0.64)	1.84(0.01)	44.28(0.65)	7.90	8
0.4506	42.48(0.63)	1.75(0.01)	44.23(0.64)	7.91	9
0.5223	43.30(0.53)	1.43(0.01)	44.74(0.54)	6.97	10
0.5506	43.38(0.52)	1.33(0.01)	44.71(0.52)	6.35	11
0.6089	42.38(0.29)	1.14(0.00)	43.52(0.29)	5.65	12
0.6372	42.10(0.25)	1.07(0.00)	43.17(0.26)	5.85	13
0.6912	42.22(0.25)	0.95(0.00)	43.17(0.26)	5.90	14
0.7096	42.41(0.26)	0.91(0.00)	43.32(0.26)	5.38	15
0.7745	42.28(0.24)	0.80(0.00)	43.08(0.24)	7.09	16
0.7778	42.32(0.24)	0.79(0.00)	43.12(0.24)	6.91	17
0.7929	42.35(0.23)	0.77(0.00)	43.12(0.24)	6.53	18
0.7962	41.50(0.19)	0.76(0.00)	42.26(0.19)	6.11	19
0.8679	41.60(0.19)	0.67(0.00)	42.26(0.19)	8.20	20
0.8962	41.53(0.18)	0.63(0.00)	42.16(0.19)	7.66	21
0.9545	41.48(0.18)	0.57(0.00)	42.05(0.18)	7.60	22
0.9795	41.61(0.18)	0.55(0.00)	42.16(0.19)	7.50	23
0.9828	41.57(0.18)	0.54(0.00)	42.12(0.18)	6.61	24

TABLE C.26: Scan of fit windows on E5 for the s contribution using Padé [1,1].

Q_{cut}^2 [GeV ²]	a_μ^{I}	a_μ^{II}	a_μ^{HLO}	$\chi_{\text{corr}}^2/\text{dof}$	N
0.1297	45.07(4.96)	7.97(0.22)	53.04(5.17)	0.35	5
0.1539	47.26(3.99)	6.69(0.13)	53.95(4.11)	0.25	6
0.1621	42.94(1.64)	6.23(0.08)	49.17(1.71)	0.21	7
0.1924	43.10(1.41)	5.12(0.06)	48.22(1.46)	0.59	8
0.2006	43.17(1.28)	4.89(0.05)	48.06(1.33)	0.68	9
0.2328	43.74(0.79)	4.12(0.03)	47.86(0.82)	0.59	10
0.2451	43.88(0.78)	3.88(0.03)	47.76(0.81)	0.52	11
0.2713	43.90(0.60)	3.43(0.03)	47.33(0.63)	0.52	12
0.2836	43.25(0.45)	3.22(0.02)	46.47(0.47)	0.53	13
0.3078	43.69(0.45)	2.92(0.02)	46.61(0.47)	0.89	14
0.3159	43.98(0.45)	2.82(0.02)	46.80(0.46)	0.73	15
0.3456	44.21(0.42)	2.52(0.02)	46.73(0.43)	0.98	16
0.3463	44.33(0.42)	2.52(0.02)	46.85(0.43)	0.85	17
0.3538	44.35(0.41)	2.46(0.02)	46.80(0.42)	0.90	18
0.3544	43.78(0.35)	2.44(0.02)	46.22(0.36)	0.85	19
0.3866	44.14(0.36)	2.19(0.01)	46.33(0.37)	1.17	20
0.3990	43.94(0.33)	2.10(0.01)	46.04(0.34)	1.10	21
0.4251	44.10(0.32)	1.93(0.01)	46.04(0.33)	1.25	22
0.4368	44.61(0.35)	1.87(0.01)	46.48(0.36)	1.18	23
0.4375	44.58(0.35)	1.86(0.01)	46.44(0.36)	0.67	24
0.4616	44.67(0.33)	1.73(0.01)	46.41(0.34)	0.64	25
0.4698	44.57(0.34)	1.70(0.01)	46.26(0.35)	0.67	26
0.4804	44.40(0.32)	1.64(0.01)	46.05(0.33)	0.78	27
0.4995	44.66(0.33)	1.56(0.01)	46.22(0.34)	0.92	28
0.5001	44.70(0.33)	1.56(0.01)	46.25(0.34)	0.76	29
0.5077	44.90(0.35)	1.53(0.01)	46.43(0.35)	0.70	30
0.5190	44.89(0.35)	1.48(0.01)	46.37(0.36)	0.61	31
0.5405	44.97(0.34)	1.40(0.01)	46.37(0.35)	0.65	32
0.5528	44.89(0.33)	1.35(0.01)	46.24(0.34)	0.55	33
0.5784	45.25(0.37)	1.27(0.01)	46.52(0.38)	0.61	34
0.5790	45.25(0.36)	1.27(0.01)	46.52(0.37)	0.60	35
0.5907	44.06(0.29)	1.23(0.01)	45.29(0.30)	0.46	36
0.6129	44.13(0.30)	1.17(0.01)	45.29(0.30)	1.69	37
0.6155	44.13(0.30)	1.16(0.01)	45.29(0.30)	1.67	38
0.6211	44.02(0.29)	1.15(0.01)	45.17(0.30)	1.98	39
0.6343	44.08(0.29)	1.11(0.01)	45.19(0.30)	1.83	40
0.6514	44.15(0.29)	1.07(0.01)	45.22(0.30)	1.90	41
0.6534	44.10(0.29)	1.06(0.01)	45.17(0.30)	1.86	42
0.6596	44.14(0.29)	1.05(0.01)	45.20(0.30)	1.86	43
0.6615	44.18(0.29)	1.05(0.01)	45.23(0.30)	1.79	44
0.6728	44.25(0.29)	1.02(0.01)	45.27(0.30)	1.84	45
0.6944	44.20(0.29)	0.97(0.01)	45.18(0.30)	1.82	46
0.7041	44.29(0.29)	0.95(0.01)	45.24(0.30)	1.79	47
0.7322	44.32(0.29)	0.90(0.00)	45.22(0.30)	1.73	48
0.7426	44.34(0.29)	0.88(0.00)	45.22(0.29)	1.71	49

TABLE C.27: Scan of fit windows on F6 for the s contribution using Padé [1,1].

Q_{cut}^2 [GeV ²]	a_μ^{I}	a_μ^{II}	a_μ^{HLO}	$\chi_{\text{corr}}^2/\text{dof}$	N
0.1297	36.17(2.74)	7.60(0.15)	43.78(2.88)	3.03	5
0.1539	39.56(2.80)	6.47(0.10)	46.03(2.88)	2.25	6
0.1621	42.75(1.61)	6.16(0.09)	48.91(1.69)	1.82	7
0.1924	43.28(1.55)	5.11(0.07)	48.39(1.60)	1.67	8
0.2006	42.50(1.37)	4.86(0.06)	47.36(1.42)	1.53	9
0.2328	43.29(0.81)	4.11(0.04)	47.40(0.84)	1.75	10
0.2451	43.53(0.81)	3.88(0.04)	47.40(0.83)	1.53	11
0.2713	43.69(0.64)	3.43(0.03)	47.12(0.66)	1.37	12
0.2836	44.24(0.53)	3.26(0.03)	47.50(0.54)	1.26	13
0.3078	44.50(0.51)	2.95(0.02)	47.45(0.53)	1.18	14
0.3159	44.66(0.50)	2.86(0.02)	47.52(0.52)	1.09	15
0.3456	44.91(0.49)	2.56(0.02)	47.47(0.50)	0.85	16
0.3463	44.92(0.49)	2.55(0.02)	47.47(0.50)	0.80	17
0.3538	45.00(0.48)	2.48(0.02)	47.48(0.49)	0.75	18
0.3544	44.97(0.47)	2.48(0.02)	47.44(0.49)	0.71	19
0.3866	45.12(0.46)	2.21(0.02)	47.33(0.47)	0.69	20
0.3990	45.21(0.45)	2.13(0.02)	47.33(0.46)	0.68	21
0.4251	45.24(0.42)	1.95(0.01)	47.19(0.43)	0.62	22
0.4368	45.29(0.42)	1.88(0.01)	47.18(0.43)	0.63	23
0.4375	45.27(0.42)	1.88(0.01)	47.15(0.43)	0.61	24
0.4616	45.31(0.40)	1.75(0.01)	47.06(0.41)	0.59	25
0.4698	45.13(0.41)	1.70(0.01)	46.83(0.42)	0.53	26
0.4804	44.76(0.38)	1.65(0.01)	46.41(0.39)	0.78	27
0.4995	44.88(0.39)	1.56(0.01)	46.45(0.40)	1.01	28
0.5001	44.86(0.38)	1.56(0.01)	46.43(0.39)	0.98	29
0.5077	45.30(0.55)	1.53(0.01)	46.83(0.55)	0.97	30
0.5190	45.43(0.54)	1.49(0.01)	46.92(0.55)	0.90	31
0.5405	45.34(0.52)	1.41(0.01)	46.74(0.53)	0.83	32
0.5528	45.58(0.52)	1.36(0.01)	46.94(0.53)	0.84	33
0.5784	45.74(0.50)	1.28(0.01)	47.02(0.51)	0.75	34
0.5790	45.52(0.49)	1.27(0.01)	46.80(0.49)	0.67	35
0.5907	44.59(0.42)	1.23(0.01)	45.83(0.43)	0.73	36
0.6129	44.70(0.43)	1.17(0.01)	45.87(0.43)	1.15	37
0.6155	44.29(0.37)	1.16(0.01)	45.45(0.37)	1.12	38
0.6211	44.49(0.35)	1.14(0.01)	45.63(0.35)	1.19	39
0.6343	44.37(0.34)	1.10(0.01)	45.47(0.35)	1.22	40
0.6514	44.41(0.34)	1.06(0.01)	45.47(0.35)	1.33	41
0.6534	44.42(0.34)	1.06(0.01)	45.47(0.35)	1.31	42
0.6596	44.43(0.34)	1.04(0.01)	45.48(0.35)	1.30	43
0.6615	44.56(0.34)	1.04(0.01)	45.60(0.35)	1.24	44
0.6728	44.63(0.34)	1.02(0.01)	45.64(0.35)	1.25	45
0.6944	44.63(0.34)	0.97(0.01)	45.60(0.35)	1.20	46
0.7041	44.69(0.34)	0.95(0.01)	45.64(0.35)	1.21	47
0.7322	44.68(0.35)	0.89(0.01)	45.57(0.35)	1.17	48
0.7426	44.65(0.34)	0.87(0.01)	45.52(0.35)	1.16	49

TABLE C.28: Scan of fit windows on F7 for the s contribution using Padé [1,1].

Q_{cut}^2 [GeV ²]	a_μ^{I}	a_μ^{II}	a_μ^{HLO}	$\chi_{\text{corr}}^2/\text{dof}$	N
0.0730	33.58(3.41)	12.82(0.33)	46.39(3.72)	0.81	5
0.0866	39.59(3.80)	11.16(0.26)	50.75(3.99)	0.58	6
0.0912	37.32(1.98)	10.58(0.22)	47.90(2.14)	1.21	7
0.1083	39.01(1.96)	9.09(0.16)	48.09(2.09)	1.12	8
0.1129	38.20(1.31)	8.68(0.14)	46.89(1.39)	0.94	9
0.1310	39.54(0.76)	7.53(0.10)	47.07(0.82)	0.91	10
0.1379	40.13(0.66)	7.17(0.09)	47.29(0.72)	0.80	11
0.1527	40.86(0.59)	6.47(0.08)	47.33(0.63)	0.74	12
0.1596	41.24(0.53)	6.19(0.07)	47.43(0.57)	0.67	13
0.1732	41.79(0.52)	5.68(0.06)	47.47(0.56)	0.62	14
0.1778	42.08(0.50)	5.53(0.06)	47.60(0.54)	0.57	15
0.1947	42.55(0.48)	5.02(0.05)	47.57(0.52)	0.57	16
0.1949	42.56(0.48)	5.02(0.05)	47.58(0.52)	0.52	17
0.1993	42.70(0.48)	4.90(0.05)	47.59(0.52)	0.54	18
0.1995	42.75(0.50)	4.89(0.05)	47.64(0.54)	0.51	19
0.2177	43.19(0.48)	4.44(0.04)	47.63(0.52)	0.47	20
0.2245	43.39(0.48)	4.30(0.04)	47.69(0.51)	0.45	21
0.2393	43.61(0.48)	3.99(0.04)	47.60(0.51)	0.40	22
0.2460	43.70(0.48)	3.86(0.04)	47.57(0.50)	0.42	23
0.2462	43.70(0.47)	3.86(0.04)	47.56(0.50)	0.41	24
0.2598	43.98(0.46)	3.63(0.03)	47.61(0.49)	0.39	25
0.2644	43.97(0.47)	3.55(0.03)	47.52(0.49)	0.37	26
0.2708	44.21(0.51)	3.46(0.03)	47.66(0.53)	0.35	27
0.2813	44.34(0.50)	3.30(0.03)	47.64(0.52)	0.33	28
0.2815	44.28(0.42)	3.30(0.03)	47.57(0.44)	0.31	29
0.2859	44.59(0.55)	3.24(0.03)	47.83(0.57)	0.30	30
0.2924	44.67(0.54)	3.15(0.03)	47.82(0.56)	0.27	31
0.3043	44.75(0.51)	3.00(0.03)	47.76(0.53)	0.26	32
0.3112	44.80(0.52)	2.92(0.03)	47.72(0.53)	0.25	33
0.3257	44.92(0.51)	2.76(0.02)	47.68(0.53)	0.26	34
0.3259	44.94(0.48)	2.76(0.02)	47.70(0.50)	0.25	35

TABLE C.29: Scan of fit windows on G8 for the s contribution using Padé [1,1].

Q_{cut}^2 [GeV ²]	a_μ^{I}	a_μ^{II}	a_μ^{HLO}	$\chi_{\text{corr}}^2/\text{dof}$	N
0.3326	44.69(0.45)	2.68(0.02)	47.37(0.47)	0.24	36
0.3456	44.84(0.45)	2.56(0.02)	47.39(0.46)	0.31	37
0.3464	44.44(0.42)	2.54(0.02)	46.98(0.44)	0.30	38
0.3502	44.45(0.43)	2.51(0.02)	46.95(0.45)	0.47	39
0.3574	44.41(0.42)	2.44(0.02)	46.84(0.43)	0.45	40
0.3673	44.58(0.42)	2.35(0.02)	46.93(0.44)	0.45	41
0.3679	44.82(0.44)	2.36(0.02)	47.18(0.45)	0.46	42
0.3719	44.96(0.44)	2.33(0.02)	47.29(0.45)	0.37	43
0.3725	45.21(0.46)	2.33(0.02)	47.54(0.48)	0.35	44
0.3791	45.32(0.46)	2.28(0.02)	47.60(0.48)	0.29	45
0.3909	45.33(0.45)	2.19(0.02)	47.52(0.47)	0.26	46
0.3969	45.44(0.45)	2.15(0.02)	47.59(0.46)	0.26	47
0.4123	44.91(0.39)	2.02(0.02)	46.93(0.41)	0.23	48
0.4186	44.98(0.39)	1.98(0.02)	46.97(0.41)	0.40	49
0.4192	44.94(0.40)	1.98(0.02)	46.92(0.41)	0.40	50
0.4295	44.94(0.39)	1.92(0.02)	46.85(0.41)	0.39	51
0.4322	44.94(0.39)	1.90(0.02)	46.84(0.40)	0.39	52
0.4368	44.96(0.39)	1.87(0.01)	46.83(0.40)	0.39	53
0.4440	45.03(0.40)	1.83(0.01)	46.86(0.41)	0.38	54
0.4511	45.04(0.40)	1.79(0.01)	46.83(0.41)	0.38	55
0.4539	45.10(0.40)	1.78(0.01)	46.88(0.41)	0.38	56
0.4545	45.10(0.40)	1.78(0.01)	46.88(0.41)	0.38	57
0.4585	45.19(0.42)	1.76(0.01)	46.95(0.43)	0.37	58
0.4655	45.18(0.41)	1.72(0.01)	46.90(0.42)	0.37	59
0.4657	45.15(0.41)	1.72(0.01)	46.87(0.42)	0.37	60
0.4767	45.25(0.41)	1.67(0.01)	46.91(0.42)	0.36	61
0.4835	45.39(0.42)	1.64(0.01)	47.03(0.43)	0.36	62
0.4983	45.49(0.42)	1.57(0.01)	47.06(0.43)	0.34	63
0.4989	45.50(0.42)	1.57(0.01)	47.07(0.43)	0.33	64
0.5052	45.43(0.38)	1.54(0.01)	46.97(0.39)	0.32	65
0.5161	45.44(0.38)	1.49(0.01)	46.94(0.39)	0.32	66
0.5188	45.46(0.40)	1.48(0.01)	46.94(0.41)	0.33	67
0.5234	45.47(0.38)	1.47(0.01)	46.93(0.39)	0.32	68
0.5306	45.42(0.37)	1.44(0.01)	46.86(0.38)	0.32	69

TABLE C.30: Scan of fit windows on G8 for the s contribution using Padé [1,1].

Q_{cut}^2 [GeV ²]	a_μ^{I}	a_μ^{II}	a_μ^{HLO}	$\chi_{\text{corr}}^2/\text{dof}$	N
0.2378	42.28(3.75)	3.88(0.09)	46.16(3.84)	2.65	5
0.2821	41.34(2.59)	3.15(0.05)	44.49(2.64)	2.05	6
0.2971	40.79(1.20)	2.95(0.03)	43.75(1.23)	1.65	7
0.3527	41.54(1.11)	2.39(0.02)	43.93(1.14)	1.34	8
0.3676	41.36(1.08)	2.27(0.02)	43.63(1.10)	1.14	9
0.4267	41.32(0.82)	1.86(0.02)	43.18(0.83)	1.32	10
0.4493	41.41(0.80)	1.74(0.01)	43.15(0.81)	1.20	11
0.4973	41.85(0.63)	1.52(0.01)	43.37(0.64)	1.07	12
0.5199	41.37(0.47)	1.42(0.01)	42.80(0.48)	0.98	13
0.5641	41.47(0.47)	1.27(0.01)	42.74(0.48)	1.02	14
0.5791	41.79(0.45)	1.23(0.01)	43.02(0.45)	0.93	15
0.6335	42.18(0.37)	1.08(0.01)	43.26(0.38)	1.12	16
0.6347	42.07(0.40)	1.08(0.01)	43.15(0.41)	1.10	17
0.6485	42.10(0.40)	1.05(0.01)	43.15(0.41)	1.01	18
0.6497	41.43(0.38)	1.04(0.01)	42.47(0.39)	0.94	19
0.7087	41.74(0.40)	0.92(0.01)	42.65(0.40)	1.42	20
0.7313	41.74(0.33)	0.87(0.00)	42.62(0.33)	1.29	21
0.7793	41.77(0.31)	0.79(0.00)	42.56(0.31)	1.22	22
0.8007	41.86(0.31)	0.76(0.00)	42.62(0.31)	1.17	23
0.8019	41.83(0.30)	0.76(0.00)	42.59(0.31)	0.93	24
0.8462	41.85(0.30)	0.70(0.00)	42.55(0.31)	0.90	25
0.8612	41.78(0.30)	0.68(0.00)	42.46(0.30)	0.90	26
0.8807	41.63(0.30)	0.66(0.00)	42.29(0.30)	1.00	27
0.9156	41.78(0.30)	0.62(0.00)	42.40(0.30)	1.60	28
0.9168	41.78(0.30)	0.62(0.00)	42.40(0.30)	1.43	29
0.9306	41.86(0.28)	0.61(0.00)	42.47(0.28)	1.55	30
0.9513	41.85(0.28)	0.58(0.00)	42.43(0.28)	1.50	31
0.9908	41.88(0.27)	0.55(0.00)	42.43(0.28)	1.46	32
1.0134	41.86(0.27)	0.53(0.00)	42.39(0.27)	1.38	33
1.0602	41.86(0.27)	0.49(0.00)	42.35(0.27)	1.22	34

TABLE C.31: Scan of fit windows on N5 for the s contribution using Padé [1,1].

Q_{cut}^2 [GeV ²]	a_μ^{I}	a_μ^{II}	a_μ^{HLO}	$\chi_{\text{corr}}^2/\text{dof}$	N
0.2378	44.27(2.78)	4.14(0.07)	48.41(2.84)	2.56	5
0.2821	43.54(2.16)	3.36(0.04)	46.89(2.19)	2.37	6
0.2971	43.39(0.91)	3.15(0.03)	46.54(0.93)	2.00	7
0.3527	44.89(0.81)	2.56(0.02)	47.44(0.83)	1.60	8
0.3676	44.99(0.80)	2.43(0.02)	47.42(0.81)	1.95	9
0.4267	46.26(0.66)	2.00(0.01)	48.26(0.67)	1.68	10
0.4493	46.07(0.63)	1.86(0.01)	47.93(0.64)	1.84	11
0.4973	45.46(0.36)	1.61(0.01)	47.08(0.37)	2.13	12
0.5199	45.45(0.31)	1.52(0.01)	46.97(0.32)	2.18	13
0.5641	45.61(0.31)	1.35(0.01)	46.97(0.32)	2.01	14
0.5791	46.02(0.35)	1.31(0.01)	47.33(0.36)	1.84	15
0.6335	45.64(0.29)	1.14(0.00)	46.79(0.29)	1.88	16
0.6347	45.64(0.29)	1.14(0.00)	46.78(0.29)	2.24	17
0.6485	45.61(0.29)	1.11(0.00)	46.72(0.30)	2.10	18
0.6497	45.38(0.29)	1.10(0.00)	46.48(0.30)	2.00	19
0.7087	45.65(0.29)	0.97(0.00)	46.62(0.30)	2.54	20
0.7313	45.06(0.24)	0.92(0.00)	45.98(0.24)	2.05	21
0.7793	45.07(0.23)	0.84(0.00)	45.91(0.23)	2.62	22
0.8007	45.14(0.23)	0.80(0.00)	45.94(0.24)	2.65	23
0.8019	45.05(0.23)	0.80(0.00)	45.85(0.23)	2.34	24
0.8462	45.04(0.23)	0.74(0.00)	45.78(0.23)	2.26	25
0.8612	45.00(0.23)	0.72(0.00)	45.71(0.23)	2.19	26
0.8807	44.95(0.23)	0.69(0.00)	45.64(0.23)	2.39	27
0.9156	44.94(0.22)	0.65(0.00)	45.58(0.23)	3.18	28
0.9168	44.92(0.22)	0.65(0.00)	45.57(0.23)	2.65	29
0.9306	44.92(0.22)	0.63(0.00)	45.56(0.22)	2.71	30
0.9513	44.84(0.22)	0.61(0.00)	45.45(0.22)	2.63	31
0.9908	44.83(0.22)	0.57(0.00)	45.40(0.22)	2.43	32
1.0134	44.72(0.22)	0.55(0.00)	45.26(0.22)	2.54	33
1.0602	44.62(0.22)	0.51(0.00)	45.12(0.22)	2.96	34

TABLE C.32: Scan of fit windows on N6 for the s contribution using Padé [1,1].

Q_{cut}^2 [GeV ²]	a_μ^{I}	a_μ^{II}	a_μ^{HLO}	$\chi_{\text{corr}}^2/\text{dof}$	N
0.1338	46.78(5.50)	8.06(0.24)	54.84(5.72)	0.44	5
0.1588	39.63(2.81)	6.53(0.11)	46.17(2.91)	0.71	6
0.1672	42.12(1.88)	6.23(0.10)	48.34(1.96)	2.20	7
0.1985	44.84(1.76)	5.16(0.07)	49.99(1.83)	1.86	8
0.2069	44.66(1.53)	4.91(0.07)	49.57(1.58)	2.50	9
0.2402	45.98(1.15)	4.16(0.05)	50.14(1.19)	2.17	10
0.2528	46.41(1.13)	3.93(0.05)	50.34(1.16)	1.94	11
0.2799	46.67(0.90)	3.50(0.04)	50.17(0.93)	1.81	12
0.2926	45.55(0.67)	3.25(0.03)	48.80(0.69)	1.24	13
0.3175	45.82(0.67)	2.94(0.03)	48.76(0.68)	1.59	14
0.3260	45.89(0.63)	2.87(0.03)	48.76(0.65)	1.43	15
0.3569	46.15(0.60)	2.56(0.02)	48.70(0.62)	1.11	16
0.3572	45.93(0.59)	2.54(0.02)	48.46(0.60)	1.03	17
0.3653	46.09(0.59)	2.47(0.02)	48.56(0.60)	1.22	18
0.3657	45.99(0.59)	2.47(0.02)	48.46(0.60)	1.10	19
0.3990	46.16(0.56)	2.20(0.02)	48.36(0.58)	1.08	20
0.4116	46.23(0.56)	2.11(0.02)	48.34(0.57)	1.02	21
0.4387	45.84(0.50)	1.93(0.02)	47.77(0.51)	0.97	22
0.4509	45.94(0.46)	1.86(0.02)	47.80(0.47)	1.15	23
0.4513	45.96(0.49)	1.86(0.02)	47.82(0.50)	1.09	24
0.4763	45.94(0.44)	1.73(0.01)	47.67(0.45)	1.02	25
0.4847	45.88(0.43)	1.69(0.01)	47.57(0.44)	1.00	26
0.4964	45.67(0.40)	1.64(0.01)	47.31(0.41)	0.90	27
0.5156	45.78(0.41)	1.55(0.01)	47.33(0.43)	0.87	28
0.5160	45.81(0.41)	1.55(0.01)	47.36(0.42)	0.85	29
0.5241	46.03(0.49)	1.52(0.01)	47.55(0.50)	0.81	30
0.5361	46.16(0.44)	1.47(0.01)	47.63(0.45)	0.78	31
0.5578	46.13(0.48)	1.38(0.01)	47.51(0.49)	0.74	32
0.5704	46.35(0.49)	1.34(0.01)	47.69(0.49)	0.79	33
0.5971	46.57(0.48)	1.26(0.01)	47.84(0.49)	0.71	34
0.5975	46.43(0.47)	1.26(0.01)	47.69(0.48)	0.61	35
0.6097	46.13(0.42)	1.23(0.01)	47.36(0.43)	0.64	36
0.6335	46.21(0.42)	1.16(0.01)	47.37(0.43)	0.67	37
0.6351	46.12(0.43)	1.15(0.01)	47.27(0.44)	0.65	38
0.6420	46.26(0.42)	1.14(0.01)	47.39(0.43)	0.77	39
0.6551	46.15(0.41)	1.10(0.01)	47.24(0.42)	0.78	40
0.6732	46.16(0.41)	1.05(0.01)	47.22(0.42)	0.86	41
0.6744	45.98(0.40)	1.05(0.01)	47.04(0.41)	0.84	42
0.6817	46.00(0.40)	1.03(0.01)	47.03(0.40)	0.80	43
0.6828	45.99(0.39)	1.03(0.01)	47.03(0.40)	0.77	44

TABLE C.33: Scan of fit windows on O7 for the s contribution using Padé [1,1].

C.1.2.2 Fit ansatz: Padé [2,1]

Q_{cut}^2 [GeV ²]	a_μ^{I}	a_μ^{II}	a_μ^{HLO}	$\chi_{\text{corr}}^2/\text{dof}$	N
0.2215	43.72(11.90)	3.25(0.16)	46.97(12.06)	4.61	5
0.2625	43.10(11.47)	3.25(0.15)	46.35(11.62)	2.92	6
0.2765	35.96(2.93)	2.97(0.07)	38.93(2.99)	2.21	7
0.3283	46.27(12.80)	2.50(0.11)	48.77(12.91)	1.73	8
0.3423	46.11(12.24)	1.96(0.07)	48.07(12.30)	1.52	9
0.3967	37.54(2.79)	1.79(0.03)	39.32(2.81)	1.28	10
0.4182	39.03(1.71)	1.57(0.02)	40.61(1.72)	1.61	11
0.4625	38.90(1.32)	1.57(0.02)	40.47(1.33)	1.43	12
0.4840	39.46(1.62)	1.48(0.02)	40.95(1.63)	1.29	13
0.5250	39.69(1.59)	1.33(0.01)	41.02(1.60)	1.14	14
0.5390	40.94(1.53)	1.14(0.01)	42.08(1.53)	1.02	15
0.5883	40.19(1.02)	1.13(0.01)	41.31(1.02)	1.26	16
0.5908	40.11(0.95)	1.13(0.01)	41.24(0.96)	1.23	17
0.6022	40.24(0.94)	1.09(0.01)	41.33(0.95)	1.15	18
0.6048	41.10(1.02)	1.10(0.01)	42.19(1.03)	1.05	19
0.6592	41.57(1.25)	0.92(0.01)	42.50(1.25)	0.98	20
0.6807	41.12(0.94)	0.92(0.01)	42.04(0.94)	1.07	21
0.7250	40.59(0.84)	0.84(0.01)	41.42(0.84)	0.90	22
0.7440	39.87(0.79)	0.80(0.01)	40.67(0.80)	0.95	23
0.7465	39.52(0.89)	0.80(0.01)	40.32(0.89)	1.09	24

TABLE C.34: Scan of fit windows on A3 for the s contribution using Padé [2,1].

Q_{cut}^2 [GeV ²]	a_μ^{I}	a_μ^{II}	a_μ^{HLO}	$\chi_{\text{corr}}^2/\text{dof}$	N
0.2215	37.59(8.57)	3.25(0.12)	40.84(8.68)	1.20	5
0.2625	35.23(1.94)	3.23(0.04)	38.47(1.97)	1.61	6
0.2765	38.67(0.92)	3.08(0.03)	41.75(0.95)	2.12	7
0.3283	39.79(2.71)	2.50(0.04)	42.30(2.75)	2.61	8
0.3423	41.52(2.36)	1.98(0.02)	43.50(2.38)	2.35	9
0.3967	40.67(1.72)	1.85(0.02)	42.52(1.74)	4.68	10
0.4182	41.97(1.33)	1.62(0.01)	43.59(1.34)	4.29	11
0.4625	42.63(1.24)	1.63(0.01)	44.25(1.25)	3.79	12
0.4840	42.77(1.23)	1.53(0.01)	44.30(1.24)	3.41	13
0.5250	42.91(1.23)	1.37(0.01)	44.28(1.24)	3.33	14
0.5390	43.70(1.08)	1.17(0.01)	44.87(1.08)	3.02	15
0.5883	43.83(0.93)	1.16(0.01)	45.00(0.94)	2.86	16
0.5908	43.69(0.89)	1.16(0.01)	44.85(0.90)	2.52	17
0.6022	43.84(0.90)	1.13(0.01)	44.97(0.91)	2.36	18
0.6048	44.26(0.85)	1.13(0.01)	45.39(0.85)	2.14	19
0.6592	44.61(0.87)	0.95(0.01)	45.55(0.87)	2.07	20
0.6807	44.29(0.80)	0.95(0.01)	45.24(0.81)	1.92	21
0.7250	44.15(0.78)	0.86(0.01)	45.01(0.79)	1.78	22
0.7440	43.28(0.70)	0.82(0.00)	44.10(0.70)	1.75	23
0.7465	43.18(0.72)	0.82(0.00)	43.99(0.72)	2.06	24

TABLE C.35: Scan of fit windows on A4 for the s contribution using Padé [2,1].

Q_{cut}^2 [GeV ²]	a_μ^{I}	a_μ^{II}	a_μ^{HLO}	$\chi_{\text{corr}}^2/\text{dof}$	N
0.2215	66.35(14.18)	3.67(0.19)	70.02(14.35)	0.69	5
0.2625	67.02(12.47)	3.66(0.17)	70.69(12.64)	1.79	6
0.2765	62.03(23.41)	3.39(0.26)	65.42(23.67)	1.19	7
0.3283	40.92(4.20)	2.54(0.06)	43.46(4.25)	1.54	8
0.3423	42.51(4.18)	2.01(0.04)	44.52(4.22)	1.32	9
0.3967	44.76(4.85)	1.89(0.04)	46.65(4.88)	1.35	10
0.4182	41.69(1.41)	1.63(0.02)	43.33(1.42)	1.21	11
0.4625	41.37(1.83)	1.63(0.02)	43.00(1.84)	1.16	12
0.4840	42.36(1.62)	1.53(0.02)	43.89(1.63)	1.13	13
0.5250	42.46(1.60)	1.37(0.01)	43.83(1.62)	1.08	14
0.5390	43.72(1.52)	1.18(0.01)	44.90(1.53)	0.98	15
0.5883	44.42(1.21)	1.17(0.01)	45.59(1.21)	1.09	16
0.5908	44.03(1.12)	1.17(0.01)	45.20(1.12)	1.04	17
0.6022	44.30(1.16)	1.13(0.01)	45.43(1.17)	1.02	18
0.6048	45.79(1.20)	1.14(0.01)	46.93(1.21)	0.97	19
0.6592	47.00(1.49)	0.96(0.01)	47.96(1.50)	1.10	20
0.6807	45.38(1.05)	0.95(0.01)	46.33(1.06)	1.04	21
0.7250	45.00(1.04)	0.87(0.01)	45.87(1.04)	1.13	22
0.7440	43.48(0.94)	0.83(0.01)	44.31(0.95)	1.27	23
0.7465	43.71(0.94)	0.83(0.01)	44.54(0.94)	1.71	24

TABLE C.36: Scan of fit windows on A5 for the s contribution using Padé [2,1].

Q_{cut}^2 [GeV ²]	a_μ^{I}	a_μ^{II}	a_μ^{HLO}	$\chi_{\text{corr}}^2/\text{dof}$	N
0.0985	34.30(3.09)	8.04(0.15)	42.34(3.21)	0.76	5
0.1169	37.08(3.30)	8.10(0.14)	45.18(3.40)	0.45	6
0.1231	36.40(3.14)	6.49(0.10)	42.89(3.23)	0.38	7
0.1461	40.86(3.48)	6.56(0.11)	47.42(3.58)	0.34	8
0.1523	40.49(3.09)	6.27(0.09)	46.76(3.16)	0.33	9
0.1768	38.94(0.64)	5.33(0.04)	44.26(0.67)	0.32	10
0.1862	39.28(1.04)	5.04(0.04)	44.32(1.08)	0.34	11
0.2060	39.49(0.65)	4.50(0.03)	43.99(0.68)	0.32	12
0.2154	39.96(0.99)	4.28(0.03)	44.25(1.02)	0.21	13
0.2338	40.47(1.06)	3.91(0.03)	44.38(1.08)	0.22	14
0.2400	40.65(0.99)	3.42(0.02)	44.06(1.01)	0.21	15
0.2625	41.01(1.07)	3.42(0.03)	44.43(1.09)	0.19	16
0.2630	42.31(1.07)	3.42(0.03)	45.74(1.09)	0.17	17
0.2687	42.36(1.07)	3.34(0.02)	45.70(1.09)	0.29	18
0.2692	42.78(1.54)	3.33(0.03)	46.11(1.57)	0.28	19
0.2937	42.99(1.59)	3.00(0.02)	45.99(1.61)	0.25	20
0.3030	41.49(1.58)	2.87(0.02)	44.36(1.60)	0.24	21
0.3229	42.61(0.83)	2.66(0.02)	45.27(0.84)	0.24	22
0.3318	42.90(1.13)	2.57(0.02)	45.47(1.14)	0.24	23
0.3323	42.94(1.26)	2.41(0.02)	45.35(1.27)	0.23	24
0.3506	42.83(1.12)	2.40(0.02)	45.23(1.14)	0.22	25
0.3568	43.25(0.98)	2.29(0.02)	45.54(0.99)	0.22	26
0.3649	43.11(0.71)	2.29(0.01)	45.40(0.72)	0.22	27
0.3794	43.37(0.79)	2.17(0.01)	45.54(0.80)	0.21	28
0.3799	43.49(0.77)	2.13(0.01)	45.63(0.78)	0.23	29
0.3856	43.52(0.78)	2.07(0.01)	45.60(0.79)	0.22	30
0.3942	43.62(0.85)	1.97(0.01)	45.58(0.85)	0.21	31
0.4105	43.68(0.76)	1.91(0.01)	45.59(0.77)	0.23	32
0.4199	44.04(0.86)	1.91(0.01)	45.96(0.87)	0.24	33
0.4393	42.78(0.71)	1.79(0.01)	44.57(0.72)	0.20	34
0.4398	43.80(0.94)	1.80(0.01)	45.59(0.95)	0.29	35
0.4487	44.34(0.60)	1.67(0.01)	46.01(0.61)	0.26	36
0.4655	44.61(0.62)	1.66(0.01)	46.26(0.63)	0.26	37
0.4675	44.59(0.60)	1.66(0.01)	46.25(0.61)	0.27	38
0.4717	44.70(0.60)	1.59(0.01)	46.29(0.61)	0.25	39
0.4818	44.43(0.57)	1.59(0.01)	46.02(0.58)	0.36	40
0.4948	44.68(0.59)	1.52(0.01)	46.20(0.60)	0.43	41
0.4963	44.54(0.58)	1.51(0.01)	46.05(0.59)	0.45	42
0.5010	44.52(0.59)	1.50(0.01)	46.02(0.60)	0.43	43
0.5025	44.57(0.63)	1.50(0.01)	46.06(0.64)	0.59	44
0.5111	44.52(0.65)	1.40(0.01)	45.92(0.66)	0.69	45
0.5274	45.31(0.65)	1.40(0.01)	46.71(0.66)	0.77	46
0.5348	45.53(0.72)	1.38(0.01)	46.90(0.73)	0.45	47
0.5562	46.17(0.81)	1.31(0.01)	47.48(0.81)	0.58	48
0.5640	45.33(0.77)	1.27(0.01)	46.60(0.78)	0.44	49

TABLE C.37: Scan of fit windows on B6 for the s contribution using Padé [2,1].

Q_{cut}^2 [GeV ²]	a_μ^{I}	a_μ^{II}	a_μ^{HLO}	$\chi_{\text{corr}}^2/\text{dof}$	N
0.2916	80.22(8.49)	3.47(0.11)	83.69(8.60)	22.62	5
0.3456	83.19(7.56)	2.80(0.07)	85.99(7.62)	12.78	6
0.3640	40.54(15.21)	2.30(0.14)	42.84(15.35)	8.63	7
0.4322	53.56(7.14)	1.93(0.05)	55.49(7.19)	9.87	8
0.4506	53.81(6.92)	1.82(0.04)	55.63(6.97)	8.00	9
0.5223	45.65(2.65)	1.44(0.02)	47.10(2.66)	6.71	10
0.5506	43.52(0.84)	1.33(0.01)	44.85(0.84)	7.08	11
0.6089	44.15(0.79)	1.15(0.01)	45.30(0.79)	6.35	12
0.6372	44.21(0.79)	1.08(0.01)	45.29(0.80)	5.76	13
0.6912	44.36(0.79)	0.96(0.00)	45.31(0.79)	5.58	14
0.7096	45.63(0.71)	0.93(0.00)	46.55(0.72)	5.03	15
0.7745	45.02(0.61)	0.81(0.00)	45.83(0.61)	5.33	16
0.7778	44.94(0.58)	0.80(0.00)	45.74(0.58)	5.27	17
0.7929	45.35(0.61)	0.78(0.00)	46.13(0.61)	4.91	18
0.7962	45.58(0.55)	0.78(0.00)	46.36(0.55)	4.21	19
0.8679	45.56(0.55)	0.68(0.00)	46.23(0.56)	3.82	20
0.8962	45.35(0.51)	0.64(0.00)	45.99(0.52)	3.98	21
0.9545	45.17(0.49)	0.58(0.00)	45.75(0.49)	3.81	22
0.9795	44.09(0.44)	0.55(0.00)	44.65(0.45)	3.71	23
0.9828	44.04(0.47)	0.55(0.00)	44.59(0.47)	4.72	24

TABLE C.38: Scan of fit windows on E5 for the s contribution using Padé [2,1].

Q_{cut}^2 [GeV 2]	a_μ^{I}	a_μ^{II}	a_μ^{HLO}	$\chi_{\text{corr}}^2/\text{dof}$	N
0.1297	43.40(6.18)	7.90(0.24)	51.31(6.41)	0.70	5
0.1539	44.89(3.85)	6.62(0.13)	51.51(3.96)	0.35	6
0.1621	49.71(7.63)	6.39(0.18)	56.10(7.80)	0.24	7
0.1924	49.34(6.72)	5.26(0.12)	54.61(6.84)	0.60	8
0.2006	48.99(6.29)	5.01(0.11)	54.00(6.40)	0.49	9
0.2328	47.89(4.76)	4.19(0.08)	52.09(4.83)	0.43	10
0.2451	45.75(2.21)	3.91(0.04)	49.66(2.25)	0.43	11
0.2713	46.92(2.41)	3.48(0.04)	50.40(2.45)	0.43	12
0.2836	47.95(2.35)	3.30(0.04)	51.25(2.38)	0.34	13
0.3078	47.89(2.24)	2.98(0.03)	50.88(2.27)	0.37	14
0.3159	48.51(1.93)	2.89(0.03)	51.40(1.95)	0.33	15
0.3456	48.32(2.06)	2.57(0.02)	50.90(2.08)	0.30	16
0.3463	47.80(1.47)	2.56(0.02)	50.36(1.48)	0.40	17
0.3538	48.05(1.53)	2.50(0.02)	50.55(1.54)	0.31	18
0.3544	46.43(0.93)	2.47(0.02)	48.90(0.94)	0.28	19
0.3866	48.09(1.33)	2.22(0.02)	50.32(1.35)	0.41	20
0.3990	47.14(0.98)	2.12(0.01)	49.27(0.99)	0.32	21
0.4251	46.14(0.81)	1.94(0.01)	48.09(0.82)	0.40	22
0.4368	45.07(0.90)	1.87(0.01)	46.94(0.91)	0.70	23
0.4375	45.53(1.35)	1.87(0.01)	47.40(1.36)	0.68	24
0.4616	44.60(0.59)	1.73(0.01)	46.33(0.60)	0.63	25
0.4698	46.88(1.08)	1.70(0.01)	48.59(1.09)	0.70	26
0.4804	46.15(0.69)	1.65(0.01)	47.80(0.70)	0.49	27
0.4995	46.06(0.65)	1.56(0.01)	47.62(0.66)	0.51	28
0.5001	46.43(0.68)	1.56(0.01)	48.00(0.69)	0.47	29
0.5077	46.13(0.64)	1.53(0.01)	47.66(0.65)	0.31	30
0.5190	46.80(0.79)	1.49(0.01)	48.29(0.79)	0.40	31
0.5405	46.22(0.74)	1.40(0.01)	47.62(0.74)	0.35	32
0.5528	46.32(0.70)	1.36(0.01)	47.68(0.71)	0.42	33
0.5784	46.57(0.68)	1.28(0.01)	47.85(0.69)	0.41	34
0.5790	46.21(0.79)	1.27(0.01)	47.48(0.80)	0.40	35
0.5907	47.11(0.61)	1.24(0.01)	48.35(0.61)	0.40	36
0.6129	47.00(0.60)	1.18(0.01)	48.18(0.61)	0.47	37
0.6155	46.68(0.51)	1.17(0.01)	47.85(0.51)	0.58	38
0.6211	47.90(0.66)	1.16(0.01)	49.05(0.66)	0.60	39
0.6343	47.61(0.60)	1.12(0.01)	48.73(0.60)	0.29	40
0.6514	47.61(0.60)	1.08(0.01)	48.69(0.60)	0.29	41
0.6534	47.49(0.59)	1.07(0.01)	48.56(0.60)	0.40	42
0.6596	47.84(0.70)	1.06(0.01)	48.90(0.70)	0.43	43
0.6615	48.38(0.73)	1.06(0.01)	49.44(0.73)	0.62	44
0.6728	47.74(0.70)	1.03(0.01)	48.77(0.70)	0.52	45
0.6944	47.85(0.66)	0.98(0.01)	48.83(0.66)	0.88	46
0.7041	48.52(0.76)	0.97(0.01)	49.48(0.77)	0.59	47
0.7322	47.84(0.71)	0.91(0.01)	48.74(0.71)	0.72	48
0.7426	47.56(0.72)	0.89(0.01)	48.45(0.73)	0.86	49

TABLE C.39: Scan of fit windows on F6 for the s contribution using Padé [2,1].

Q_{cut}^2 [GeV ²]	a_μ^{I}	a_μ^{II}	a_μ^{HLO}	$\chi_{\text{corr}}^2/\text{dof}$	N
0.1297	42.36(8.27)	7.81(0.31)	50.16(8.58)	5.27	5
0.1539	47.12(7.78)	6.65(0.20)	53.78(7.98)	3.14	6
0.1621	41.74(5.38)	6.14(0.14)	47.88(5.53)	2.22	7
0.1924	46.97(7.12)	5.17(0.13)	52.14(7.24)	2.06	8
0.2006	45.55(5.70)	4.91(0.10)	50.46(5.80)	1.71	9
0.2328	45.29(3.62)	4.14(0.07)	49.43(3.67)	1.93	10
0.2451	43.63(1.56)	3.88(0.04)	47.51(1.59)	1.70	11
0.2713	44.76(1.87)	3.44(0.04)	48.20(1.89)	1.54	12
0.2836	43.93(1.47)	3.26(0.03)	47.19(1.49)	1.36	13
0.3078	44.45(1.52)	2.95(0.03)	47.40(1.54)	1.29	14
0.3159	44.08(1.15)	2.85(0.02)	46.93(1.16)	1.19	15
0.3456	44.55(1.33)	2.55(0.02)	47.10(1.35)	0.90	16
0.3463	44.95(1.04)	2.55(0.02)	47.50(1.06)	0.86	17
0.3538	44.95(1.07)	2.48(0.02)	47.43(1.08)	0.81	18
0.3544	44.42(1.26)	2.47(0.02)	46.89(1.28)	0.75	19
0.3866	45.55(1.42)	2.22(0.02)	47.77(1.44)	0.72	20
0.3990	45.03(1.35)	2.13(0.02)	47.16(1.36)	0.72	21
0.4251	45.75(0.82)	1.96(0.01)	47.71(0.83)	0.66	22
0.4368	46.01(1.00)	1.89(0.01)	47.90(1.01)	0.63	23
0.4375	46.12(1.05)	1.89(0.01)	48.00(1.06)	0.60	24
0.4616	45.87(0.96)	1.75(0.01)	47.62(0.97)	0.57	25
0.4698	46.73(0.95)	1.71(0.01)	48.45(0.96)	0.54	26
0.4804	46.82(0.76)	1.66(0.01)	48.48(0.77)	0.64	27
0.4995	47.13(0.82)	1.58(0.01)	48.71(0.83)	0.61	28
0.5001	47.09(0.80)	1.57(0.01)	48.67(0.81)	0.57	29
0.5077	47.22(0.84)	1.54(0.01)	48.76(0.84)	0.56	30
0.5190	47.38(0.87)	1.50(0.01)	48.88(0.88)	0.54	31
0.5405	47.48(0.86)	1.42(0.01)	48.89(0.87)	0.52	32
0.5528	47.54(0.91)	1.37(0.01)	48.91(0.92)	0.49	33
0.5784	46.75(0.78)	1.28(0.01)	48.03(0.78)	0.52	34
0.5790	47.18(0.86)	1.28(0.01)	48.45(0.86)	0.59	35
0.5907	47.54(0.81)	1.24(0.01)	48.79(0.81)	0.57	36
0.6129	47.78(0.83)	1.18(0.01)	48.96(0.84)	0.54	37
0.6155	47.62(0.81)	1.17(0.01)	48.79(0.82)	0.53	38
0.6211	47.33(0.69)	1.16(0.01)	48.49(0.70)	0.53	39
0.6343	47.16(0.64)	1.12(0.01)	48.29(0.64)	0.51	40
0.6514	47.05(0.63)	1.08(0.01)	48.12(0.63)	0.49	41
0.6534	46.94(0.60)	1.07(0.01)	48.02(0.61)	0.57	42
0.6596	47.09(0.65)	1.06(0.01)	48.15(0.66)	0.56	43
0.6615	46.98(0.66)	1.05(0.01)	48.04(0.67)	0.63	44
0.6728	46.41(0.63)	1.03(0.01)	47.44(0.64)	0.78	45
0.6944	47.69(0.72)	0.98(0.01)	48.67(0.72)	0.93	46
0.7041	47.72(0.75)	0.96(0.01)	48.68(0.75)	0.62	47
0.7322	47.73(0.72)	0.91(0.01)	48.63(0.73)	0.68	48
0.7426	47.25(0.66)	0.89(0.01)	48.14(0.66)	0.57	49

TABLE C.40: Scan of fit windows on F7 for the s contribution using Padé [2,1].

Q_{cut}^2 [GeV ²]	a_μ^{I}	a_μ^{II}	a_μ^{HLO}	$\chi_{\text{corr}}^2/\text{dof}$	N
0.0730	34.86(4.24)	12.90(0.36)	47.76(4.56)	1.62	5
0.0866	39.30(3.33)	11.14(0.25)	50.44(3.50)	0.84	6
0.0912	38.16(2.97)	10.61(0.25)	48.77(3.14)	1.54	7
0.1083	38.73(2.25)	9.08(0.17)	47.80(2.40)	1.40	8
0.1129	39.03(2.23)	8.71(0.16)	47.74(2.35)	1.13	9
0.1310	39.56(2.13)	7.53(0.12)	47.09(2.22)	1.06	10
0.1379	39.78(0.62)	7.16(0.09)	46.94(0.68)	0.91	11
0.1527	40.47(0.58)	6.47(0.08)	46.94(0.62)	0.81	12
0.1596	40.78(0.48)	6.18(0.07)	46.96(0.52)	0.72	13
0.1732	41.31(0.54)	5.67(0.06)	46.98(0.58)	0.65	14
0.1778	42.00(0.89)	5.53(0.06)	47.53(0.93)	0.59	15
0.1947	42.39(0.93)	5.02(0.05)	47.41(0.96)	0.61	16
0.1949	42.99(0.99)	5.02(0.05)	48.01(1.02)	0.56	17
0.1993	42.99(0.97)	4.90(0.05)	47.89(1.00)	0.56	18
0.1995	42.80(1.21)	4.89(0.05)	47.70(1.24)	0.54	19
0.2177	43.66(1.39)	4.45(0.05)	48.11(1.42)	0.50	20
0.2245	42.82(0.46)	4.29(0.04)	47.11(0.49)	0.47	21
0.2393	44.09(0.91)	4.00(0.04)	48.09(0.94)	0.40	22
0.2460	44.38(1.22)	3.87(0.04)	48.25(1.25)	0.42	23
0.2462	44.39(1.31)	3.86(0.04)	48.26(1.33)	0.41	24
0.2598	43.85(0.99)	3.62(0.03)	47.48(1.01)	0.40	25
0.2644	44.38(0.96)	3.56(0.03)	47.94(0.98)	0.38	26
0.2708	44.16(0.90)	3.46(0.03)	47.62(0.92)	0.36	27
0.2813	44.02(0.98)	3.30(0.03)	47.31(1.00)	0.34	28
0.2815	44.33(0.85)	3.30(0.03)	47.63(0.86)	0.32	29
0.2859	44.38(0.77)	3.24(0.03)	47.62(0.79)	0.31	30
0.2924	43.89(0.69)	3.15(0.03)	47.04(0.71)	0.28	31
0.3043	44.39(0.83)	3.00(0.03)	47.39(0.85)	0.23	32
0.3112	44.73(0.84)	2.92(0.03)	47.66(0.86)	0.25	33
0.3257	44.76(0.93)	2.76(0.02)	47.52(0.95)	0.26	34
0.3259	44.54(0.90)	2.76(0.02)	47.29(0.92)	0.26	35

TABLE C.41: Scan of fit windows on G8 for the s contribution using Padé [2,1].

Q_{cut}^2 [GeV ²]	a_μ^{I}	a_μ^{II}	a_μ^{HLO}	$\chi_{\text{corr}}^2/\text{dof}$	N
0.3326	45.49(0.87)	2.69(0.02)	48.18(0.89)	0.24	36
0.3456	45.64(0.94)	2.56(0.02)	48.20(0.95)	0.28	37
0.3464	46.04(0.78)	2.55(0.02)	48.59(0.80)	0.28	38
0.3502	46.09(0.79)	2.52(0.02)	48.61(0.80)	0.28	39
0.3574	46.02(0.74)	2.46(0.02)	48.48(0.76)	0.26	40
0.3673	46.28(0.78)	2.37(0.02)	48.65(0.80)	0.25	41
0.3679	45.96(0.71)	2.37(0.02)	48.32(0.72)	0.27	42
0.3719	46.03(0.76)	2.33(0.02)	48.36(0.78)	0.26	43
0.3725	45.91(0.82)	2.33(0.02)	48.24(0.83)	0.27	44
0.3791	45.61(0.95)	2.28(0.02)	47.89(0.96)	0.26	45
0.3909	46.06(0.82)	2.19(0.02)	48.26(0.84)	0.26	46
0.3969	45.71(0.99)	2.15(0.02)	47.86(1.00)	0.24	47
0.4123	45.50(0.93)	2.02(0.02)	47.53(0.94)	0.24	48
0.4186	44.88(0.92)	1.98(0.02)	46.87(0.92)	0.39	49
0.4192	45.11(0.66)	1.98(0.02)	47.09(0.67)	0.40	50
0.4295	46.02(0.79)	1.92(0.02)	47.94(0.80)	0.39	51
0.4322	46.09(0.78)	1.91(0.02)	48.00(0.79)	0.34	52
0.4368	46.60(0.89)	1.89(0.02)	48.49(0.90)	0.32	53
0.4440	46.67(0.95)	1.84(0.02)	48.51(0.96)	0.28	54
0.4511	46.91(0.87)	1.81(0.01)	48.72(0.88)	0.30	55
0.4539	47.16(1.04)	1.79(0.01)	48.95(1.05)	0.25	56
0.4545	46.85(1.00)	1.79(0.01)	48.64(1.01)	0.28	57
0.4585	46.64(1.08)	1.76(0.01)	48.40(1.08)	0.29	58
0.4655	46.78(0.93)	1.73(0.01)	48.51(0.94)	0.32	59
0.4657	46.99(0.92)	1.73(0.01)	48.72(0.93)	0.29	60
0.4767	47.25(1.09)	1.67(0.01)	48.92(1.10)	0.26	61
0.4835	45.52(0.73)	1.64(0.01)	47.16(0.74)	0.27	62
0.4983	44.79(0.87)	1.57(0.01)	46.36(0.88)	0.34	63
0.4989	45.08(0.61)	1.57(0.01)	46.65(0.61)	0.32	64
0.5052	45.45(0.58)	1.54(0.01)	46.99(0.59)	0.31	65
0.5161	45.73(0.67)	1.50(0.01)	47.22(0.68)	0.33	66
0.5188	46.07(1.21)	1.49(0.01)	47.55(1.21)	0.33	67
0.5234	45.86(0.76)	1.47(0.01)	47.33(0.76)	0.32	68
0.5306	46.19(0.69)	1.44(0.01)	47.63(0.70)	0.32	69

TABLE C.42: Scan of fit windows on G8 for the s contribution using Padé [2,1].

Q_{cut}^2 [GeV ²]	a_μ^{I}	a_μ^{II}	a_μ^{HLO}	$\chi_{\text{corr}}^2/\text{dof}$	N
0.2378	74.87(11.87)	4.36(0.20)	79.23(12.06)	4.47	5
0.2821	74.28(9.57)	3.50(0.11)	77.78(9.69)	2.25	6
0.2971	61.63(21.16)	3.18(0.20)	64.81(21.36)	1.51	7
0.3527	41.51(3.82)	2.39(0.04)	43.90(3.87)	1.32	8
0.3676	42.43(3.34)	2.28(0.04)	44.71(3.37)	1.37	9
0.4267	43.27(3.27)	1.88(0.03)	45.15(3.29)	1.51	10
0.4493	41.52(1.29)	1.74(0.02)	43.26(1.30)	1.31	11
0.4973	41.57(1.40)	1.52(0.01)	43.09(1.41)	1.20	12
0.5199	42.47(1.29)	1.43(0.01)	43.90(1.30)	1.09	13
0.5641	42.67(1.30)	1.28(0.01)	43.95(1.31)	1.03	14
0.5791	43.56(1.21)	1.24(0.01)	44.80(1.22)	0.92	15
0.6335	42.18(0.85)	1.08(0.01)	43.26(0.86)	0.97	16
0.6347	42.75(0.99)	1.08(0.01)	43.83(0.99)	1.18	17
0.6485	42.91(1.04)	1.05(0.01)	43.96(1.05)	1.04	18
0.6497	43.65(0.83)	1.05(0.01)	44.70(0.84)	0.96	19
0.7087	44.09(0.97)	0.93(0.01)	45.01(0.97)	0.82	20
0.7313	43.05(0.74)	0.88(0.01)	43.93(0.75)	0.85	21
0.7793	42.98(0.71)	0.80(0.01)	43.78(0.71)	1.05	22
0.8007	42.44(0.71)	0.76(0.00)	43.20(0.71)	1.03	23
0.8019	42.47(0.70)	0.76(0.00)	43.23(0.71)	0.94	24
0.8462	42.60(0.77)	0.70(0.00)	43.30(0.78)	0.89	25
0.8612	42.84(0.74)	0.68(0.00)	43.52(0.75)	0.89	26
0.8807	43.70(0.64)	0.66(0.00)	44.36(0.64)	0.93	27
0.9156	43.15(0.63)	0.62(0.00)	43.77(0.63)	1.02	28
0.9168	43.79(0.63)	0.62(0.00)	44.41(0.63)	1.23	29
0.9306	43.82(0.62)	0.61(0.00)	44.43(0.62)	1.04	30
0.9513	43.62(0.57)	0.59(0.00)	44.21(0.57)	1.03	31
0.9908	43.46(0.55)	0.55(0.00)	44.01(0.56)	1.03	32
1.0134	43.06(0.54)	0.53(0.00)	43.59(0.54)	1.03	33
1.0602	43.00(0.46)	0.49(0.00)	43.49(0.46)	1.02	34

TABLE C.43: Scan of fit windows on N5 for the s contribution using Padé [2,1].

Q_{cut}^2 [GeV ²]	a_μ^{I}	a_μ^{II}	a_μ^{HLO}	$\chi_{\text{corr}}^2/\text{dof}$	N
0.2378	75.38(8.93)	4.58(0.15)	79.96(9.08)	3.96	5
0.2821	75.51(8.07)	3.69(0.09)	79.21(8.16)	2.06	6
0.2971	63.79(19.68)	3.38(0.19)	67.16(19.86)	1.38	7
0.3527	42.78(0.78)	2.53(0.02)	45.32(0.80)	1.45	8
0.3676	42.88(0.84)	2.41(0.02)	45.29(0.85)	1.97	9
0.4267	43.60(0.55)	1.98(0.01)	45.58(0.56)	1.71	10
0.4493	44.48(0.73)	1.86(0.01)	46.34(0.74)	1.56	11
0.4973	45.68(0.85)	1.62(0.01)	47.30(0.85)	1.48	12
0.5199	45.73(0.84)	1.52(0.01)	47.24(0.85)	2.41	13
0.5641	45.88(0.85)	1.36(0.01)	47.23(0.85)	2.20	14
0.5791	46.25(0.87)	1.31(0.01)	47.56(0.88)	2.00	15
0.6335	47.06(0.66)	1.15(0.01)	48.21(0.66)	2.04	16
0.6347	46.90(0.63)	1.15(0.01)	48.05(0.63)	1.95	17
0.6485	46.95(0.64)	1.11(0.01)	48.06(0.64)	1.87	18
0.6497	47.47(0.66)	1.11(0.01)	48.58(0.66)	1.74	19
0.7087	47.53(0.77)	0.98(0.00)	48.51(0.78)	1.81	20
0.7313	47.31(0.57)	0.93(0.00)	48.24(0.58)	1.72	21
0.7793	47.34(0.55)	0.85(0.00)	48.18(0.55)	1.63	22
0.8007	47.08(0.52)	0.81(0.00)	47.89(0.53)	1.56	23
0.8019	47.18(0.55)	0.81(0.00)	47.98(0.55)	1.50	24
0.8462	47.37(0.57)	0.74(0.00)	48.12(0.58)	1.41	25
0.8612	47.51(0.57)	0.72(0.00)	48.24(0.57)	1.32	26
0.8807	47.32(0.44)	0.70(0.00)	48.01(0.44)	1.39	27
0.9156	47.35(0.49)	0.66(0.00)	48.00(0.49)	1.32	28
0.9168	47.36(0.48)	0.65(0.00)	48.02(0.48)	1.36	29
0.9306	47.34(0.47)	0.64(0.00)	47.98(0.47)	1.29	30
0.9513	47.16(0.46)	0.62(0.00)	47.78(0.46)	1.26	31
0.9908	47.11(0.43)	0.58(0.00)	47.69(0.43)	1.27	32
1.0134	46.84(0.37)	0.56(0.00)	47.40(0.38)	1.24	33
1.0602	46.72(0.34)	0.51(0.00)	47.23(0.34)	1.23	34

TABLE C.44: Scan of fit windows on N6 for the s contribution using Padé [2,1].

Q_{cut}^2 [GeV ²]	a_μ^{I}	a_μ^{II}	a_μ^{HLO}	$\chi_{\text{corr}}^2/\text{dof}$	N
0.1338	45.47(4.48)	8.01(0.21)	53.49(4.67)	0.87	5
0.1588	45.16(8.07)	6.66(0.21)	51.81(8.26)	0.96	6
0.1672	43.32(6.62)	6.25(0.17)	49.57(6.78)	2.83	7
0.1985	44.08(1.45)	5.16(0.07)	49.23(1.50)	2.32	8
0.2069	43.91(1.28)	4.91(0.07)	48.82(1.34)	2.73	9
0.2402	44.71(0.97)	4.14(0.05)	48.85(1.01)	2.34	10
0.2528	44.95(0.98)	3.90(0.04)	48.85(1.01)	2.01	11
0.2799	44.86(0.75)	3.47(0.04)	48.33(0.78)	1.75	12
0.2926	45.11(1.53)	3.24(0.04)	48.35(1.55)	1.07	13
0.3175	45.48(1.56)	2.94(0.03)	48.42(1.58)	1.74	14
0.3260	46.50(1.68)	2.88(0.03)	49.37(1.70)	1.56	15
0.3569	46.71(1.80)	2.56(0.03)	49.27(1.82)	1.19	16
0.3572	44.68(0.82)	2.52(0.02)	47.21(0.84)	1.10	17
0.3653	45.02(0.95)	2.46(0.02)	47.48(0.97)	1.18	18
0.3657	45.08(1.05)	2.46(0.02)	47.54(1.07)	1.10	19
0.3990	45.26(1.13)	2.20(0.02)	47.45(1.15)	1.12	20
0.4116	45.51(1.15)	2.11(0.02)	47.62(1.16)	1.05	21
0.4387	47.11(1.02)	1.94(0.02)	49.05(1.03)	1.00	22
0.4509	47.28(1.15)	1.87(0.02)	49.15(1.17)	1.10	23
0.4513	47.33(1.28)	1.87(0.02)	49.21(1.30)	1.06	24
0.4763	47.41(1.11)	1.74(0.02)	49.15(1.11)	1.01	25
0.4847	47.51(1.09)	1.70(0.02)	49.21(1.10)	0.95	26
0.4964	47.26(0.95)	1.65(0.01)	48.91(0.96)	0.82	27
0.5156	47.47(1.04)	1.57(0.01)	49.04(1.05)	0.74	28
0.5160	47.16(0.98)	1.56(0.01)	48.72(0.99)	0.74	29
0.5241	47.17(1.01)	1.53(0.01)	48.70(1.02)	0.75	30
0.5361	46.81(0.95)	1.47(0.01)	48.28(0.96)	0.74	31
0.5578	47.12(0.87)	1.39(0.01)	48.51(0.88)	0.75	32
0.5704	46.33(1.03)	1.34(0.01)	47.67(1.04)	0.74	33
0.5971	46.26(0.78)	1.26(0.01)	47.52(0.78)	0.73	34
0.5975	46.30(0.93)	1.26(0.01)	47.56(0.94)	0.62	35
0.6097	46.78(0.70)	1.23(0.01)	48.01(0.70)	0.66	36
0.6335	46.81(0.70)	1.16(0.01)	47.97(0.71)	0.64	37
0.6351	47.52(0.73)	1.16(0.01)	48.68(0.74)	0.63	38
0.6420	47.39(0.62)	1.14(0.01)	48.53(0.62)	0.62	39
0.6551	47.44(0.60)	1.10(0.01)	48.54(0.60)	0.62	40
0.6732	47.56(0.61)	1.06(0.01)	48.62(0.62)	0.61	41
0.6744	47.10(0.57)	1.06(0.01)	48.16(0.58)	0.58	42
0.6817	47.46(0.65)	1.04(0.01)	48.50(0.66)	0.61	43
0.6828	47.44(0.68)	1.04(0.01)	48.48(0.68)	0.57	44

TABLE C.45: Scan of fit windows on O7 for the s contribution using Padé [2,1].

C.1.3 The light-quark contribution

C.1.3.1 Fit ansatz: Padé [1,1]

Q_{cut}^2 [GeV ²]	a_μ^{I}	a_μ^{II}	a_μ^{HLO}	$\chi_{\text{corr}}^2/\text{dof}$	N
0.2215	6.64(0.24)	0.77(0.02)	7.42(0.25)	0.38	5
0.2625	6.89(0.23)	0.77(0.02)	7.66(0.25)	0.26	6
0.2765	6.87(0.12)	0.73(0.01)	7.60(0.12)	0.85	7
0.3283	7.35(0.62)	0.61(0.01)	7.96(0.63)	0.69	8
0.3423	7.06(0.45)	0.49(0.01)	7.54(0.46)	0.40	9
0.3967	7.55(0.31)	0.47(0.01)	8.02(0.32)	0.72	10
0.4182	7.68(0.32)	0.42(0.01)	8.10(0.33)	0.29	11
0.4625	7.79(0.25)	0.42(0.01)	8.21(0.25)	0.30	12
0.4840	7.69(0.25)	0.40(0.00)	8.09(0.25)	0.26	13
0.5250	7.34(0.35)	0.36(0.00)	7.70(0.36)	0.45	14
0.5390	7.98(0.23)	0.32(0.00)	8.30(0.23)	0.36	15
0.5883	7.95(0.21)	0.32(0.00)	8.27(0.21)	0.71	16
0.5908	7.23(0.17)	0.31(0.00)	7.54(0.17)	0.71	17
0.6022	7.33(0.16)	0.31(0.00)	7.63(0.16)	0.23	18
0.6048	7.28(0.14)	0.31(0.00)	7.59(0.15)	0.13	19
0.6592	7.34(0.14)	0.26(0.00)	7.60(0.14)	0.15	20
0.6807	7.28(0.20)	0.26(0.00)	7.54(0.20)	0.16	21
0.7250	7.09(0.09)	0.24(0.00)	7.34(0.09)	0.14	22
0.7440	7.09(0.10)	0.23(0.00)	7.33(0.10)	0.20	23
0.7465	7.10(0.11)	0.23(0.00)	7.33(0.11)	0.42	24

TABLE C.46: Scan of fit windows on A3 for the c contribution using Padé [1,1].

Q_{cut}^2 [GeV ²]	a_μ^{I}	a_μ^{II}	a_μ^{HLO}	$\chi_{\text{corr}}^2/\text{dof}$	N
0.2215	6.36(0.18)	0.73(0.01)	7.09(0.19)	0.08	5
0.2625	6.53(0.17)	0.73(0.01)	7.26(0.18)	0.21	6
0.2765	6.56(0.31)	0.69(0.01)	7.25(0.32)	0.26	7
0.3283	7.04(0.52)	0.58(0.01)	7.62(0.53)	0.22	8
0.3423	7.12(0.52)	0.47(0.01)	7.60(0.53)	0.14	9
0.3967	6.98(0.24)	0.45(0.01)	7.43(0.24)	0.13	10
0.4182	7.07(0.25)	0.40(0.00)	7.47(0.25)	0.14	11
0.4625	7.29(0.20)	0.40(0.00)	7.69(0.20)	0.17	12
0.4840	7.10(0.20)	0.38(0.00)	7.48(0.20)	0.26	13
0.5250	6.76(0.20)	0.34(0.00)	7.10(0.20)	0.50	14
0.5390	7.62(0.19)	0.30(0.00)	7.93(0.19)	0.16	15
0.5883	6.89(0.22)	0.30(0.00)	7.19(0.22)	1.60	16
0.5908	6.89(0.14)	0.30(0.00)	7.19(0.14)	0.16	17
0.6022	7.00(0.13)	0.29(0.00)	7.30(0.13)	0.15	18
0.6048	6.97(0.11)	0.29(0.00)	7.26(0.11)	0.20	19
0.6592	6.99(0.11)	0.25(0.00)	7.25(0.11)	0.21	20
0.6807	6.92(0.14)	0.25(0.00)	7.17(0.14)	0.12	21
0.7250	6.85(0.07)	0.23(0.00)	7.08(0.07)	0.10	22
0.7440	6.84(0.07)	0.23(0.00)	7.06(0.07)	0.06	23
0.7465	6.83(0.08)	0.23(0.00)	7.05(0.08)	0.14	24

TABLE C.47: Scan of fit windows on A4 for the c contribution using Padé [1,1].

Q_{cut}^2 [GeV ²]	a_μ^{I}	a_μ^{II}	a_μ^{HLO}	$\chi_{\text{corr}}^2/\text{dof}$	N
0.2215	6.20(0.79)	0.72(0.02)	6.92(0.81)	3.08	5
0.2625	6.20(0.21)	0.72(0.02)	6.92(0.22)	2.82	6
0.2765	6.38(0.46)	0.68(0.02)	7.06(0.48)	2.14	7
0.3283	6.83(0.65)	0.57(0.01)	7.41(0.66)	1.71	8
0.3423	6.66(0.56)	0.47(0.01)	7.13(0.57)	1.45	9
0.3967	6.36(0.08)	0.44(0.01)	6.81(0.09)	1.30	10
0.4182	6.43(0.03)	0.40(0.01)	6.83(0.03)	1.49	11
0.4625	6.55(0.15)	0.40(0.01)	6.95(0.15)	1.35	12
0.4840	6.49(0.03)	0.38(0.01)	6.87(0.03)	1.56	13
0.5250	6.53(0.03)	0.35(0.00)	6.88(0.03)	1.14	14
0.5390	6.49(0.03)	0.30(0.00)	6.80(0.03)	1.22	15
0.5883	6.51(0.03)	0.30(0.00)	6.81(0.03)	0.99	16
0.5908	6.50(0.08)	0.30(0.00)	6.80(0.08)	0.91	17
0.6022	6.66(0.14)	0.29(0.00)	6.96(0.14)	1.05	18
0.6048	6.58(0.11)	0.29(0.00)	6.87(0.11)	1.41	19
0.6592	6.56(0.09)	0.25(0.00)	6.81(0.09)	1.25	20
0.6807	6.49(0.03)	0.25(0.00)	6.74(0.03)	0.87	21
0.7250	6.62(0.09)	0.23(0.00)	6.85(0.09)	0.74	22
0.7440	6.55(0.08)	0.23(0.00)	6.77(0.08)	0.80	23
0.7465	6.50(0.07)	0.22(0.00)	6.73(0.07)	0.57	24

TABLE C.48: Scan of fit windows on A5 for the c contribution using Padé [1,1].

Q_{cut}^2 [GeV ²]	a_μ^{I}	a_μ^{II}	a_μ^{HLO}	$\chi_{\text{corr}}^2/\text{dof}$	N
0.0985	9.99(3.56)	1.55(0.15)	11.54(3.69)	0.05	5
0.1169	4.74(0.55)	1.48(0.11)	6.22(0.62)	0.04	6
0.1231	5.67(0.30)	1.29(0.07)	6.96(0.33)	0.37	7
0.1461	5.75(0.29)	1.28(0.07)	7.03(0.32)	0.99	8
0.1523	5.86(0.30)	1.23(0.07)	7.09(0.33)	0.61	9
0.1768	6.11(0.22)	1.06(0.05)	7.18(0.24)	0.50	10
0.1862	5.91(0.06)	1.01(0.04)	6.92(0.08)	0.46	11
0.2060	6.00(0.06)	0.91(0.03)	6.91(0.07)	0.55	12
0.2154	6.03(0.06)	0.87(0.03)	6.90(0.07)	0.38	13
0.2338	6.30(0.47)	0.81(0.03)	7.11(0.48)	0.37	14
0.2400	6.26(0.45)	0.72(0.02)	6.98(0.46)	0.41	15
0.2625	6.55(0.50)	0.72(0.02)	7.27(0.52)	0.38	16
0.2630	5.83(0.36)	0.69(0.03)	6.52(0.38)	0.36	17
0.2687	5.63(0.46)	0.66(0.03)	6.30(0.48)	0.33	18
0.2692	5.94(0.33)	0.68(0.03)	6.62(0.35)	0.30	19
0.2937	5.98(0.27)	0.62(0.02)	6.61(0.28)	0.39	20
0.3030	6.26(0.32)	0.62(0.02)	6.88(0.33)	0.37	21
0.3229	6.29(0.10)	0.58(0.02)	6.87(0.11)	0.32	22
0.3318	6.29(0.10)	0.56(0.01)	6.85(0.11)	0.30	23
0.3323	6.28(0.10)	0.53(0.01)	6.81(0.11)	0.35	24
0.3506	6.30(0.10)	0.53(0.01)	6.83(0.11)	0.35	25
0.3568	6.31(0.09)	0.51(0.01)	6.82(0.10)	0.36	26
0.3649	6.35(0.11)	0.51(0.01)	6.86(0.12)	0.34	27
0.3794	6.36(0.11)	0.49(0.01)	6.85(0.12)	0.33	28
0.3799	6.48(0.16)	0.49(0.01)	6.96(0.16)	0.35	29
0.3856	6.21(0.61)	0.47(0.01)	6.68(0.62)	0.29	30
0.3942	6.36(0.74)	0.45(0.01)	6.80(0.75)	0.23	31
0.4105	6.37(0.75)	0.43(0.01)	6.80(0.75)	0.22	32
0.4199	8.10(1.96)	0.44(0.02)	8.54(1.97)	0.19	33
0.4393	7.93(1.38)	0.41(0.01)	8.34(1.39)	0.12	34
0.4398	7.47(1.78)	0.42(0.01)	7.89(1.79)	0.08	35
0.4487	7.40(1.25)	0.38(0.01)	7.79(1.25)	0.19	36
0.4655	7.18(0.98)	0.38(0.01)	7.56(0.98)	0.13	37
0.4675	8.53(1.58)	0.39(0.01)	8.92(1.59)	0.11	38
0.4717	6.43(0.19)	0.38(0.01)	6.81(0.20)	0.19	39
0.4818	6.43(0.21)	0.38(0.01)	6.81(0.21)	0.23	40
0.4948	6.45(0.22)	0.36(0.01)	6.81(0.22)	0.23	41
0.4963	6.52(0.21)	0.36(0.01)	6.88(0.22)	0.22	42
0.5010	6.46(0.20)	0.36(0.01)	6.82(0.20)	0.20	43
0.5025	6.48(0.17)	0.36(0.01)	6.84(0.17)	0.21	44
0.5111	6.47(0.17)	0.34(0.01)	6.81(0.17)	0.18	45
0.5274	6.50(0.16)	0.34(0.01)	6.84(0.17)	0.19	46
0.5348	6.37(0.03)	0.33(0.01)	6.70(0.03)	0.18	47
0.5562	6.38(0.03)	0.32(0.01)	6.70(0.03)	0.17	48
0.5640	6.38(0.03)	0.31(0.01)	6.69(0.03)	0.17	49

TABLE C.49: Scan of fit windows on B6 for the c contribution using Padé [1,1].

Q_{cut}^2 [GeV ²]	a_μ^{I}	a_μ^{II}	a_μ^{HLO}	$\chi_{\text{corr}}^2/\text{dof}$	N
0.2916	8.50(3.22)	0.75(0.04)	9.25(3.27)	0.36	5
0.3456	7.32(0.10)	0.62(0.01)	7.94(0.10)	0.33	6
0.3640	7.34(0.05)	0.58(0.01)	7.93(0.05)	1.04	7
0.4322	7.79(0.30)	0.48(0.00)	8.28(0.30)	0.84	8
0.4506	7.76(0.26)	0.46(0.00)	8.22(0.26)	0.31	9
0.5223	7.70(0.06)	0.39(0.00)	8.09(0.06)	0.33	10
0.5506	7.86(0.14)	0.37(0.00)	8.22(0.14)	0.32	11
0.6089	8.05(0.10)	0.33(0.00)	8.38(0.10)	0.32	12
0.6372	7.91(0.11)	0.31(0.00)	8.22(0.11)	0.56	13
0.6912	7.62(0.14)	0.28(0.00)	7.90(0.14)	1.16	14
0.7096	8.05(0.07)	0.27(0.00)	8.32(0.07)	0.30	15
0.7745	8.06(0.07)	0.24(0.00)	8.30(0.07)	1.11	16
0.7778	7.54(0.07)	0.24(0.00)	7.79(0.07)	0.98	17
0.7929	7.66(0.06)	0.24(0.00)	7.89(0.06)	0.29	18
0.7962	7.60(0.07)	0.23(0.00)	7.83(0.07)	0.90	19
0.8679	7.68(0.06)	0.21(0.00)	7.89(0.06)	0.58	20
0.8962	7.43(0.09)	0.20(0.00)	7.63(0.09)	0.95	21
0.9545	7.57(0.04)	0.18(0.00)	7.75(0.04)	0.74	22
0.9795	7.53(0.04)	0.18(0.00)	7.71(0.04)	0.16	23
0.9828	7.51(0.05)	0.18(0.00)	7.69(0.05)	1.09	24

TABLE C.50: Scan of fit windows on E5 for the c contribution using Padé [1,1].

Q_{cut}^2 [GeV ²]	a_μ^{I}	a_μ^{II}	a_μ^{HLO}	$\chi_{\text{corr}}^2/\text{dof}$	N
0.1297	14.19(4.83)	1.74(0.15)	15.93(4.96)	0.01	5
0.1539	12.85(5.95)	1.43(0.12)	14.28(6.06)	0.51	6
0.1621	6.54(0.16)	1.29(0.03)	7.83(0.18)	0.42	7
0.1924	6.61(0.16)	1.09(0.03)	7.70(0.17)	1.12	8
0.2006	6.67(0.16)	1.05(0.03)	7.72(0.17)	0.80	9
0.2328	6.80(0.12)	0.91(0.02)	7.71(0.12)	0.71	10
0.2451	6.91(0.04)	0.86(0.02)	7.77(0.05)	0.62	11
0.2713	7.09(0.25)	0.77(0.01)	7.87(0.25)	0.60	12
0.2836	7.02(0.04)	0.74(0.01)	7.76(0.04)	0.66	13
0.3078	7.10(0.04)	0.68(0.01)	7.78(0.05)	0.58	14
0.3159	7.12(0.04)	0.66(0.01)	7.78(0.04)	0.51	15
0.3456	7.16(0.04)	0.61(0.01)	7.77(0.04)	0.46	16
0.3463	7.02(0.15)	0.60(0.01)	7.62(0.16)	0.41	17
0.3538	7.02(0.16)	0.58(0.01)	7.60(0.16)	0.38	18
0.3544	7.00(0.19)	0.58(0.01)	7.58(0.20)	0.38	19
0.3866	7.02(0.14)	0.53(0.01)	7.55(0.15)	0.35	20
0.3990	7.02(0.16)	0.51(0.01)	7.53(0.17)	0.31	21
0.4251	7.24(0.07)	0.48(0.01)	7.72(0.07)	0.30	22
0.4368	7.25(0.07)	0.47(0.01)	7.73(0.07)	0.33	23
0.4375	7.25(0.07)	0.47(0.01)	7.72(0.07)	0.34	24
0.4616	7.27(0.07)	0.45(0.01)	7.72(0.07)	0.34	25
0.4698	7.29(0.06)	0.44(0.00)	7.72(0.07)	0.34	26
0.4804	7.32(0.08)	0.43(0.01)	7.75(0.08)	0.32	27
0.4995	7.34(0.08)	0.41(0.00)	7.75(0.08)	0.30	28
0.5001	7.24(0.02)	0.40(0.00)	7.64(0.02)	0.32	29
0.5077	7.63(0.37)	0.40(0.00)	8.03(0.37)	0.42	30
0.5190	7.62(0.43)	0.39(0.00)	8.01(0.43)	0.31	31
0.5405	7.78(0.41)	0.37(0.00)	8.16(0.41)	0.30	32
0.5528	7.71(0.50)	0.36(0.00)	8.08(0.50)	0.29	33
0.5784	7.82(0.48)	0.35(0.00)	8.17(0.48)	0.30	34
0.5790	7.48(0.45)	0.34(0.00)	7.83(0.45)	0.29	35
0.5907	7.58(0.42)	0.33(0.00)	7.91(0.43)	0.27	36
0.6129	7.73(0.45)	0.32(0.00)	8.05(0.45)	0.25	37
0.6155	7.81(0.61)	0.32(0.00)	8.13(0.62)	0.25	38
0.6211	7.51(0.44)	0.32(0.00)	7.83(0.44)	0.29	39
0.6343	7.64(0.50)	0.31(0.00)	7.95(0.50)	0.29	40
0.6514	7.68(0.50)	0.30(0.00)	7.98(0.50)	0.28	41
0.6534	7.65(0.46)	0.30(0.00)	7.95(0.46)	0.27	42
0.6596	7.51(0.44)	0.29(0.00)	7.80(0.44)	0.26	43
0.6615	7.27(0.02)	0.29(0.00)	7.56(0.02)	0.25	44
0.6728	7.30(0.35)	0.28(0.00)	7.58(0.35)	0.21	45
0.6944	7.35(0.31)	0.27(0.00)	7.63(0.31)	0.23	46
0.7041	7.28(0.26)	0.27(0.00)	7.54(0.27)	0.22	47
0.7322	7.41(0.29)	0.26(0.00)	7.66(0.29)	0.20	48
0.7426	7.64(0.37)	0.25(0.00)	7.90(0.38)	0.20	49

TABLE C.51: Scan of fit windows on F6 for the c contribution using Padé [1,1].

Q_{cut}^2 [GeV 2]	a_μ^{I}	a_μ^{II}	a_μ^{HLO}	$\chi_{\text{corr}}^2/\text{dof}$	N
0.1297	7.67(0.38)	1.69(0.07)	9.36(0.43)	0.05	5
0.1539	10.80(7.81)	1.49(0.15)	12.29(7.97)	0.08	6
0.1621	10.84(1.83)	1.41(0.06)	12.25(1.89)	0.10	7
0.1924	11.58(1.92)	1.19(0.05)	12.77(1.96)	0.08	8
0.2006	11.84(1.99)	1.15(0.05)	12.99(2.03)	0.08	9
0.2328	7.72(0.50)	0.93(0.02)	8.65(0.51)	0.07	10
0.2451	7.61(0.52)	0.89(0.02)	8.50(0.53)	1.36	11
0.2713	7.33(0.35)	0.79(0.01)	8.13(0.36)	1.70	12
0.2836	7.37(0.36)	0.76(0.01)	8.13(0.37)	1.45	13
0.3078	7.82(0.60)	0.70(0.01)	8.52(0.60)	1.32	14
0.3159	7.96(0.58)	0.68(0.01)	8.64(0.59)	1.24	15
0.3456	7.85(0.48)	0.62(0.01)	8.47(0.48)	1.12	16
0.3463	7.27(0.22)	0.62(0.01)	7.88(0.23)	1.06	17
0.3538	7.44(0.27)	0.60(0.01)	8.05(0.27)	1.17	18
0.3544	7.36(0.20)	0.61(0.01)	7.97(0.20)	1.21	19
0.3866	7.35(0.20)	0.55(0.01)	7.90(0.20)	1.07	20
0.3990	7.26(0.10)	0.53(0.01)	7.79(0.11)	1.02	21
0.4251	9.83(0.83)	0.52(0.01)	10.34(0.84)	0.91	22
0.4368	9.74(0.80)	0.50(0.01)	10.25(0.81)	0.32	23
0.4375	9.70(0.78)	0.50(0.01)	10.20(0.79)	0.28	24
0.4616	9.93(0.78)	0.47(0.01)	10.40(0.78)	0.27	25
0.4698	10.09(0.83)	0.46(0.01)	10.55(0.83)	0.30	26
0.4804	10.45(0.92)	0.46(0.01)	10.90(0.92)	0.31	27
0.4995	10.24(0.86)	0.43(0.01)	10.67(0.86)	0.28	28
0.5001	10.43(1.01)	0.43(0.01)	10.87(1.01)	0.28	29
0.5077	10.23(0.87)	0.43(0.01)	10.65(0.88)	0.27	30
0.5190	8.73(0.66)	0.40(0.01)	9.14(0.66)	0.23	31
0.5405	8.53(0.52)	0.38(0.00)	8.91(0.53)	0.47	32
0.5528	9.53(0.83)	0.38(0.01)	9.91(0.84)	0.47	33
0.5784	9.37(0.71)	0.36(0.00)	9.73(0.71)	0.34	34
0.5790	9.63(1.02)	0.36(0.01)	9.99(1.02)	0.32	35
0.5907	8.99(0.73)	0.35(0.01)	9.34(0.74)	0.37	36
0.6129	8.84(0.62)	0.33(0.00)	9.17(0.62)	0.38	37
0.6155	10.71(1.01)	0.34(0.01)	11.05(1.02)	0.37	38
0.6211	9.37(0.89)	0.33(0.01)	9.70(0.89)	0.20	39
0.6343	9.28(0.85)	0.32(0.01)	9.60(0.85)	0.41	40
0.6514	9.15(0.79)	0.31(0.00)	9.46(0.80)	0.37	41
0.6534	8.79(0.66)	0.31(0.00)	9.10(0.66)	0.37	42
0.6596	9.42(0.80)	0.31(0.00)	9.73(0.80)	0.38	43
0.6615	8.93(0.82)	0.30(0.00)	9.23(0.82)	0.33	44
0.6728	9.18(0.79)	0.30(0.00)	9.48(0.79)	0.38	45
0.6944	8.56(0.67)	0.28(0.00)	8.85(0.67)	0.35	46
0.7041	8.31(0.63)	0.28(0.00)	8.58(0.63)	0.43	47
0.7322	7.95(0.51)	0.26(0.00)	8.21(0.52)	0.43	48
0.7426	8.07(0.45)	0.26(0.00)	8.33(0.46)	0.44	49

TABLE C.52: Scan of fit windows on F7 for the c contribution using Padé [1,1].

Q_{cut}^2 [GeV ²]	a_μ^{I}	a_μ^{II}	a_μ^{HLO}	$\chi_{\text{corr}}^2/\text{dof}$	N
0.0730	7.23(0.66)	2.81(0.20)	10.04(0.81)	0.90	5
0.0866	9.87(3.34)	2.51(0.19)	12.38(3.47)	0.60	6
0.0912	12.74(3.21)	2.48(0.18)	15.22(3.36)	0.65	7
0.1083	13.56(3.08)	2.12(0.13)	15.68(3.19)	0.55	8
0.1129	14.03(3.20)	2.06(0.13)	16.08(3.30)	0.48	9
0.1310	6.91(0.69)	1.60(0.07)	8.50(0.73)	0.40	10
0.1379	6.91(0.71)	1.52(0.06)	8.43(0.74)	1.23	11
0.1527	6.90(0.57)	1.37(0.04)	8.27(0.58)	1.14	12
0.1596	6.60(0.07)	1.30(0.03)	7.90(0.08)	1.02	13
0.1732	6.71(0.08)	1.21(0.03)	7.92(0.09)	0.92	14
0.1778	6.94(0.63)	1.19(0.03)	8.13(0.65)	0.86	15
0.1947	6.82(0.43)	1.10(0.03)	7.91(0.44)	0.81	16
0.1949	7.03(0.30)	1.10(0.03)	8.13(0.31)	0.74	17
0.1993	7.06(0.32)	1.09(0.03)	8.15(0.34)	0.66	18
0.1995	7.46(0.41)	1.11(0.03)	8.57(0.43)	0.64	19
0.2177	7.27(0.30)	1.00(0.03)	8.27(0.32)	0.48	20
0.2245	7.27(0.30)	0.96(0.02)	8.24(0.32)	0.47	21
0.2393	9.47(1.39)	0.95(0.04)	10.42(1.42)	0.46	22
0.2460	9.24(1.39)	0.92(0.03)	10.16(1.42)	0.35	23
0.2462	9.14(1.39)	0.92(0.03)	10.06(1.42)	0.31	24
0.2598	9.31(1.38)	0.87(0.03)	10.18(1.41)	0.30	25
0.2644	9.44(1.46)	0.86(0.03)	10.30(1.48)	0.30	26
0.2708	9.85(1.50)	0.84(0.03)	10.69(1.53)	0.30	27
0.2813	9.46(1.47)	0.80(0.03)	10.26(1.50)	0.27	28
0.2815	10.13(1.59)	0.81(0.03)	10.94(1.61)	0.27	29
0.2859	9.19(1.37)	0.79(0.03)	9.98(1.39)	0.25	30
0.2924	9.16(1.42)	0.77(0.03)	9.93(1.44)	0.26	31
0.3043	8.83(1.16)	0.73(0.02)	9.56(1.17)	0.26	32
0.3112	8.78(1.20)	0.71(0.02)	9.49(1.22)	0.25	33
0.3257	8.73(1.13)	0.68(0.02)	9.41(1.14)	0.24	34
0.3259	8.55(1.24)	0.68(0.02)	9.22(1.25)	0.23	35

TABLE C.53: Scan of fit windows on G8 for the c contribution using Padé [1,1].

Q_{cut}^2 [GeV ²]	a_μ^{I}	a_μ^{II}	a_μ^{HLO}	$\chi_{\text{corr}}^2/\text{dof}$	N
0.3326	8.33(0.99)	0.66(0.02)	8.99(1.00)	0.23	36
0.3456	8.41(0.95)	0.63(0.02)	9.05(0.97)	0.22	37
0.3464	8.94(1.75)	0.64(0.02)	9.58(1.76)	0.21	38
0.3502	8.03(0.39)	0.63(0.01)	8.66(0.41)	0.20	39
0.3574	7.92(0.37)	0.61(0.01)	8.53(0.38)	0.13	40
0.3673	8.21(0.95)	0.59(0.01)	8.80(0.96)	0.14	41
0.3679	8.61(1.08)	0.59(0.01)	9.20(1.09)	0.16	42
0.3719	9.87(2.02)	0.60(0.02)	10.46(2.04)	0.17	43
0.3725	9.13(1.62)	0.59(0.02)	9.73(1.63)	0.17	44
0.3791	9.05(1.65)	0.58(0.02)	9.62(1.66)	0.17	45
0.3909	7.71(0.70)	0.55(0.01)	8.26(0.71)	0.17	46
0.3969	8.16(0.89)	0.54(0.01)	8.70(0.90)	0.17	47
0.4123	8.10(0.79)	0.52(0.01)	8.62(0.80)	0.18	48
0.4186	8.14(0.72)	0.51(0.01)	8.65(0.73)	0.18	49
0.4192	8.25(0.78)	0.51(0.01)	8.76(0.79)	0.16	50
0.4295	8.20(0.75)	0.49(0.01)	8.70(0.75)	0.17	51
0.4322	8.44(0.99)	0.49(0.01)	8.93(1.00)	0.17	52
0.4368	8.11(0.77)	0.48(0.01)	8.60(0.78)	0.17	53
0.4440	8.42(0.86)	0.48(0.01)	8.90(0.87)	0.16	54
0.4511	8.39(0.85)	0.47(0.01)	8.86(0.86)	0.16	55
0.4539	8.40(0.83)	0.47(0.01)	8.86(0.84)	0.15	56
0.4545	8.49(0.87)	0.47(0.01)	8.96(0.88)	0.15	57
0.4585	8.63(0.96)	0.46(0.01)	9.09(0.97)	0.15	58
0.4655	8.53(0.91)	0.45(0.01)	8.98(0.91)	0.14	59
0.4657	8.44(0.91)	0.45(0.01)	8.89(0.92)	0.14	60
0.4767	8.20(0.81)	0.44(0.01)	8.64(0.81)	0.14	61
0.4835	8.23(0.82)	0.43(0.01)	8.66(0.82)	0.14	62
0.4983	8.27(0.81)	0.42(0.01)	8.69(0.82)	0.14	63
0.4989	8.15(0.72)	0.41(0.01)	8.56(0.72)	0.14	64
0.5052	8.06(0.69)	0.41(0.01)	8.47(0.70)	0.14	65
0.5161	8.04(0.67)	0.40(0.01)	8.44(0.67)	0.14	66
0.5188	8.18(0.74)	0.40(0.01)	8.57(0.74)	0.14	67
0.5234	8.15(0.70)	0.39(0.01)	8.54(0.70)	0.14	68
0.5306	8.11(0.73)	0.39(0.01)	8.50(0.73)	0.14	69

TABLE C.54: Scan of fit windows on G8 for the c contribution using Padé [1,1].

Q_{cut}^2 [GeV ²]	a_μ^{I}	a_μ^{II}	a_μ^{HLO}	$\chi_{\text{corr}}^2/\text{dof}$	N
0.2378	8.31(0.23)	1.06(0.02)	9.37(0.24)	0.56	5
0.2821	8.50(0.23)	0.90(0.01)	9.40(0.24)	0.72	6
0.2971	8.74(0.53)	0.85(0.01)	9.60(0.55)	0.62	7
0.3527	9.09(0.64)	0.71(0.01)	9.80(0.65)	0.54	8
0.3676	9.06(0.61)	0.68(0.01)	9.74(0.61)	0.43	9
0.4267	8.70(0.21)	0.57(0.01)	9.27(0.22)	0.34	10
0.4493	8.79(0.21)	0.54(0.00)	9.33(0.22)	0.37	11
0.4973	9.11(0.21)	0.49(0.00)	9.60(0.21)	0.40	12
0.5199	8.94(0.21)	0.46(0.00)	9.41(0.21)	0.58	13
0.5641	8.76(0.03)	0.42(0.00)	9.18(0.03)	0.35	14
0.5791	8.74(0.02)	0.41(0.00)	9.15(0.03)	0.21	15
0.6335	8.91(0.19)	0.37(0.00)	9.28(0.20)	0.19	16
0.6347	9.06(0.16)	0.37(0.00)	9.42(0.16)	0.21	17
0.6485	9.21(0.15)	0.36(0.00)	9.57(0.15)	0.35	18
0.6497	9.17(0.13)	0.36(0.00)	9.52(0.13)	0.53	19
0.7087	9.16(0.13)	0.32(0.00)	9.48(0.13)	0.50	20
0.7313	9.06(0.17)	0.31(0.00)	9.37(0.17)	0.36	21
0.7793	9.17(0.09)	0.29(0.00)	9.46(0.09)	0.31	22
0.8007	9.15(0.10)	0.28(0.00)	9.42(0.10)	0.25	23
0.8019	9.13(0.11)	0.28(0.00)	9.41(0.11)	0.19	24
0.8462	9.13(0.12)	0.26(0.00)	9.38(0.12)	0.18	25
0.8612	9.17(0.15)	0.25(0.00)	9.42(0.15)	0.24	26
0.8807	9.34(0.27)	0.24(0.00)	9.58(0.27)	0.23	27
0.9156	9.37(0.27)	0.23(0.00)	9.61(0.28)	0.22	28
0.9168	9.13(0.51)	0.23(0.00)	9.36(0.51)	0.22	29
0.9306	9.13(0.24)	0.23(0.00)	9.36(0.24)	0.20	30
0.9513	9.03(0.30)	0.22(0.00)	9.25(0.30)	0.17	31
0.9908	9.15(0.26)	0.21(0.00)	9.35(0.26)	0.16	32
1.0134	9.30(0.37)	0.20(0.00)	9.51(0.38)	0.16	33
1.0602	9.40(0.34)	0.19(0.00)	9.59(0.34)	0.16	34

TABLE C.55: Scan of fit windows on N5 for the c contribution using Padé [1,1].

Q_{cut}^2 [GeV ²]	a_μ^{I}	a_μ^{II}	a_μ^{HLO}	$\chi_{\text{corr}}^2/\text{dof}$	N
0.2378	18.10(5.86)	1.22(0.08)	19.32(5.94)	0.10	5
0.2821	9.86(3.66)	0.92(0.04)	10.79(3.69)	0.15	6
0.2971	9.05(0.53)	0.87(0.01)	9.92(0.54)	1.06	7
0.3527	9.44(0.58)	0.72(0.01)	10.17(0.59)	0.87	8
0.3676	9.44(0.57)	0.69(0.01)	10.14(0.58)	0.62	9
0.4267	9.24(0.23)	0.59(0.00)	9.82(0.23)	0.53	10
0.4493	9.43(0.24)	0.56(0.00)	9.99(0.25)	0.51	11
0.4973	9.59(0.18)	0.50(0.00)	10.08(0.18)	0.77	12
0.5199	9.44(0.19)	0.47(0.00)	9.91(0.19)	0.63	13
0.5641	9.10(0.26)	0.43(0.00)	9.52(0.27)	0.94	14
0.5791	9.15(0.26)	0.41(0.00)	9.57(0.26)	0.68	15
0.6335	9.23(0.21)	0.37(0.00)	9.60(0.21)	0.64	16
0.6347	9.04(0.15)	0.37(0.00)	9.41(0.15)	0.57	17
0.6485	9.14(0.13)	0.36(0.00)	9.50(0.13)	0.52	18
0.6497	9.14(0.12)	0.36(0.00)	9.50(0.12)	0.34	19
0.7087	9.23(0.12)	0.32(0.00)	9.55(0.12)	0.30	20
0.7313	9.18(0.16)	0.31(0.00)	9.50(0.17)	0.39	21
0.7793	9.12(0.07)	0.29(0.00)	9.41(0.07)	0.39	22
0.8007	9.10(0.08)	0.28(0.00)	9.38(0.08)	0.35	23
0.8019	9.09(0.09)	0.28(0.00)	9.37(0.09)	0.53	24
0.8462	9.01(0.10)	0.26(0.00)	9.27(0.11)	0.59	25
0.8612	9.05(0.13)	0.25(0.00)	9.30(0.13)	0.46	26
0.8807	8.97(0.22)	0.24(0.00)	9.22(0.22)	0.43	27
0.9156	9.16(0.25)	0.23(0.00)	9.39(0.25)	0.41	28
0.9168	9.64(0.45)	0.23(0.00)	9.88(0.45)	0.58	29
0.9306	9.53(0.20)	0.23(0.00)	9.76(0.20)	0.62	30
0.9513	9.61(0.25)	0.22(0.00)	9.83(0.25)	0.36	31
0.9908	9.75(0.20)	0.21(0.00)	9.96(0.20)	0.34	32
1.0134	9.92(0.28)	0.21(0.00)	10.13(0.28)	0.32	33
1.0602	9.93(0.25)	0.19(0.00)	10.12(0.25)	0.31	34

TABLE C.56: Scan of fit windows on N6 for the c contribution using Padé [1,1].

Q_{cut}^2 [GeV ²]	a_μ^{I}	a_μ^{II}	a_μ^{HLO}	$\chi_{\text{corr}}^2/\text{dof}$	N
0.1338	10.28(4.43)	1.96(0.19)	12.24(4.61)	0.15	5
0.1588	8.06(0.58)	1.71(0.10)	9.77(0.64)	0.34	6
0.1672	8.08(0.99)	1.61(0.09)	9.69(1.03)	0.85	7
0.1985	8.47(1.13)	1.35(0.06)	9.83(1.15)	0.69	8
0.2069	8.52(1.12)	1.30(0.06)	9.82(1.13)	0.53	9
0.2402	8.62(0.59)	1.11(0.05)	9.73(0.61)	0.45	10
0.2528	8.65(0.58)	1.05(0.04)	9.70(0.59)	0.40	11
0.2799	8.76(0.50)	0.95(0.03)	9.71(0.51)	0.36	12
0.2926	8.91(0.53)	0.90(0.03)	9.81(0.54)	0.32	13
0.3175	8.90(0.64)	0.82(0.03)	9.72(0.65)	0.28	14
0.3260	8.85(0.62)	0.80(0.03)	9.65(0.62)	0.25	15
0.3569	9.13(0.61)	0.73(0.02)	9.85(0.62)	0.24	16
0.3572	8.66(0.35)	0.71(0.02)	9.37(0.36)	0.22	17
0.3653	8.69(0.33)	0.70(0.02)	9.39(0.34)	0.19	18
0.3657	8.53(0.28)	0.70(0.02)	9.23(0.29)	0.18	19
0.3990	8.60(0.27)	0.64(0.02)	9.23(0.28)	0.19	20
0.4116	8.58(0.27)	0.62(0.02)	9.19(0.27)	0.18	21
0.4387	8.66(0.08)	0.58(0.01)	9.24(0.09)	0.17	22
0.4509	9.21(0.92)	0.57(0.02)	9.78(0.93)	0.17	23
0.4513	9.45(0.99)	0.57(0.02)	10.03(1.00)	0.21	24
0.4763	9.35(0.96)	0.54(0.01)	9.89(0.97)	0.20	25
0.4847	8.67(0.03)	0.52(0.01)	9.19(0.04)	0.19	26
0.4964	8.68(0.03)	0.50(0.01)	9.19(0.04)	0.20	27
0.5156	8.75(0.38)	0.48(0.01)	9.23(0.38)	0.20	28
0.5160	9.29(0.90)	0.49(0.01)	9.77(0.90)	0.22	29
0.5241	9.55(0.64)	0.48(0.01)	10.03(0.65)	0.22	30
0.5361	9.63(0.82)	0.47(0.01)	10.10(0.83)	0.15	31
0.5578	9.81(0.70)	0.45(0.01)	10.25(0.70)	0.15	32
0.5704	10.23(1.02)	0.44(0.01)	10.67(1.03)	0.13	33
0.5971	10.23(0.93)	0.41(0.01)	10.64(0.93)	0.12	34
0.5975	10.46(1.23)	0.42(0.01)	10.88(1.24)	0.11	35
0.6097	10.17(0.94)	0.40(0.01)	10.57(0.94)	0.11	36
0.6335	10.13(0.80)	0.38(0.01)	10.51(0.81)	0.10	37
0.6351	10.50(1.41)	0.39(0.01)	10.89(1.42)	0.09	38
0.6420	9.49(1.01)	0.38(0.01)	9.87(1.01)	0.16	39
0.6551	10.04(1.18)	0.37(0.01)	10.41(1.18)	0.18	40
0.6732	10.17(1.08)	0.36(0.01)	10.53(1.09)	0.15	41
0.6744	9.87(0.98)	0.36(0.01)	10.23(0.98)	0.14	42
0.6817	9.72(1.15)	0.35(0.01)	10.07(1.16)	0.14	43
0.6828	9.07(0.79)	0.35(0.01)	9.41(0.80)	0.14	44

TABLE C.57: Scan of fit windows on O7 for the c contribution using Padé [1,1].

C.1.3.2 Fit ansatz: Polynomial of $O(Q^2)$

Q_{cut}^2 [GeV ²]	a_μ^{I}	a_μ^{II}	a_μ^{HLO}	$\chi_{\text{corr}}^2/\text{dof}$	N
0.2215	6.64(0.24)	0.77(0.02)	7.42(0.25)	0.25	5
0.2625	6.89(0.23)	0.77(0.02)	7.66(0.25)	0.19	6
0.2765	6.87(0.12)	0.73(0.01)	7.60(0.12)	0.68	7
0.3283	6.84(0.11)	0.61(0.01)	7.44(0.12)	0.58	8
0.3423	6.69(0.02)	0.49(0.01)	7.18(0.03)	0.42	9
0.3967	6.72(0.08)	0.45(0.01)	7.17(0.08)	0.68	10
0.4182	6.78(0.03)	0.41(0.01)	7.19(0.03)	1.21	11
0.4625	6.83(0.03)	0.40(0.01)	7.23(0.03)	1.13	12
0.4840	6.84(0.03)	0.38(0.00)	7.22(0.03)	1.81	13
0.5250	6.89(0.03)	0.35(0.00)	7.25(0.03)	1.55	14
0.5390	6.80(0.02)	0.30(0.00)	7.10(0.03)	0.47	15
0.5883	6.81(0.02)	0.30(0.00)	7.11(0.03)	3.26	16
0.5908	6.86(0.02)	0.31(0.00)	7.17(0.03)	3.27	17
0.6022	6.86(0.02)	0.30(0.00)	7.16(0.03)	0.55	18
0.6048	6.84(0.02)	0.30(0.00)	7.14(0.03)	0.72	19
0.6592	6.86(0.02)	0.26(0.00)	7.12(0.03)	0.72	20
0.6807	6.84(0.02)	0.26(0.00)	7.10(0.03)	0.88	21
0.7250	6.85(0.02)	0.24(0.00)	7.09(0.03)	0.40	22
0.7440	6.84(0.02)	0.23(0.00)	7.07(0.03)	0.56	23
0.7465	6.82(0.02)	0.23(0.00)	7.05(0.03)	0.75	24

TABLE C.58: Scan of fit windows on A3 for the c contribution using a Polynomial of $O(Q^2)$.

Q_{cut}^2 [GeV ²]	a_μ^{I}	a_μ^{II}	a_μ^{HLO}	$\chi_{\text{corr}}^2/\text{dof}$	N
0.2215	6.36(0.18)	0.73(0.01)	7.09(0.19)	0.05	5
0.2625	6.53(0.17)	0.73(0.01)	7.26(0.18)	0.16	6
0.2765	6.53(0.09)	0.69(0.01)	7.22(0.09)	0.21	7
0.3283	6.51(0.09)	0.57(0.01)	7.08(0.09)	0.18	8
0.3423	6.52(0.09)	0.47(0.01)	6.99(0.09)	0.27	9
0.3967	6.48(0.06)	0.44(0.00)	6.92(0.07)	0.29	10
0.4182	6.53(0.02)	0.39(0.00)	6.92(0.03)	0.69	11
0.4625	6.58(0.02)	0.39(0.00)	6.97(0.03)	0.66	12
0.4840	6.59(0.02)	0.37(0.00)	6.96(0.03)	1.57	13
0.5250	6.63(0.02)	0.34(0.00)	6.97(0.03)	1.09	14
0.5390	6.53(0.02)	0.29(0.00)	6.82(0.02)	0.16	15
0.5883	6.61(0.02)	0.30(0.00)	6.91(0.02)	4.50	16
0.5908	6.60(0.02)	0.30(0.00)	6.90(0.02)	0.26	17
0.6022	6.60(0.02)	0.29(0.00)	6.89(0.02)	0.46	18
0.6048	6.59(0.02)	0.29(0.00)	6.87(0.02)	0.83	19
0.6592	6.60(0.02)	0.25(0.00)	6.85(0.02)	0.95	20
0.6807	6.58(0.02)	0.25(0.00)	6.83(0.02)	0.93	21
0.7250	6.59(0.02)	0.23(0.00)	6.82(0.02)	0.41	22
0.7440	6.58(0.02)	0.22(0.00)	6.81(0.02)	0.78	23
0.7465	6.57(0.02)	0.22(0.00)	6.79(0.02)	0.73	24

TABLE C.59: Scan of fit windows on A4 for the c contribution using a Polynomial of $O(Q^2)$.

Q_{cut}^2 [GeV ²]	a_μ^{I}	a_μ^{II}	a_μ^{HLO}	$\chi_{\text{corr}}^2/\text{dof}$	N
0.2215	6.05(0.22)	0.72(0.02)	6.77(0.23)	2.05	5
0.2625	6.20(0.21)	0.72(0.02)	6.92(0.22)	2.12	6
0.2765	6.17(0.11)	0.68(0.02)	6.85(0.12)	1.71	7
0.3283	6.16(0.11)	0.57(0.01)	6.72(0.11)	1.45	8
0.3423	6.17(0.11)	0.46(0.01)	6.64(0.12)	1.40	9
0.3967	6.36(0.08)	0.44(0.01)	6.81(0.09)	1.22	10
0.4182	6.43(0.03)	0.40(0.01)	6.83(0.03)	1.32	11
0.4625	6.48(0.03)	0.40(0.01)	6.87(0.03)	1.22	12
0.4840	6.49(0.03)	0.38(0.01)	6.87(0.03)	1.43	13
0.5250	6.53(0.03)	0.35(0.00)	6.88(0.03)	1.05	14
0.5390	6.49(0.03)	0.30(0.00)	6.80(0.03)	1.12	15
0.5883	6.51(0.03)	0.30(0.00)	6.81(0.03)	0.92	16
0.5908	6.50(0.03)	0.30(0.00)	6.80(0.03)	0.85	17
0.6022	6.50(0.03)	0.29(0.00)	6.80(0.03)	0.99	18
0.6048	6.49(0.03)	0.29(0.00)	6.79(0.03)	1.41	19
0.6592	6.51(0.03)	0.25(0.00)	6.76(0.03)	1.21	20
0.6807	6.49(0.03)	0.25(0.00)	6.74(0.03)	0.83	21
0.7250	6.50(0.03)	0.23(0.00)	6.74(0.03)	0.70	22
0.7440	6.49(0.03)	0.23(0.00)	6.72(0.03)	0.85	23
0.7465	6.48(0.03)	0.22(0.00)	6.70(0.03)	0.56	24

TABLE C.60: Scan of fit windows on A5 for the c contribution using a Polynomial of $O(Q^2)$.

Q_{cut}^2 [GeV 2]	a_μ^{I}	a_μ^{II}	a_μ^{HLO}	$\chi_{\text{corr}}^2/\text{dof}$	N
0.0985	4.27(0.59)	1.41(0.10)	5.68(0.66)	0.06	5
0.1169	4.74(0.55)	1.48(0.11)	6.22(0.62)	0.05	6
0.1231	5.67(0.30)	1.29(0.07)	6.96(0.33)	0.29	7
0.1461	5.75(0.29)	1.28(0.07)	7.03(0.32)	0.83	8
0.1523	5.86(0.30)	1.23(0.07)	7.09(0.33)	0.52	9
0.1768	6.11(0.22)	1.06(0.05)	7.18(0.24)	0.44	10
0.1862	5.91(0.06)	1.01(0.04)	6.92(0.08)	0.41	11
0.2060	6.00(0.06)	0.91(0.03)	6.91(0.07)	0.49	12
0.2154	6.03(0.06)	0.87(0.03)	6.90(0.07)	0.34	13
0.2338	6.10(0.07)	0.81(0.03)	6.91(0.08)	0.34	14
0.2400	6.12(0.06)	0.72(0.02)	6.84(0.07)	0.39	15
0.2625	6.17(0.06)	0.72(0.02)	6.89(0.07)	0.35	16
0.2630	5.83(0.36)	0.69(0.03)	6.52(0.38)	0.36	17
0.2687	5.60(0.36)	0.67(0.03)	6.26(0.37)	0.31	18
0.2692	5.94(0.33)	0.68(0.03)	6.62(0.35)	0.29	19
0.2937	5.98(0.27)	0.62(0.02)	6.61(0.28)	0.37	20
0.3030	6.26(0.32)	0.62(0.02)	6.88(0.33)	0.35	21
0.3229	6.29(0.10)	0.58(0.02)	6.87(0.11)	0.31	22
0.3318	6.29(0.10)	0.56(0.01)	6.85(0.11)	0.29	23
0.3323	6.28(0.10)	0.53(0.01)	6.81(0.11)	0.33	24
0.3506	6.30(0.10)	0.53(0.01)	6.83(0.11)	0.33	25
0.3568	6.31(0.09)	0.51(0.01)	6.82(0.10)	0.34	26
0.3649	6.35(0.11)	0.51(0.01)	6.86(0.12)	0.33	27
0.3794	6.36(0.11)	0.49(0.01)	6.85(0.12)	0.31	28
0.3799	6.48(0.16)	0.49(0.01)	6.96(0.16)	0.33	29
0.3856	5.97(0.28)	0.46(0.01)	6.44(0.29)	0.28	30
0.3942	5.99(0.32)	0.44(0.01)	6.43(0.33)	0.22	31
0.4105	5.83(0.34)	0.43(0.01)	6.26(0.35)	0.22	32
0.4199	5.97(0.33)	0.43(0.01)	6.40(0.34)	0.20	33
0.4393	5.90(0.32)	0.40(0.01)	6.30(0.33)	0.22	34
0.4398	6.14(0.29)	0.41(0.01)	6.55(0.30)	0.20	35
0.4487	6.04(0.30)	0.38(0.01)	6.42(0.31)	0.21	36
0.4655	5.96(0.31)	0.38(0.01)	6.33(0.32)	0.18	37
0.4675	6.29(0.23)	0.38(0.01)	6.68(0.24)	0.17	38
0.4717	6.43(0.19)	0.38(0.01)	6.81(0.20)	0.23	39
0.4818	6.43(0.21)	0.38(0.01)	6.81(0.21)	0.23	40
0.4948	6.45(0.22)	0.36(0.01)	6.81(0.22)	0.22	41
0.4963	6.52(0.21)	0.36(0.01)	6.88(0.22)	0.22	42
0.5010	6.46(0.20)	0.36(0.01)	6.82(0.20)	0.20	43
0.5025	6.48(0.17)	0.36(0.01)	6.84(0.17)	0.21	44
0.5111	6.47(0.17)	0.34(0.01)	6.81(0.17)	0.17	45
0.5274	6.50(0.16)	0.34(0.01)	6.84(0.17)	0.18	46
0.5348	6.37(0.03)	0.33(0.01)	6.70(0.03)	0.18	47
0.5562	6.38(0.03)	0.32(0.01)	6.70(0.03)	0.17	48
0.5640	6.38(0.03)	0.31(0.01)	6.69(0.03)	0.16	49

TABLE C.61: Scan of fit windows on B6 for the c contribution using a Polynomial of $O(Q^2)$.

Q_{cut}^2 [GeV ²]	a_μ^{I}	a_μ^{II}	a_μ^{HLO}	$\chi_{\text{corr}}^2/\text{dof}$	N
0.2916	7.17(0.10)	0.73(0.01)	7.90(0.10)	0.41	5
0.3456	7.32(0.10)	0.62(0.01)	7.94(0.10)	0.31	6
0.3640	7.34(0.05)	0.58(0.01)	7.93(0.05)	0.83	7
0.4322	7.31(0.05)	0.48(0.00)	7.79(0.05)	0.70	8
0.4506	7.30(0.01)	0.46(0.00)	7.76(0.01)	0.69	9
0.5223	7.37(0.01)	0.38(0.00)	7.76(0.01)	0.69	10
0.5506	7.33(0.01)	0.36(0.00)	7.69(0.01)	3.60	11
0.6089	7.36(0.01)	0.32(0.00)	7.68(0.01)	1.95	12
0.6372	7.37(0.01)	0.31(0.00)	7.67(0.01)	5.59	13
0.6912	7.39(0.01)	0.28(0.00)	7.67(0.01)	3.53	14
0.7096	7.33(0.01)	0.27(0.00)	7.60(0.01)	0.50	15
0.7745	7.34(0.01)	0.24(0.00)	7.58(0.01)	9.42	16
0.7778	7.38(0.01)	0.24(0.00)	7.62(0.01)	8.67	17
0.7929	7.38(0.01)	0.24(0.00)	7.61(0.01)	0.69	18
0.7962	7.36(0.01)	0.23(0.00)	7.59(0.01)	2.06	19
0.8679	7.37(0.01)	0.21(0.00)	7.58(0.01)	1.34	20
0.8962	7.33(0.01)	0.20(0.00)	7.53(0.01)	2.34	21
0.9545	7.34(0.01)	0.18(0.00)	7.53(0.01)	0.76	22
0.9795	7.33(0.01)	0.18(0.00)	7.51(0.01)	1.85	23
0.9828	7.31(0.01)	0.18(0.00)	7.49(0.01)	2.09	24

TABLE C.62: Scan of fit windows on E5 for the c contribution using a Polynomial of $O(Q^2)$.

Q_{cut}^2 [GeV ²]	a_μ^{I}	a_μ^{II}	a_μ^{HLO}	$\chi_{\text{corr}}^2/\text{dof}$	N
0.1297	5.86(0.35)	1.52(0.07)	7.38(0.39)	0.35	5
0.1539	6.01(0.33)	1.30(0.04)	7.30(0.36)	0.70	6
0.1621	6.54(0.16)	1.29(0.03)	7.83(0.18)	0.59	7
0.1924	6.61(0.16)	1.09(0.03)	7.70(0.17)	0.93	8
0.2006	6.67(0.16)	1.05(0.03)	7.72(0.17)	0.68	9
0.2328	6.80(0.12)	0.91(0.02)	7.71(0.12)	0.62	10
0.2451	6.91(0.04)	0.86(0.02)	7.77(0.05)	0.55	11
0.2713	6.99(0.04)	0.77(0.01)	7.76(0.05)	0.54	12
0.2836	7.02(0.04)	0.74(0.01)	7.76(0.04)	0.61	13
0.3078	7.10(0.04)	0.68(0.01)	7.78(0.05)	0.53	14
0.3159	7.12(0.04)	0.66(0.01)	7.78(0.04)	0.47	15
0.3456	7.16(0.04)	0.61(0.01)	7.77(0.04)	0.43	16
0.3463	7.02(0.15)	0.60(0.01)	7.62(0.16)	0.38	17
0.3538	7.02(0.16)	0.58(0.01)	7.60(0.16)	0.36	18
0.3544	7.00(0.19)	0.58(0.01)	7.58(0.20)	0.35	19
0.3866	7.02(0.14)	0.53(0.01)	7.55(0.15)	0.33	20
0.3990	7.02(0.16)	0.51(0.01)	7.53(0.17)	0.29	21
0.4251	7.24(0.07)	0.48(0.01)	7.72(0.07)	0.28	22
0.4368	7.25(0.07)	0.47(0.01)	7.73(0.07)	0.31	23
0.4375	7.25(0.07)	0.47(0.01)	7.72(0.07)	0.32	24
0.4616	7.27(0.07)	0.45(0.01)	7.72(0.07)	0.33	25
0.4698	7.29(0.06)	0.44(0.00)	7.72(0.07)	0.33	26
0.4804	7.32(0.08)	0.43(0.01)	7.75(0.08)	0.31	27
0.4995	7.34(0.08)	0.41(0.00)	7.75(0.08)	0.29	28
0.5001	7.24(0.02)	0.40(0.00)	7.64(0.02)	0.31	29
0.5077	7.25(0.02)	0.40(0.00)	7.65(0.02)	0.41	30
0.5190	7.25(0.02)	0.39(0.00)	7.64(0.02)	0.33	31
0.5405	7.25(0.02)	0.37(0.00)	7.62(0.02)	0.31	32
0.5528	7.26(0.02)	0.36(0.00)	7.62(0.02)	0.34	33
0.5784	7.26(0.02)	0.34(0.00)	7.60(0.02)	0.31	34
0.5790	7.25(0.02)	0.34(0.00)	7.59(0.02)	0.32	35
0.5907	7.26(0.02)	0.33(0.00)	7.59(0.02)	0.27	36
0.6129	7.26(0.02)	0.32(0.00)	7.58(0.02)	0.26	37
0.6155	7.27(0.02)	0.32(0.00)	7.59(0.02)	0.28	38
0.6211	7.28(0.02)	0.31(0.00)	7.59(0.02)	0.30	39
0.6343	7.29(0.02)	0.31(0.00)	7.60(0.02)	0.29	40
0.6514	7.29(0.02)	0.30(0.00)	7.59(0.02)	0.28	41
0.6534	7.29(0.02)	0.30(0.00)	7.58(0.02)	0.27	42
0.6596	7.28(0.02)	0.29(0.00)	7.57(0.02)	0.27	43
0.6615	7.27(0.02)	0.29(0.00)	7.56(0.02)	0.25	44
0.6728	7.26(0.02)	0.28(0.00)	7.54(0.02)	0.21	45
0.6944	7.27(0.02)	0.27(0.00)	7.55(0.02)	0.22	46
0.7041	7.26(0.02)	0.27(0.00)	7.53(0.02)	0.22	47
0.7322	7.27(0.02)	0.26(0.00)	7.53(0.02)	0.20	48
0.7426	7.26(0.02)	0.25(0.00)	7.52(0.02)	0.20	49

TABLE C.63: Scan of fit windows on F6 for the c contribution using a Polynomial of $O(Q^2)$.

Q_{cut}^2 [GeV ²]	a_μ^{I}	a_μ^{II}	a_μ^{HLO}	$\chi_{\text{corr}}^2/\text{dof}$	N
0.1297	7.67(0.38)	1.69(0.07)	9.36(0.43)	0.04	5
0.1539	7.85(0.38)	1.43(0.04)	9.28(0.41)	0.06	6
0.1621	7.03(0.19)	1.30(0.03)	8.33(0.21)	0.13	7
0.1924	7.07(0.19)	1.09(0.02)	8.16(0.20)	1.30	8
0.2006	7.05(0.19)	1.05(0.02)	8.10(0.21)	1.52	9
0.2328	7.19(0.13)	0.91(0.02)	8.10(0.14)	1.50	10
0.2451	6.94(0.04)	0.88(0.02)	7.82(0.05)	1.35	11
0.2713	7.03(0.04)	0.79(0.01)	7.81(0.05)	1.70	12
0.2836	7.06(0.04)	0.75(0.01)	7.81(0.05)	1.38	13
0.3078	7.13(0.04)	0.70(0.01)	7.83(0.05)	1.26	14
0.3159	7.13(0.04)	0.68(0.01)	7.81(0.04)	1.27	15
0.3456	7.18(0.04)	0.62(0.01)	7.79(0.04)	1.21	16
0.3463	7.20(0.13)	0.62(0.01)	7.81(0.13)	1.14	17
0.3538	7.18(0.13)	0.61(0.01)	7.78(0.14)	1.10	18
0.3544	7.36(0.16)	0.61(0.01)	7.97(0.17)	1.21	19
0.3866	7.28(0.13)	0.55(0.01)	7.83(0.13)	1.01	20
0.3990	7.26(0.10)	0.53(0.01)	7.79(0.11)	0.97	21
0.4251	7.30(0.06)	0.49(0.01)	7.79(0.07)	0.86	22
0.4368	7.31(0.06)	0.48(0.01)	7.79(0.07)	0.76	23
0.4375	7.31(0.06)	0.48(0.01)	7.79(0.07)	0.72	24
0.4616	7.33(0.06)	0.45(0.01)	7.78(0.07)	0.71	25
0.4698	7.32(0.06)	0.44(0.01)	7.77(0.07)	0.79	26
0.4804	7.39(0.08)	0.43(0.01)	7.82(0.09)	0.78	27
0.4995	7.41(0.09)	0.42(0.00)	7.83(0.09)	0.71	28
0.5001	7.69(0.14)	0.42(0.01)	8.11(0.15)	0.70	29
0.5077	7.21(0.11)	0.40(0.00)	7.61(0.12)	0.53	30
0.5190	7.24(0.03)	0.39(0.00)	7.64(0.03)	0.78	31
0.5405	7.25(0.03)	0.38(0.00)	7.62(0.03)	0.73	32
0.5528	7.25(0.03)	0.37(0.00)	7.62(0.03)	0.74	33
0.5784	7.25(0.03)	0.35(0.00)	7.60(0.03)	0.70	34
0.5790	7.24(0.03)	0.35(0.00)	7.59(0.03)	0.71	35
0.5907	7.25(0.03)	0.34(0.00)	7.59(0.03)	0.61	36
0.6129	7.25(0.03)	0.32(0.00)	7.58(0.03)	0.59	37
0.6155	7.27(0.03)	0.32(0.00)	7.59(0.03)	0.60	38
0.6211	7.27(0.03)	0.32(0.00)	7.59(0.03)	0.61	39
0.6343	7.28(0.03)	0.31(0.00)	7.59(0.03)	0.59	40
0.6514	7.28(0.03)	0.30(0.00)	7.58(0.03)	0.56	41
0.6534	7.28(0.03)	0.30(0.00)	7.58(0.03)	0.55	42
0.6596	7.27(0.03)	0.30(0.00)	7.57(0.03)	0.55	43
0.6615	7.26(0.03)	0.29(0.00)	7.56(0.03)	0.57	44
0.6728	7.25(0.03)	0.29(0.00)	7.54(0.03)	0.51	45
0.6944	7.27(0.03)	0.28(0.00)	7.54(0.03)	0.53	46
0.7041	7.26(0.03)	0.27(0.00)	7.53(0.03)	0.53	47
0.7322	7.26(0.03)	0.26(0.00)	7.52(0.03)	0.50	48
0.7426	7.26(0.03)	0.25(0.00)	7.51(0.03)	0.48	49

TABLE C.64: Scan of fit windows on F7 for the c contribution using a Polynomial of $O(Q^2)$.

Q_{cut}^2 [GeV ²]	a_μ^{I}	a_μ^{II}	a_μ^{HLO}	$\chi_{\text{corr}}^2/\text{dof}$	N
0.0730	7.23(0.66)	2.81(0.20)	10.04(0.81)	0.60	5
0.0866	7.39(0.67)	2.41(0.14)	9.81(0.78)	0.45	6
0.0912	6.11(0.34)	2.13(0.11)	8.24(0.41)	0.56	7
0.1083	6.24(0.34)	1.83(0.08)	8.07(0.38)	1.41	8
0.1129	6.22(0.35)	1.77(0.08)	7.99(0.39)	1.38	9
0.1310	6.53(0.25)	1.57(0.06)	8.11(0.28)	1.23	10
0.1379	6.42(0.07)	1.50(0.05)	7.91(0.09)	1.11	11
0.1527	6.54(0.07)	1.36(0.04)	7.90(0.08)	1.06	12
0.1596	6.60(0.07)	1.30(0.03)	7.90(0.08)	0.95	13
0.1732	6.71(0.08)	1.21(0.03)	7.92(0.09)	0.84	14
0.1778	6.72(0.07)	1.18(0.03)	7.91(0.08)	0.80	15
0.1947	6.81(0.07)	1.10(0.03)	7.90(0.08)	0.76	16
0.1949	7.03(0.30)	1.10(0.03)	8.13(0.31)	0.69	17
0.1993	7.06(0.32)	1.09(0.03)	8.15(0.34)	0.62	18
0.1995	7.46(0.41)	1.11(0.03)	8.57(0.43)	0.60	19
0.2177	7.27(0.30)	1.00(0.03)	8.27(0.32)	0.45	20
0.2245	7.27(0.30)	0.96(0.02)	8.24(0.32)	0.44	21
0.2393	7.00(0.13)	0.90(0.02)	7.90(0.13)	0.43	22
0.2460	7.05(0.13)	0.88(0.02)	7.93(0.13)	0.48	23
0.2462	7.06(0.13)	0.88(0.02)	7.94(0.13)	0.41	24
0.2598	7.08(0.13)	0.83(0.02)	7.92(0.13)	0.39	25
0.2644	7.08(0.13)	0.82(0.02)	7.90(0.13)	0.40	26
0.2708	7.12(0.17)	0.80(0.02)	7.92(0.17)	0.40	27
0.2813	7.17(0.17)	0.77(0.02)	7.94(0.18)	0.38	28
0.2815	7.31(0.26)	0.77(0.02)	8.08(0.27)	0.35	29
0.2859	7.09(0.26)	0.75(0.02)	7.84(0.27)	0.34	30
0.2924	7.20(0.30)	0.73(0.02)	7.94(0.31)	0.36	31
0.3043	7.24(0.29)	0.70(0.02)	7.95(0.30)	0.34	32
0.3112	7.44(0.35)	0.70(0.02)	8.14(0.37)	0.32	33
0.3257	7.46(0.35)	0.66(0.01)	8.13(0.36)	0.28	34
0.3259	7.56(0.35)	0.66(0.02)	8.22(0.36)	0.27	35

TABLE C.65: Scan of fit windows on G8 for the c contribution using a Polynomial of $O(Q^2)$.

Q_{cut}^2 [GeV ²]	a_μ^{I}	a_μ^{II}	a_μ^{HLO}	$\chi_{\text{corr}}^2/\text{dof}$	N
0.3326	7.56(0.33)	0.65(0.01)	8.21(0.35)	0.24	36
0.3456	7.54(0.32)	0.62(0.01)	8.16(0.33)	0.23	37
0.3464	7.66(0.35)	0.63(0.01)	8.29(0.36)	0.23	38
0.3502	8.03(0.39)	0.63(0.01)	8.66(0.41)	0.21	39
0.3574	7.92(0.37)	0.61(0.01)	8.53(0.38)	0.12	40
0.3673	7.79(0.34)	0.59(0.01)	8.38(0.35)	0.14	41
0.3679	7.68(0.32)	0.58(0.01)	8.26(0.33)	0.16	42
0.3719	7.49(0.29)	0.57(0.01)	8.06(0.30)	0.18	43
0.3725	7.50(0.27)	0.57(0.01)	8.07(0.28)	0.22	44
0.3791	7.56(0.28)	0.56(0.01)	8.12(0.29)	0.20	45
0.3909	7.70(0.30)	0.55(0.01)	8.25(0.31)	0.19	46
0.3969	7.56(0.27)	0.53(0.01)	8.10(0.27)	0.17	47
0.4123	7.55(0.25)	0.51(0.01)	8.06(0.26)	0.18	48
0.4186	7.59(0.26)	0.50(0.01)	8.09(0.26)	0.18	49
0.4192	7.52(0.26)	0.50(0.01)	8.02(0.27)	0.17	50
0.4295	7.52(0.26)	0.49(0.01)	8.01(0.27)	0.18	51
0.4322	7.54(0.27)	0.48(0.01)	8.03(0.28)	0.18	52
0.4368	7.64(0.29)	0.48(0.01)	8.12(0.29)	0.18	53
0.4440	7.25(0.10)	0.47(0.01)	7.71(0.10)	0.16	54
0.4511	7.25(0.10)	0.46(0.01)	7.71(0.10)	0.19	55
0.4539	7.24(0.09)	0.45(0.01)	7.70(0.10)	0.19	56
0.4545	7.25(0.09)	0.45(0.01)	7.70(0.10)	0.19	57
0.4585	7.26(0.10)	0.45(0.01)	7.71(0.11)	0.19	58
0.4655	7.27(0.10)	0.44(0.01)	7.71(0.11)	0.18	59
0.4657	7.28(0.11)	0.44(0.01)	7.73(0.11)	0.17	60
0.4767	7.30(0.11)	0.43(0.01)	7.73(0.11)	0.17	61
0.4835	7.28(0.10)	0.42(0.00)	7.70(0.10)	0.17	62
0.4983	7.28(0.09)	0.41(0.00)	7.69(0.10)	0.16	63
0.4989	7.27(0.09)	0.41(0.00)	7.67(0.09)	0.17	64
0.5052	7.29(0.10)	0.40(0.00)	7.69(0.10)	0.16	65
0.5161	7.29(0.09)	0.39(0.00)	7.68(0.09)	0.16	66
0.5188	7.28(0.09)	0.39(0.00)	7.67(0.09)	0.16	67
0.5234	7.27(0.09)	0.39(0.00)	7.66(0.09)	0.16	68
0.5306	7.29(0.09)	0.38(0.00)	7.67(0.09)	0.16	69

TABLE C.66: Scan of fit windows on G8 for the c contribution using a Polynomial of $O(Q^2)$.

Q_{cut}^2 [GeV ²]	a_μ^{I}	a_μ^{II}	a_μ^{HLO}	$\chi_{\text{corr}}^2/\text{dof}$	N
0.2378	8.31(0.23)	1.06(0.02)	9.37(0.24)	0.42	5
0.2821	8.50(0.23)	0.90(0.01)	9.40(0.24)	0.54	6
0.2971	8.41(0.11)	0.85(0.01)	9.25(0.12)	0.49	7
0.3527	8.46(0.10)	0.70(0.01)	9.16(0.11)	0.49	8
0.3676	8.47(0.10)	0.67(0.01)	9.14(0.11)	0.50	9
0.4267	8.54(0.07)	0.57(0.00)	9.11(0.08)	0.41	10
0.4493	8.63(0.03)	0.54(0.00)	9.17(0.03)	0.37	11
0.4973	8.68(0.03)	0.48(0.00)	9.17(0.03)	0.39	12
0.5199	8.70(0.03)	0.46(0.00)	9.16(0.03)	0.92	13
0.5641	8.76(0.03)	0.42(0.00)	9.18(0.03)	0.43	14
0.5791	8.74(0.02)	0.41(0.00)	9.15(0.03)	0.20	15
0.6335	8.76(0.02)	0.37(0.00)	9.13(0.03)	0.18	16
0.6347	8.74(0.02)	0.37(0.00)	9.11(0.02)	0.22	17
0.6485	8.74(0.02)	0.36(0.00)	9.10(0.02)	0.57	18
0.6497	8.72(0.02)	0.35(0.00)	9.07(0.02)	1.13	19
0.7087	8.74(0.02)	0.32(0.00)	9.06(0.02)	1.13	20
0.7313	8.71(0.02)	0.31(0.00)	9.02(0.02)	0.93	21
0.7793	8.73(0.02)	0.28(0.00)	9.02(0.02)	0.51	22
0.8007	8.72(0.02)	0.27(0.00)	9.00(0.02)	1.47	23
0.8019	8.70(0.02)	0.27(0.00)	8.98(0.02)	1.13	24
0.8462	8.69(0.02)	0.26(0.00)	8.94(0.02)	0.93	25
0.8612	8.68(0.02)	0.25(0.00)	8.93(0.02)	0.77	26
0.8807	8.68(0.02)	0.24(0.00)	8.92(0.02)	0.64	27
0.9156	8.68(0.02)	0.23(0.00)	8.91(0.02)	0.44	28
0.9168	8.65(0.02)	0.23(0.00)	8.88(0.02)	0.44	29
0.9306	8.65(0.02)	0.22(0.00)	8.88(0.02)	0.22	30
0.9513	8.64(0.02)	0.22(0.00)	8.85(0.02)	0.32	31
0.9908	8.63(0.02)	0.21(0.00)	8.84(0.02)	0.21	32
1.0134	8.62(0.02)	0.20(0.00)	8.82(0.02)	0.30	33
1.0602	8.61(0.02)	0.19(0.00)	8.80(0.02)	0.27	34

TABLE C.67: Scan of fit windows on N5 for the c contribution using a Polynomial of $O(Q^2)$.

Q_{cut}^2 [GeV ²]	a_μ^{I}	a_μ^{II}	a_μ^{HLO}	$\chi_{\text{corr}}^2/\text{dof}$	N
0.2378	8.47(0.19)	1.08(0.01)	9.55(0.20)	0.88	5
0.2821	8.65(0.19)	0.91(0.01)	9.56(0.20)	1.01	6
0.2971	8.56(0.09)	0.85(0.01)	9.41(0.09)	0.90	7
0.3527	8.60(0.09)	0.71(0.00)	9.31(0.09)	0.86	8
0.3676	8.61(0.09)	0.68(0.00)	9.29(0.09)	0.87	9
0.4267	8.53(0.06)	0.58(0.00)	9.10(0.06)	0.77	10
0.4493	8.67(0.02)	0.55(0.00)	9.22(0.02)	1.71	11
0.4973	8.72(0.02)	0.49(0.00)	9.21(0.02)	1.77	12
0.5199	8.73(0.02)	0.47(0.00)	9.20(0.02)	3.00	13
0.5641	8.79(0.02)	0.42(0.00)	9.21(0.02)	2.12	14
0.5791	8.78(0.02)	0.41(0.00)	9.19(0.02)	0.75	15
0.6335	8.80(0.02)	0.37(0.00)	9.17(0.02)	0.75	16
0.6347	8.80(0.02)	0.37(0.00)	9.17(0.02)	0.83	17
0.6485	8.80(0.02)	0.36(0.00)	9.16(0.02)	0.66	18
0.6497	8.78(0.02)	0.36(0.00)	9.14(0.02)	0.73	19
0.7087	8.81(0.02)	0.32(0.00)	9.13(0.02)	0.81	20
0.7313	8.78(0.02)	0.31(0.00)	9.09(0.02)	1.08	21
0.7793	8.80(0.02)	0.28(0.00)	9.08(0.02)	0.70	22
0.8007	8.79(0.02)	0.28(0.00)	9.07(0.02)	1.36	23
0.8019	8.77(0.02)	0.28(0.00)	9.05(0.02)	1.22	24
0.8462	8.76(0.02)	0.26(0.00)	9.01(0.02)	1.13	25
0.8612	8.75(0.02)	0.25(0.00)	9.00(0.02)	0.69	26
0.8807	8.75(0.02)	0.24(0.00)	8.99(0.02)	0.62	27
0.9156	8.74(0.02)	0.23(0.00)	8.97(0.02)	0.43	28
0.9168	8.72(0.02)	0.23(0.00)	8.95(0.02)	0.66	29
0.9306	8.72(0.02)	0.23(0.00)	8.95(0.02)	0.73	30
0.9513	8.71(0.02)	0.22(0.00)	8.93(0.02)	1.02	31
0.9908	8.70(0.02)	0.21(0.00)	8.91(0.02)	0.86	32
1.0134	8.69(0.02)	0.20(0.00)	8.89(0.02)	1.38	33
1.0602	8.68(0.02)	0.19(0.00)	8.87(0.02)	1.04	34

TABLE C.68: Scan of fit windows on N6 for the c contribution using a Polynomial of $O(Q^2)$.

Q_{cut}^2 [GeV ²]	a_μ^{I}	a_μ^{II}	a_μ^{HLO}	$\chi_{\text{corr}}^2/\text{dof}$	N
0.1338	7.60(0.58)	1.89(0.11)	9.49(0.65)	0.10	5
0.1588	8.06(0.58)	1.71(0.10)	9.77(0.64)	0.29	6
0.1672	8.02(0.29)	1.61(0.09)	9.63(0.33)	0.68	7
0.1985	8.14(0.29)	1.34(0.07)	9.48(0.31)	0.57	8
0.2069	8.20(0.29)	1.29(0.06)	9.48(0.31)	0.46	9
0.2402	8.25(0.20)	1.10(0.05)	9.35(0.21)	0.40	10
0.2528	8.27(0.06)	1.04(0.04)	9.32(0.07)	0.38	11
0.2799	8.37(0.06)	0.94(0.03)	9.30(0.07)	0.35	12
0.2926	8.40(0.06)	0.90(0.03)	9.30(0.07)	0.33	13
0.3175	8.49(0.06)	0.82(0.03)	9.31(0.07)	0.32	14
0.3260	8.51(0.05)	0.80(0.02)	9.31(0.06)	0.26	15
0.3569	8.57(0.05)	0.73(0.02)	9.30(0.05)	0.24	16
0.3572	8.44(0.15)	0.72(0.02)	9.16(0.15)	0.26	17
0.3653	8.45(0.17)	0.70(0.02)	9.15(0.17)	0.20	18
0.3657	8.47(0.23)	0.70(0.02)	9.17(0.24)	0.20	19
0.3990	8.48(0.17)	0.64(0.02)	9.12(0.18)	0.19	20
0.4116	8.54(0.15)	0.62(0.02)	9.15(0.15)	0.18	21
0.4387	8.66(0.08)	0.58(0.01)	9.24(0.09)	0.16	22
0.4509	8.68(0.09)	0.56(0.01)	9.24(0.09)	0.16	23
0.4513	8.67(0.09)	0.56(0.01)	9.23(0.09)	0.20	24
0.4763	8.69(0.08)	0.53(0.01)	9.22(0.09)	0.21	25
0.4847	8.67(0.03)	0.52(0.01)	9.19(0.04)	0.19	26
0.4964	8.68(0.03)	0.50(0.01)	9.19(0.04)	0.19	27
0.5156	8.69(0.03)	0.48(0.01)	9.17(0.04)	0.19	28
0.5160	8.68(0.03)	0.48(0.01)	9.16(0.04)	0.21	29
0.5241	8.68(0.03)	0.47(0.01)	9.16(0.04)	0.22	30
0.5361	8.68(0.03)	0.46(0.01)	9.14(0.03)	0.22	31
0.5578	8.69(0.03)	0.44(0.01)	9.13(0.03)	0.20	32
0.5704	8.69(0.03)	0.43(0.01)	9.12(0.03)	0.23	33
0.5971	8.70(0.03)	0.41(0.01)	9.11(0.03)	0.21	34
0.5975	8.69(0.03)	0.40(0.01)	9.09(0.03)	0.21	35
0.6097	8.70(0.03)	0.39(0.01)	9.09(0.03)	0.19	36
0.6335	8.70(0.03)	0.38(0.01)	9.08(0.03)	0.18	37
0.6351	8.71(0.03)	0.38(0.01)	9.08(0.03)	0.20	38
0.6420	8.71(0.03)	0.37(0.01)	9.08(0.03)	0.20	39
0.6551	8.72(0.03)	0.36(0.01)	9.08(0.03)	0.19	40
0.6732	8.72(0.03)	0.35(0.01)	9.07(0.03)	0.18	41
0.6744	8.71(0.03)	0.35(0.01)	9.06(0.03)	0.19	42
0.6817	8.70(0.03)	0.34(0.01)	9.05(0.03)	0.18	43
0.6828	8.69(0.03)	0.34(0.01)	9.04(0.03)	0.16	44

TABLE C.69: Scan of fit windows on O7 for the c contribution using a Polynomial of $O(Q^2)$.

C.2 Results for the time moments

C.2.1 The light-quark contribution

The figures C.1, and C.2 contain tests for the convergence of the sums for the time moments (see equations (4.31, 4.32)) on G8 for Π_3 , and Π_4 , respectively.

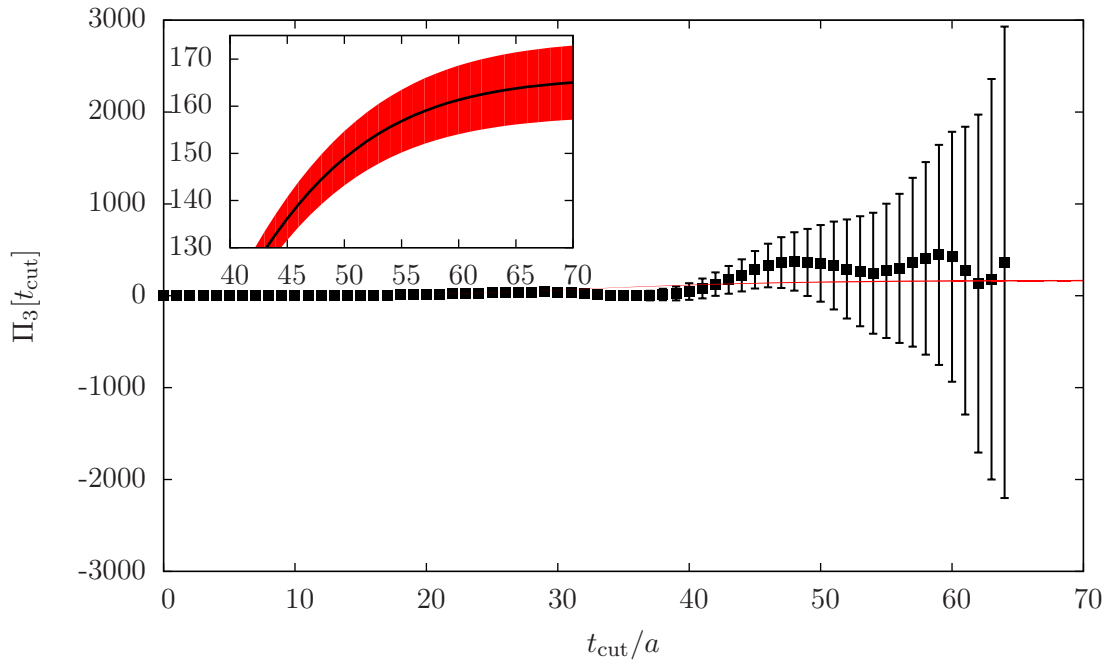


FIGURE C.1: Test of the convergence of the sums in equations (4.31, 4.32) on G8 for the light-quark contribution for Π_3 .

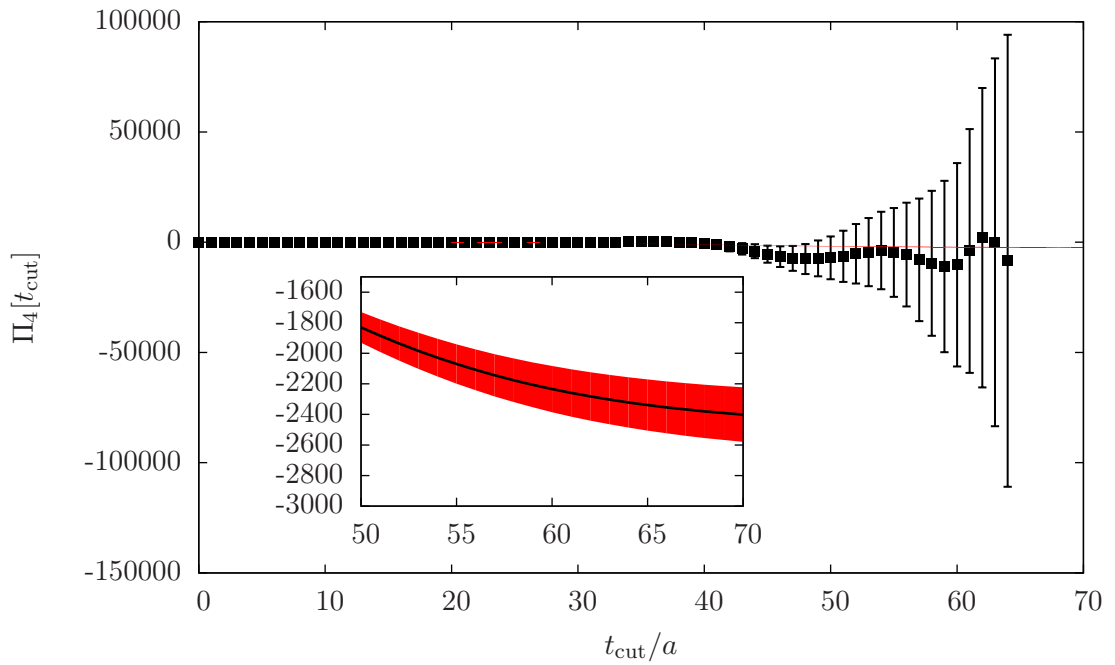


FIGURE C.2: Test of the convergence of the sums in equations (4.31, 4.32) on G8 for the light-quark contribution for Π_4 .

C.2.2 The strange-quark contribution

In the table C.70 we list the results for the time moments for the strange-quark contribution in lattice units. The figures C.3, C.4, C.5, C.6, and C.7 contain tests for the convergence of the sums for the time moments (see equations (4.31, 4.32)) on G8 for Π_0 , Π_1 , Π_2 , Π_3 , and Π_4 , respectively.

Ens.	t/a	Π_0	Π_1	Π_2	Π_3	Π_4
A3	$t_{\text{trunc}} - 1$	-0.016957(70)	0.05337(35)	-0.2518(29)	1.268(26)	-6.46(20)
	$t_{\text{trunc}} + 1$	-0.016911(72)	0.05297(38)	-0.2515(29)	1.275(25)	-6.50(20)
	$t_{\text{trunc}} \pm 0$	-0.016930(71)	0.05315(36)	-0.2516(29)	1.271(26)	-6.48(20)
A4	$t_{\text{trunc}} - 1$	-0.017074(57)	0.05568(29)	-0.2752(25)	1.456(23)	-7.81(18)
	$t_{\text{trunc}} + 1$	-0.017027(59)	0.05529(32)	-0.2752(24)	1.465(22)	-7.85(18)
	$t_{\text{trunc}} \pm 0$	-0.017047(58)	0.05547(30)	-0.2752(25)	1.461(22)	-7.82(18)
A5	$t_{\text{trunc}} - 1$	-0.017038(77)	0.05575(39)	-0.2769(38)	1.479(36)	-8.04(30)
	$t_{\text{trunc}} + 1$	-0.016991(79)	0.05536(43)	-0.2768(37)	1.488(36)	-8.08(30)
	$t_{\text{trunc}} \pm 0$	-0.017011(78)	0.05555(41)	-0.2769(38)	1.484(36)	-8.06(30)
B6	$t_{\text{trunc}} - 1$	-0.017232(65)	0.05807(30)	-0.3016(27)	1.701(30)	-9.81(27)
	$t_{\text{trunc}} + 1$	-0.017186(67)	0.05770(35)	-0.3018(29)	1.711(30)	-9.85(27)
	$t_{\text{trunc}} \pm 0$	-0.017207(66)	0.05789(32)	-0.3019(28)	1.707(30)	-9.83(28)
E5	$t_{\text{trunc}} - 1$	-0.018108(37)	0.07287(29)	-0.4798(35)	3.429(45)	-24.68(50)
	$t_{\text{trunc}} + 1$	-0.018094(37)	0.07258(30)	-0.4782(33)	3.434(43)	-24.78(49)
	$t_{\text{trunc}} \pm 0$	-0.018100(37)	0.07271(30)	-0.4790(34)	3.432(44)	-24.73(50)
F6	$t_{\text{trunc}} - 1$	-0.018321(65)	0.07675(47)	-0.5290(52)	3.951(69)	-29.73(80)
	$t_{\text{trunc}} + 1$	-0.018306(65)	0.07645(50)	-0.5274(52)	3.958(67)	-29.84(79)
	$t_{\text{trunc}} \pm 0$	-0.018313(65)	0.07659(48)	-0.5282(52)	3.955(68)	-29.78(80)
F7	$t_{\text{trunc}} - 1$	-0.018359(77)	0.07844(55)	-0.5595(61)	4.355(82)	-34.23(99)
	$t_{\text{trunc}} + 1$	-0.018344(78)	0.07814(57)	-0.5582(60)	4.366(80)	-34.37(98)
	$t_{\text{trunc}} \pm 0$	-0.018351(78)	0.07827(56)	-0.5588(60)	4.360(81)	-34.30(99)
G8	$t_{\text{trunc}} - 1$	-0.018451(87)	0.08028(61)	-0.5859(76)	4.657(105)	-37.47(1.28)
	$t_{\text{trunc}} + 1$	-0.018431(88)	0.07993(65)	-0.5848(74)	4.670(102)	-37.61(1.27)
	$t_{\text{trunc}} \pm 0$	-0.018440(87)	0.08010(63)	-0.5855(75)	4.665(104)	-37.54(1.27)
N5	$t_{\text{trunc}} - 1$	-0.020219(64)	0.13051(77)	-1.5483(180)	20.216(422)	-268.62(8.48)
	$t_{\text{trunc}} + 1$	-0.020205(65)	0.13016(81)	-1.5475(177)	20.261(417)	-269.21(8.43)
	$t_{\text{trunc}} \pm 0$	-0.020211(65)	0.13033(79)	-1.5480(179)	20.240(420)	-268.91(8.45)
N6	$t_{\text{trunc}} - 1$	-0.020562(52)	0.13752(64)	-1.6797(142)	22.361(333)	-301.48(6.61)
	$t_{\text{trunc}} + 1$	-0.020546(53)	0.13716(66)	-1.6793(138)	22.414(327)	-302.15(6.57)
	$t_{\text{trunc}} \pm 0$	-0.020553(52)	0.13733(65)	-1.6795(141)	22.387(330)	-301.80(6.59)
O7	$t_{\text{trunc}} - 1$	-0.020603(92)	0.14135(110)	-1.7741(257)	24.338(629)	-339.18(13.14)
	$t_{\text{trunc}} + 1$	-0.020587(93)	0.14097(115)	-1.7736(254)	24.394(621)	-339.87(13.10)
	$t_{\text{trunc}} \pm 0$	-0.020594(93)	0.14115(112)	-1.7739(255)	24.366(626)	-339.51(13.13)

TABLE C.70: Results for the time moments of equations (4.32, 4.33) for the strange-quark contribution in lattice units. The precision for each time moment is shown as percentage. t_{trunc} refers to the values listed in table 4.6.

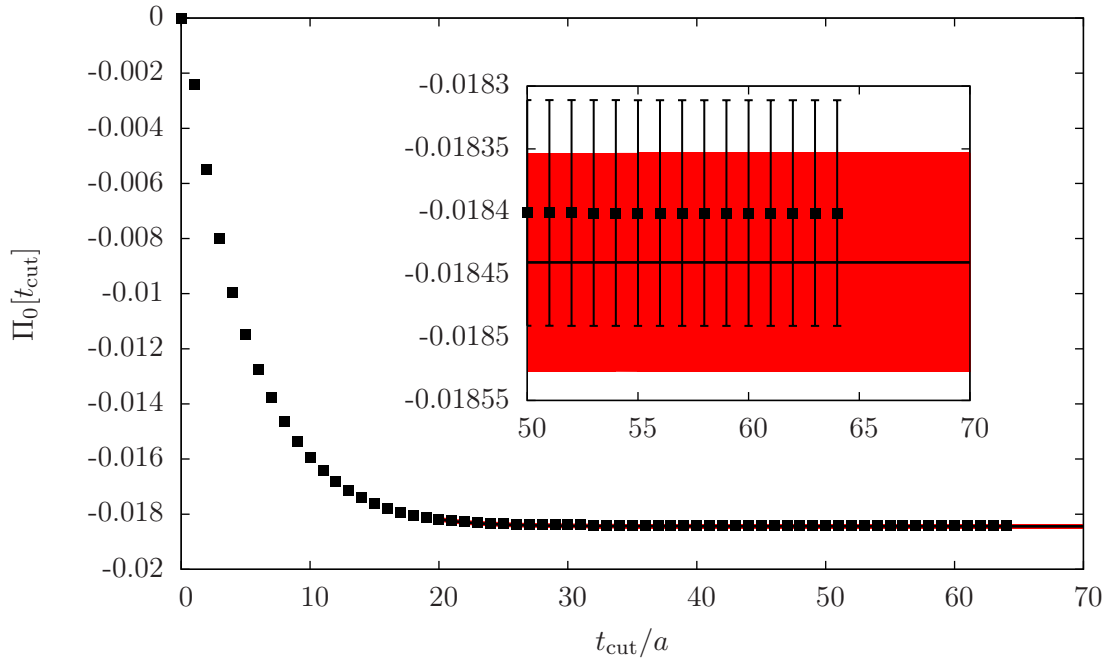


FIGURE C.3: Test of the convergence of the sums in equations (4.31, 4.32) on G8 for the strange-quark contribution for Π_0 .

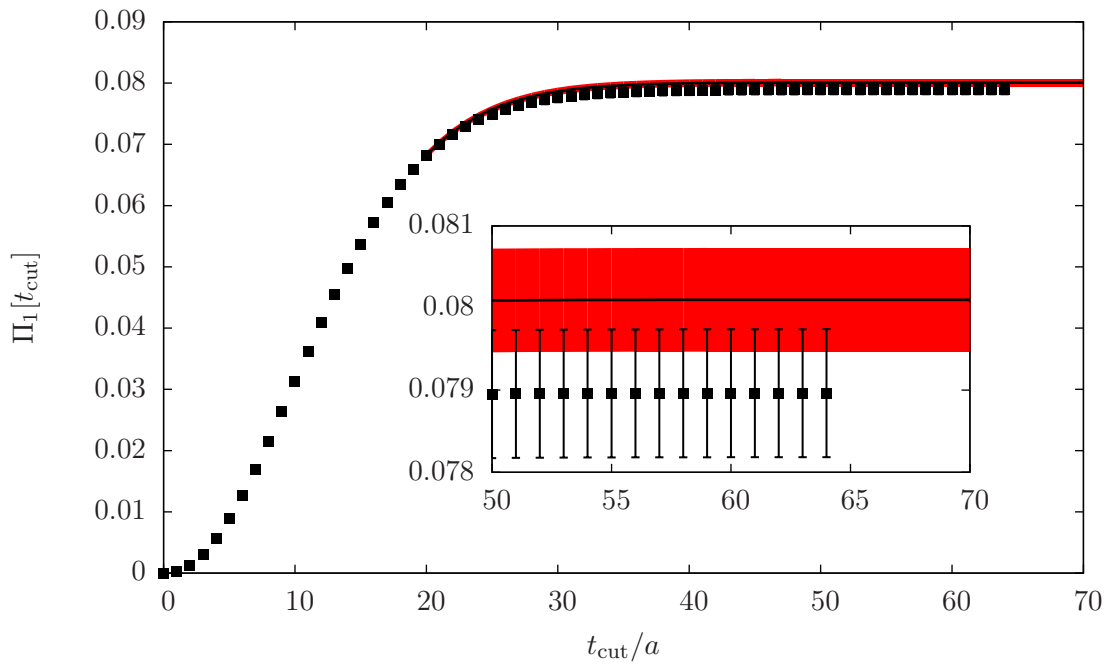


FIGURE C.4: Test of the convergence of the sums in equations (4.31, 4.32) on G8 for the strange-quark contribution for Π_1 .

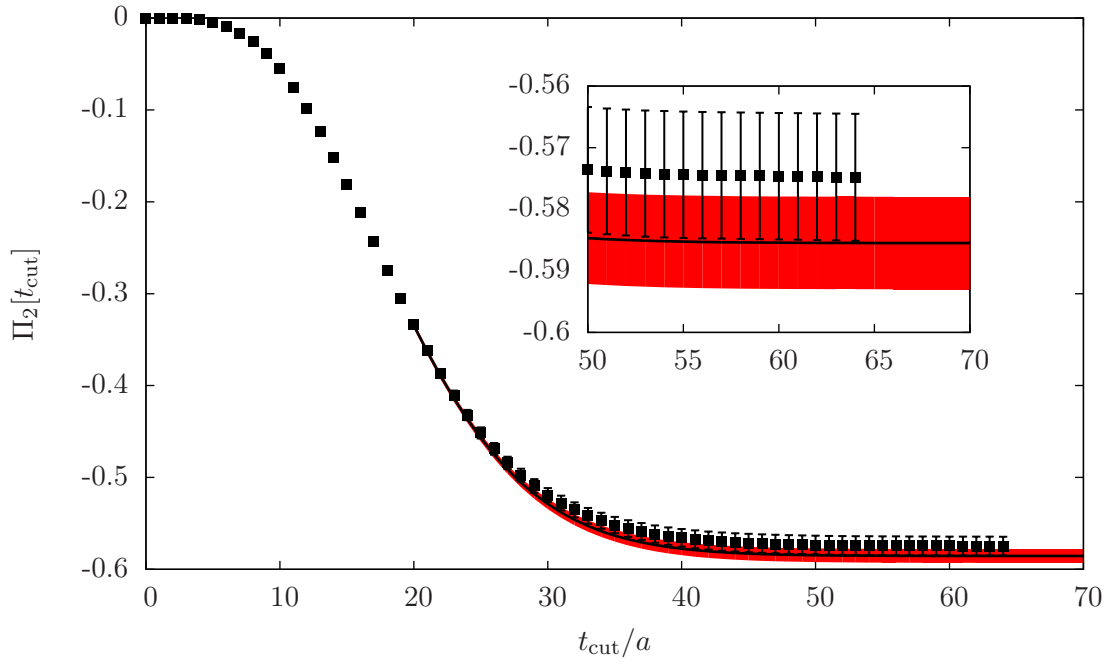


FIGURE C.5: Test of the convergence of the sums in equations (4.31, 4.32) on G8 for the strange-quark contribution for Π_2 .

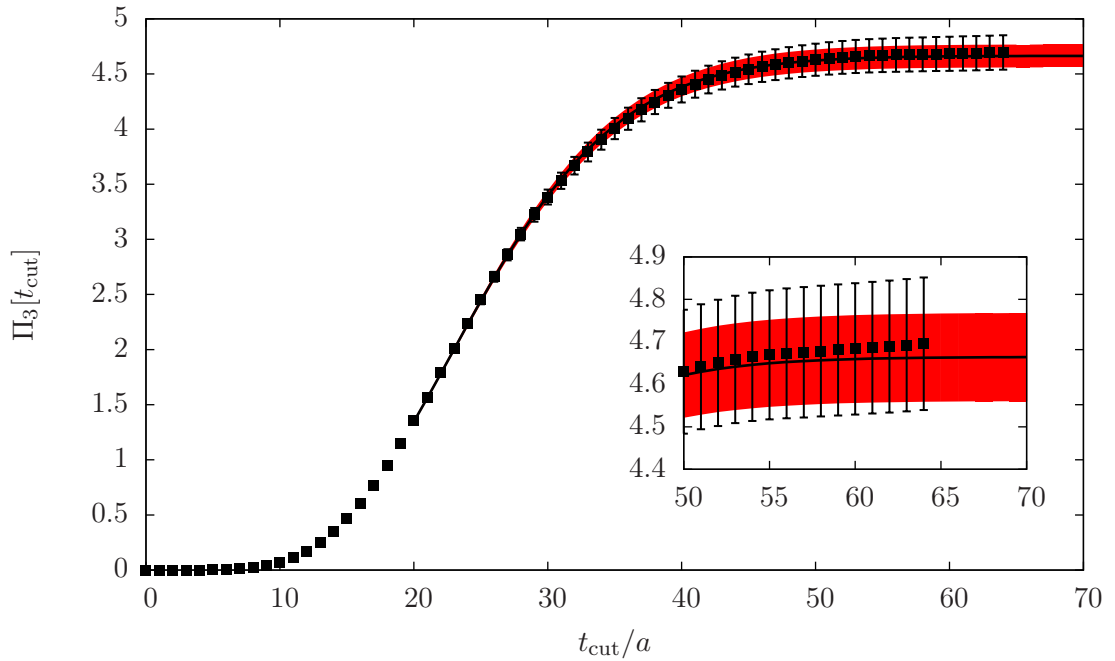


FIGURE C.6: Test of the convergence of the sums in equations (4.31, 4.32) on G8 for the strange-quark contribution for Π_3 .

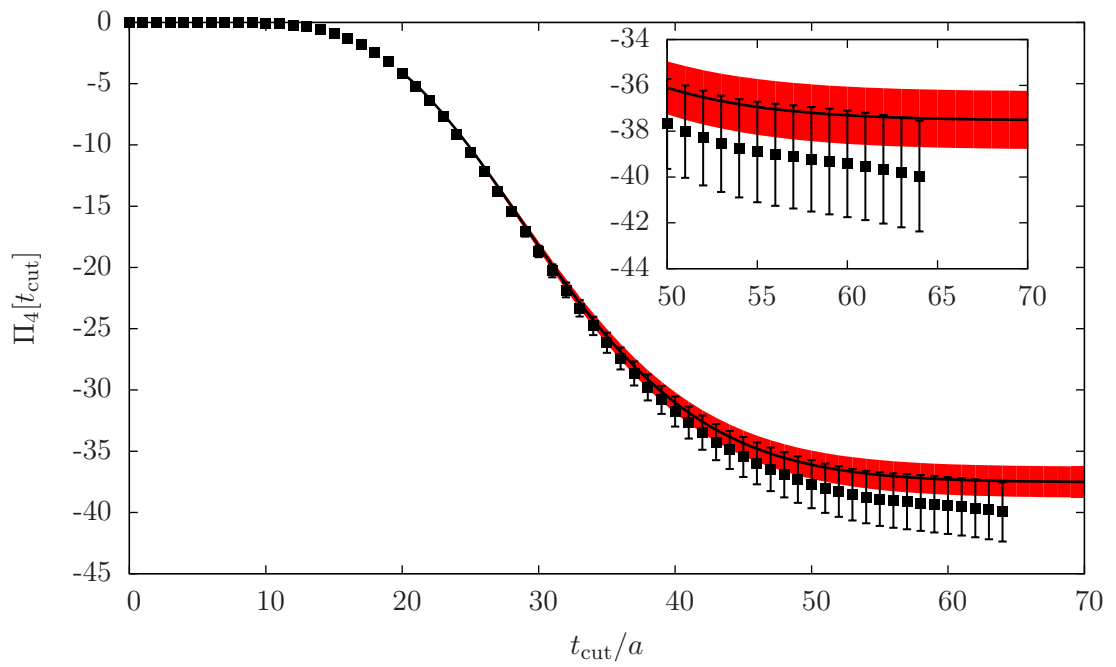


FIGURE C.7: Test of the convergence of the sums in equations (4.31, 4.32) on G8 for the strange-quark contribution for Π_4 .

C.2.3 The charm-quark contribution

In the table C.71 we list the results for the time moments for the charm-quark contribution in lattice units. The figures C.8, C.9, C.10, C.11, and C.12 contain tests for the convergence of the sums for the time moments (see equations (4.31, 4.32)) on G8 for $\Pi_0, \Pi_1, \Pi_2, \Pi_3,$ and $\Pi_4,$ respectively.

Ens.	t/a	Π_0	Π_1	Π_2	Π_3	Π_4
A3	$t_{\text{trunc}} - 1$	-0.013013(42)	0.007091(27)	-0.004211(19)	0.002748(14)	-0.001911(10)
	$t_{\text{trunc}} + 1$	-0.013013(42)	0.007090(27)	-0.004205(19)	0.002732(14)	-0.001885(10)
	$t_{\text{trunc}} \pm 0$	-0.013013(42)	0.007090(27)	-0.004207(19)	0.002738(14)	-0.001895(10)
A4	$t_{\text{trunc}} - 1$	-0.012589(36)	0.006779(22)	-0.003952(15)	0.002526(11)	-0.001721(08)
	$t_{\text{trunc}} + 1$	-0.012589(36)	0.006778(22)	-0.003947(15)	0.002512(11)	-0.001698(08)
	$t_{\text{trunc}} \pm 0$	-0.012589(36)	0.006778(22)	-0.003948(15)	0.002517(11)	-0.001707(08)
A5	$t_{\text{trunc}} - 1$	-0.012429(48)	0.006633(29)	-0.003837(20)	0.002435(14)	-0.001648(10)
	$t_{\text{trunc}} + 1$	-0.012429(48)	0.006632(29)	-0.003832(20)	0.002422(14)	-0.001626(10)
	$t_{\text{trunc}} \pm 0$	-0.012429(48)	0.006632(29)	-0.003834(20)	0.002427(14)	-0.001635(10)
B6	$t_{\text{trunc}} - 1$	-0.012306(57)	0.006526(33)	-0.003749(21)	0.002362(15)	-0.001587(10)
	$t_{\text{trunc}} + 1$	-0.012306(57)	0.006525(33)	-0.003745(21)	0.002350(15)	-0.001566(11)
	$t_{\text{trunc}} \pm 0$	-0.012306(57)	0.006525(33)	-0.003746(21)	0.002355(15)	-0.001575(11)
E5	$t_{\text{trunc}} - 1$	-0.015959(26)	0.010194(20)	-0.007501(17)	0.006199(16)	-0.005479(16)
	$t_{\text{trunc}} + 1$	-0.015959(26)	0.010194(20)	-0.007500(17)	0.006195(16)	-0.005467(16)
	$t_{\text{trunc}} \pm 0$	-0.015959(26)	0.010194(20)	-0.007501(17)	0.006196(16)	-0.005472(16)
F6	$t_{\text{trunc}} - 1$	-0.015810(46)	0.010022(33)	-0.007307(29)	0.005982(27)	-0.005240(26)
	$t_{\text{trunc}} + 1$	-0.015810(46)	0.010021(33)	-0.007307(29)	0.005979(27)	-0.005229(27)
	$t_{\text{trunc}} \pm 0$	-0.015810(46)	0.010021(33)	-0.007307(29)	0.005980(27)	-0.005234(26)
F7	$t_{\text{trunc}} - 1$	-0.015784(51)	0.010046(39)	-0.007342(34)	0.006027(31)	-0.005297(30)
	$t_{\text{trunc}} + 1$	-0.015784(51)	0.010046(39)	-0.007342(34)	0.006024(32)	-0.005286(31)
	$t_{\text{trunc}} \pm 0$	-0.015784(51)	0.010046(39)	-0.007342(34)	0.006025(32)	-0.005290(30)
G8	$t_{\text{trunc}} - 1$	-0.015854(56)	0.010048(43)	-0.007334(37)	0.006016(35)	-0.005288(33)
	$t_{\text{trunc}} + 1$	-0.015854(56)	0.010048(43)	-0.007333(37)	0.006011(35)	-0.005271(34)
	$t_{\text{trunc}} \pm 0$	-0.015854(56)	0.010048(43)	-0.007334(37)	0.006013(35)	-0.005278(34)
N5	$t_{\text{trunc}} - 1$	-0.024221(54)	0.022855(63)	-0.028668(93)	0.042427(157)	-0.068055(267)
	$t_{\text{trunc}} + 1$	-0.024221(54)	0.022854(63)	-0.028660(94)	0.042368(157)	-0.067778(275)
	$t_{\text{trunc}} \pm 0$	-0.024221(54)	0.022855(63)	-0.028663(94)	0.042392(157)	-0.067897(271)
N6	$t_{\text{trunc}} - 1$	-0.024316(44)	0.023020(51)	-0.029006(78)	0.043171(132)	-0.069713(226)
	$t_{\text{trunc}} + 1$	-0.024316(44)	0.023020(51)	-0.028998(79)	0.043108(133)	-0.069421(234)
	$t_{\text{trunc}} \pm 0$	-0.024316(44)	0.023020(51)	-0.029001(79)	0.043133(133)	-0.069546(231)
O7	$t_{\text{trunc}} - 1$	-0.024134(80)	0.022733(99)	-0.028478(149)	0.042160(245)	-0.067741(411)
	$t_{\text{trunc}} + 1$	-0.024134(80)	0.022732(99)	-0.028470(149)	0.042100(247)	-0.067464(423)
	$t_{\text{trunc}} \pm 0$	-0.024134(80)	0.022732(99)	-0.028473(149)	0.042124(246)	-0.067584(418)

TABLE C.71: Results for the time moments of equations (4.32, 4.33) for the charm-quark contribution in lattice units. The precision for each time moment is shown as percentage. t_{trunc} refers to the values listed in table 4.6.

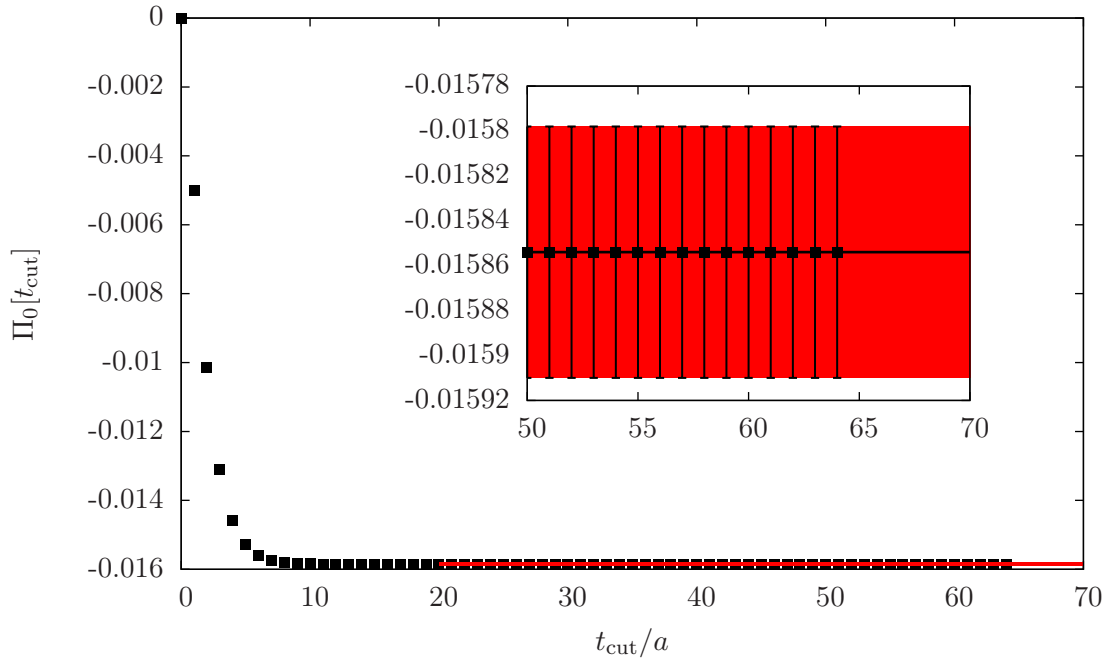


FIGURE C.8: Test of the convergence of the sums in equations (4.31, 4.32) on G8 for the charm-quark contribution for Π_0 .

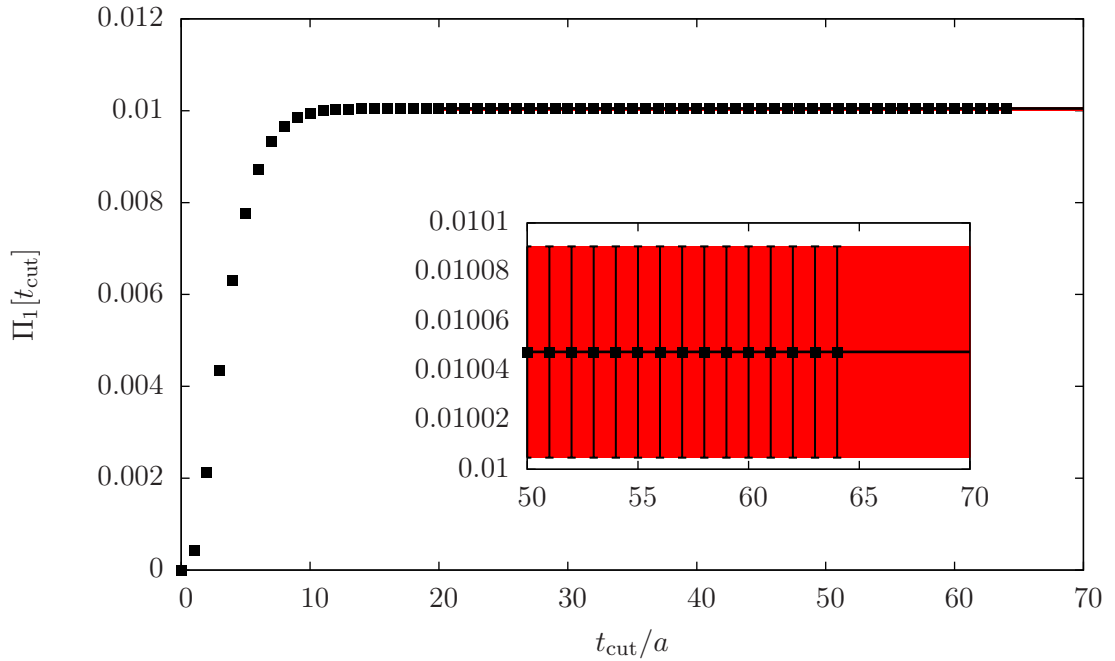


FIGURE C.9: Test of the convergence of the sums in equations (4.31, 4.32) on G8 for the charm-quark contribution for Π_1 .

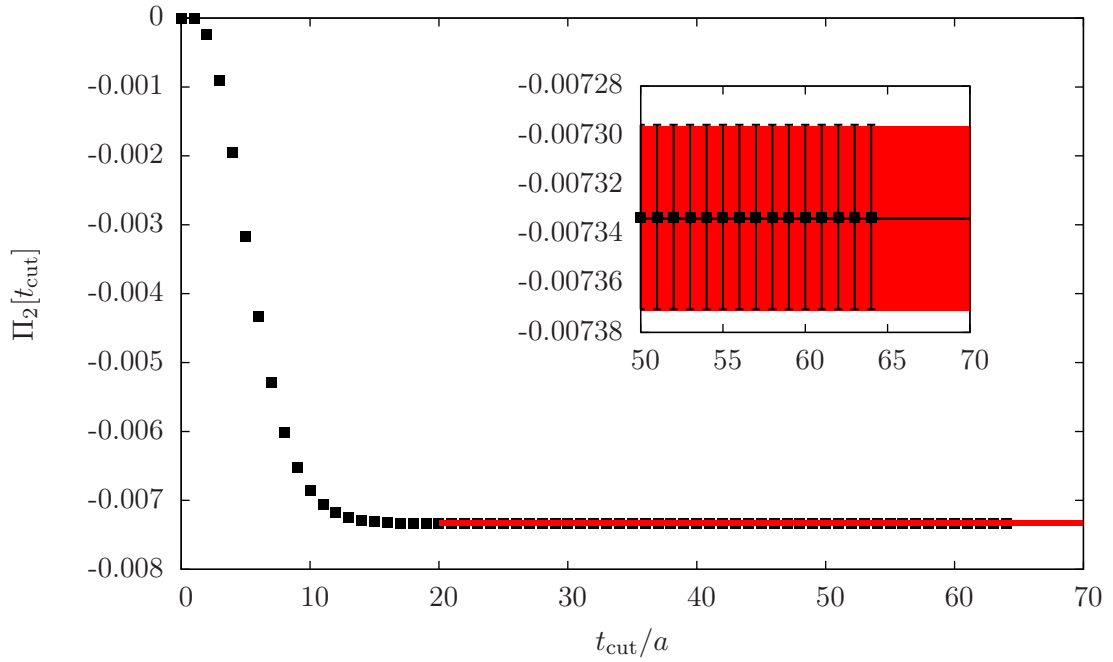


FIGURE C.10: Test of the convergence of the sums in equations (4.31, 4.32) on G8 for the charm-quark contribution for Π_2 .

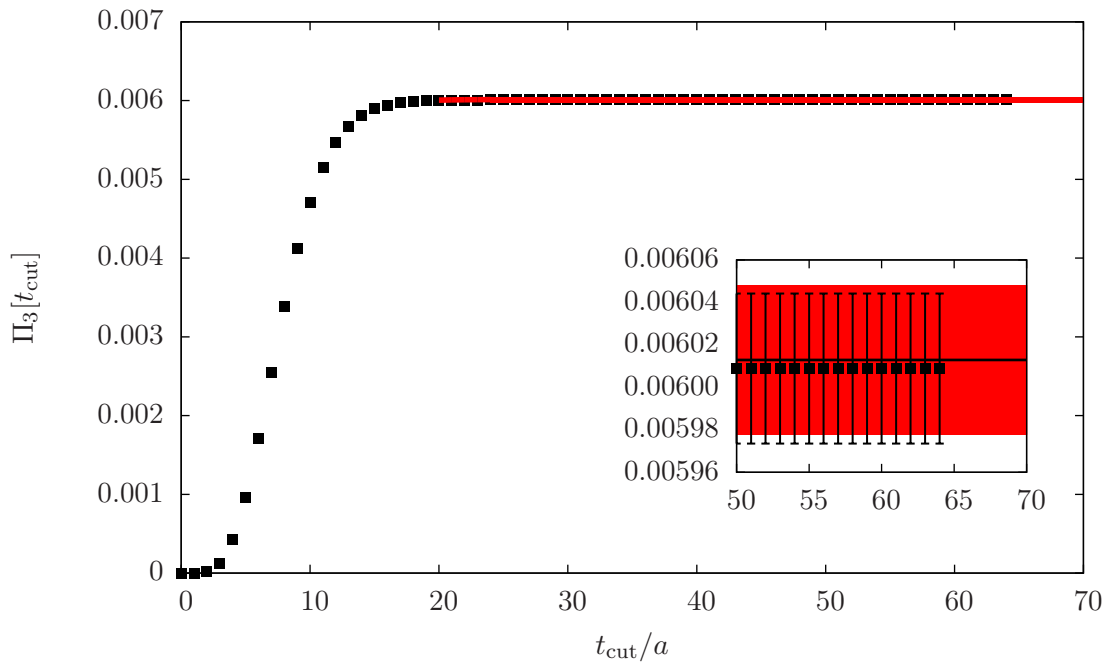


FIGURE C.11: Test of the convergence of the sums in equations (4.31, 4.32) on G8 for the charm-quark contribution for Π_3 .

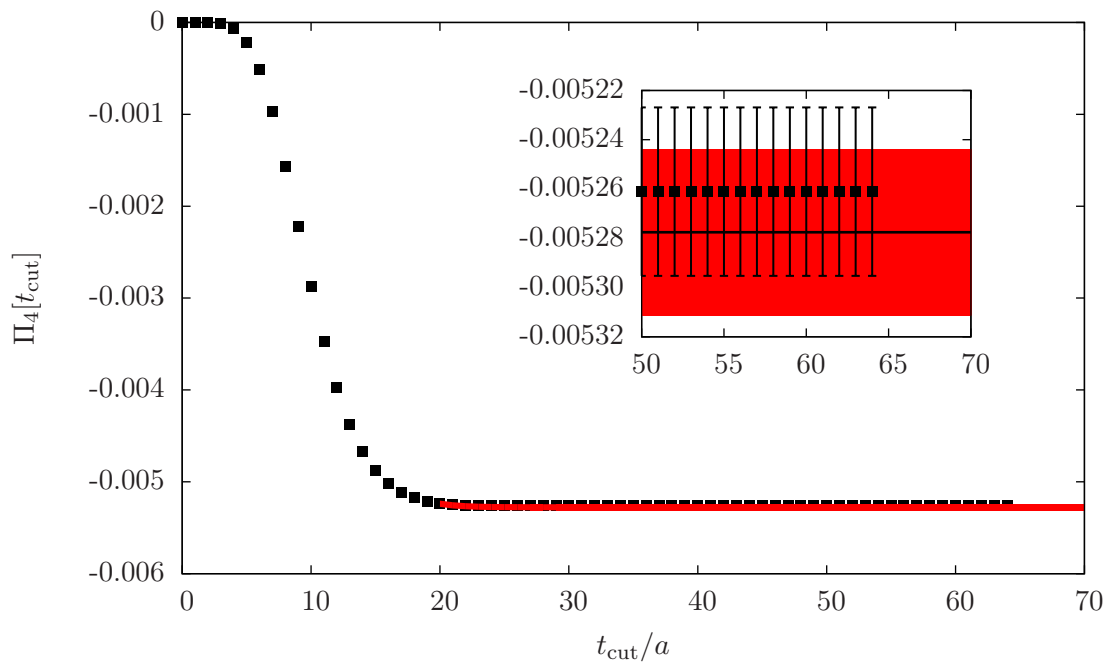


FIGURE C.12: Test of the convergence of the sums in equations (4.31, 4.32) on G8 for the charm-quark contribution for Π_4 .

C.3 The extrapolation to the physical point

We collect the individual results for the different fit ansätze for the extrapolations to the physical point and cuts on the data that enter the fit in the following tables.

C.3.1 Results for the hybrid method

C.3.1.1 The light-quark contribution

a_μ^{HLO}	%	p-val.	$\chi_{\text{uncorr}}^2/\text{dof}$	cuts	fit ansatz
$Q_{\text{cut}}^2 \approx 0.5 \text{ GeV}^2$					
601.26(35.90)	6.0	0.12	1.50	-	$a_\mu^{\text{E},O(a)}(m_\pi^2, a)$
579.54(33.71)	5.8	0.06	1.71	-	$a_\mu^{\text{F},O(a)}(m_\pi^2, a)$
682.19(47.23)	6.9	0.29	1.21	$m_\pi < 400 \text{ MeV}$	$a_\mu^{\text{E},O(a)}(m_\pi^2, a)$
643.84(42.67)	6.6	0.21	1.35	$m_\pi < 400 \text{ MeV}$	$a_\mu^{\text{F},O(a)}(m_\pi^2, a)$
532.22(17.74)	3.3	0.68	0.67	$a < 0.070 \text{ fm}$	$a_\mu^{\text{E}}(m_\pi^2)$
528.28(15.64)	3.0	0.83	0.47	$a < 0.070 \text{ fm}$	$a_\mu^{\text{F}}(m_\pi^2)$
522.07(17.29)	3.3	0.60	0.69	$m_\pi < 400 \text{ MeV}, a < 0.070 \text{ fm}$	$a_\mu^{\text{E}}(m_\pi^2)$
524.27(19.93)	3.8	0.61	0.68	$m_\pi < 400 \text{ MeV}, a < 0.070 \text{ fm}$	$a_\mu^{\text{F}}(m_\pi^2)$
$Q_{\text{cut}}^2 < 0.5 \text{ GeV}^2$					
581.37(44.13)	7.6	0.29	1.18	-	$a_\mu^{\text{E},O(a)}(m_\pi^2, a)$
559.85(41.74)	7.5	0.20	1.33	-	$a_\mu^{\text{F},O(a)}(m_\pi^2, a)$
664.88(66.47)	10.0	0.36	1.10	$m_\pi < 400 \text{ MeV}$	$a_\mu^{\text{E},O(a)}(m_\pi^2, a)$
624.98(59.81)	9.6	0.28	1.23	$m_\pi < 400 \text{ MeV}$	$a_\mu^{\text{F},O(a)}(m_\pi^2, a)$
542.35(22.95)	4.2	0.70	0.64	$a < 0.070 \text{ fm}$	$a_\mu^{\text{E}}(m_\pi^2)$
537.98(21.12)	3.9	0.75	0.58	$a < 0.070 \text{ fm}$	$a_\mu^{\text{F}}(m_\pi^2)$
539.16(28.03)	5.2	0.44	0.94	$m_\pi < 400 \text{ MeV}, a < 0.070 \text{ fm}$	$a_\mu^{\text{E}}(m_\pi^2)$
544.62(28.67)	5.3	0.57	0.74	$m_\pi < 400 \text{ MeV}, a < 0.070 \text{ fm}$	$a_\mu^{\text{F}}(m_\pi^2)$

TABLE C.72: Results for the extrapolation to the physical point for a_μ^{HLO} for the light-quark contribution in units of 10^{10} using a simultaneous fit to data with and without m_V -rescaling.

C.3.2 Results for a_μ^{HLO} via time moments

C.3.2.1 The light-quark contribution

Time moments: ud					
a_μ^{HLO}	%	p-val.	$\chi_{\text{uncorr}}^2/\text{dof}$	cuts	fit ansatz
$t_{\text{trunc}} - 1$					
564.29(14.32)	2.5	1.74e-08	7.08	-	$a_\mu^{\text{A},O(a)}(m_\pi^2, a)$
550.15(13.67)	2.5	8.32e-10	8.04	-	$a_\mu^{\text{B},O(a)}(m_\pi^2, a)$
555.88(16.87)	3.0	6.66e-09	10.98	$m_\pi < 400\text{MeV}$	$a_\mu^{\text{A},O(a)}(m_\pi^2, a)$
555.68(16.99)	3.1	3.22e-08	10.16	$m_\pi < 400\text{MeV}$	$a_\mu^{\text{B},O(a)}(m_\pi^2, a)$
556.07(8.47)	1.5	8.70e-07	8.42	$a < 0.070\text{fm}$	$a_\mu^{\text{A}}(m_\pi^2)$
548.43(7.68)	1.4	6.13e-06	7.38	$a < 0.070\text{fm}$	$a_\mu^{\text{B}}(m_\pi^2)$
538.29(6.95)	1.3	1.64e-05	11.02	$m_\pi < 400\text{MeV} a < 0.070\text{fm}$	$a_\mu^{\text{A}}(m_\pi^2)$
527.98(9.79)	1.9	3.14e-05	10.37	$m_\pi < 400\text{MeV} a < 0.070\text{fm}$	$a_\mu^{\text{B}}(m_\pi^2)$
$t_{\text{trunc}} \pm 0$					
561.39(15.18)	2.7	1.48e-06	5.66	-	$a_\mu^{\text{A},O(a)}(m_\pi^2, a)$
545.47(14.29)	2.6	1.14e-07	6.49	-	$a_\mu^{\text{B},O(a)}(m_\pi^2, a)$
557.26(19.45)	3.5	6.77e-07	8.55	$m_\pi < 400\text{MeV}$	$a_\mu^{\text{A},O(a)}(m_\pi^2, a)$
556.68(19.20)	3.4	2.31e-06	7.90	$m_\pi < 400\text{MeV}$	$a_\mu^{\text{B},O(a)}(m_\pi^2, a)$
555.41(10.37)	1.9	2.37e-05	6.66	$a < 0.070\text{fm}$	$a_\mu^{\text{A}}(m_\pi^2)$
547.37(9.35)	1.7	1.02e-04	5.87	$a < 0.070\text{fm}$	$a_\mu^{\text{B}}(m_\pi^2)$
536.20(8.49)	1.6	1.39e-04	8.88	$m_\pi < 400\text{MeV} a < 0.070\text{fm}$	$a_\mu^{\text{A}}(m_\pi^2)$
528.23(11.87)	2.2	1.84e-04	8.60	$m_\pi < 400\text{MeV} a < 0.070\text{fm}$	$a_\mu^{\text{B}}(m_\pi^2)$
$t_{\text{trunc}} - 0$					
558.09(15.51)	2.8	5.81e-05	4.45	-	$a_\mu^{\text{A},O(a)}(m_\pi^2, a)$
542.34(14.52)	2.7	6.42e-06	5.18	-	$a_\mu^{\text{B},O(a)}(m_\pi^2, a)$
555.58(19.94)	3.6	3.00e-05	6.53	$m_\pi < 400\text{MeV}$	$a_\mu^{\text{A},O(a)}(m_\pi^2, a)$
554.43(19.50)	3.5	7.18e-05	6.06	$m_\pi < 400\text{MeV}$	$a_\mu^{\text{B},O(a)}(m_\pi^2, a)$
552.80(11.22)	2.0	2.95e-04	5.29	$a < 0.070\text{fm}$	$a_\mu^{\text{A}}(m_\pi^2)$
544.62(10.09)	1.9	8.82e-04	4.69	$a < 0.070\text{fm}$	$a_\mu^{\text{B}}(m_\pi^2)$
533.33(9.57)	1.8	8.67e-04	7.05	$m_\pi < 400\text{MeV} a < 0.070\text{fm}$	$a_\mu^{\text{A}}(m_\pi^2)$
527.83(12.82)	2.4	9.72e-04	6.94	$m_\pi < 400\text{MeV} a < 0.070\text{fm}$	$a_\mu^{\text{B}}(m_\pi^2)$

TABLE C.73: Results for the determination of a_μ^{HLO} at the physical point in units of 10^{10} for the light-quark contribution using time moments.

Time moments: ud					
a_μ^{HLO}	%	p-val.	$\chi_{\text{uncorr}}^2/\text{dof}$	cuts	fit ansatz
$t_{\text{trunc}} - 1$					
503.78(16.66)	3.3	1.79e-02	2.31	-	$a_\mu^{\text{C},O(a)}(m_\pi^2, a)$
526.38(19.75)	3.8	7.99e-02	1.97	$m_\pi < 400\text{MeV}$	$a_\mu^{\text{C},O(a)}(m_\pi^2, a)$
535.12(15.67)	2.9	7.58e-02	2.00	$a < 0.070\text{fm}$	$a_\mu^{\text{C}}(m_\pi^2)$
519.03(16.91)	3.3	5.39e-02	2.55	$m_\pi < 400\text{MeV} a < 0.070\text{fm}$	$a_\mu^{\text{C}}(m_\pi^2)$
$t_{\text{trunc}} \pm 0$					
505.13(18.07)	3.6	1.92e-02	2.29	-	$a_\mu^{\text{C},O(a)}(m_\pi^2, a)$
528.50(21.03)	4.0	8.38e-02	1.94	$m_\pi < 400\text{MeV}$	$a_\mu^{\text{C},O(a)}(m_\pi^2, a)$
533.95(15.62)	2.9	7.19e-02	2.02	$a < 0.070\text{fm}$	$a_\mu^{\text{C}}(m_\pi^2)$
517.59(17.01)	3.3	5.17e-02	2.58	$m_\pi < 400\text{MeV} a < 0.070\text{fm}$	$a_\mu^{\text{C}}(m_\pi^2)$
$t_{\text{trunc}} + 1$					
505.35(18.78)	3.7	2.39e-02	2.21	-	$a_\mu^{\text{C},O(a)}(m_\pi^2, a)$
529.34(21.98)	4.2	1.04e-01	1.83	$m_\pi < 400\text{MeV}$	$a_\mu^{\text{C},O(a)}(m_\pi^2, a)$
532.75(15.58)	2.9	7.86e-02	1.98	$a < 0.070\text{fm}$	$a_\mu^{\text{C}}(m_\pi^2)$
515.75(16.96)	3.3	5.96e-02	2.47	$m_\pi < 400\text{MeV} a < 0.070\text{fm}$	$a_\mu^{\text{C}}(m_\pi^2)$

TABLE C.74: Results for the determination of a_μ^{HLO} at the physical point in units of 10^{10} for the light-quark contribution with m_V -rescaling using time moments.

Time moments: ud					
a_μ^{HLO}	%	p-val.	$\chi_{\text{uncorr}}^2/\text{dof}$	cuts	fit ansatz
$t_{\text{trunc}} - 1$					
554.97(9.74)	1.8	5.00e-12	5.52	-	$a_\mu^{\text{E},O(a)}(m_\pi^2, a)$
538.09(9.32)	1.7	4.09e-13	5.89	-	$a_\mu^{\text{F},O(a)}(m_\pi^2, a)$
551.57(12.95)	2.3	3.27e-10	6.55	$m_\pi < 400\text{MeV}$	$a_\mu^{\text{E},O(a)}(m_\pi^2, a)$
547.18(12.29)	2.2	3.75e-09	5.99	$m_\pi < 400\text{MeV}$	$a_\mu^{\text{F},O(a)}(m_\pi^2, a)$
542.47(7.81)	1.4	4.74e-09	5.94	$a < 0.070\text{fm}$	$a_\mu^{\text{E}}(m_\pi^2)$
534.70(5.80)	1.1	4.05e-07	4.90	$a < 0.070\text{fm}$	$a_\mu^{\text{F}}(m_\pi^2)$
525.77(5.23)	1.0	3.41e-06	5.92	$m_\pi < 400\text{MeV} a < 0.070\text{fm}$	$a_\mu^{\text{E}}(m_\pi^2)$
517.52(7.69)	1.5	8.37e-06	5.58	$m_\pi < 400\text{MeV} a < 0.070\text{fm}$	$a_\mu^{\text{F}}(m_\pi^2)$
$t_{\text{trunc}} \pm 0$					
550.86(10.52)	1.9	3.76e-09	4.53	-	$a_\mu^{\text{E},O(a)}(m_\pi^2, a)$
533.58(9.86)	1.8	6.66e-10	4.79	-	$a_\mu^{\text{F},O(a)}(m_\pi^2, a)$
551.87(14.80)	2.7	1.36e-07	5.16	$m_\pi < 400\text{MeV}$	$a_\mu^{\text{E},O(a)}(m_\pi^2, a)$
547.92(13.67)	2.5	8.66e-07	4.72	$m_\pi < 400\text{MeV}$	$a_\mu^{\text{F},O(a)}(m_\pi^2, a)$
539.06(9.28)	1.7	5.58e-07	4.83	$a < 0.070\text{fm}$	$a_\mu^{\text{E}}(m_\pi^2)$
532.92(7.24)	1.4	1.50e-05	4.03	$a < 0.070\text{fm}$	$a_\mu^{\text{F}}(m_\pi^2)$
523.06(6.68)	1.3	5.23e-05	4.89	$m_\pi < 400\text{MeV} a < 0.070\text{fm}$	$a_\mu^{\text{E}}(m_\pi^2)$
516.11(9.55)	1.9	8.61e-05	4.70	$m_\pi < 400\text{MeV} a < 0.070\text{fm}$	$a_\mu^{\text{F}}(m_\pi^2)$
$t_{\text{trunc}} + 1$					
547.37(11.00)	2.0	5.77e-07	3.73	-	$a_\mu^{\text{E},O(a)}(m_\pi^2, a)$
531.10(10.27)	1.9	1.47e-07	3.95	-	$a_\mu^{\text{F},O(a)}(m_\pi^2, a)$
550.62(15.96)	2.9	1.48e-05	4.03	$m_\pi < 400\text{MeV}$	$a_\mu^{\text{E},O(a)}(m_\pi^2, a)$
546.39(14.54)	2.7	5.32e-05	3.72	$m_\pi < 400\text{MeV}$	$a_\mu^{\text{F},O(a)}(m_\pi^2, a)$
536.18(9.82)	1.8	1.74e-05	3.99	$a < 0.070\text{fm}$	$a_\mu^{\text{E}}(m_\pi^2)$
530.49(7.76)	1.5	2.05e-04	3.37	$a < 0.070\text{fm}$	$a_\mu^{\text{F}}(m_\pi^2)$
520.13(7.51)	1.4	4.87e-04	4.03	$m_\pi < 400\text{MeV} a < 0.070\text{fm}$	$a_\mu^{\text{E}}(m_\pi^2)$
514.40(10.47)	2.0	6.60e-04	3.91	$m_\pi < 400\text{MeV} a < 0.070\text{fm}$	$a_\mu^{\text{F}}(m_\pi^2)$

TABLE C.75: Results for the determination of a_μ^{HLO} at the physical point in units of 10^{10} for the light-quark contribution based on a simultaneous fit to data with and without m_V -rescaling using time moments.

List of Figures

1.1	Particle content of the Standard Model of particle physics.	4
1.2	Diagrams for the self-interactions of gluons.	5
1.3	Fermion and gauge fields on the lattice	8
1.4	Illustration of the terms contributing to $Q_{\mu\nu}(n)$ in the $\mu - \nu$ plane.	12
1.5	t_0 of D100t	17
1.6	Topological charge of D100t	19
1.7	Auto-correlations	21
1.8	Quark flow diagram of a meson 2-pt. correlator	22
1.9	Error vs bootstrap sample on G8	25
2.1	Diagrams for the determination of Z_V	31
2.2	Quark flow diagram of the HVP	32
2.3	The VPF on G8 for ud	36
2.4	Plot of the non perturbative estimates of Z_V	37
2.5	The Ward identity	38
2.6	The Ward identity with respect to twist angles	39
2.7	Quantification of the violation of the Ward identity	40
3.1	Contributions to the running of $\Delta\alpha_{\text{QED}}^{\text{had}}$	42
3.2	The VPF on G8 for the light-, strange- and charm-quark	45
3.3	Intermediate steps for the Adler function for the Plateau of Slopes method	48
3.4	Results for the Adler function on G8 by flavour for the Plateau of Slopes method	49
3.5	Intermediate steps for the Adler function for the Curvature Limit method	51
3.6	Results for the Adler function on G8 by flavour for the Curvature Limit method	52
3.7	Comparison of methods to extract the Adler function on G8 by flavour	53
3.8	a -dependence at fixed $m_\pi \approx 270$ MeV for ud for the Plateau of Slopes method	57
3.9	a -dependence at fixed Q^2 and fixed $m_\pi \approx 270$ MeV for ud for the Plateau of Slopes method	58
3.10	m_π -dependence at fixed a for ud for the Plateau of Slopes method	58
3.11	m_π -dependence at fixed Q^2 for ud for the Plateau of Slopes method	59
3.12	The Adler function at the physical point for ud	60
3.13	a -dependence at fixed $m_\pi \approx 270$ MeV for s for the Plateau of Slopes method	62
3.14	a -dependence at fixed Q^2 and fixed $m_\pi \approx 270$ MeV for s for the Plateau of Slopes method	63

3.15	m_π -dependence at fixed a for s for the Plateau of Slopes method	63
3.16	m_π -dependence at fixed Q^2 for s for the Plateau of Slopes method	64
3.17	The Adler function at the physical point for s	64
3.18	a -dependence at fixed $m_\pi \approx 270$ MeV for c for the Plateau of Slopes method	67
3.19	a -dependence at fixed Q^2 and fixed $m_\pi \approx 270$ MeV for c for the Plateau of Slopes method	67
3.20	m_π -dependence at fixed a for c for the Plateau of Slopes method	68
3.21	m_π -dependence at fixed Q^2 for c for the Plateau of Slopes method	69
3.22	The Adler function at the physical point for c	69
3.23	The Adler function at the physical point for uds	71
3.24	The Adler function at the physical point for $udsc$	72
3.25	Determination of $\Delta\alpha_{\text{QED}}^{\text{had}}(Q^2)$ for ud	73
3.26	Determination of $\Delta\alpha_{\text{QED}}^{\text{had}}(Q^2)$ for s	74
3.27	Determination of $\Delta\alpha_{\text{QED}}^{\text{had}}(Q^2)$ for c	75
3.28	Determination of $\Delta\alpha_{\text{QED}}^{\text{had}}(Q^2)$ for uds and $udsc$	77
4.1	Illustration of the measurement of a_μ	82
4.2	Illustration of the spin and angular momentum	82
4.3	LO contributions to a_μ	84
4.4	NLO hadronic contribution to a_μ	84
4.5	Kernel of the convolution integral for a_μ^{HLO} on G8 for ud	85
4.6	Kernel of the convolution integral for a_μ^{HLO} with and without m_V -rescaling.	86
4.7	Padé [1,1] fit to VPF on G8 for ud	88
4.8	Results for a_μ^{HLO} for ud	92
4.9	Results for a_μ^{HLO} for s	92
4.10	Polynomial fit of $O(Q^2)$ on G8 for c	94
4.11	Results for a_μ^{HLO} for c	95
4.12	Light vector masses with respect to m_π^2	98
4.13	Convergence of time moments for G8 for ud for Π_0	100
4.14	Convergence of time moments for G8 for ud for Π_1 and Π_2	101
4.15	renormalized VPF for ud on G8	102
4.16	Results for a_μ^{HLO} for ud via time moments at $t_{\text{trunc}} \pm \{0, 1\}$	105
4.17	Results for a_μ^{HLO} for ud via time moments	105
4.18	Results for a_μ^{HLO} for s via time moments at $t_{\text{trunc}} \pm \{0, 1\}$	107
4.19	Results for a_μ^{HLO} for s via time moments	107
4.20	Results for a_μ^{HLO} for c via time moments at $t_{\text{trunc}} \pm \{0, 1\}$	109
4.21	Results for a_μ^{HLO} for c via time moments	109
4.22	A -type fit for the extrapolation of a_μ^{HLO} for ud for the hybrid method	111
4.23	B -type fit for the extrapolation of a_μ^{HLO} for ud via time moments	112
4.24	C -type fit for the extrapolation of a_μ^{HLO} for ud with m_V -rescaling	113
4.25	E -type fit for the extrapolation of a_μ^{HLO} for ud	115
4.26	C -type fit for the extrapolation of a_μ^{HLO} for s	117
4.27	D -type fit for the extrapolation of a_μ^{HLO} for c	118
4.28	Kernel of the convolution integral to determine a_μ^{HLO} from the Adler function	123
4.29	Comparison of a_μ^{HLO} from different methods	125

4.30	Comparison of a_μ^{HLO} for two, three, and four flavours	127
4.31	Comparison of a_μ^{HLO} for s and c	127
B.1	a -dependence at fixed $m_\pi \approx 270$ MeV for ud for the Curvature Limit method	139
B.2	a -dependence at fixed Q^2 and fixed $m_\pi \approx 270$ MeV for ud for the Curvature Limit method	139
B.3	m_π -dependence at fixed a for ud for the Curvature Limit method	140
B.4	m_π -dependence at fixed Q^2 for ud for the Curvature Limit method	140
B.5	a -dependence at fixed $m_\pi \approx 270$ MeV for s for the Curvature Limit method	141
B.6	a -dependence at fixed Q^2 and fixed $m_\pi \approx 270$ MeV for s for the Curvature Limit method	142
B.7	m_π -dependence at fixed a for s for the Curvature Limit method	142
B.8	m_π -dependence at fixed Q^2 for s for the Curvature Limit method	143
B.9	a -dependence at fixed $m_\pi \approx 270$ MeV for c for the Plateau of Slopes method	144
B.10	a -dependence at fixed Q^2 and fixed $m_\pi \approx 270$ MeV for c for the Plateau of Slopes method	144
B.11	m_π -dependence at fixed a for c for the Curvature Limit method	145
B.12	m_π -dependence at fixed Q^2 for c for the Curvature Limit method	145
C.1	Convergence of time moments for G8 for ud for Π_3	213
C.2	Convergence of time moments for G8 for ud for Π_4	214
C.3	Convergence of time moments for G8 for s for Π_0	216
C.4	Convergence of time moments for G8 for s for Π_1	216
C.5	Convergence of time moments for G8 for s for Π_2	217
C.6	Convergence of time moments for G8 for s for Π_3	217
C.7	Convergence of time moments for G8 for s for Π_4	218
C.8	Convergence of time moments for G8 for s for Π_0	220
C.9	Convergence of time moments for G8 for s for Π_1	220
C.10	Convergence of time moments for G8 for s for Π_2	221
C.11	Convergence of time moments for G8 for s for Π_3	221
C.12	Convergence of time moments for G8 for s for Π_4	222

List of Tables

2.1	CLS ensembles	35
2.2	Hopping parameters κ_f used in this study [44]. The light-quark masses are degenerate.	35
2.3	Number of measurements	36
2.4	Non perturbatives estimates of Z_V	37
3.1	Details for the fit results of the Adler function for ud for both methods.	56
3.2	The Adler function for ud and systematic error contributions.	59
3.3	Details for the fit results of the Adler function for s (Plateau of Slopes method)	61
3.4	The Adler function for s and systematic error contributions.	65
3.5	Details for the fit results of the Adler function for c	66
3.6	The Adler function for c and systematic error contributions.	70
3.7	Relative contributions to the systematic error for $\Delta\alpha_{\text{QED}}^{\text{had}}$ for ud	73
3.8	Relative contributions to the systematic error for $\Delta\alpha_{\text{QED}}^{\text{had}}$ for s	75
3.9	Relative contributions to the systematic error for $\Delta\alpha_{\text{QED}}^{\text{had}}$ for c	76
4.1	G8 ud Padé [1,1]	89
4.2	Results for the hybrid method for a_μ^{HLO} for ud	91
4.3	Results for the hybrid method for a_μ^{HLO} for ud with m_V -rescaling	91
4.4	Results for the hybrid method for a_μ^{HLO} for s	93
4.5	Results for the hybrid method for a_μ^{HLO} for c	94
4.6	m_V and A for all ensembles and flavours	98
4.7	Time moments for ud	99
4.8	Results for a_μ^{HLO} for ud for Padé [1,1] using time moments	103
4.9	Results for a_μ^{HLO} for ud for Padé [2,1] using time moments	104
4.10	Results for a_μ^{HLO} for s for Padé [1,1] and [2,1] using time moments	106
4.11	Results for a_μ^{HLO} for c for Padé [1,1] and [2,1]	108
4.12	Results for a_μ^{HLO} at the physical point for ud using the hybrid method	114
4.13	Results for a_μ^{HLO} at the physical point for s	116
4.14	Results for a_μ^{HLO} at the physical point for c using the hybrid method	118
4.15	Results for a_μ^{HLO} at the physical point for c using time moments	119
4.16	Results for a_μ^{HLO} at the physical point for all flavours with the extended frequentist method	121
4.17	Contributions to the systematic error estimate for a_μ^{HLO} using the extended frequentist method	122
4.18	Results for a_μ^{HLO} from the Adler function	123

4.19	Contributions to the systematic error for a_μ^{HLO} from the Adler function	124
B.1	a_μ^{HLO} determined via the Adler function for the light-quark contribution	146
B.2	a_μ^{HLO} determined via the Adler function for the strange-quark contribution	147
B.3	a_μ^{HLO} determined via the Adler function for the charm-quark contribution	148
C.1	A3 ud Padé [1,1]	150
C.2	A4 ud Padé [1,1]	150
C.3	A5 ud Padé [1,1]	151
C.4	B6 ud Padé [1,1]	152
C.5	E5 ud Padé [1,1]	153
C.6	F6 ud Padé [1,1]	154
C.7	F7 ud Padé [1,1]	155
C.8	N5 ud Padé [1,1]	156
C.9	N6 ud Padé [1,1]	157
C.10	O7 ud Padé [1,1]	158
C.11	A3 ud Padé [2,1]	159
C.12	A4 ud Padé [2,1]	159
C.13	A5 ud Padé [2,1]	160
C.14	B6 ud Padé [2,1]	161
C.15	E5 ud Padé [2,1]	162
C.16	F6 ud Padé [2,1]	163
C.17	F7 ud Padé [2,1]	164
C.18	G8 ud Padé [2,1]	165
C.19	N5 ud Padé [2,1]	166
C.20	N6 ud Padé [2,1]	167
C.21	O7 ud Padé [2,1]	168
C.22	A3 s Padé [1,1]	169
C.23	A4 s Padé [1,1]	170
C.24	A5 s Padé [1,1]	170
C.25	B6 s Padé [1,1]	171
C.26	E5 s Padé [1,1]	172
C.27	F6 s Padé [1,1]	173
C.28	F7 s Padé [1,1]	174
C.29	G8 s Padé [1,1]	175
C.30	G8 s Padé [1,1]	176
C.31	N5 s Padé [1,1]	177
C.32	N6 s Padé [1,1]	178
C.33	O7 s Padé [1,1]	179
C.34	A3 s Padé [2,1]	180
C.35	A4 s Padé [2,1]	180
C.36	A5 s Padé [2,1]	181
C.37	B6 s Padé [2,1]	182
C.38	E5 s Padé [2,1]	183
C.39	F6 s Padé [2,1]	184
C.40	F7 s Padé [2,1]	185
C.41	G8 s Padé [2,1]	186

C.42 G8 <i>s</i> Padé [2,1]	187
C.43 N5 <i>s</i> Padé [2,1]	188
C.44 N6 <i>s</i> Padé [2,1]	189
C.45 O7 <i>s</i> Padé [2,1]	190
C.46 A3 <i>c</i> Padé [1,1]	191
C.47 A4 <i>c</i> Padé [1,1]	192
C.48 A5 <i>c</i> Padé [1,1]	192
C.49 B6 <i>c</i> Padé [1,1]	193
C.50 E5 <i>c</i> Padé [1,1]	194
C.51 F6 <i>c</i> Padé [1,1]	195
C.52 F7 <i>c</i> Padé [1,1]	196
C.53 G8 <i>c</i> Padé [1,1]	197
C.54 G8 <i>c</i> Padé [1,1]	198
C.55 N5 <i>c</i> Padé [1,1]	199
C.56 N6 <i>c</i> Padé [1,1]	200
C.57 O7 <i>c</i> Padé [1,1]	201
C.58 A3 <i>c</i> Polynomial of $O(Q^2)$	202
C.59 A4 <i>c</i> Polynomial of $O(Q^2)$	203
C.60 A5 <i>c</i> Polynomial of $O(Q^2)$	203
C.61 B6 <i>c</i> Polynomial of $O(Q^2)$	204
C.62 E5 <i>c</i> Polynomial of $O(Q^2)$	205
C.63 F6 <i>c</i> Polynomial of $O(Q^2)$	206
C.64 F7 <i>c</i> Polynomial of $O(Q^2)$	207
C.65 G8 <i>c</i> Polynomial of $O(Q^2)$	208
C.66 G8 <i>c</i> Polynomial of $O(Q^2)$	209
C.67 N5 <i>c</i> Polynomial of $O(Q^2)$	210
C.68 N6 <i>c</i> Polynomial of $O(Q^2)$	211
C.69 O7 <i>c</i> Polynomial of $O(Q^2)$	212
C.70 Results for the time moments of equations (4.32, 4.33) for the strange- quark contribution in lattice units. The precision for each time moment is shown as percentage. t_{trunc} refers to the values listed in table 4.6. . . .	215
C.71 Results for the time moments of equations (4.32, 4.33) for the charm- quark contribution in lattice units. The precision for each time moment is shown as percentage. t_{trunc} refers to the values listed in table 4.6. . . .	219
C.72 Results for a_μ^{HLO} at the physical point for ud using the hybrid method with a simultaneous fit to data with and without m_V -rescaling	223
C.73 Results for a_μ^{HLO} at the physical point for ud using time moments	224
C.74 Results for a_μ^{HLO} at the physical point for ud using time moments	225
C.75 Results for a_μ^{HLO} at the physical point for ud using time moments	226

Bibliography

- [1] **Particle Data Group** Collaboration, K. Olive *et al.*, “Review of Particle Physics,” *Chin.Phys.* **C38** (2014) 090001.
- [2] R. Carey, K. Lynch, J. Miller, B. Roberts, W. Morse, *et al.*, “The New (g-2) Experiment: A proposal to measure the muon anomalous magnetic moment to ± 0.14 ppm precision,”.
- [3] P. Fayet, “ u -boson production in e^+e^- annihilations, ψ and Υ decays, and light dark matter,” *Phys. Rev. D* **75** (Jun, 2007) 115017.
- [4] M. Pospelov, “Secluded $u(1)$ below the weak scale,” *Phys. Rev. D* **80** (Nov, 2009) 095002.
- [5] D. Tucker-Smith and I. Yavin, “Muonic hydrogen and MeV forces,” *Phys. Rev.* **D83** (2011) 101702, [arXiv:1011.4922 \[hep-ph\]](#).
- [6] H. Merkel *et al.*, “Searches for dark photons at the Mainz Microtron,” *AIP Conf. Proc.* **1563** (2013) 143–146.
- [7] D. J. Gross and F. Wilczek, “Ultraviolet Behavior of Nonabelian Gauge Theories,” *Phys. Rev. Lett.* **30** (1973) 1343–1346.
- [8] **ATLAS** Collaboration, G. Aad *et al.*, “Observation of a new particle in the search for the Standard Model Higgs boson with the ATLAS detector at the LHC,” *Phys. Lett.* **B716** (2012) 1–29, [arXiv:1207.7214 \[hep-ex\]](#).
- [9] **CMS** Collaboration, S. Chatrchyan *et al.*, “Observation of a new boson at a mass of 125 GeV with the CMS experiment at the LHC,” *Phys. Lett.* **B716** (2012) 30–61, [arXiv:1207.7235 \[hep-ex\]](#).
- [10] C. Gattringer and C. B. Lang, “Quantum chromodynamics on the lattice,” *Lect. Notes Phys.* **788** (2010) 1–343.
- [11] M. Creutz, *Quarks, gluons and lattices*. Cambridge Univ. Press, Cambridge, UK, 1985.

- [12] I. Montvay and G. Münster, *Quantum fields on a lattice*. Cambridge University Press, 1997.
- [13] J. Smit, “Introduction to quantum fields on a lattice: A robust mate,” *Cambridge Lect. Notes Phys.* **15** (2002) 1–271.
- [14] H. Wittig, “QCD on the lattice,”.
- [15] H. B. Nielsen and M. Ninomiya, “Absence of Neutrinos on a Lattice. 1. Proof by Homotopy Theory,” *Nucl. Phys.* **B185** (1981) 20. [,533(1980)].
- [16] H. B. Nielsen and M. Ninomiya, “No Go Theorem for Regularizing Chiral Fermions,” *Phys. Lett.* **B105** (1981) 219–223.
- [17] H. B. Nielsen and M. Ninomiya, “Absence of Neutrinos on a Lattice. 2. Intuitive Topological Proof,” *Nucl. Phys.* **B193** (1981) 173–194.
- [18] J. B. Kogut and L. Susskind, “Hamiltonian Formulation of Wilson’s Lattice Gauge Theories,” *Phys.Rev.* **D11** (1975) 395–408.
- [19] K. G. Wilson, “Confinement of Quarks,” *Phys. Rev.* **D10** (1974) 2445–2459. [45(1974)].
- [20] K. Symanzik, “Continuum Limit and Improved Action in Lattice Theories. 1. Principles and ϕ^4 Theory,” *Nucl.Phys.* **B226** (1983) 187.
- [21] K. Symanzik, “Continuum Limit and Improved Action in Lattice Theories. 2. $O(N)$ Nonlinear Sigma Model in Perturbation Theory,” *Nucl.Phys.* **B226** (1983) 205.
- [22] B. Sheikholeslami and R. Wohlert, “Improved Continuum Limit Lattice Action for QCD with Wilson Fermions,” *Nucl.Phys.* **B259** (1985) 572.
- [23] M. Lüscher, S. Sint, R. Sommer, P. Weisz, and U. Wolff, “Nonperturbative $O(a)$ improvement of lattice QCD,” *Nucl.Phys.* **B491** (1997) 323–343, [arXiv:hep-lat/9609035](https://arxiv.org/abs/hep-lat/9609035) [hep-lat].
- [24] R. Gupta, A. Morel, E. de Rafael, and F. David, “Probing the standard model of particle interactions. Proceedings, Summer School in Theoretical Physics, NATO Advanced Study Institute, 68th session, Les Houches, France, July 28-September 5, 1997. Pt. 1, 2,”.
- [25] **ALPHA** Collaboration, K. Jansen and R. Sommer, “ $O(\alpha)$ improvement of lattice QCD with two flavors of Wilson quarks,” *Nucl.Phys.* **B530** (1998) 185–203, [arXiv:hep-lat/9803017](https://arxiv.org/abs/hep-lat/9803017) [hep-lat].

- [26] N. Metropolis *et al.* *J. Chem. Phys.* **21**, 1087 (1953) .
- [27] M. Creutz, “Monte Carlo Study of Quantized SU(2) Gauge Theory,” *Phys. Rev.* **D21** (1980) 2308–2315.
- [28] S. L. Adler, “An Overrelaxation Method for the Monte Carlo Evaluation of the Partition Function for Multiquadratic Actions,” *Phys. Rev.* **D23** (1981) 2901.
- [29] C. Whitmer, “Over-relaxation methods for Monte Carlo simulations of quadratic and multiquadratic actions,” *Phys. Rev.* **29** (1984) 306.
- [30] M. Creutz, “MICROCANONICAL MONTE CARLO SIMULATION,” *Phys. Rev. Lett.* **50** (1983) 1411.
- [31] D. J. E. Callaway and A. Rahman, “Lattice Gauge Theory in Microcanonical Ensemble,” *Phys. Rev.* **D28** (1983) 1506.
- [32] S. Duane, A. D. Kennedy, B. J. Pendleton, and D. Roweth, “Hybrid Monte Carlo,” *Phys. Lett.* **B195** (1987) 216–222.
- [33] G. Parisi and Y. Wu, “Perturbation Theory Without Gauge Fixing,” *Sci. Sin.* **24** (1981) 483.
- [34] J. R. Klauder, “STOCHASTIC QUANTIZATION,” *Acta Phys. Austriaca Suppl.* **25** (1983) 251–281.
- [35] P. H. Damgaard and H. Huffel, “Stochastic Quantization,” *Phys. Rept.* **152** (1987) 227.
- [36] M. Lüscher, “Solution of the dirac equation in lattice qcd using a domain decomposition method,” *Comput. Phys. Commun.* **156** (2004) 209–220, [arXiv:hep-lat/0310048](https://arxiv.org/abs/hep-lat/0310048) [[hep-lat](#)].
- [37] M. Lüscher, “Schwarz-preconditioned HMC algorithm for two-flavour lattice QCD,” *Comput. Phys. Commun.* **165** (2005) 199–220, [arXiv:hep-lat/0409106](https://arxiv.org/abs/hep-lat/0409106) [[hep-lat](#)].
- [38] M. Lüscher, “Computational Strategies in Lattice QCD,” in *Modern perspectives in lattice QCD: Quantum field theory and high performance computing. Proceedings, International School, 93rd Session, Les Houches, France, August 3-28, 2009.*
- [39] M. Hasenbusch and K. Jansen, “Speeding up lattice QCD simulations with clover improved Wilson fermions,” *Nucl. Phys.* **B659** (2003) 299–320, [arXiv:hep-lat/0211042](https://arxiv.org/abs/hep-lat/0211042) [[hep-lat](#)].

- [40] M. Bruno, D. Djukanovic, G. P. Engel, A. Francis, G. Herdoiza, *et al.*, “Simulation of QCD with $N_f = 2 + 1$ flavors of non-perturbatively improved Wilson fermions,” *JHEP* **1502** (2015) 043, [arXiv:1411.3982 \[hep-lat\]](#).
- [41] M. Lüscher and P. Weisz, “On-Shell Improved Lattice Gauge Theories,” *Commun. Math. Phys.* **97** (1985) 59. [Erratum: *Commun. Math. Phys.* 98,433(1985)].
- [42] M. Lüscher, “Properties and uses of the Wilson flow in lattice QCD,” *JHEP* **08** (2010) 071, [arXiv:1006.4518 \[hep-lat\]](#). [Erratum: *JHEP*03,092(2014)].
- [43] M. Lüscher, “openQCD package,”
<http://luscher.web.cern.ch/luscher/openQCD/>.
- [44] P. Fritzscht, F. Knechtli, B. Leder, M. Marinkovic, S. Schäfer, *et al.*, “The strange quark mass and Lambda parameter of two flavor QCD,” *Nucl.Phys.* **B865** (2012) 397–429, [arXiv:1205.5380 \[hep-lat\]](#).
- [45] M. Lüscher, “Topology, the Wilson flow and the HMC algorithm,” *PoS LATTICE2010* (2010) 015, [arXiv:1009.5877 \[hep-lat\]](#).
- [46] M. Lüscher and S. Schaefer, “Lattice QCD without topology barriers,” *JHEP* **07** (2011) 036, [arXiv:1105.4749 \[hep-lat\]](#).
- [47] M. Lüscher and S. Schaefer, “Lattice QCD with open boundary conditions and twisted-mass reweighting,” *Comput. Phys. Commun.* **184** (2013) 519–528, [arXiv:1206.2809 \[hep-lat\]](#).
- [48] L. Del Debbio, H. Panagopoulos, and E. Vicari, “theta dependence of SU(N) gauge theories,” *JHEP* **08** (2002) 044, [arXiv:hep-th/0204125 \[hep-th\]](#).
- [49] S. Schaefer, R. Sommer, and F. Virotta, “Investigating the critical slowing down of QCD simulations,” *PoS LAT2009* (2009) 032, [arXiv:0910.1465 \[hep-lat\]](#).
- [50] **ALPHA** Collaboration, U. Wolff, “Monte Carlo errors with less errors,” *Comput. Phys. Commun.* **156** (2004) 143–153, [arXiv:hep-lat/0306017 \[hep-lat\]](#). [Erratum: *Comput. Phys. Commun.*176,383(2007)].
- [51] M. Lüscher, “DD-HMC package,”
<http://luscher.web.cern.ch/luscher/DD-HMC/index.html>.
- [52] S. Güsken, “A Study of smearing techniques for hadron correlation functions,” *Nucl. Phys. Proc. Suppl.* **17** (1990) 361–364.

- [53] S. Güsken *et al.*, “Non-singlet axial vector couplings of the baryon octet in lattice QCD,” *Phys. Lett. B* **227** no. CERN-TH-5380-89. WU-B-89-9, (May, 1989) 266–269. 9 p. <https://cds.cern.ch/record/197601>.
- [54] C. Alexandrou *et al.*, “B meson properties from lattice QCD,” *Phys. Lett.* **B256** (1991) 60–67.
- [55] UKQCD Collaboration, C. R. Allton *et al.*, “Gauge invariant smearing and matrix correlators using Wilson fermions at Beta = 6.2,” *Phys. Rev.* **D47** (1993) 5128–5137, [arXiv:hep-lat/9303009](https://arxiv.org/abs/hep-lat/9303009) [hep-lat].
- [56] S. Capitani, M. Della Morte, D. Djukanovic, G. von Hippel, J. Hua, B. Jäger, B. Knippschild, H. B. Meyer, T. D. Rae, and H. Wittig, “Nucleon electromagnetic form factors in two-flavor QCD,” *Phys. Rev.* **D92** no. 5, (2015) 054511, [arXiv:1504.04628](https://arxiv.org/abs/1504.04628) [hep-lat].
- [57] B. Efron, “Bootstrap Methods: Another Look at the Jackknife,” *The Annals of Statistics* **Vol. 7, No. 1.** (1979) pp. 1–26.
- [58] W.-M. Yao *et al.*, “Review of Particle Physics,” *Journal of Physics G* **33** (2006) 1+. <http://pdg.lbl.gov>.
- [59] S. Durr *et al.*, “Ab-Initio Determination of Light Hadron Masses,” *Science* **322** (2008) 1224–1227, [arXiv:0906.3599](https://arxiv.org/abs/0906.3599) [hep-lat].
- [60] JLQCD, CP-PACS Collaboration, A. Ukawa, “Computational cost of full QCD simulations experienced by CP-PACS and JLQCD Collaborations,” *Nucl. Phys. Proc. Suppl.* **106** (2002) 195–196. [195(2002)].
- [61] M. Luscher, S. Sint, R. Sommer, and H. Wittig, “Nonperturbative determination of the axial current normalization constant in O(a) improved lattice QCD,” *Nucl. Phys.* **B491** (1997) 344–364, [arXiv:hep-lat/9611015](https://arxiv.org/abs/hep-lat/9611015) [hep-lat].
- [62] M. Della Morte and A. Jüttner, “Quark disconnected diagrams in chiral perturbation theory,” *JHEP* **11** (2010) 154, [arXiv:1009.3783](https://arxiv.org/abs/1009.3783) [hep-lat].
- [63] D. Bernecker and H. B. Meyer, “Vector Correlators in Lattice QCD: Methods and applications,” *Eur. Phys. J.* **A47** (2011) 148, [arXiv:1107.4388](https://arxiv.org/abs/1107.4388) [hep-lat].
- [64] V. Gülpers, A. Francis, B. Jäger, H. Meyer, G. von Hippel, and H. Wittig, “The leading disconnected contribution to the anomalous magnetic moment of the muon,” *PoS LATTICE2014* (2014) 128, [arXiv:1411.7592](https://arxiv.org/abs/1411.7592) [hep-lat].
- [65] C. T. Sachrajda and G. Villadoro, “Twisted boundary conditions in lattice simulations,” *Phys. Lett.* **B609** (2005) 73–85, [arXiv:hep-lat/0411033](https://arxiv.org/abs/hep-lat/0411033) [hep-lat].

- [66] P. F. Bedaque and J.-W. Chen, “Twisted valence quarks and hadron interactions on the lattice,” *Phys. Lett.* **B616** (2005) 208–214, [arXiv:hep-lat/0412023 \[hep-lat\]](#).
- [67] G. M. de Divitiis, R. Petronzio, and N. Tantalo, “On the discretization of physical momenta in lattice QCD,” *Phys. Lett.* **B595** (2004) 408–413, [arXiv:hep-lat/0405002 \[hep-lat\]](#).
- [68] S. Lottini and R. Sommer, “private communications,”.
- [69] G. von Hippel, “private communications,”.
- [70] J. Green, “private communications,”.
- [71] C. Aubin, T. Blum, M. Golterman, and S. Peris, “Hadronic vacuum polarization with twisted boundary conditions,” *Phys.Rev.* **D88** no. 7, (2013) 074505, [arXiv:1307.4701 \[hep-lat\]](#).
- [72] H. Horch, G. Herdoíza, B. Jäger, H. Wittig, M. Della Morte, *et al.*, “Computing the Adler function from the vacuum polarization function,” *PoS LATTICE2013* (2014) 304, [arXiv:1311.6975 \[hep-lat\]](#).
- [73] A. Petermann, “La normalisation des constantes dans la théorie des quanta Normalization of constants in the quanta theory,” *Helv. Phys. Acta* **26** (1953) 499–520.
- [74] N. N. Bogolyubov and D. V. Shirkov, “Charge renormalization group in quantum field theory,” *Nuovo Cim.* **3** (1956) 845–863.
- [75] M. Gell-Mann and F. E. Low, “Quantum electrodynamics at small distances,” *Phys. Rev.* **95** (1954) 1300–1312.
- [76] M. Davier, A. Hoecker, B. Malaescu, and Z. Zhang, “Reevaluation of the Hadronic Contributions to the Muon $g-2$ and to $\alpha(M_Z)$,” *Eur. Phys. J.* **C71** (2011) 1515, [arXiv:1010.4180 \[hep-ph\]](#). [Erratum: *Eur. Phys. J.* **C72**,1874(2012)].
- [77] **OPAL** Collaboration, G. Abbiendi *et al.*, “Tests of the standard model and constraints on new physics from measurements of fermion pair production at 189-GeV to 209-GeV at LEP,” *Eur. Phys. J.* **C33** (2004) 173–212, [arXiv:hep-ex/0309053 \[hep-ex\]](#).
- [78] F. Jegerlehner, “Electroweak effective couplings for future precision experiments,” *Nuovo Cim.* **C034S1** (2011) 31–40, [arXiv:1107.4683 \[hep-ph\]](#).

- [79] K. Hagiwara, R. Liao, A. D. Martin, D. Nomura, and T. Teubner, “ $(g - 2)_\mu$ and $\alpha(M_Z^2)$ re-evaluated using new precise data,” *J. Phys.* **G38** (2011) 085003, [arXiv:1105.3149 \[hep-ph\]](#).
- [80] F. Jegerlehner, “The Running fine structure constant $\alpha(E)$ via the Adler function,” *Nucl. Phys. Proc. Suppl.* **181-182** (2008) 135–140, [arXiv:0807.4206 \[hep-ph\]](#).
- [81] S. L. Adler, “Some Simple Vacuum Polarization Phenomenology: $e^+e^- \rightarrow$ Hadrons: The mu - Mesic Atom x-Ray Discrepancy and $(g-2)$ of the Muon,” *Phys.Rev.* **D10** (1974) 3714.
- [82] F. Jegerlehner, “The anomalous magnetic moment of the muon,” *Springer Tracts Mod.Phys.* **226** (2008) 1–426.
- [83] S. Eidelman, F. Jegerlehner, A. Kataev, and O. Veretin, “Testing nonperturbative strong interaction effects via the Adler function,” *Phys.Lett.* **B454** (1999) 369–380, [arXiv:hep-ph/9812521 \[hep-ph\]](#).
- [84] M. Della Morte, B. Jäger, A. Jüttner, and H. Wittig, “Towards a precise lattice determination of the leading hadronic contribution to $(g - 2)_\mu$,” *JHEP* **03** (2012) 055, [arXiv:1112.2894 \[hep-lat\]](#).
- [85] C. Aubin, T. Blum, M. Golterman, and S. Peris, “Model-independent parametrization of the hadronic vacuum polarization and $g - 2$ for the muon on the lattice,” *Phys. Rev.* **D86** (2012) 054509, [arXiv:1205.3695 \[hep-lat\]](#).
- [86] F. Jegerlehner, “pQCD-Adler package,” <http://www-com.physik.hu-berlin.de/~fjeger/software.html>.
- [87] F. Jegerlehner, “The Effective fine structure constant at TESLA energies,” [arXiv:hep-ph/0105283 \[hep-ph\]](#).
- [88] F. Jegerlehner, “The effective fine structure constant and other SM running couplings, alphaQED package,” <http://www-com.physik.hu-berlin.de/~fjeger/software.html>.
- [89] **Muon g-2** Collaboration, G. Bennett *et al.*, “Final Report of the Muon E821 Anomalous Magnetic Moment Measurement at BNL,” *Phys.Rev.* **D73** (2006) 072003, [arXiv:hep-ex/0602035 \[hep-ex\]](#).
- [90] J. M. Paley, “Measurement of the anomalous magnetic moment of the negative muon to 0.7 parts per million,”

- [91] F. Farley and E. Picasso, “The Muon $g-2$ experiments,” *Adv.Ser.Direct.High Energy Phys.* **7** (1990) 479–559.
- [92] V. Hughes, “The anomalous magnetic moment of the muon,” *Int.J.Mod.Phys.* **A18S1** (2003) 215–272.
- [93] T. Aoyama, M. Hayakawa, T. Kinoshita, and M. Nio, “Complete Tenth-Order QED Contribution to the Muon $g-2$,” *Phys.Rev.Lett.* **109** (2012) 111808, [arXiv:1205.5370 \[hep-ph\]](#).
- [94] T. Aoyama, M. Hayakawa, T. Kinoshita, and M. Nio, “Tenth-Order QED Contribution to the Electron $g-2$ and an Improved Value of the Fine Structure Constant,” *Phys.Rev.Lett.* **109** (2012) 111807, [arXiv:1205.5368 \[hep-ph\]](#).
- [95] T. Kinoshita and M. Nio, “Improved α^4 term of the electron anomalous magnetic moment,” *Phys.Rev.* **D73** (2006) 013003, [arXiv:hep-ph/0507249 \[hep-ph\]](#).
- [96] T. Aoyama, M. Hayakawa, T. Kinoshita, and M. Nio, “Revised value of the eighth-order electron $g-2$,” *Phys.Rev.Lett.* **99** (2007) 110406, [arXiv:0706.3496 \[hep-ph\]](#).
- [97] T. Kinoshita and M. Nio, “Improved α^4 term of the muon anomalous magnetic moment,” *Phys.Rev.* **D70** (2004) 113001, [arXiv:hep-ph/0402206 \[hep-ph\]](#).
- [98] T. Kinoshita *Nucl. Phys.* **B144** (2005) 206 (Proc. Supp.).
- [99] T. Kinoshita and M. Nio, “The Tenth-order QED contribution to the lepton $g-2$: Evaluation of dominant α^5 terms of muon $g-2$,” *Phys.Rev.* **D73** (2006) 053007, [arXiv:hep-ph/0512330 \[hep-ph\]](#).
- [100] A. Kataev, “The Comments on QED contributions to $(g-2)(\mu)$,” [arXiv:hep-ph/0602098 \[hep-ph\]](#).
- [101] M. Passera *J. Phys.* **G31** (2005) 75.
- [102] R. Jackiw and S. Weinberg *Phys. Rev.* **D5**, 2396 (1972) .
- [103] G. Altarelli *et al. Phys. Lett.* **B40**, 415 (1972) .
- [104] I. Bars and M. Yoshimura *Phys. Rev.* **D6**, 374 (1972) .
- [105] K. Fujikawa, B. W. Lee, and A. Sanda *Phys. Rev.* **D6**, 2923 (1972) .
- [106] C. Gnendiger, D. Stöckinger, and H. Stöckinger-Kim *Phys. Rev.* **D88** (2013) 053005.

- [107] A. Czarnecki *et al.* *Phys. Rev. D* **67**, 073006, Erratum *ibid.* *Phys. Rev.* **D73**, 119901 (2003) .
- [108] S. Heinemeyer, D. Stöckinger, and G. Weiglein *Nucl. Phys.* **B699** (2004) 103.
- [109] T. Gribouk and A. Czarnecki *Phys. Rev.* **D72** (2005) 053016.
- [110] A. Czarnecki, B. Krause, and W. J. Marciano *Phys. Rev. Lett.* **76** (1996) 3267.
- [111] A. Czarnecki, B. Krause, and W. Marciano *Phys. Rev.* **D52** (1995) 2619.
- [112] S. Peris, M. Perrottet, and E. de Rafael *Phys. Lett.* **B355** (1995) 523.
- [113] T. Kukhto *et al.* *Nucl. Phys.* **B371** (1992) 567.
- [114] M. Davier *et al.* *Eur. Phys. J.* **C71** (2011) 1515.
- [115] J. Prades, E. de Rafael, and A. Vainshtein, “Hadronic Light-by-Light Scattering Contribution to the Muon Anomalous Magnetic Moment,” [arXiv:0901.0306](https://arxiv.org/abs/0901.0306) [[hep-ph](https://arxiv.org/archive/hep)].
- [116] T. Blum, S. Chowdhury, M. Hayakawa, and T. Izubuchi, “Hadronic light-by-light scattering contribution to the muon anomalous magnetic moment from lattice QCD,” *Phys. Rev. Lett.* **114** no. 1, (2015) 012001, [arXiv:1407.2923](https://arxiv.org/abs/1407.2923) [[hep-lat](https://arxiv.org/archive/hep)].
- [117] J. Green, N. Asmussen, O. Gryniuk, G. von Hippel, H. B. Meyer, A. Nyffeler, and V. Pascalutsa, “Direct calculation of hadronic light-by-light scattering,” in *Proceedings, 33rd International Symposium on Lattice Field Theory (Lattice 2015)*.
- [118] M. Golterman, K. Maltman, and S. Peris, “New strategy for the lattice evaluation of the leading order hadronic contribution to $(g - 2)_\mu$,” *Phys. Rev.* **D90** no. 7, (2014) 074508, [arXiv:1405.2389](https://arxiv.org/abs/1405.2389) [[hep-lat](https://arxiv.org/archive/hep)].
- [119] D. B. Renner, X. Feng, K. Jansen, and M. Petschlies, “Nonperturbative QCD corrections to electroweak observables,” *PoS LATTICE2011* (2012) 022, [arXiv:1206.3113](https://arxiv.org/abs/1206.3113) [[hep-lat](https://arxiv.org/archive/hep)].
- [120] **HPQCD** Collaboration, B. Chakraborty, C. T. H. Davies, G. C. Donald, R. J. Dowdall, J. Koponen, G. P. Lepage, and T. Teubner, “Strange and charm quark contributions to the anomalous magnetic moment of the muon,” *Phys. Rev.* **D89** no. 11, (2014) 114501, [arXiv:1403.1778](https://arxiv.org/abs/1403.1778) [[hep-lat](https://arxiv.org/archive/hep)].
- [121] B. Chakraborty, C. T. H. Davies, P. G. de Oliveira, J. Koponen, and G. P. Lepage, “The hadronic vacuum polarization contribution to a_μ from full lattice QCD,” [arXiv:1601.03071](https://arxiv.org/abs/1601.03071) [[hep-lat](https://arxiv.org/archive/hep)].

- [122] Della Morte, M. and Francis, A. and Gülpers, V. and Herdoiza, G. and von Hippel, G. and Horch, H. and Jäger, B., and Meyer, H.B., and Wittig, H., “The hadronic vacuum polarisation contribution to the muon $g-2$ from lattice QCD,” *in preparation* .
- [123] B. e. Lautrup, A. Peterman, and E. de Rafael, “Recent developments in the comparison between theory and experiments in quantum electrodynamics,” *Phys. Rept.* **3** (1972) 193.
- [124] M. Knecht, “The Anomalous magnetic moment of the muon: A Theoretical introduction,” *Lect. Notes Phys.* **629** (2004) 37–84, [arXiv:hep-ph/0307239 \[hep-ph\]](#).
- [125] **ETM** Collaboration, F. Burger, X. Feng, G. Hotzel, K. Jansen, M. Petschlies, and D. B. Renner, “Four-Flavour Leading-Order Hadronic Contribution To The Muon Anomalous Magnetic Moment,” *JHEP* **02** (2014) 099, [arXiv:1308.4327 \[hep-lat\]](#).
- [126] P. Boyle, L. Del Debbio, E. Kerrane, and J. Zanotti, “Lattice Determination of the Hadronic Contribution to the Muon $g - 2$ using Dynamical Domain Wall Fermions,” *Phys. Rev.* **D85** (2012) 074504, [arXiv:1107.1497 \[hep-lat\]](#).
- [127] C. Aubin and T. Blum, “Calculating the hadronic vacuum polarization and leading hadronic contribution to the muon anomalous magnetic moment with improved staggered quarks,” *Phys. Rev.* **D75** (2007) 114502, [arXiv:hep-lat/0608011 \[hep-lat\]](#).
- [128] X. Feng, K. Jansen, M. Petschlies, and D. B. Renner, “Two-flavor QCD correction to lepton magnetic moments at leading-order in the electromagnetic coupling,” *Phys. Rev. Lett.* **107** (2011) 081802, [arXiv:1103.4818 \[hep-lat\]](#).
- [129] **RBC/UKQCD** Collaboration, T. Blum *et al.*, “Lattice calculation of the leading strange quark-connected contribution to the muon $g - 2$,” *JHEP* **04** (2016) 063, [arXiv:1602.01767 \[hep-lat\]](#).
- [130] **Budapest-Marseille-Wuppertal** Collaboration, R. Malak, Z. Fodor, C. Hoelbling, L. Lellouch, A. Sastre, and K. Szabo, “Finite-volume corrections to the leading-order hadronic contribution to $g_\mu - 2$,” *PoS LATTICE2014* (2015) 161, [arXiv:1502.02172 \[hep-lat\]](#).
- [131] C. Aubin, T. Blum, P. Chau, M. Golterman, S. Peris, and C. Tu, “Finite-volume effects in the hadronic vacuum polarization,” in *Proceedings, 33rd International Symposium on Lattice Field Theory (Lattice 2015)*.

-
- [132] H. Meyer, “private communications,”.
- [133] A. Francis, B. Jäger, H. B. Meyer, and H. Wittig, “A new representation of the Adler function for lattice QCD,” *Phys. Rev.* **D88** (2013) 054502, [arXiv:1306.2532 \[hep-lat\]](#).

Lebenslauf

- **06/2012 - 09/2016** - Doktorand am Institut für Kernphysik, Johannes Gutenberg Universität Mainz.
- **04/2012 - 06/2012** - Wissenschaftliche Hilfskraft in der AG Wittig am Institut für Kernphysik, Johannes Gutenberg Universität Mainz..
- **04/2006 - 02/2012** - Studium der Physik, Johannes Gutenberg Universität Mainz.
- **05/2005 - 01/2006** - Zivildienst beim Deutschen Roten Kreuz in Alzey als Rettungssanitäter.
- **08/1996 - 03/2005** - Abitur am Elisabeth-Langgässer Gymnasium, Alzey.
- **08/1992 - 07/1996** - Besuch der Grundschule Kriegsfeld.
- **05/02/1986** - Geboren in Kirchheimbolanden.